The relationship between near-wake structure and heat transfer for an oscillating circular cylinder in cross-flow

Thesis by
Tait Sherman Pottebaum

In Partial Fulfillment of
the Requirements for the Degree of
Doctor of Philosophy

California Institute of Technology

Pasadena, California

2003

(Defended April 11, 2003)

Acknowledgements

First, I would like to thank my advisor, Professor Mory Gharib. You have taught me about much more than just fluid mechanics and performing experiments. I appreciate the support, freedom and understanding that you have given me. Thank you for believing that where I go and the person I am when I leave Caltech are as much a part of your job as the research that I did while I was here.

I would also like to thank Professor Tony Leonard, Professor Anatol Roshko and Joe Klamo for their many comments, suggestions and insights throughout the process of doing this research. Professor Leonard also served on my thesis committee and provided useful feedback on this thesis. I also appreciate the sense of camaraderie that Joe Klamo brought to the Noah Lab.

I also would like to thank the other members of my thesis committee: Professors Joe Shepherd, Melany Hunt and Mark Richardson.

I could not have learned what I needed to know without the help of many others in the Gharib group. In particular, I want to thank Han Park, Dana Dabiri and David Jeon for their assistance with experimental techniques.

Finally, I want to thank those people whose contributions are less tangible, but equally important. To Sarah and to my entire family, thank you for being my support and motivation. Thank you to my friends at GALCIT, Gabe Acevedo-Bolton, Matt Fago and Mike Rubel, for making this whole experience more fun.

This research was supported by NSF Grant CTS-9903346.

This thesis is dedicated to my wife, Sarah,

for all the love and support she has given me through this process

and for her everlasting faith in my capabilities.

Abstract

A series of experiments were carried out in order to understand the relationship between wake structure and heat transfer for a transversely oscillating circular cylinder in cross-flow and to explore the dynamics of the vortex formation process in the wake. The cylinder's heat transfer coefficient was determined over a range of oscillation amplitudes up to 1.5 cylinder diameters and oscillation frequencies up to 5 times the stationary cylinder natural shedding frequency. The results were compared to established relationships between oscillation conditions and wake structure. Digital particle image thermometry/velocimetry (DPIT/V) was used to measure the temperature and velocity fields in the near-wake for a set of cases chosen to be representative of the variety of wake structures that exist for this type of flow. The experiments were carried out in a water tunnel at a Reynolds number of 690.

It was found that wake structure and heat transfer both significantly affect one another. The wake mode, a label indicating the number and type of vortices shed in each oscillation period, is directly related to the observed heat transfer enhancement. The dynamics of the vortex formation process, including the trajectories of the vortices during roll-up, explain this relationship. The streamwise spacing between shed vortices was also shown to affect heat transfer coefficient for the 2S mode, which consists of two single vortices shed per cycle. The streamwise spacing is believed to influence entrainment of freestream temperature fluid by the forming vortices, thereby affecting the temperature gradient at the cylinder base. This effect may exist for other wake modes, as well.

The cylinder’s transverse velocity was shown to influence the heat transfer by affecting the circulation of the wake vortices. For a fixed wake structure, the effectiveness of the wake vortices at enhancing heat transfer depends on their circulation. Also, the cylinder’s transverse velocity continually changes the orientation of the wake with respect to the freestream flow, thereby spreading the main source of heat transfer enhancement—the vortices near the cylinder base—over a larger portion of the cylinder surface.

Previously observed heat transfer enhancement associated with oscillations at frequencies near the natural shedding frequency and its harmonics were shown to be limited to amplitudes of less than about 0.5 cylinder diameters.

A new phenomenon was discovered in which the wake structure switches back and forth between distinct wake modes. Temperature induced variations in the fluid viscosity are believed to be the cause of this mode-switching. It is hypothesized that the viscosity variations change the vorticity and kinetic energy fluxes into the wake, thereby changing the wake mode and the heat transfer coefficient. This discovery underscores the role of viscosity and shear layer fluxes in determining wake mode, potentially leading to improved understanding of wake vortex formation and pinch-off processes in general.

Aspect ratio appears to play a role in determining the heat transfer coefficient mainly for non-oscillating cylinders. The heat transfer is also affected by aspect ratio for oscillation conditions characterized by weak synchronization of the wake to the oscillation frequency.

Table of Contents

List of Figures

List of Tables

List of Symbols

Roman symbols

A	oscillation amplitude
b	index of phase bin
B	blue intensity
B	number of phase bins
C	specific heat capacity
C_w	specific heat capacity of water
D	cylinder diameter
f	frequency of cylinder oscillation
f_{St}	Strouhal frequency, natural shedding frequency of non-oscillating cylinder
f^*	non-dimensional oscillation frequency (fD/U)
f^*_{St}	non-dimensional Strouhal frequency (f_{St}D/U)
g	acceleration due to gravity
G	green intensity
Gr	Grashof number $\left(\frac{g\beta(T_{surf}-T_\infty)D^3}{\nu^2}\right)$
h	average heat transfer coefficient
h_0	average heat transfer coefficient of non-oscillating cylinder
h_θ	local heat transfer coefficient
H	hue angle
I	intensity
k	thermal conductivity
k_a	thermal conductivity of region a in the model of cylinder structure
k_b	thermal conductivity of region b in the model of cylinder structure
k_c	thermal conductivity of region c in the model of cylinder structure
k_d	thermal conductivity of region d in the model of cylinder structure
k_w	thermal conductivity of water
L	cylinder length
n	index of snapshot
n_b	index of snapshot in phase bin b
N	number of snapshots
N_b	number of snapshots in phase bin b
Nu	average Nusselt number, average non-dimensional heat transfer coefficient (hD/k)
Nu_0	average Nusselt number of non-oscillating cylinder
Nu_θ	local Nusselt number
p_{in}	heating power input to cylinder per unit volume
P_{in}	total heating power input to cylinder
Pr	Prandtl number (ν/α)
r	radial distance of an arbitrary point from the cylinder axis
R	radial distance of a fixed point from the cylinder axis

R	red intensity
R_a	outer radius of region a in the model of cylinder structure
R_b	outer radius of region b in the model of cylinder structure
R_c	outer radius of region c in the model of cylinder structure
R_d	outer radius of region d in the model of cylinder structure
Re	Reynolds number (UD/ν)
Ri	Richardson number (Gr/Re^2)
S	saturation
t	time
T	temperature
$\tilde{T}$	difference between the temperature distribution inside the cylinder and the initial condition for time-dependent heat transfer model
T_{tc}	temperature of the thermocouple embedded in cylinder
T_{surf}	surface temperature of cylinder
T_∞	freestream temperature
T^*	normalized temperature ($(T-T_\infty)/(T_{surf}-T_\infty)$)
u	velocity component in the x-direction
$\underline{u}$	velocity vector
U	freestream velocity
v	velocity component in the y-direction
v_1	first hue-saturation color component
v_2	second hue-saturation color component
V_{rms}	root-mean-square of the cylinder transverse speed
x	direction of the freestream flow
y	transverse direction (perpendicular to freestream and cylinder axis)
z	direction of the cylinder axis

Greek symbols

α	thermal diffusivity ($k/\rho C$)
α_w	thermal diffusivity of water
β	volumetric coefficient of thermal expansion
$\delta(\,)$	differential amount of the following quantity
$\delta_{(\,)}$	uncertainty in the subscripted quantity
Γ	circulation
η	vortex shedding angle
ϕ	phase of cylinder motion
λ	wavelength of cylinder oscillation
λ_f	formation length of wake
ν	kinematic viscosity
θ	angular coordinate (0 = upstream stagnation point)
ρ	density
ρ_w	density of water
τ	cylinder thermal time constant
ω	vorticity component in the z direction

1 Introduction

1.1 Introduction

Understanding heat transfer from transversely oscillating circular cylinders in cross-flow is an important and challenging engineering problem. The basic arrangement of interest is shown in Figure 1.1. A heated cylinder is in a cross-flow and oscillates in the direction perpendicular to the freestream velocity, U, and to the cylinder axis.

Vortex-induced vibration is known to occur for long, cylindrical elements in tube-bank heat exchangers. This makes it important to understand how oscillations affect the heat transfer so that equipment can be properly designed. The possibility of exploiting oscillation effects in new heat exchanger designs over a wide range of length scale, either through forced or vortex-induced vibrations, also requires that the relationship between oscillations and heat transfer be understood.

Many areas of fluid mechanics are involved in understanding this type of flow. Convective heat transfer, fluid-structure interactions, separated flows and vortex dynamics are all involved in relating cylinder oscillations to heat transfer. This makes for an interesting but challenging problem.

While it is evident from a review of the literature that the wake structure is the connection between oscillations and heat transfer, the mechanism of this connection is not understood. In addition, it is not known how the cylinder oscillations determine the wake structure or what other factors, if any, are involved in this process. Therefore, there are two main goals of this study. First, to understand the mechanism through which transverse cylinder oscillations modify the heat transfer from the cylinder to the cross-flow. This goal is pursued by focusing on changes to the wake structure produced by oscillations and on how the wake structure in turn affects the heat transfer. Second, to explore the dynamics of the vortex formation processes in the wake, which has broad relevance beyond just heat transfer applications.

This thesis presents the results of experiments on heat transfer from transversely oscillating circular cylinders. Two sets of experiments were carried out. In the first set, the cylinder's heat transfer coefficient was measured for a wide range of oscillation conditions, and the results were compared to known relationships between oscillation conditions and wake structure. The second set of experiments used digital particle image thermometry/velocimetry to measure the temperature and velocity fields in the near-wake for a smaller set of cases. This allowed the vortex formation process and the effects of wake structure on heat transfer to be examined directly.

1.2 Reviews

1.2.1 Circular cylinder wakes

The wake of a smooth, circular cylinder in a steady freestream flow can take several different forms. The form of the wake is primarily determined by the Reynolds number

$$\mathrm{Re} = \frac{UD}{\nu}, \qquad (1.1)$$

where U is the freestream velocity, D is the cylinder diameter, and ν is the kinematic viscosity of the fluid. This parameter indicates the relative magnitude of inertial and viscous forces. Changes in the form of the wake are related to stability transitions of various parts of the flow, such as the boundary layers or the free shear layers, if they exist, and these transitions occur at particular values of the Reynolds number.

For all Reynolds numbers, there is a stagnation point at the leading edge of the cylinder. From this stagnation point, boundary layers grow along the cylinder surface. For sufficiently low Reynolds numbers (Re < ~5), these boundary layers remain attached to the surface all the way to the trailing edge of the cylinder, where there is a second stagnation point. For higher Reynolds numbers, the boundary layers separate (Taneda, 1956). If the boundary layers remain laminar (Re < $\sim 2 \cdot 10^5$), the separation point is at about 80° from the forward stagnation point. For turbulent boundary layers, the separation point moves downstream to around 140° from the forward stagnation point. This results in a significantly narrower wake than in the laminar boundary layer case.

The vorticity in the free shear layers formed by the separated boundary layers rolls up into vortices in the wake. For Re < ~40, these vortices are steady and the wake is symmetric with respect to the cylinder centerline. At Reynolds numbers greater than about 40 the symmetric wake is unstable, and the Kármán Vortex Street is formed as vortices are shed from alternating sides of the cylinder. The frequency at which vortices are shed is known as the Strouhal frequency, f_{St}. The non-dimensional shedding frequency, or Strouhal number

$$St = \frac{f_{St} D}{U}, \tag{1.2}$$

is a function of the Reynolds number. A compilation of data on this relationship is shown in Figure 1.2.

Additional transitions of the cylinder wake relate to turbulence and three-dimensionality in the wake. The cylinder wake is three dimensional for Re > ~180 (Williamson 1988). Above Reynolds number about 1000, the separated shear layers are turbulent.

Aspect ratio is also known to affect the wake of a circular cylinder. Norberg (1994) presents a review of these effects.

The wake of a cylinder that is oscillating sinusoidally in the direction transverse to the freestream direction can be significantly different than the wake of a non-oscillating cylinder. Williamson and Roshko (1988) systematically studied the structure of wakes produced under different oscillation conditions. They identified several distinct distributions of vortices in the wake, which they referred to as wake modes. These modes are shown in Figure 1.3. They identified the relevant non-dimensional parameters for determining the wake mode as the amplitude ratio, A/D, and the wavelength ratio, λ/D, where λ is the wavelength of the sinusoidal oscillations in a coordinate system moving with the freestream. The regions of the parameter space defined by A/D and λ/D where the various wake modes occur are indicated in Figure 1.4.

It is important to note that the experiments conducted to locate these regions were carried out over a range of Reynolds numbers from 300 – 1000. The exact position of the mode boundaries has been observed by the present author to depend on Reynolds number, though the general shape and approximate locations remain consistent with the boundaries identified by Williamson and Roshko (1988).

Discussions with Williamson and with Roshko have confirmed that they observed Reynolds number dependence as well.

The location of the 2S/2P boundary agrees well with the oscillation conditions at which Bishop and Hassan (1964) observed an abrupt phase change in fluid forcing on the cylinder. The precise location of the phase change depended on whether the wavelength of oscillation was increasing or decreasing, so the 2S/2P boundary may exhibit hysteresis. Also, vortex-induced vibration experiments with flexible cylinders and elastically mounted cylinders have found that for a range of non-dimensional freestream velocities, the cylinder response appears to follow the 2S/2P boundary (Brika and Laneville, 1993; Khalak and Williamson, 1999). These findings indicate that the details of the wake structure significantly affect, or accurately reflect, global behavior of the flow past the cylinder, including transverse forcing.

In the Williamson and Roshko (1988) study, experiments were conducted in a tow-tank so the wavelength, λ, was a natural metric to use to describe the cylinder oscillations. For flow in a water tunnel, as was used in the current study, the wavelength is not a parameter that is directly measured or controlled. A more convenient parameter is the frequency of oscillation, f. The frequency is non-dimensionalized as

$$f^* = \frac{fD}{U}. \tag{1.3}$$

This can be related to λ/D by

$$\frac{\lambda}{D} = \frac{U/f}{D} = \frac{U}{fD} = \frac{1}{f^*}. \tag{1.4}$$

Jeon and Gharib (2003) investigated the mechanism by which the cylinder oscillations determine the wake structure. Using starting flows past cylinders and two-degree-of-freedom (transverse and streamwise) forced oscillations, the authors were able to study the roll-up process of the wake vortices. They found that a pinch-off process takes place, analogous to the process that occurs for vortex rings produced by piston-cylinder devices (Gharib et al., 1998) and by starting buoyant plumes (Pottebaum and Gharib, 2003). In their model, a wake vortex pinches-off from the separated shear layer that supplies it with vorticity when the non-dimensional kinetic energy of the shear layer is lower than that of the forming vortex. This suggests that the timing of the vortex pinch-off, and therefore the resulting wake mode, are determined by the flux of mass, momentum, energy and vorticity in the separated shear layers, which is affected by the cylinder oscillations.

1.2.2 Heat transfer from non-oscillating cylinders

Heat transfer from non-oscillating cylinders has been studied extensively and is considered well understood. The heat transfer process is intimately connected to the boundary layer on the cylinder and the wake formation process.

At each point on the cylinder surface there is a local heat transfer coefficient that is a function of the fluid velocity and temperature at that location. Given the geometry of the flow, it is simplest to represent the location by its angle from the upstream stagnation point, as shown in Figure 1.5. The local heat transfer coefficient is defined as

$$h_\theta \equiv \frac{\delta P/\delta A}{T_{surf,\theta} - T_\infty}, \tag{1.5}$$

where δP is the differential amount of power transferred, δA is the differential surface area, $T_{surf,\theta}$ is the local cylinder surface temperature, and T_∞ is the freestream temperature. This quantity is then non-dimensionalized by the cylinder diameter, D, and the thermal conductivity of the fluid, k, to form the local Nusselt number

$$Nu_\theta = \frac{h_\theta D}{k}. \tag{1.6}$$

Figure 1.6 shows the local Nusselt number as a function of angular position for several Reynolds numbers. On the leading side of the cylinder, the boundary layers are attached, and the local heat transfer coefficient initially decreases with increasing angular coordinate as the boundary layer becomes thicker and hotter. If the boundary layers become turbulent while attached, the local heat transfer coefficient increases in the turbulent portion due to the increased mixing within the boundary layer. Downstream of the separation point, the local heat transfer coefficient is generally lower than for the region where the boundary layer is attached.

For engineering purposes, the average heat transfer coefficient over the entire cylinder is of greater interest than the local heat transfer coefficients. The average heat transfer coefficient is defined as

$$h \equiv \frac{P/A}{\overline{T_{surf,\theta}} - T_\infty} = \frac{P/\pi DL}{T_{surf} - T_\infty}, \tag{1.7}$$

where P is the total power transferred through the surface area A and $T_{surf} = \overline{T_{surf,\theta}}$ is the average cylinder surface temperature. Due to the way in which the heat transfer coefficient is defined, $h \neq \overline{h_\theta}$. Throughout this study, the absence of the adjective "local" or the subscript θ indicates that the quantity is the average over the cylinder surface. The average Nusselt number is then

$$Nu = \frac{hD}{k}. \tag{1.8}$$

Many empirical correlations with the Nusselt number exist. One widely used correlation is that of Hilpert (1933)

$$Nu = C Re^m Pr^{1/3}, \tag{1.9}$$

where $Pr = \nu/\alpha$ is the Prandtl number, α is the thermal diffusivity of the fluid, and the Reynolds and Prandtl numbers are evaluated at the fluid film temperature. The values for the parameters C and m are listed in Table 1.1 for various Reynolds number ranges. Another frequently used empirical correlation is that proposed by Zhukauskas (1972)

$$Nu = C Re^m Pr^n \left(\frac{Pr}{Pr_s} \right)^{1/4}, \tag{1.10}$$

with Re and Pr evaluated at the freestream temperature, and Pr_s evaluated at the cylinder surface temperature. With the proper values for the parameters, this fit is valid in the range $0.7 < Pr < 500$ and $1 < Re < 10^6$. The values of C and m for various Reynolds number ranges are listed in Table 1.2. The exponent n depends on the Prandtl number and takes the value 0.37 for $Pr \leq 10$ or 0.36 for $Pr > 10$.

1.2.3 Heat transfer from transversely oscillating cylinders in cross-flow

Heat transfer from transversely oscillating cylinders in cross-flow was first studied by Sreenivassan and Ramachandram (1961) over the range 2500 < Re <

15000 in air. They concluded that transverse oscillations had no effect on heat transfer. This is likely because the oscillation frequencies used in their experiments were much lower than the natural shedding frequency. Though they considered amplitude ratios up to 1.8, the largest value of f^* in their study was 0.07, which is only about 1/3 of the natural shedding frequency.

Later experiments have found that heat transfer from a cylinder is enhanced by transverse oscillations near the Strouhal frequency. Kezios and Prasanna (1966), working in the range 5500 < Re < 14000, found that heat transfer was enhanced by about 20% for small amplitude (0.02 < A/D < 0.075) oscillations at the Strouhal frequency. They found that this enhancement exceeded the expected increase in heat transfer if the effect was only due to the higher effective freestream velocity.

Saxena and Laird (1978) measured local heat transfer coefficients using thermocouples embedded in the cylinder surface. They conducted experiments at Re = 3500 in water over the range $0.89 \le A/D \le 1.99$ and $0.28 \le f/f_{St} \le 0.83$. Their results indicate that local heat transfer coefficients increase as the oscillation frequency approaches the Strouhal frequency. On the downstream half of the cylinder, local heat transfer coefficients were observed to increase by 50% to 60% for the highest amplitudes and frequencies. Heat transfer enhancement on the downstream half of the cylinder was consistently about 15% higher than for the leading half of the cylinder.

Cheng et al. (1997) conducted experiments at Re = 200, 500 and 1000 in air. Amplitude ratios of 0.138, 0.314 and 0.628 were explored over the range $f^* \le 0.3$, and heat transfer enhancement of up to 34% was observed. Enhancement near the Strouhal frequency was attributed to lock-on, or synchronization of the wake with the cylinder oscillations. High heat transfer coefficients at large amplitude ratios and high f^*, particularly for the highest Reynolds number, were attributed to a vague "turbulence effect."

Park (1998) conducted experiments in water at Reynolds numbers of 550, 610, 1100 and 3500. He considered frequencies up to $f^* = 1.05$ for two amplitude ratios, 0.1 and 0.2. Park found that heat transfer was significantly enhanced at frequencies corresponding to the Strouhal frequency and to 3 times the Strouhal frequency. For the larger amplitude ratio, Park also found that heat transfer was enhanced at 2 times the Strouhal frequency. Some of Park's results for $A/D = 0.2$ are shown in Figure 1.7. Using digital particle image thermometry/velocimetry, Park was able to show that the heat transfer enhancement was correlated with a shortening of the vortex roll-up distance. He suggested that the closer proximity of the vortices to the cylinder allowed hot, stagnant fluid to be moved away from the cylinder base.

Gau et al. (1999) performed experiments in air at Reynolds numbers of 1600, 3200 and 4800. They measured the local heat transfer coefficient for small amplitude ratios of 0.016, 0.032 and 0.064 in the range $0.5 \leq f/f_{St} \leq 3.0$. A sample of Gau et al.'s results is shown in Figure 1.8. Heat transfer is significantly enhanced at 1 and 3 times the Strouhal frequency, and the most significant enhancement occurs near the trailing edge of the cylinder for these cases. This is consistent with the other cases studied, as well.

Numerical simulations have also been used to study heat transfer from transversely oscillating cylinders. Karanth et al. (1994) computed the flow and heat transfer for Re = 200 and Pr = 1 at amplitude ratios of 0.25 and 0.5 for f^* = 0.2. They predicted increases in the time-averaged heat transfer coefficient of 1.4% and 4.6% for the two cases. The location of the highest local heat transfer coefficient was found to vary as a function of time, though it was always on the leading half of the cylinder. The largest increases in local heat transfer were observed close to the trailing edge.

Cheng and Hong (1997) also performed computations at Re = 200. They examined cases in the range $f^* \leq 0.3$ and A/D ≤ 0.7 with Pr = 0.71 and 7.0. For oscillations at the natural shedding frequency, heat transfer was significantly enhanced, and the magnitude of the enhancement depended on the amplitude ratio. These computational results agreed well with the experimental results of Cheng et al. (1997).

Two common trends in the above literature suggest a relationship between the wake structure and the heat transfer. First, enhanced heat transfer is observed for oscillations at the natural vortex shedding frequency of the stationary cylinder and at some of its harmonics. Second, for oscillation conditions with significant heat transfer enhancement, the largest increases in local heat transfer coefficient occur on the trailing half of the cylinder, where the influence of the trailing vortices is strongest. These facts imply that the vortex roll-up process is directly involved in determining the cylinder heat transfer coefficient. It is therefore reasonable to suspect that the heat transfer coefficient for an oscillating cylinder will be correlated with the wake mode.

The oscillation conditions explored by these various authors are summarized in Figure 1.9 with the Williamson and Roshko (1988) wake mode boundaries superimposed. While a reasonable portion of the ($1/f^*$,A/D)-plane has been investigated, it has been in bits and pieces. Different information is available for each study, and it is difficult to compare results quantitatively because the methods used to determine the Nusselt number have varied widely. The details of the setups—such as Reynolds number, aspect ratio and Prandtl number—have also varied. Therefore, a consistent picture of the dependence of heat transfer coefficient on the oscillation parameters known to determine the wake mode does not exist.

1.3 Objectives and organization

In this study the relationship between wake structure, i.e., the distribution of vorticity in the wake, and heat transfer was investigated. The goals were to determine the mechanism by which transverse cylinder oscillations affect the heat transfer coefficient and to investigate the details of the vortex formation process in the wake.

The study was carried out in two main phases. First, a survey of the parameter space was conducted in order to determine the extent to which the heat transfer coefficient is correlated with known variations in wake structure, such as wake modes and harmonics of the natural shedding frequency. In this portion of the study, described in Chapter 3, a relatively simple method of determining the heat transfer coefficient was employed for a large number of cases, and the wake structure was not directly observed.

During the first phase of the study, it was discovered that under certain circumstances the heat transfer process affects the wake structure as well as the other way around. This fact provides a new avenue from which to study the vortex formation process in the wake. The details of this phenomenon and its implications for the understanding of wakes in general are presented in Chapter 4.

The second phase of this study focused on the mechanisms by which the wake structure affects the heat transfer. Though it is evident that wake structure affects the heat transfer, exactly how this takes place is not understood. Guided by the data from the first phase of the study, a reduced set of cases was examined in greater detail. These particular cases were chosen because they are representative of the range of wake structures believed to occur in the parameter space. For these cases, the velocity and temperature fields in the flow were measured using digital particle image thermometry/velocimetry. This phase of the study is described in Chapter 5. A brief review of the digital particle image thermometry/velocimetry technique is provided in Appendix A.

Chapter 6 summarizes the findings of this study and suggests directions for future investigations.

Tables and figures for Chapter 1

Table 1.1: Parameter values in various Reynolds number ranges for empirical correlation of Nusselt number (equation 1.9) by Hilpert (1933)

Reynolds number	C	m
0.4 – 4	0.989	0.330
4 – 40	0.911	0.385
$40 - 4 \cdot 10^3$	0.683	0.466
$4 \cdot 10^3 - 4 \cdot 10^4$	0.193	0.618
$4 \cdot 10^4 - 4 \cdot 10^5$	0.027	0.805

Table 1.2: Parameter values in various Reynolds number ranges for empirical correlation of Nusselt number (equation 1.10) by Zhukauskas (1972)

Reynolds number	C	m
1 – 40	0.75	0.4
40 – 1000	0.51	0.5
$10^3 - 2 \cdot 10^5$	0.26	0.6
$2 \cdot 10^5 - 10^6$	0.076	0.7

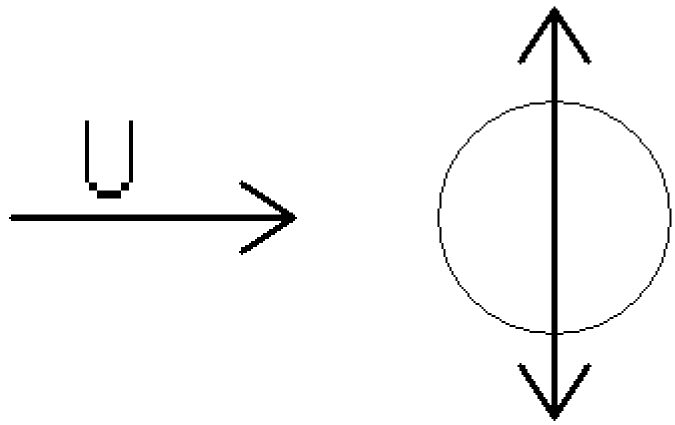

Figure 1.1: Basic flow of interest—transversely oscillating cylinder in uniform freestream flow

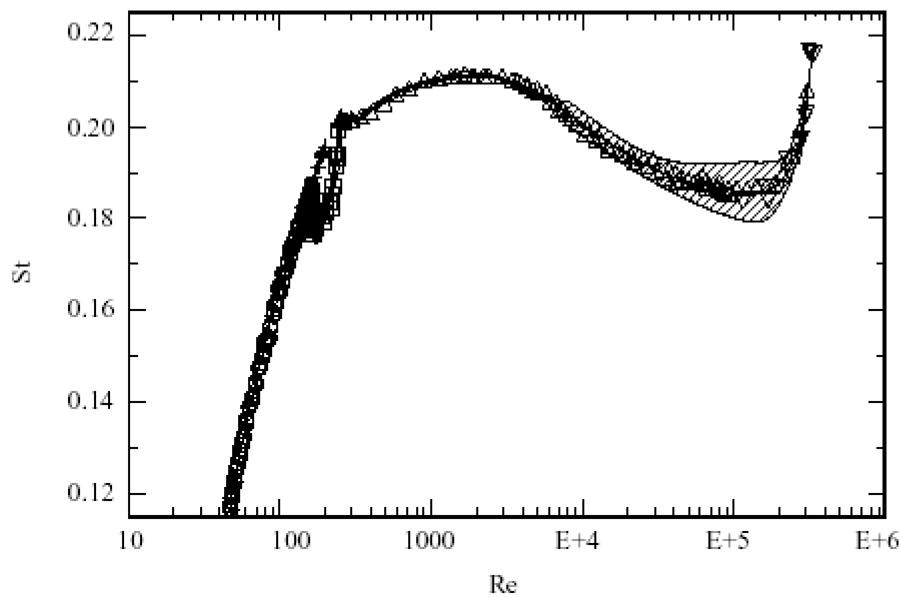

Figure 1.2: Non-dimensional vortex shedding frequency, or Strouhal number, as a function of Reynolds number. Compilation of data from various authors, figure from Norberg (2003)

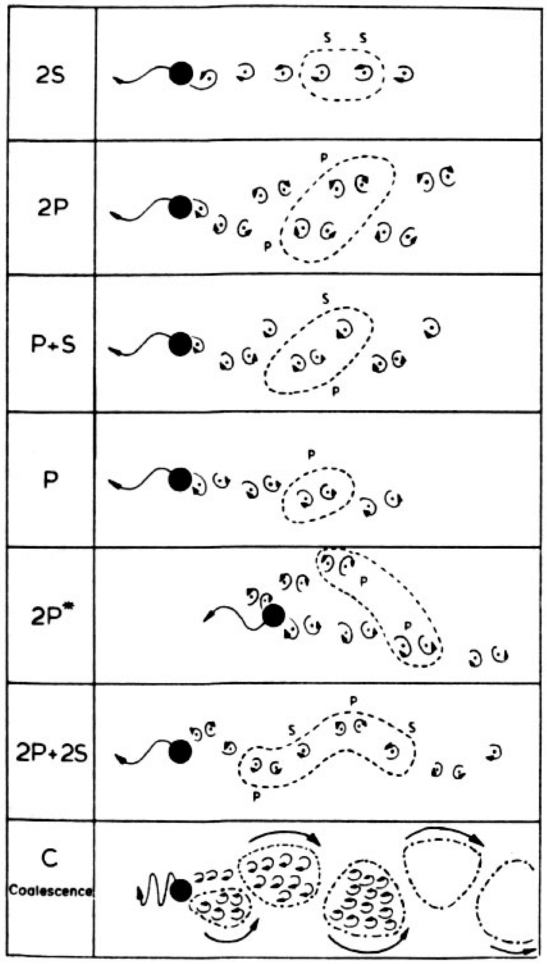

Figure 1.3: Wake modes observed by Williamson and Roshko (1988)

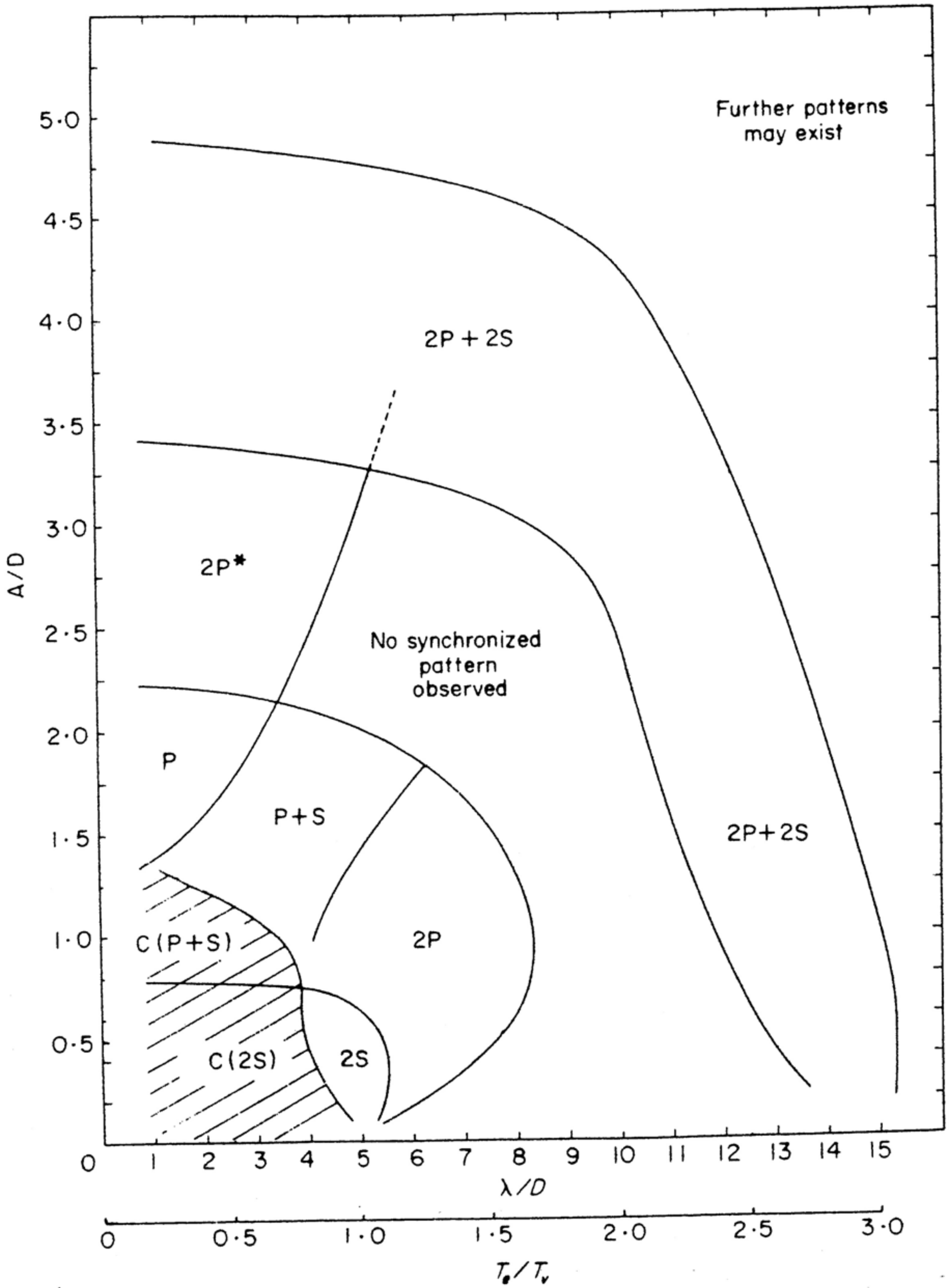

Figure 1.4: Wake mode regions identified by Williamson and Roshko (1988)

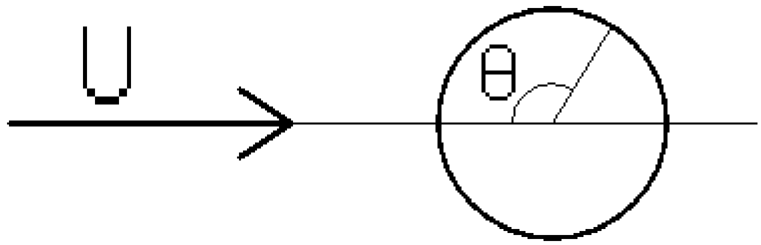

Figure 1.5: Angular coordinate, θ, measured from the upstream stagnation point

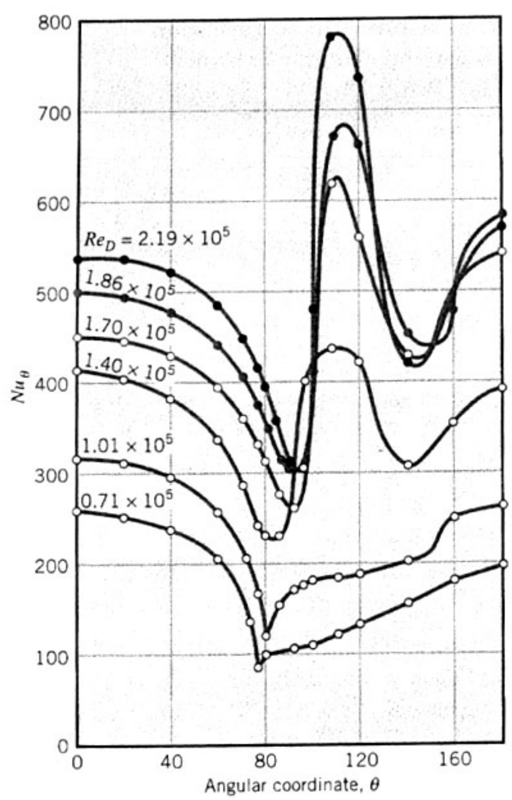

Figure 1.6: Local non-dimensional heat transfer coefficient (Nu_θ) as a function of angular position for various Reynolds numbers. From Incropera and Dewitt (1996)

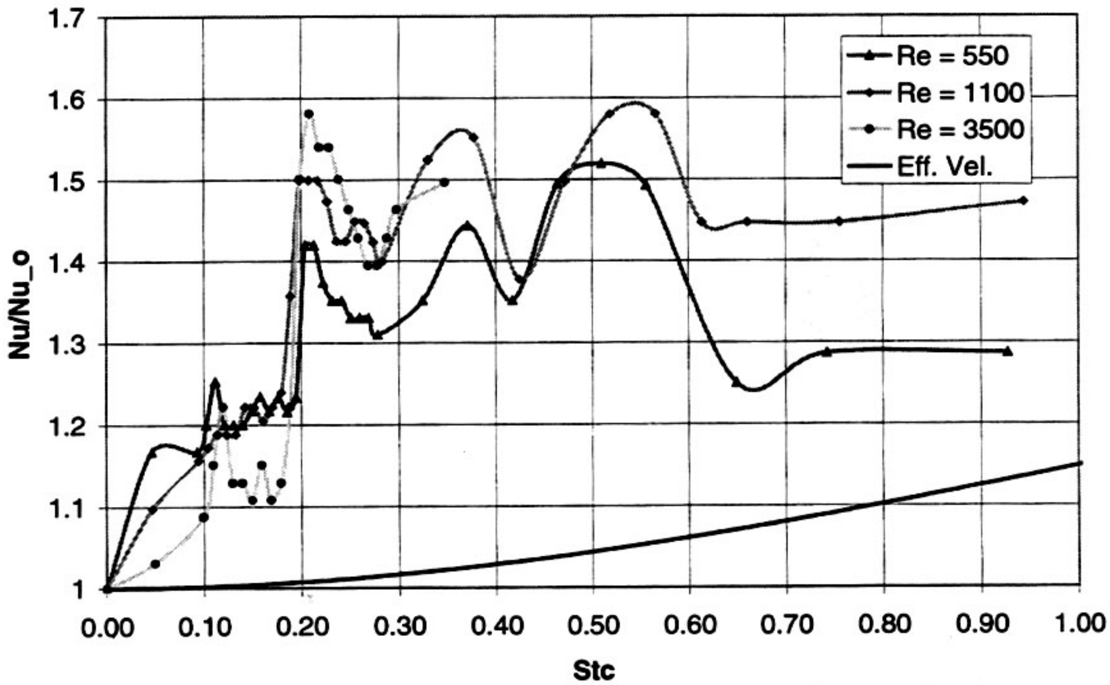

Figure 1.7: Normalized heat transfer coefficient as a function of non-dimensional oscillation frequency for A/D = 0.2 at various Reynolds numbers. From Park (1998)

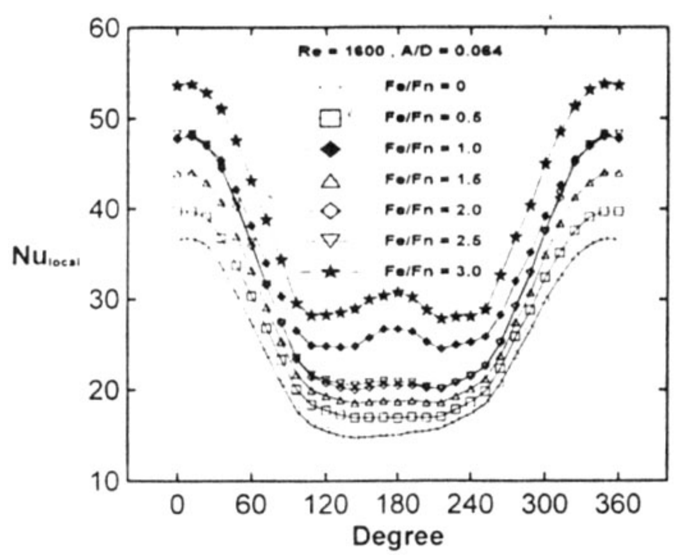

Figure 1.8: Local non-dimensional heat transfer coefficient as a function of angular position for various non-dimensional oscillation frequencies at Re = 1600 and A/D = 0.064. From Gau et al. (1999)

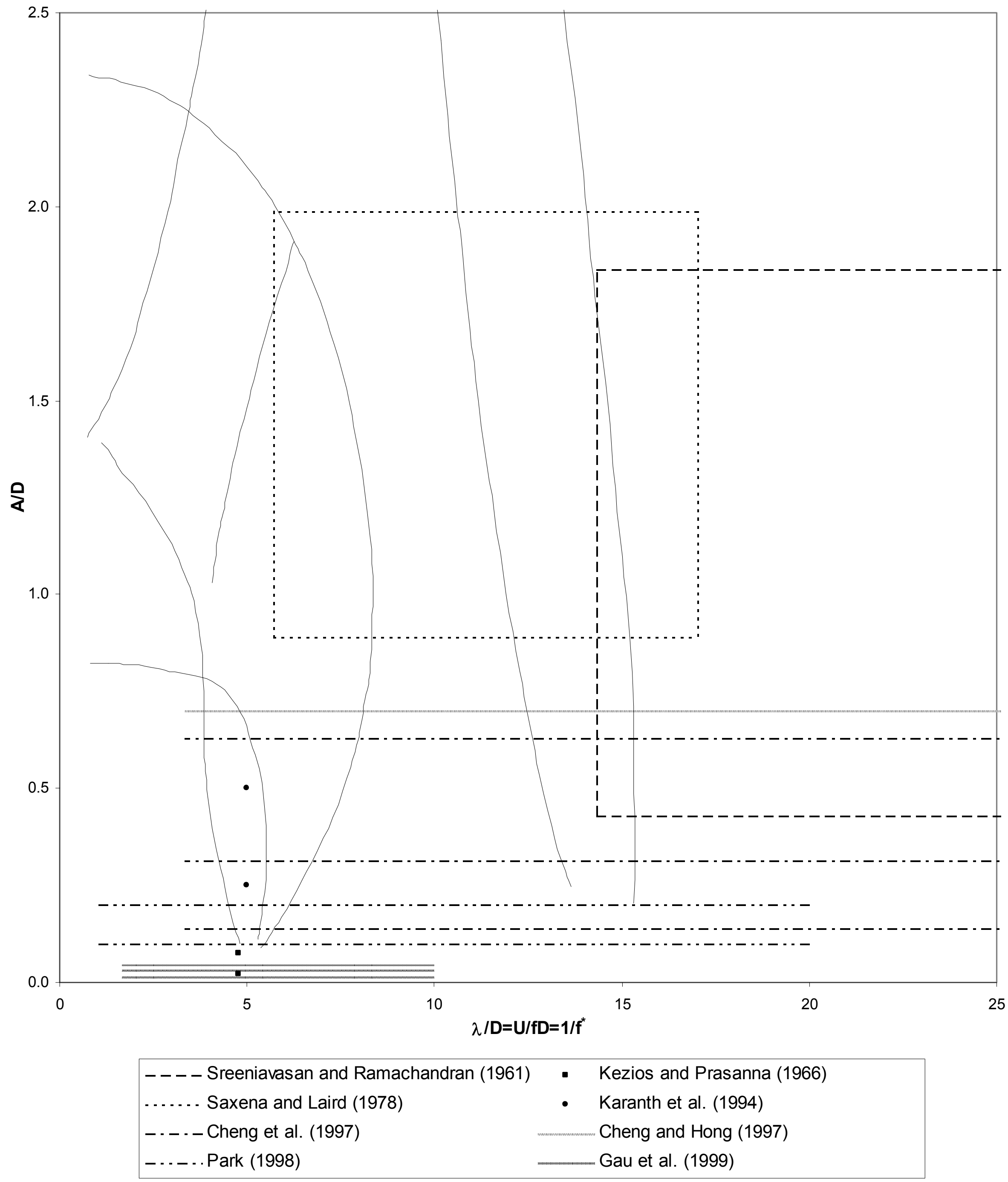

Figure 1.9: Oscillation conditions for which heat transfer has been studied by other authors with wake mode boundaries from Williamson and Roshko (1988)

2 Experimental setup and methods

2.1 Introduction

In this chapter, the details of the experimental setup and methods are presented. In §2.2 to §2.4, the setup used to produce the specific flows and conditions is described. In §2.5 to §2.7, the methods used to investigate those flows are explained. Details of each particular series of experiments are included in later chapters.

2.2 Water tunnel

The experiments in this study were carried out in the GALCIT Heat Transfer Water Tunnel. This facility is specifically designed for conducting experiments under constant freestream temperature conditions. Figure 2.1 shows a diagram of the water tunnel and the arrangement of other elements. The test section is 15.2 cm wide, 58 cm long, and has a maximum height of 16 cm. An adjustable upper wall was used to control the height of the test section and to eliminate the free surface. For all of the experiments in this study, the upper wall was located 13.3 cm above the bottom of the test section.

The water tunnel is capable of operating at speeds between 3 cm/s and 50 cm/s, and the temperature can be controlled to within ±0.02°C over a range between ambient room temperature and 60°C. In this study, the water tunnel was run at speeds of 6.40±0.10 cm/s and 9.65±0.15 cm/s. The temperature was set near 25.8°C, though the exact temperature varied slightly over the various experiments. The properties of water at 25.8°C, listed in Table 2.1, were used as characteristic values to form dimensionless quantities.

The freestream temperature of the tunnel was maintained using an actively controlled heat input and a constant-power heat sink. A schematic of the temperature control system is shown in Figure 2.2. Heat was added to the water in the tunnel by a staggered array of 16 heated cylinders (Watlow FIREROD cartridge heaters) located in the return pipes before the upstream settling section. The cartridge heaters were wired such that the total root-mean-square heating power was 1000 W when connected to AC 120 V. A proportional-integral-derivative (PID) controller (Watlow 93AA-1KA0-00RG) was used to control the power supplied to the cartridge heaters. Feedback to the controller was provided by a 3-wire platinum RTD temperature sensor (Watlow RFGB0TK070BA060) placed in the upstream settling section of the water tunnel. With the tunnel in operation, the temperature difference between the sensor location and the test section was less than the 0.02°C resolution of the reference thermometer (Fluke 2180A with Fluke Y2039 probe or Omega DP41-RTD with Fluke Y2039 probe).

A recirculating chiller (NESLAB RTE-110) provided cooling. Coils of 6.4 mm diameter copper tubing were placed in the downstream settling section and connected to the recirculating chiller such that chilled water was pumped through the coils. The set point for the chiller was purposely set well below the capability of the chiller to achieve so that it continuously operated at maximum cooling power (> 500 W), allowing for simpler tuning of the PID controller. Operating the recirculating chiller in this fashion resulted in a steady temperature offset between the chiller bath and the water tunnel that depended only on the water tunnel speed.

2.3 Heated cylinder

The cylinders used in this study were custom cartridge heaters manufactured by Watlow. Each cylinder consisted of a thin coil of high resistivity wire (80% Ni, 20% Cr) surrounded by compacted magnesium oxide insulator and encased in an Incolloy® 800 (a stainless steel alloy) sheath. In addition, each cylinder contained a type-J thermocouple embedded at the center of the heated length along the cylinder axis. Cylinders of two different diameters, 6.25 mm and 9.42 mm, were used for these experiments. This allowed a larger portion of the frequency-amplitude parameter space to be investigated. The use of different sized cylinders also allowed the effects of aspect ratio on the heat transfer to be determined. When mounted in the test section, the cylinders had aspect ratios of 21.3 and 14.2. Diagrams of the cylinders are shown in Figure 2.3, and the dimensions are summarized in Table 2.2. The thermal properties of the cylinder materials are listed in Table 2.3.

For each experiment, one cylinder was suspended vertically in the test section. A slot in the upper wall allowed the end of the cylinder to pass through. The full heated length of the cylinder was in the test section, and the unheated lead end was used to mount the cylinder on the oscillation mechanism (§2.4).

Heating power was provided to the cylinder by a variable-voltage DC power supply (Kepco BOP 50-4M). A nominal input power, P_{in}, of 63.8 W was used. This value was monitored by independently measuring the current through and the voltage across the cylinder heating wire. This level of power input was chosen because it generates temperature differences in the flow that are measurable (see §2.7) but do not cause significant buoyancy forces. The Grashoff number is defined as

$$Gr = \frac{gD^3\beta\Delta T}{\nu^2}, \tag{2.1}$$

where g is gravitational acceleration, β is the volumetric coefficient of thermal expansion for water, and ΔT is the difference between the cylinder surface temperature and the freestream temperature. The Richardson number equals the Grashoff number divided by the Reynolds number squared and gives the ratio of buoyancy forces to inertial forces in the vertical momentum equation

$$Ri = \frac{Gr}{Re^2} = \frac{gD\beta\Delta T}{U^2}. \tag{2.2}$$

Under the conditions investigated in this study, this ratio is kept below 5.4% for the 9.42 mm diameter cylinder and below 1.6% for the 6.25 mm diameter cylinder.

2.4 Cylinder oscillations

For the experiments in this study, the cylinders were oscillated sinusoidally in the direction transverse to the flow. The frequency and amplitude of the oscillations varied widely depending on the requirements of the specific experiment.

In order to achieve the necessary flexibility, the cylinder oscillations were accomplished using a closed loop motion control system. The major components of the motion control system were a programmable motion controller (Delta Tau mini-PMAC), a linear voice coil actuator (BEI Kimco LA25-42000A), and a linear optical encoder (RSF Electronics MSA 6704). Figure 2.4 shows the cylinder carriage assembly mounted above the test section, and a schematic of the motion control system is shown in Figure 2.5.

Use of a programmable motion controller allowed the period and amplitude of oscillation to be set to arbitrary values and made it simple to change the oscillation parameters between experiments. Sets of programs were developed for the controller specifying sinusoidal profiles of unit amplitude, with each program corresponding to a particular period. Profiles were specified such that the time between successive points on the profile never exceeded 1.5% of the oscillation period. The oscillation amplitude was set by changing the number of the encoder counts defined as the unit of distance.

The linear optical encoder had a resolution of 10 μm. This corresponds to 2.2% of the smallest oscillation amplitude used. The encoder was attached directly to the cylinder carriage to avoid any scaling or hysterisis problems associated with linkages.

A linear voice coil was used as the actuator. This device consists of a solenoid that moves relative to a permanent magnet. It is designed so that the force generated is linear with respect to current over the entire working range of the device. The solenoid side of the actuator was attached to the cylinder carriage, and the permanent magnet end was connected to the base plate.

The entire cylinder carriage assembly was mounted above the test section of the water tunnel. It was anchored to the building structure in the vertical and transverse directions and to a massive object in the streamwise direction in order to minimize vibrations. Other than the cylinder extending into the test section, there was no contact between the carriage assembly and the water tunnel. This prevented the transmission of any remaining vibrations.

2.5 Embedded thermocouple temperature measurements

Data from the thermocouples embedded inside the cylinders was obtained by processing the thermocouple voltage through a number of steps. A schematic of the data path is shown in Figure 2.6.

The thermocouple leads, which exit the cylinder at the same end as the power leads, were connected to a temperature transmitter (Jenco model 77) mounted on the carriage assembly. A variable DC power supply (Hewlett-Packard model 6236A) set to 24 V supplied power to the transmitter. The transmitter operates by varying its internal resistance such that the current in the power circuit is linearly related to the thermocouple temperature.

This signal was converted to a voltage by placing a resistor in the power circuit. The voltage across the resistor and an external offset voltage (0.892±0.002V) were input into a pre-amplifier (Stanford Research Systems SR560). The pre-amplifier output the filtered (low-pass with cutoff frequency 0.3Hz and attenuation of 12dB/oct) and amplified (gain of 10 or 20 depending on the transmitter being used) difference between the inputs. This resulted in the pre-amplifier output range of –5V to +5V corresponding to a temperature range of approximately 20°C to 50°C. The precise relationship between the output voltage and thermocouple temperature was determined by calibration. The output voltage was then recorded to computer using a 16-bit analog-to-digital converter (National Instruments PCI-6035E).

The overall uncertainty of the temperature measurements is estimated to be ±0.1°C. This includes the inherent uncertainty of the thermocouple voltage, noise introduced by the various electronic components, drift in the offset voltage, and the effects of the oscillations.

2.6 Determination of heat transfer coefficient

The heat transfer coefficient of the cylinder was not directly measured, but was instead deduced from the temperature at the cylinder core—as measured by the embedded thermocouple—using a steady, one-dimensional model of heat transfer inside the cylinder. This method produces results consistent with published values of heat transfer coefficient for both stationary and oscillating cylinders, but is limited by the assumption that the heat transfer coefficient is steady.

Park (1998) developed a model of heat transfer inside a similar cylinder in order to deduce the heat transfer coefficient from the cylinder core temperature. For the present study, Park's model was modified to more closely match the physical structure of the heated cylinders used.

An axisymmetric model with no axial variation was used to approximate the internal structure of the heated cylinder (described in §2.2). This geometry, consisting of four regions (a, b, c, and d), is shown in Figure 2.7. Power is added only in region b. It will be shown below that the specific values of the radii and of the material properties are not critical because the model can be calibrated. Only the functional form resulting from the model is important. The details of the model derivation can be found in Appendix B, along with a formal error analysis and an analysis of the impact of the axisymmetric assumption.

The resulting expression for the cylinder heat transfer coefficient, h, is

$$h=\left(\frac{2\pi R_d L}{P_{in}}\left(T_{tc}-T_{\infty}\right)+C_{\Delta T}\right)^{-1}, \tag{2.3}$$

where T_{tc} is the temperature of the thermocouple and $C_{\Delta T}$ is a constant given by

$$C_{\Delta T}=-R_d\left[\frac{1}{k_d}\ln\left(\frac{R_d}{R_c}\right)+\frac{1}{k_c}\ln\left(\frac{R_c}{R_b}\right)+\frac{1}{k_b}\left\{\frac{1}{2}-\left(\frac{R_a^2}{R_b^2-R_a^2}\right)\ln\left(\frac{R_b}{R_a}\right)\right\}\right]. \tag{2.4}$$

The heat transfer coefficient can then be non-dimensionalized as the Nusselt number using equation (1.8).

The key result of the one-dimensional model is that the temperature difference between the thermocouple location and the cylinder surface is directly proportional to the power input to the cylinder. The constant of proportionality depends only on the cylinder dimensions and material properties. Rewriting equation (2.3) as

$$C_{\Delta T}=\frac{1}{h}-\frac{2\pi R_d L}{P_{in}}\left(T_{tc}-T_{\infty}\right), \tag{2.5}$$

it is evident that the constant $C_{\Delta T}$ can be found by calibration rather than using the expression in equation (2.4) if known values of the heat transfer coefficient can be produced. This can be accomplished by subjecting the non-oscillating heated cylinder to a range of freestream velocities and using one of the empirical correlations mentioned in §1.2.2. By using a calibration to determine the value for $C_{\Delta T}$, some of the details of the actual system that were ignored in the model, such as temperature variations in the axial and angular directions, may be accounted for while retaining the linear relationship between power input and temperature difference.

A calibration of this type was carried out for each of the cylinders. The correlation proposed by Zhukauskas (1972), given in equation (1.10), was used to determine the “actual” heat transfer coefficient. Thirteen different water tunnel speeds were used for each cylinder. The values given by equation (2.5) for each freestream velocity were then averaged to form the best estimates of $C_{\Delta T}$, which are given in Table 2.4. The correlation from Zhukauskas requires the cylinder surface temperature to be estimated, which requires a value of $C_{\Delta T}$, so an iterative procedure was used until the best estimate for $C_{\Delta T}$ converged. For comparison, the values of $C_{\Delta T}$ determined using equation (2.4) with the radii in Table 2.5 are also given. Figure 2.8 shows the heat transfer coefficients determined using equation (2.3) with the best estimates of $C_{\Delta T}$ from the calibration plotted against the values determined using Zhukauskas' correlation.

As shown in Appendix B, the relative uncertainty in the heat transfer coefficient is given by

$$\left(\frac{\delta_h}{h}\right)^2 = \left(1 - hC_{\Delta T}\right)^2 \left[\frac{\delta_{T_{tc}}^2 + \delta_{T_\infty}^2}{\left(T_{tc} - T_\infty\right)^2} + \left(\frac{\delta_{P_{in}}}{P_{in}}\right)^2 + \left(\frac{\delta_{R_d}}{R_d}\right)^2 + \left(\frac{\delta_L}{L}\right)^2\right] + h^2 \delta_{C_{\Delta T}}^2 , \qquad (2.6)$$

where $\delta_{(\,)}$ indicates the uncertainty in the subscripted quantity. Clearly, the uncertainty depends significantly on the heat transfer coefficient itself. The terms $(1 - hC_{\Delta T})^2$ and h^2 both increase with h, amplifying the uncertainty for large values of h. In addition, the temperature uncertainties are weighted by the inverse of the measured temperature difference. As the heat transfer coefficient increases, the temperature difference decreases.

2.7 Digital particle image thermometry/velocimetry

For DPIT/V, the water tunnel was seeded with 40 μm diameter encapsulated thermochromic liquid crystal (TLC) particles (Hallcrest BM/R26C20W/S33). The thermal time constant for these particles is estimated to be 4 msec (Dabiri and Gharib 1991), which is much shorter than the characteristic timescales in the flow. These TLC particles have a red start at 26°C and a range of 20°C when illumination and viewing are from the same direction. Under the conditions used in the study (approximately 90° between illumination and viewing directions), the red start is approximately 25.4°C and the useful range of color play is about 2°C. A diagram of the illumination and imaging setup is shown in Figure 2.9.

The particles were illuminated by a horizontal sheet of pulsed white light at the mid-plane of the test section. The light sheet was formed using a new white light source constructed for this project. It consists of two xenon strobes coupled by a fiber-optic assembly. The timing control, flash-to-flash repeatability, uniformity of illumination, and maximum continuous run-time of this light source are significantly improved over those of the light source used in previous studies by Dabiri and Gharib (1991), Park (1998) and Pottebaum and Gharib (2003). At the center of the test section, the light sheet had a thickness of 5 mm. The separation time between pulses of the light sheet for each image pair was set such that the vector sum of the freestream velocity and the peak cylinder transverse velocity corresponded to a displacement of approximately 4 pixels.

The illuminated particles were imaged using a color, progressive scan CCD camera (Sony DXC-9000) at the standard NTSC video rate of 29.97 frames per second. The camera was located approximately 1.3 m from the illuminated plane, and the field of view was 67 mm x 51 mm with the larger dimension in the streamwise direction. The resulting images were recorded directly to computer hard disk in real time using an analog frame grabber (Coreco RGB-SE) and the VideoSavant software package (IO industries). Synchronization of the light pulses to the video frames was accomplished using a timing counter card (National Instruments PC-TIO-10) along with existing software and signal conditioning hardware developed in the Gharib research group.

The cylinders used in this study were not transparent, so there is a shadow in every image. No useful velocity or temperature information can be extracted from the shadow region. In addition, derivative and integral quantities, such as vorticity, circulation, or the temperature gradient, cannot be determined for points bordering the shadow region or for areas or paths that include the shadow region.

The intensity field of the recorded images was used as the input for standard DPIV processing algorithms to determine the velocity field. DPIV processing was carried out using 32 pixel by 32 pixel interrogation windows with 50% overlap. Window shifting was used to reduce errors associated with in-plane particle loss. The CCD resolution and out-of-plane particle loss are the main remaining sources of error. Overall, the measured velocities have relative uncertainties of approximately 1.5%.

The intensity field was also used to determine the phase of motion of the cylinder for oscillating cases. The cylinder position was first estimated by measuring the extent of the cylinder’s shadow in each image. Position estimates for each pair of images were then averaged together. Using the known cylinder oscillation period for a particular case and the time between image pairs (2/29.97 sec), a sine wave at the proper frequency,

$$y = A\sin(2\pi f + \phi_0), \tag{2.7}$$

was fit to the time series of position estimates in order to determine the phase of each image pair, ϕ.

Temperature field data was extracted from the color content of the DPIT/V images using a new localized calibration scheme intended to account for the effects of viewing angle on the apparent color of the TLC particles. The red-green-blue (RGB) color data for each image was converted to the hue-saturation-intensity (HSI) color scheme, and the hue angle was used as the indicator of temperature. The conversion from RGB to HSI used the relationships

$$\begin{aligned} &\begin{bmatrix} v_1 \\ v_2 \\ I \end{bmatrix} = \begin{bmatrix} 1 & -1/2 & -1/2 \\ 0 & \sqrt{3}/2 & -\sqrt{3}/2 \\ 1/3 & 1/3 & 1/3 \end{bmatrix} \begin{bmatrix} R \\ G \\ B \end{bmatrix} \\ &H = \tan^{-1}(v_2/v_1) \\ &S = \sqrt{v_1^2 + v_2^2} \end{aligned} . \tag{2.8}$$

The resulting color system is shown in Figure 2.10. Lengths in the figure are scaled by the intensity to make it applicable at any value of intensity.

The images were divided into 16 pixel by 16 pixel color-averaging windows, and each window was calibrated separately. After applying intensity and saturation thresholds, the hues of all non-black pixels in a window were averaged to define the hue for that window. The hue was then converted to temperature using a lookup table of the calibration hue values and linear interpolation between calibration temperatures. To determine the temperature on the same grid as the DPIV data, the temperature of 2 by 2 groups of averaging widows were averaged together, weighted by the number of non-black pixels in each window. The temperature fields of the two images in each image pair were then averaged together with equal weight to produce the temperature field snapshots corresponding to the DPIV velocity snapshots.

Calibration images were recorded using the same setup as the data images. The only change in the setup was that the cylinder was removed from the test section for the calibration images. Starting from a temperature below the red clearing point of the TLC particles, the tunnel temperature was slowly increased. One hundred images of the seeded flow were recorded at each calibration temperature. The calibration temperatures were spaced at approximately 0.1°C increments and covered the entire useful range of the TLC particles. The precise temperature of each set of images was monitored using the reference thermometer and recorded manually.

Hue values for the calibration images were determined in the same manner as for the data images. The same thresholds were applied, and the same color-averaging windows were used. After the hue for each window in every image was determined, the weighted-average hue for all images at a particular temperature was computed for each window. The averaging was weighted by the number of non-black pixels used to determine the hue. The calibration data was then placed into a lookup table sorted by color-averaging window and by temperature for use with the data images.

Curves of the calibration data for a sampling of color-averaging windows are shown in Figure 2.11. It was found that the useful range of the TLC particles was significantly smaller in the portion of the field of view upstream of the cylinder than in the downstream portion. Therefore, temperature data was only considered reliable in the downstream portion of the flow. Even in the downstream portion of the field of view, the calibration curves for different windows are significantly different than one another. This is why a localized calibration scheme was used.

The hue angles appear to reach a maximum value that is in the green range. This is odd because the TLC color should progress through blue. This is an artifact of the relatively lower intensity of blue particles compared to longer wavelength particles. In future work, the gain of the blue channel will be set higher than the red and green channels to expand the useful temperature range.

With the implementation described here, DPIT/V is capable of measuring temperature differences of approximately 0.1°C over a range of about 1°C. Smaller temperature differences cannot be resolved and will likely be overwhelmed by noise.

Tables and figures for Chapter 2

Table 2.1: Properties of water at 25.8°C

Density, ρ (kg/m^3)	996.8
Volumetric coefficient of thermal expansion, β (1/K)	$-2.65 \bullet 10^{-4}$
Viscosity, μ (kg/m·s)	$8.74 \bullet 10^{-4}$
Kinematic viscosity, ν (m^2/s)	$8.77 \bullet 10^{-7}$
Derivative of kinematic viscosity, $d\nu/dT$ (m^2/s·K)	$-1.92 \bullet 10^{-8}$
Thermal conductivity, k_w (W/m·K)	0.612
Specific heat capacity, C_w (J/kg·K)	$4.20 \bullet 10^{3}$
Thermal diffusivity, $\alpha = k_w/\rho C_w$ (m^2/s)	$1.46 \bullet 10^{-7}$
Prandtl number, $Pr = \nu/\alpha$	5.99

Table 2.2: Cylinder dimensions (mm)

	Small diameter cylinder	Large diameter cylinder
Outer diameter (D)	6.25	9.42
Heating wire helix radius (R_1)	1.83	2.88
Sheath inner radius (R_2)	2.43	3.81
Heating wire helix pitch	0.6	0.6
Heated length (L_H)	127	127
Lead end unheated length (L_A)	25.4	25.4
Closed end unheated length (L_B)	6.35	6.35

Table 2.3: Cylinder material properties

	Insulator	Sheath
Density, ρ (kg/m^3)	3044	8026
Thermal conductivity, k (W/m·K)	2.08	14.0
Specific heat capacity, C (J/kg·K)	879	502
Thermal diffusivity, $\alpha = k/\rho C$ (m^2/s)	$7.77 \bullet 10^{-7}$	$3.47 \bullet 10^{-6}$

Table 2.4: Values determined for $C_{\Delta T}$

method	D = 6.25 mm	D = 9.42 mm
Best estimate from calibration	-0.00024	-0.00055
Standard deviation from calibration	0.00003	0.00004
Calculated from radii and material properties	-0.00022	-0.00057

Table 2.5: Radii used in model of cylinder internal heat transfer

	D = 6.25 mm	D = 9.42 mm
R_a	2.122	2.986
R_b	2.230	3.227
R_c	2.425	3.810
R_d	3.125	4.710

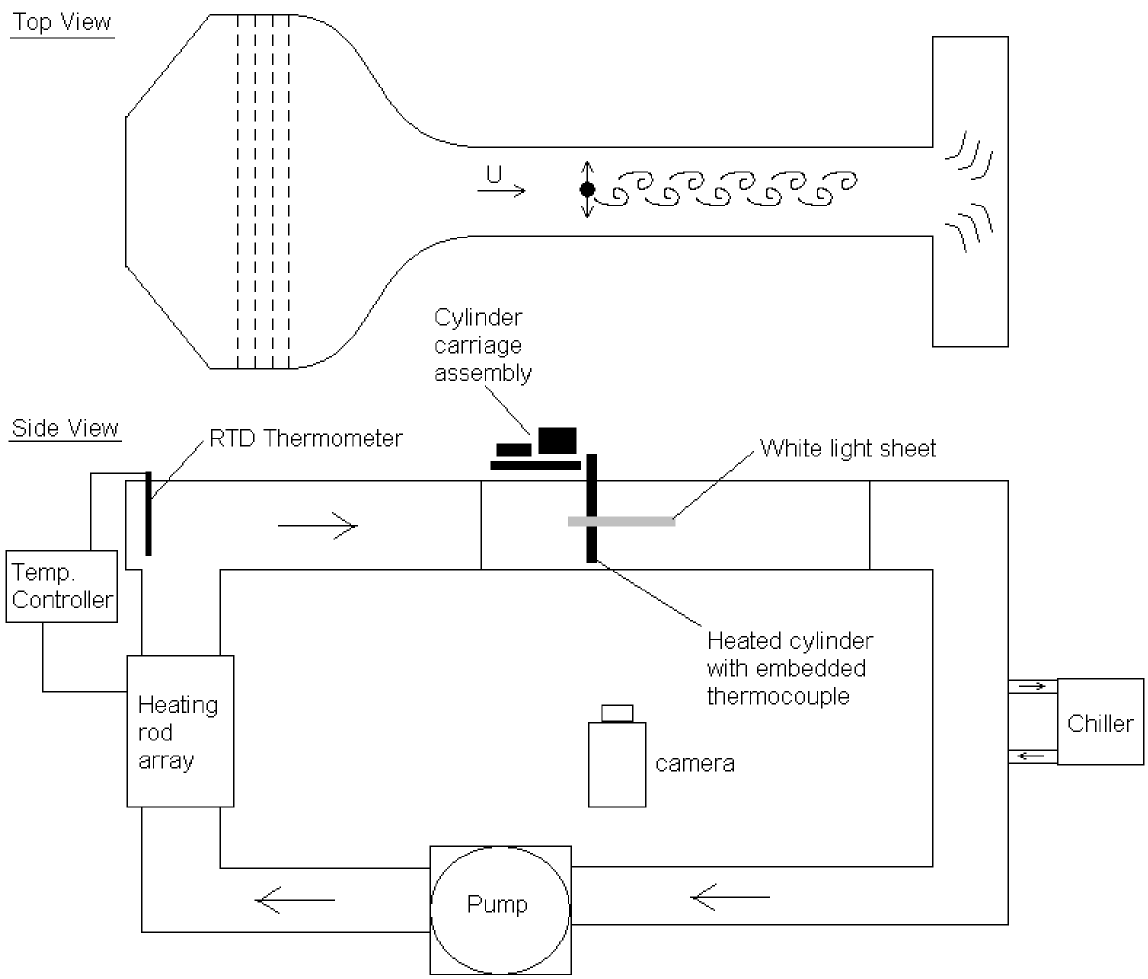

Figure 2.1: Diagram of water tunnel and basic arrangement of experiment

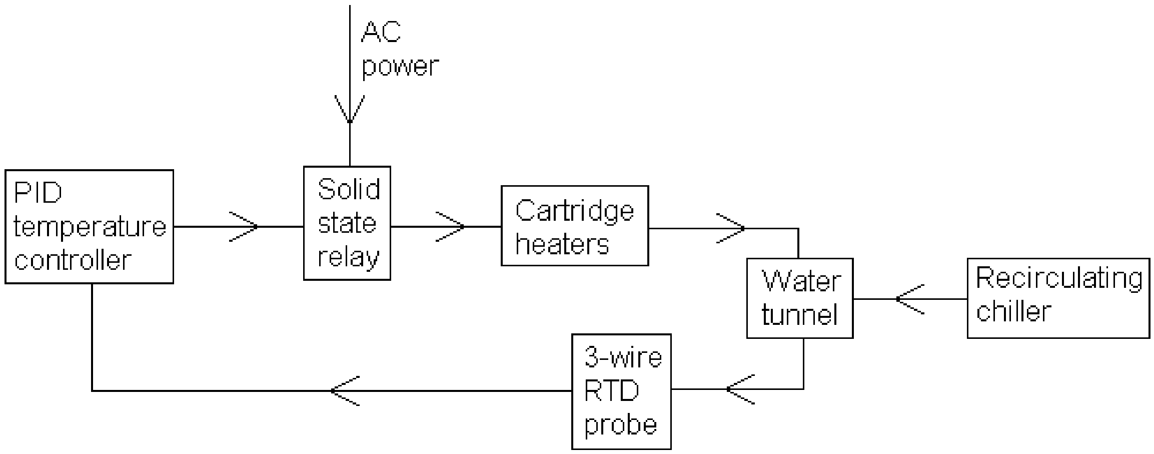

Figure 2.2: Schematic of temperature control system for the water tunnel

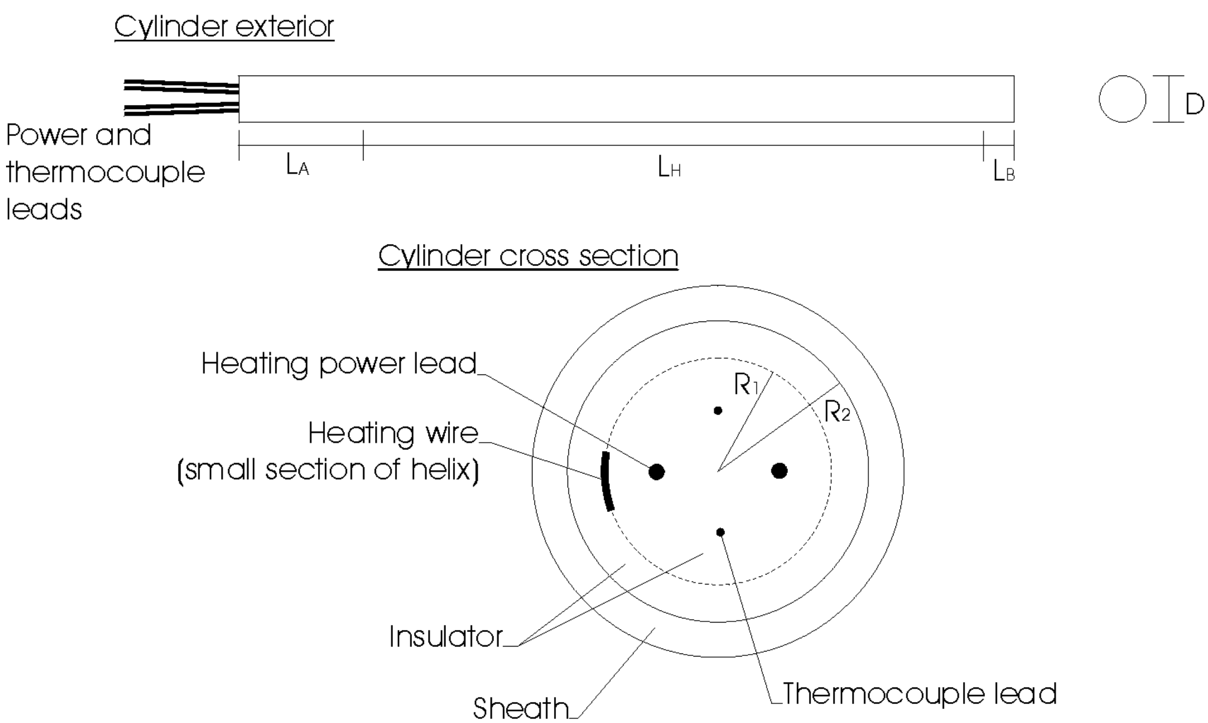

Figure 2.3: Cylinder exterior dimensions and internal structure (not to scale); dimensions are listed in Table 2.2

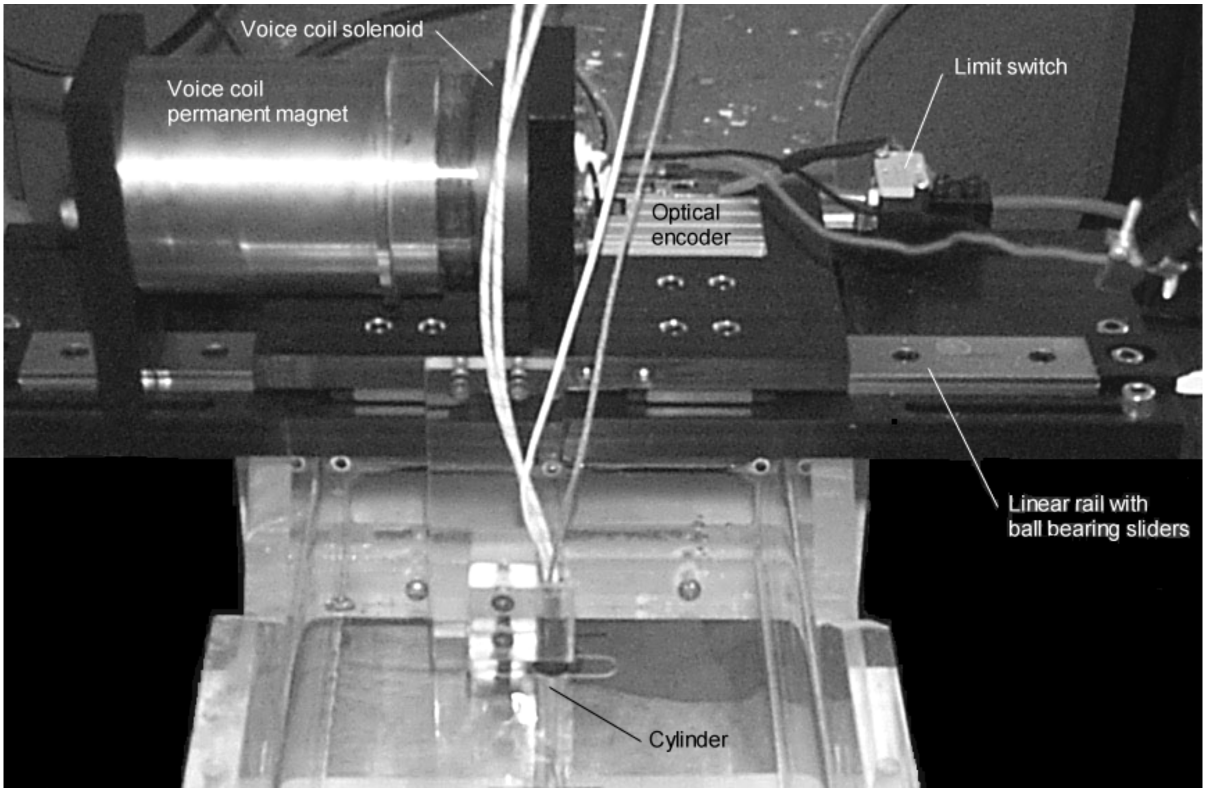

Figure 2.4: Cylinder carriage assembly mounted above the water tunnel test section; major components are labeled

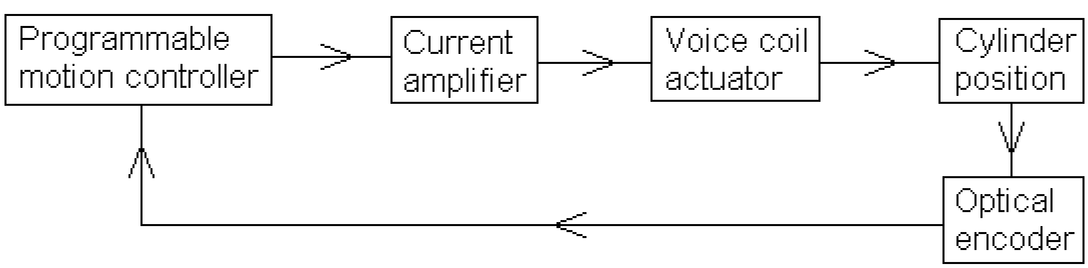

Figure 2.5: Schematic of cylinder motion control loop

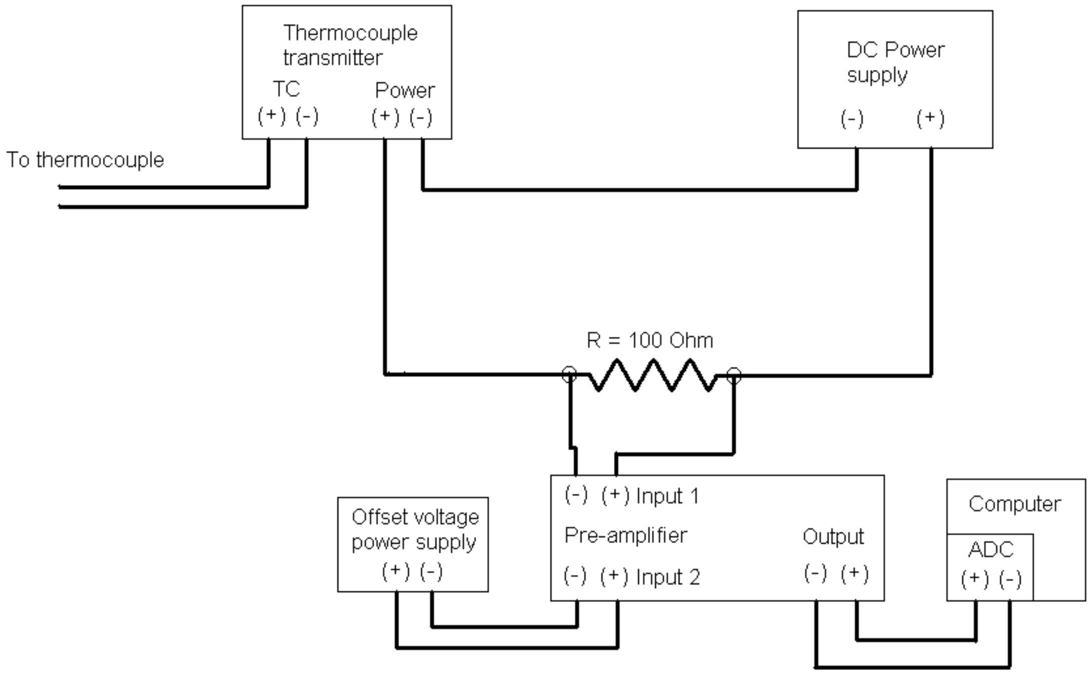

Figure 2.6: Schematic of the thermocouple data transmission path

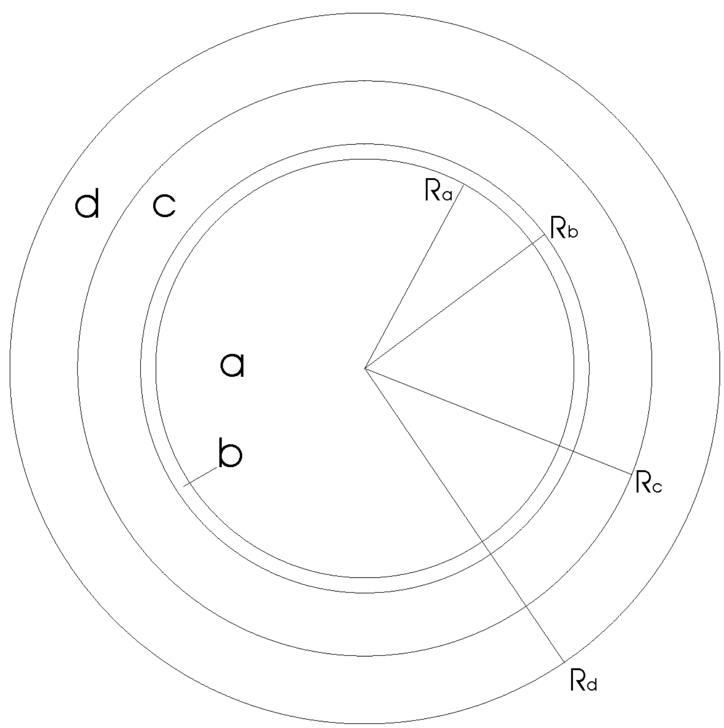

Figure 2.7: Geometry for model of heat transfer inside the cylinder

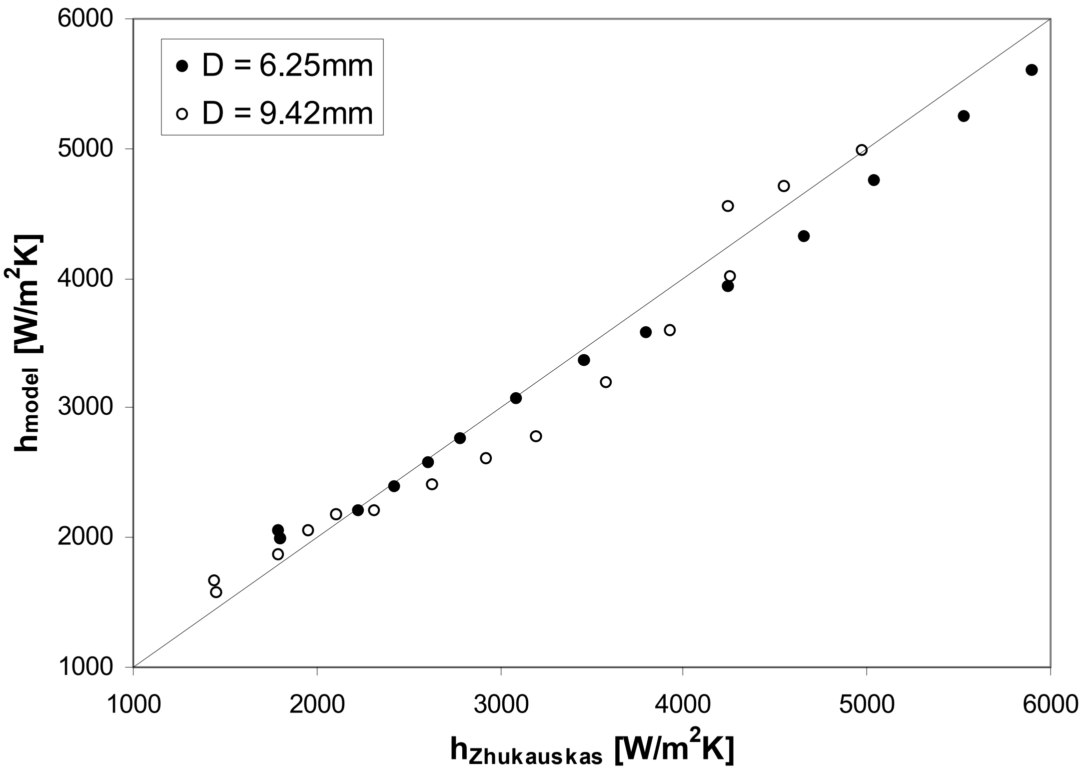

Figure 2.8: Heat transfer coefficient determined using one-dimensional model vs. heat transfer coefficient predicted by Zhukauskas (1972) correlation

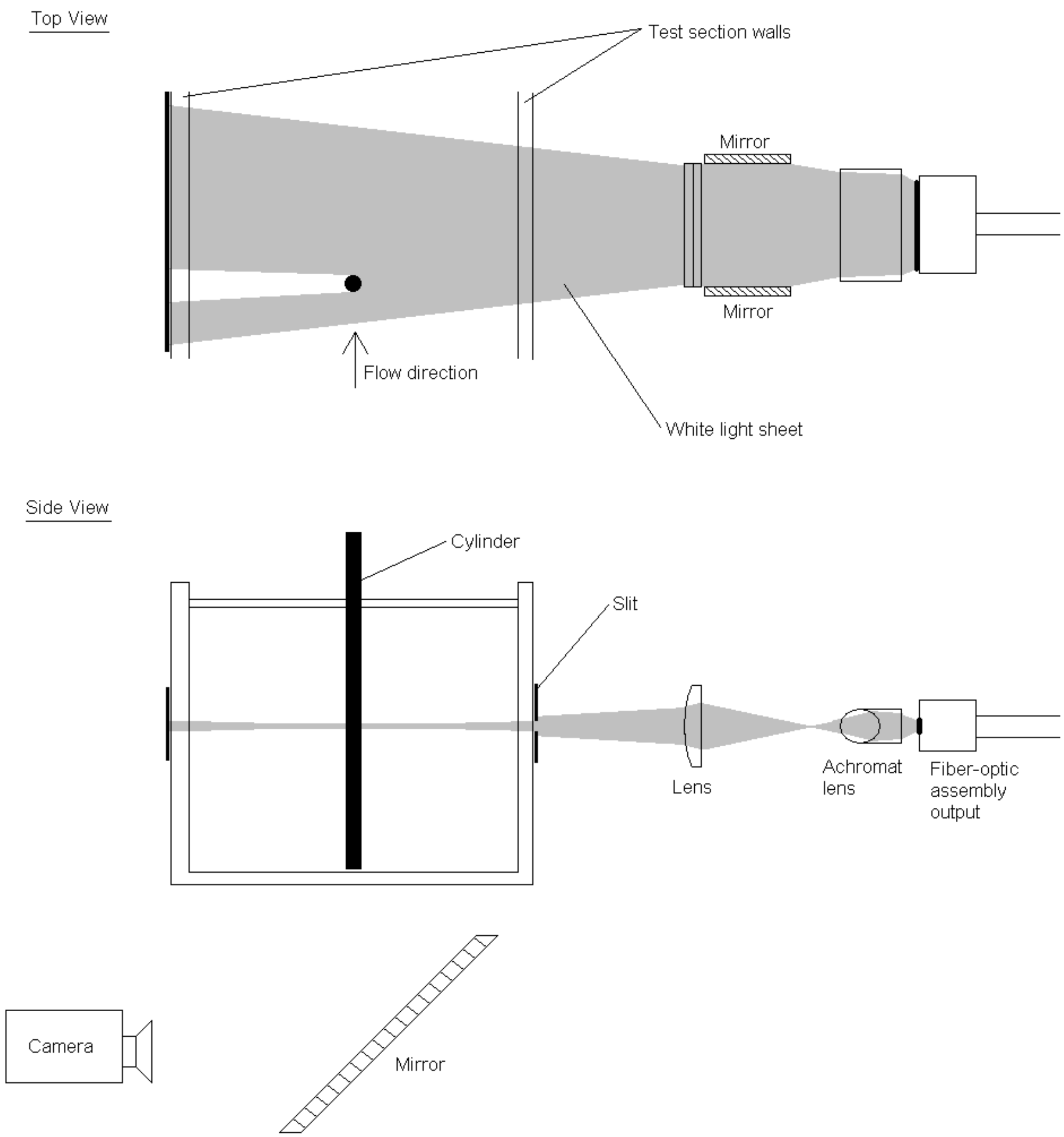

Figure 2.9: Illumination and imaging setup for digital particle image thermometry/velocimetry (not to scale)

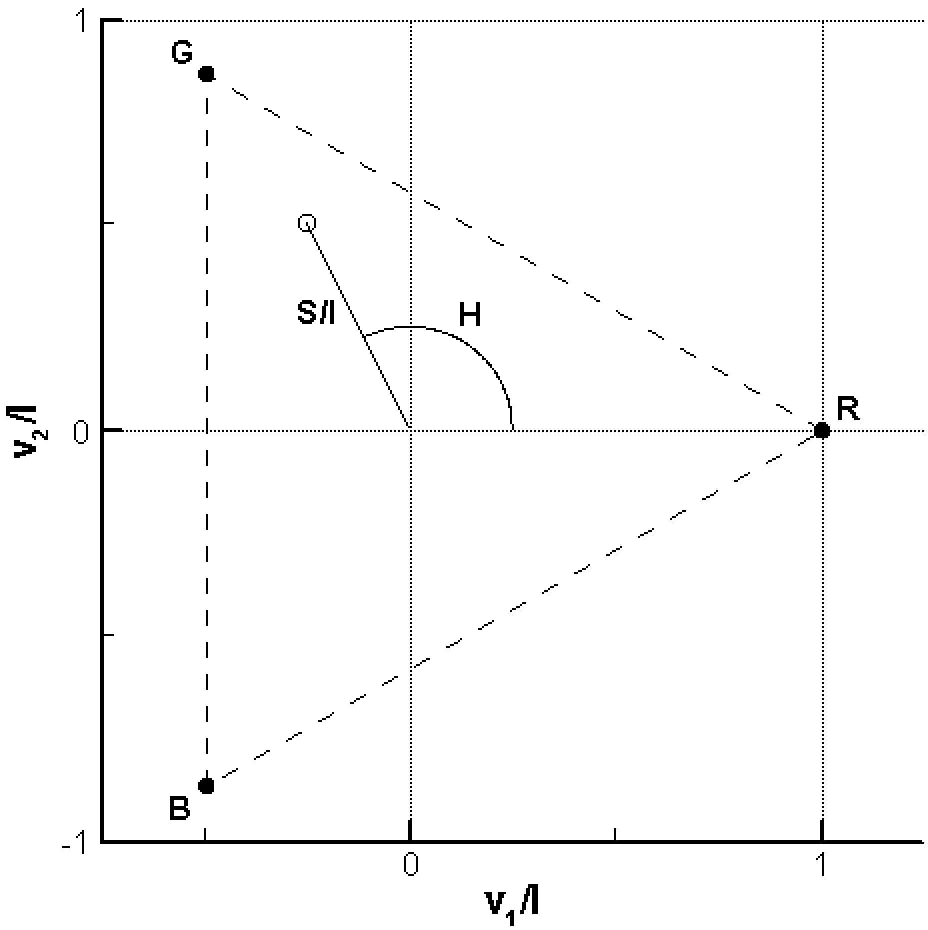

Figure 2.10: Color system used for TLC calibration; the white point is at the origin, the pure RGB primaries are labeled, hue (H) is the angle between the v_1 axis and the color measured counterclockwise, saturation (S) is the distance of a color from the origin, and intensity (I) is directed out of the paper; lengths are scaled by I to make the figure applicable for any value of I

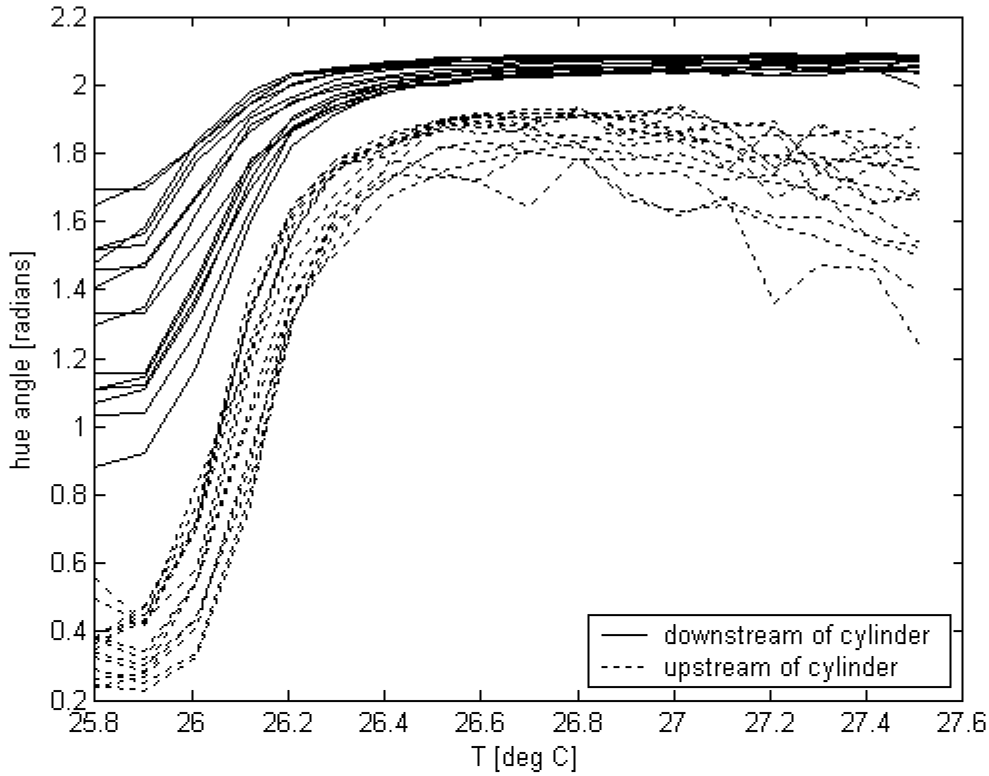

Figure 2.11: TLC calibration data for a sampling of color-averaging windows

3 Dependence of heat transfer coefficient on the frequency and amplitude of forced oscillations

3.1 Introduction

In this chapter, the effects of transverse oscillations on heat transfer are examined over a wide range of amplitudes and frequencies. The parameter space investigated was guided by the wake mode regions identified by Williamson and Roshko (1988). At each oscillation condition, the Nusselt number, or non-dimensional heat transfer coefficient, was determined by measuring the power input and the cylinder core temperature. This information was then combined with existing knowledge of oscillating circular cylinder wake structure in order to infer relationships between wake structure and heat transfer. The connection between heat transfer coefficient and transverse velocity was also examined.

3.2 Experimental conditions

As discussed in §2.2, two different diameters of cylinders were used in this set of experiments. The freestream velocity was adjusted so that the Reynolds number was the same for the non-oscillating case with each cylinder. Given the limits of the oscillation mechanism, the cylinder diameter therefore determined the range of non-dimensional frequencies and amplitudes that were accessible for each cylinder.

For the small aspect ratio cylinder (AR = 14.2, D = 9.42 mm), amplitude ratios up to A/D = 1 and non-dimensional frequencies in the range $0.061 \leq f^* \leq 1.08$ were considered. The freestream velocity for this cylinder was 6.40 ± 0.10 cm/s, resulting in a Reynolds number Re = 687. Data was obtained at 1070 distinct oscillation conditions, including 64 different frequencies and 20 amplitudes, in addition to the non-oscillating case. The specific oscillation conditions considered for this cylinder are shown in the ($1/f^*$, A/D)-plane in Figure 3.1.

Amplitude ratios up to A/D = 1.5 and non-dimensional frequencies in the range $0.061 \leq f^* \leq 0.48$ were considered for the larger aspect ratio cylinder (AR = 21.3, D = 6.25 mm). A freestream velocity of 9.65 ± 0.15 cm/s was used, giving a Reynolds number of Re = 688. A total of 765 distinct oscillation conditions—consisting of 51 frequencies and 15 amplitudes—were investigated in addition to the non-oscillating case. Figure 3.2 shows the specific oscillation conditions considered for this cylinder.

For all cases with both cylinders, the input power (P_{in}) was 63.8 ± 0.1 W and the freestream temperature (T_∞) was 25.8 ± 0.10 °C. The power input and freestream temperature for each case were measured to within ± 0.01 W and ± 0.02 °C. All other conditions were as described in Chapter 2.

3.3 Experimental setup and procedures

A single data acquisition run consisted of a set of amplitude-frequency combinations to be performed for a particular cylinder. Prior to each run, the appropriate cylinder was installed in the setup, and all electrical connections were completed and verified. The water tunnel was then started with the pump motor controllers set to the proper frequency to obtain the desired freestream velocity. The freestream temperature control system was then activated, and several hours were allowed for the water to reach the proper temperature. When the water tunnel was ready for the experiments, heating power was applied to the cylinder and the run was started.

Control of the cylinder oscillations and acquisition of data was automated using a custom LabVIEW program in order to enable the large number of cases to be considered in a reasonable period of time. The LabVIEW program communicated with the motion controller via an RS-232 serial connection. At the beginning of each run, the program loaded a file containing the particular cases to execute. For each case, there was a delay of at least 30 seconds after the cylinder motion was started to allow the cylinder to reach its new equilibrium temperature. Following the delay, voltage data from the embedded thermocouple was recorded for 200 seconds at a rate of 20 samples per second. When data acquisition was completed, the cylinder motion was stopped, and a delay of 20 seconds was imposed before beginning the next case. This delay allowed any wake structures generated by the cylinder motion to convect downstream a distance sufficient to insure that they did not affect the next case.

During each run the freestream temperature, cylinder power input and thermocouple-offset voltage were periodically monitored and recorded manually. Following each run, these values were analyzed to make sure that the conditions had been approximately constant. Measured variations in the conditions were accounted for in the data processing.

Data for the small aspect ratio cylinder cases was acquired in two separate runs. Cases with $f^* > 0.15$ ($1/f^* < 6.67$) were carried out in the first run, and the remaining cases were part of a second run at a later date. All of the large aspect ratio cylinder cases were carried out in a single run. Within each of these runs, the cases were in order of increasing amplitude and decreasing frequency, with the amplitude changing more quickly.

3.4 Results

The results of these experiments are shown in Figure 3.3 and Figure 3.4. Contours of the Nusselt number, scaled by the Nusselt number of the non-oscillating cylinder (Nu_0), are shown. The contour levels bracketing unity were selected to indicate those values that are measurably different than one. Other contour levels are spaced exponentially. While the contour levels are at the same values for the two figures, the color schemes differ because the maximum contour level is at a higher value for the large diameter cylinder data.

3.5 Discussion

3.5.1 Uncertainty and repeatability

The main sources of uncertainty in these results are the value of the constant in the model used to determine the heat transfer coefficient, $C_{\Delta T}$, and the measurement of the cylinder core temperature, T_{tc}. At the non-oscillating cylinder heat transfer coefficient, uncertainty in $C_{\Delta T}$ alone leads to an 8% to 10% uncertainty in the heat transfer coefficient. The relative uncertainty due to $C_{\Delta T}$ increases linearly with h, so this can be a very large source of error for large heat transfer coefficients. At the same time, the value of $C_{\Delta T}$ is constant for each cylinder, so this effect is systematic. Therefore, the magnitude of the heat transfer suffers from this source of error, but any trends observed are not affected.

Filtering and averaging over a large number of samples eliminates the majority of the noise in the thermocouple signal, but the thermocouple itself is an inherently imprecise device. The uncertainty in the measured temperature is estimated to be ±0.1°C. Applying equation (2.6), this corresponds to a relative uncertainty in h of 1% when $h \approx h_0$ and 7% when $h \approx 3h_0$.

The uncertainties in the other measurements used to determine h are not as significant. The combined relative uncertainties due to length, diameter and power input measurements are only about one sixth (1/6) of the uncertainty due to the thermocouple for $h \approx h_0$. Also, the relative uncertainty due to these sources increases with h at a slower rate than the uncertainty due to T_{tc}. Uncertainty in the freestream temperature measurement contributes one tenth (1/10) as much as the uncertainty in T_{tc} to the total uncertainty in h at all values of h. The additional uncertainty introduced when non-dimensionalizing h as the Nusselt number is also insignificant.

In addition to uncertainty, there is also systematic error in this experiment. The uncertainty stated above for the thermocouple of ±0.1°C applies to measurements in a single run and does not account for shifts in the data between various runs. The data reported here is the most complete set available, but smaller runs were carried out in the process of setting up and testing the experiment. For the same oscillation condition carried out in different runs, the values of Nu/Nu_0 were observed to systematically shift by up to 2%. All of the trends in heat transfer enhancement are repeatable, but the specific values of Nu/Nu_0 are not. There are a number of possible sources for this systematic shifting, including such things as drift in the analog-to-digital converter or change in the resistance at an electrical connection. Since the observed shifts are generally smaller than the uncertainty in the reported values, this does not affect the reliability of the data. However, it would be beneficial to identify the source of the shifting in order to improve future experiments.

3.5.2 Synchronization with the Strouhal frequency and its harmonics

For small amplitudes, heat transfer is significantly enhanced by oscillations near the non-oscillating cylinder shedding frequency and its harmonics, as is highlighted in Figure 3.5 and Figure 3.6. Curves of $(Re/Re_0)^{1/2}$ are included for comparison to the expected increase in heat transfer if the effect of oscillations is due only to the increase in the effective speed of the flow. At the smallest amplitudes considered, the heat transfer coefficient is significantly enhanced near frequencies of 1, 3 and $\frac{1}{3}$ times the Strouhal frequency (recall that $f^*_{St} \approx 0.21$ at this Reynolds number) for both cylinders. For amplitude ratios greater than about 0.2, heat transfer is also enhanced near 2 times the Strouhal frequency. These effects persist up to amplitude ratios of about 0.4 to 0.5. For each of the heat transfer peaks associated with Strouhal frequency harmonics $f^* \geq f^*_{St}$, the non-dimensional frequency at which the peak occurs shifts toward lower frequency as the amplitude increases. The reason for this shifting is not known.

Some aspect ratio effects are also evident in the heat transfer near Strouhal frequency harmonics. For the smaller aspect ratio cylinder, there is an elevated heat transfer coefficient at $\frac{2}{3} f^*_{St}$ ($f^* \approx 0.14$). In this same non-dimensional frequency range, the larger aspect ratio cylinder exhibits a more gradual decay away from the peak associated with the Strouhal frequency. In addition, the larger aspect ratio cylinder has a lower peak associated with $3f^*_{St}$ for A/D = 0.3, and the peak associated with $2f^*_{St}$ is not present until A/D = 0.3. The mechanism through which aspect ratio effects the heat transfer at these conditions is not evident from this data but will be investigated in Chapter 5.

The existence of these harmonic peaks is consistent with the work of other authors. The range of amplitude ratios and non-dimensional frequencies in the cases of interest is most comparable with the data of Park (1998), a sample of which was shown in Figure 1.7. While Park does not have cases at this exact Reynolds number, the observed trends in the data are very similar. The only significant disagreement pertains to the low-frequency enhanced heat transfer cases. At some Reynolds numbers and some amplitude ratios, Park found evidence of enhanced heat transfer at $\frac{1}{2}f^*_{St}$. Park did not find any evidence of enhanced heat transfer at $\frac{1}{3}f^*_{St}$ or $\frac{2}{3}f^*_{St}$. However, the correspondence between the 2P+2S wake mode and the $\frac{1}{3}f^*_{St}$ harmonic suggests that the present data is more consistent with observed fluid phenomena.

3.5.3 Wake modes

Wake mode also appears to play a significant role in determining the heat transfer coefficient. The wake mode boundaries identified by Williamson and Roshko (1988), shown in Figure 1.2, are superimposed on the contour plots of normalized Nusselt number in Figure 3.7 and Figure 3.8. There is clearly a connection between wake mode boundaries and features of the contour plots. The 2S/2P boundary, near $1/f^* = 5$, corresponds to a region of steep gradient in the

Nusselt number. At low frequency, there appears to be enhanced heat transfer in the 2P+2S mode. This is more evident in the AR = 21.3 data, but it is present in the AR = 14.2 data as well. At the highest non-dimensional frequencies observed, the contours of Nu/Nu_0 have a change in the sign of their slope for amplitude ratios between 0.7 and 0.9. While this does not correspond exactly to a wake mode boundary identified by Williamson and Roshko (1988), it is very near the C(2S)/C(P+S) boundary. Given that the exact position of the wake mode boundaries is known to vary with Reynolds number, it is likely that this slope change of the contours is related to a wake mode boundary. In the AR = 21.3 data, there is an unusual feature in the contours of Nu/Nu_0 near $1/f^* = 4$, $1.1 \leq A/D \leq 1.4$. This feature may be related to the 2P/P+S wake mode boundary.

The features of the contour plots that have been related to wake mode boundaries possess an additional characteristic of interest. In the heat transfer coefficient data, the wake mode boundaries smoothly span several oscillation conditions in the direction normal to the boundary. It might be more appropriate to describe them as transition regions rather than boundaries. This is in contrast to forced oscillation experiments for unheated cylinders reported in the literature. In those experiments, the indirect indicators of wake mode—such as the phase of the fluid forces relative to the cylinder motion—were observed to undergo abrupt transitions between individual test conditions. The nature of the observed broad transition regions will be examined in Chapter 4.

The apparent connection between wake mode and heat transfer coefficient suggests that the heat transfer process is strongly dependent on how vorticity is distributed in the wake of the cylinder. This connection will be directly examined in Chapter 5.

The “turbulence effect” referred to by Cheng et al. (1997) does not appear in the current data. Rather, the region of the parameter space in which this supposed effect was observed ($1/f^* < \sim 4$, $0.314 \le A/D \le 0.628$) is dominated by the third harmonic of the Strouhal frequency and the transition from a 2S to a C(2S) wake mode. At the time of the Cheng et al. study, these wake phenomena were not known to affect the heat transfer, so the observed heat transfer enhancement was attributed to an assumed new effect. The wake mode and harmonic effects identified the current data eliminate the need for a turbulence effect to explain the Cheng et al. (1997) data.

3.5.4 Transverse velocity

Over a significant portion of the parameter space investigated, mainly away from Strouhal frequency harmonics and wake mode boundaries, the contours of constant Nu/Nu_0 appear to be well described by straight lines that pass through the origin. Such lines also correspond to level curves of the cylinder’s transverse velocity. Based upon this observation, the normalized heat transfer coefficient is plotted versus the non-dimensional root-mean-square (rms) transverse velocity, V_{rms}/U, in Figure 3.9. Since the cylinder motion is sinusoidal, the rms transverse velocity equals $\frac{1}{\sqrt{2}}$ times the peak transverse velocity.

While there is significant scatter for V_{rms}/U less than about 1, the data appears to partially collapse for larger values of V_{rms}/U. The data for the AR = 14.2 cylinder appears to follow two main curves, with a smaller number of data points falling between the two curves. The data for the AR = 21.3 cylinder nearly all lies on one curve, though a small number of data points lie above that curve for V_{rms}/U less than about 1.7.

It is assumed that the AR = 21.3 data lies below AR = 14.2 data due to aspect ratio effects. If this is the only effect of aspect ratio, then there must be another reason why the AR = 14.2 data exhibits two behaviors while the AR = 21.3 data primarily shows only one behavior. Due to the frequency limitations of the oscillation mechanism, higher non-dimensional frequencies were achieved for the AR = 14.2 cylinder than for the AR = 21.3 cylinder. If one branch of the smaller aspect ratio data is limited to high values of f^*, this would explain the absence of that branch from the AR = 21.3 cylinder data. The small number of AR = 21.3 data points that lie above the curve following the majority of the data may, in fact, be the beginning of a second curve for that data set.

The bifurcation in the AR = 14.2 data was examined by excluding data points associated with harmonics of the Strouhal frequency and identifying the wake mode of each remaining data point. For purposes of understanding this bifurcation, the wake mode boundaries are assumed to be the previously described features of the contour plot. The results of this sorting are shown in Figure 3.10. It is apparent that the two behaviors correspond to two different types of wake modes. Since the C(2S) wake mode has the higher heat transfer coefficient, this explains why the AR = 21.3 data had a few data points above the curve being followed by the majority of data points. Only a few of the oscillation conditions considered for the higher aspect ratio cylinder were in the C(2S) wake mode region and away from harmonic effects.

3.6 Conclusion

In this chapter, the details of an investigation into the effects of transverse oscillations on the heat transfer from a circular cylinder over a large range of frequencies and amplitudes were presented. Based upon the results of this investigation, several conclusions can be drawn.

First, heat transfer is significantly enhanced by small amplitude oscillations at frequencies near the Strouhal frequency and its harmonics. While previous authors have observed this heat transfer enhancement, it was shown for the first time that this effect is limited to amplitude ratios less than about 0.5.

This investigation also revealed that the wake mode is related to the heat transfer coefficient. Many features apparent in the contour plots of normalized heat transfer coefficient correspond to known wake mode boundaries. This relationship, along with the enhanced heat transfer near the Strouhal frequency and its harmonics, strongly suggests that the wake structure, i.e., the distribution of vorticity in the wake, plays a central role in determining the heat transfer coefficient.

The transverse cylinder velocity was also shown to play a significant role in determining the heat transfer coefficient. Previous authors have unsuccessfully attempted to correlate the transverse velocity with the heat transfer coefficient. In this investigation, it was shown that within a particular wake mode and away from effects associated with the Strouhal frequency, the transverse cylinder velocity is the primary factor responsible for variations in heat transfer coefficient.

Aspect ratio also appears to play a role in determining the level of heat transfer enhancement that is achieved for a particular oscillation condition. However, the basic effects and trends observed do not depend on aspect ratio.

The largest source of error in measuring the heat transfer from a cylinder in this experiment was found to be the construction of the cylinder itself. The most beneficial modification to this experiment for future work would be to alter the design of the cylinder construction so that a more reliable method for determining the heat transfer coefficient can be developed. Such a modification might take the form of mounting multiple temperature sensing devices flush with the cylinder surface at various locations, thereby eliminating the need for a model to be used. It would also be advantageous to use a more accurate and more precise type of sensor for measuring the cylinder temperature, such as an RTD or a thermister.

Figures for Chapter 3

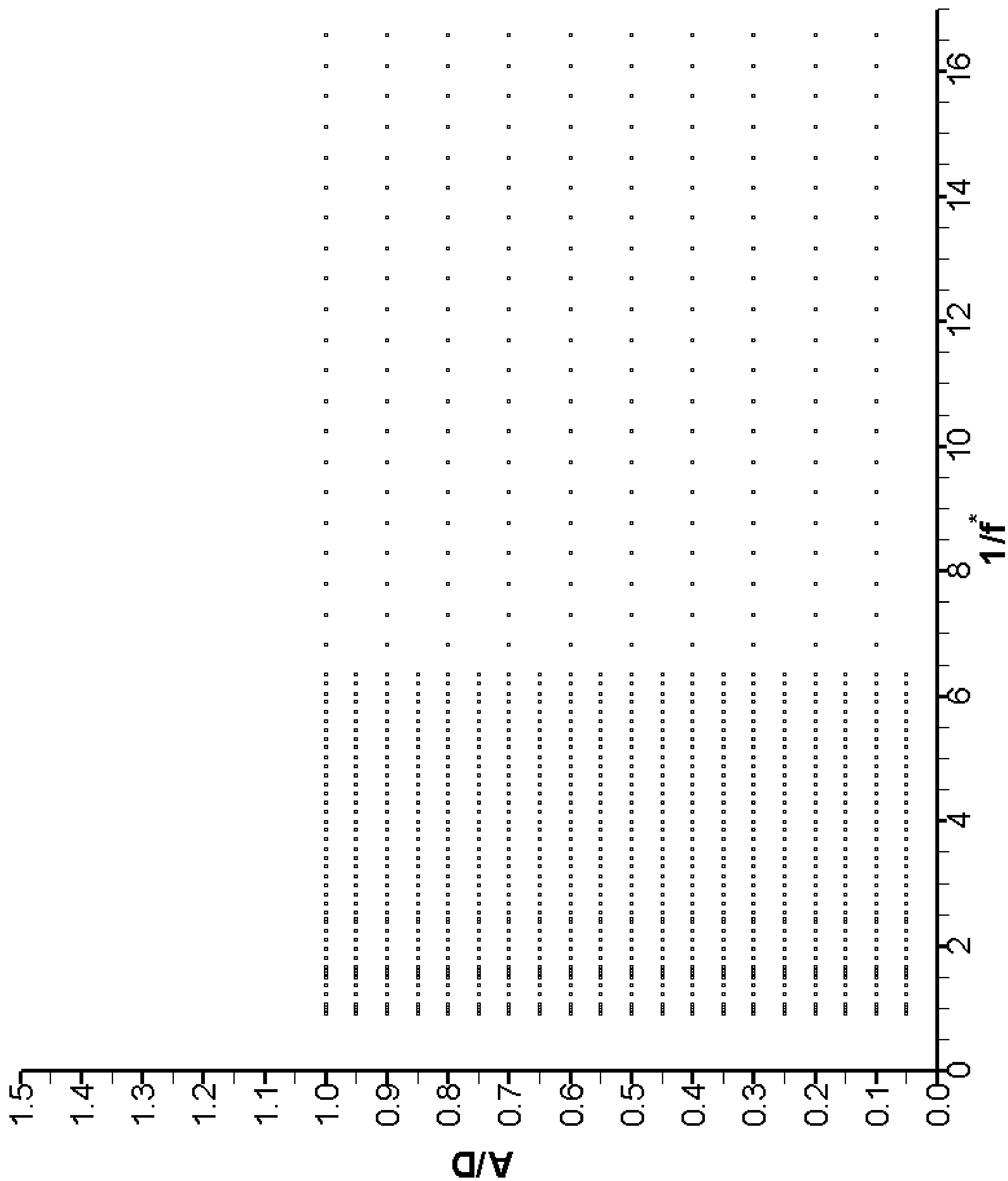

Figure 3.1: Oscillation conditions considered for the AR = 14.2 cylinder

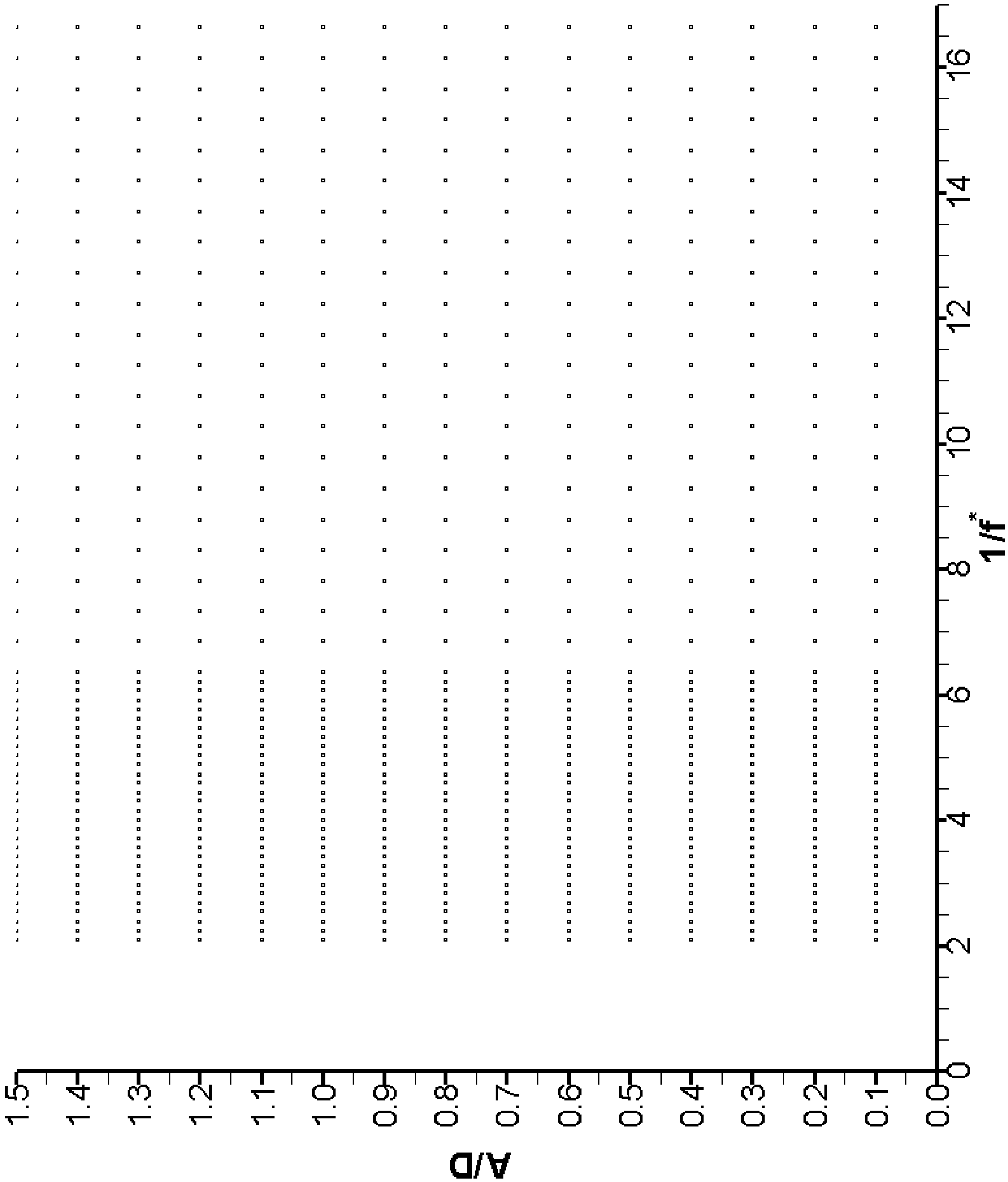

Figure 3.2: Oscillation conditions considered for the AR = 21.3 cylinder

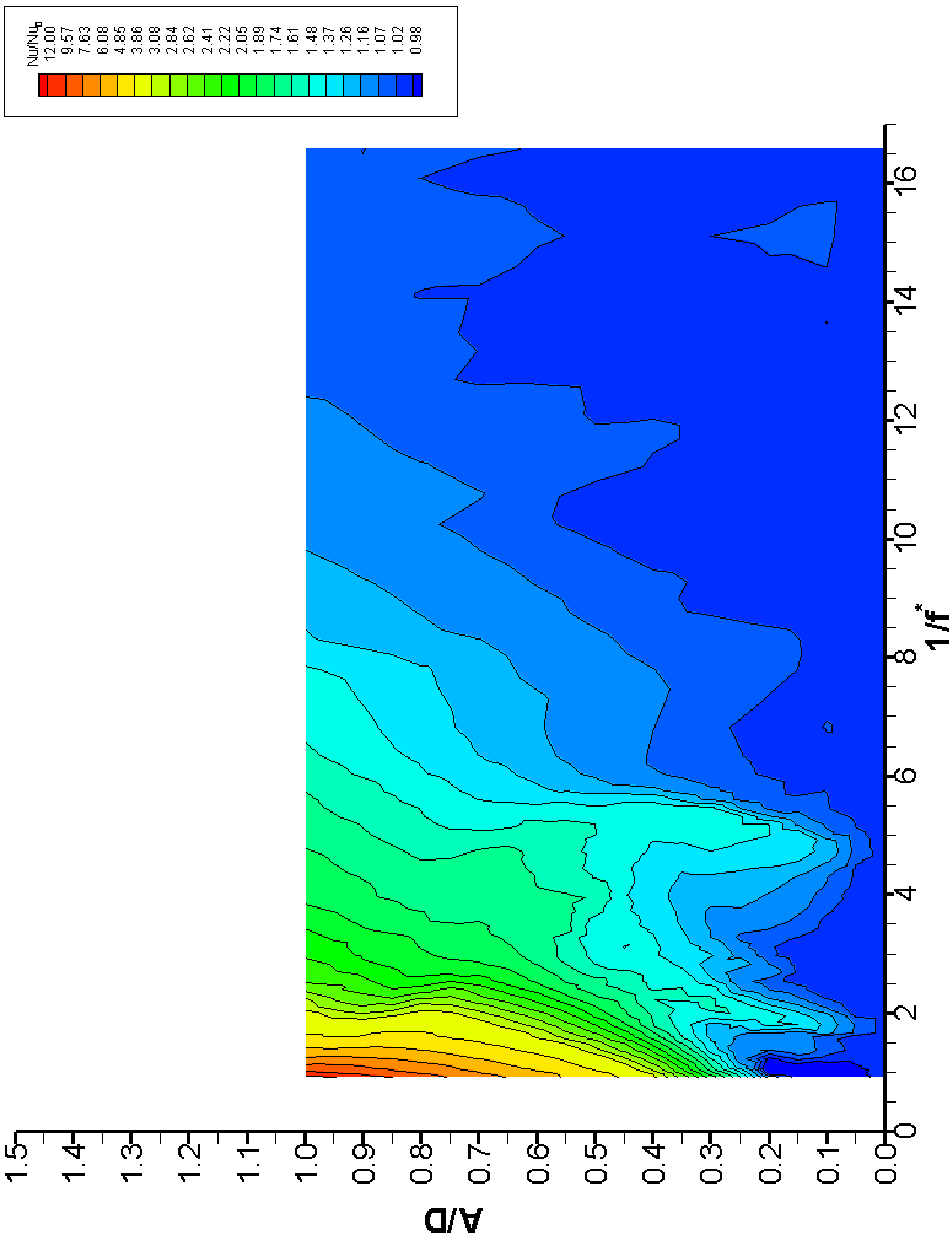

Figure 3.3: Contours of heat transfer coefficient normalized by non-oscillating cylinder heat transfer coefficient (Nu/Nu_0) for the AR = 14.2 cylinder

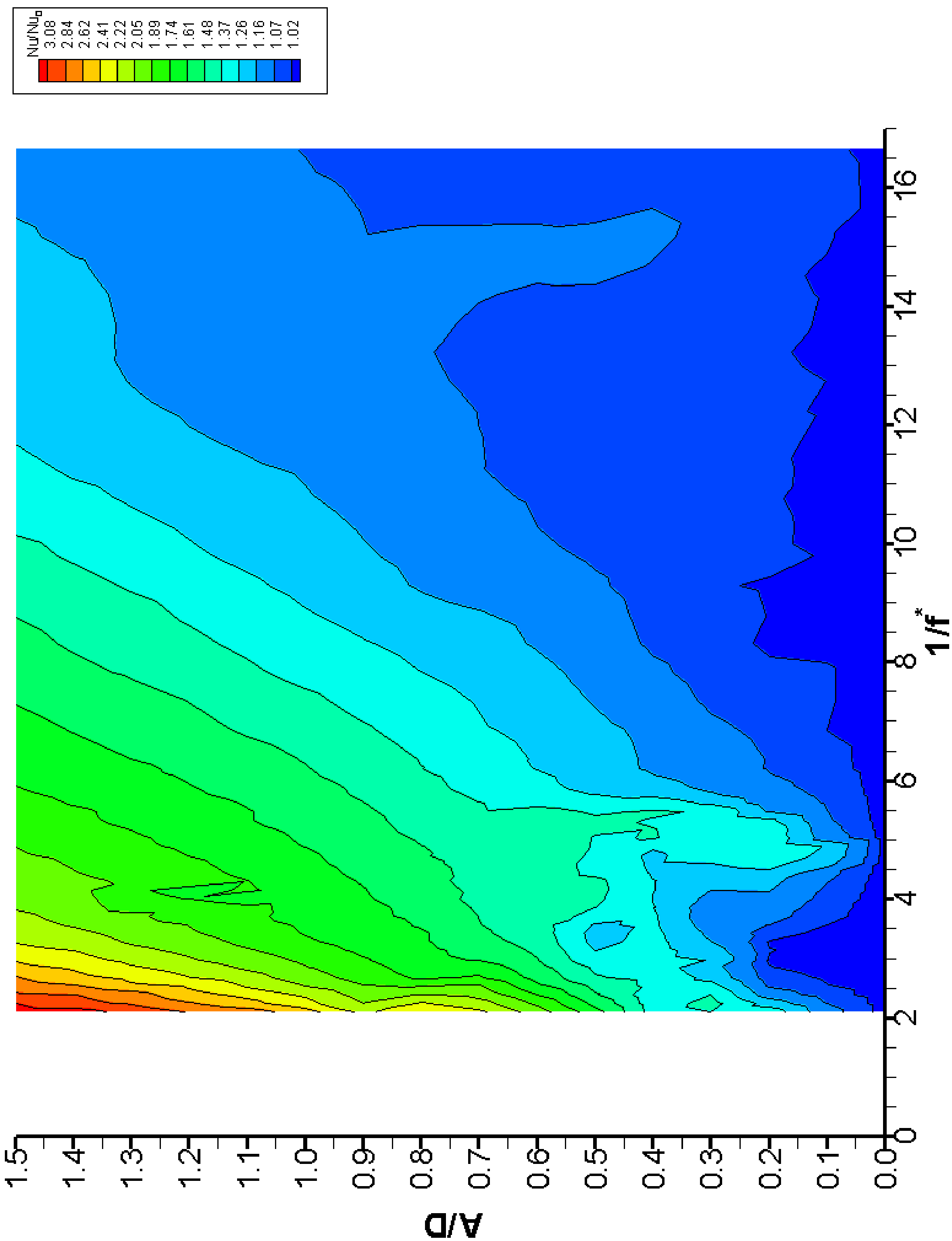

Figure 3.4: Contours of heat transfer coefficient normalized by non-oscillating cylinder heat transfer coefficient (Nu/Nu_0) for the AR = 21.3 cylinder

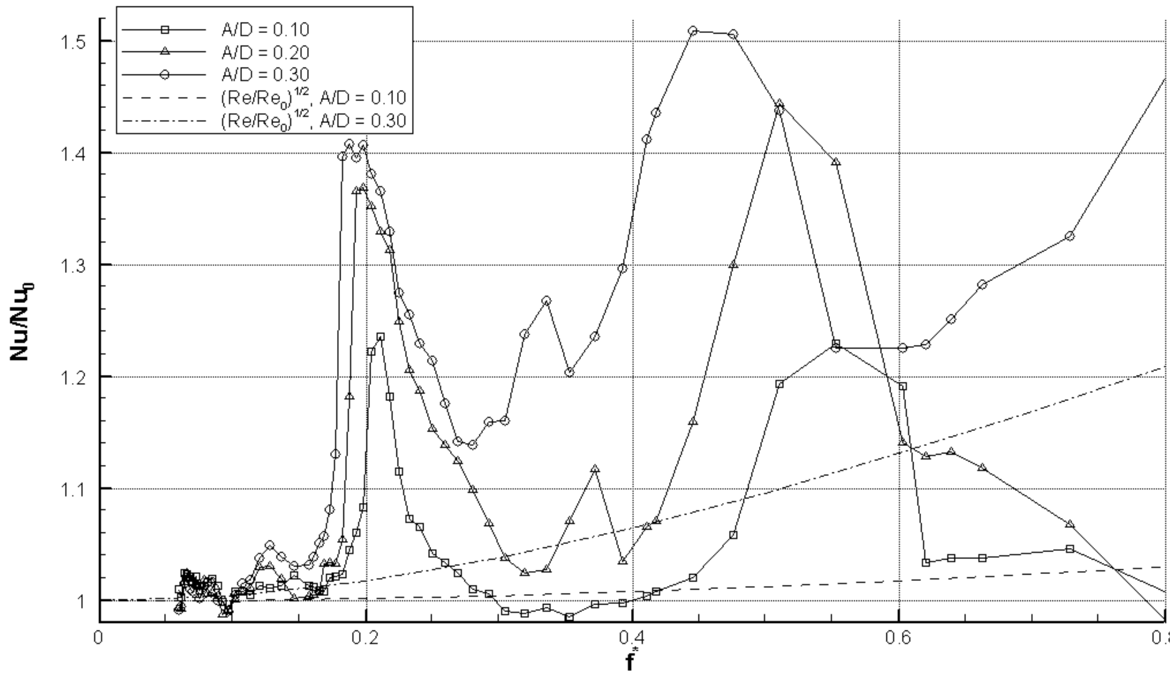

Figure 3.5: Normalized heat transfer coefficient (Nu/Nu_0) vs. non-dimensional oscillation frequency (f^*) at selected small amplitudes for the AR = 14.2 cylinder

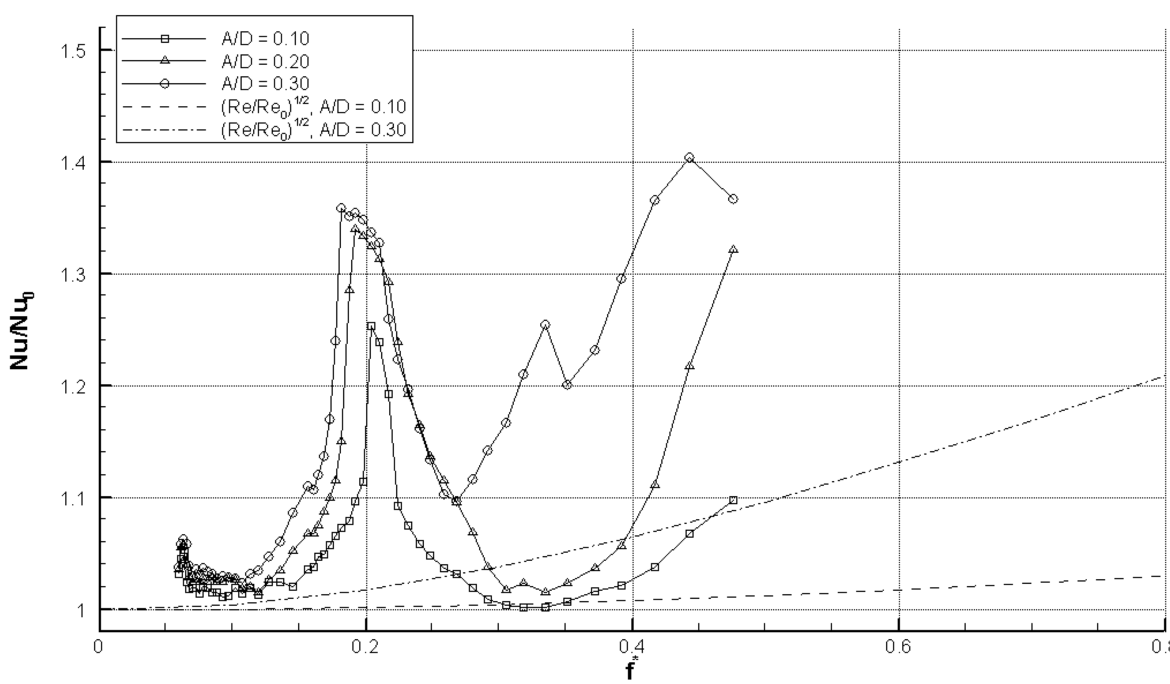

Figure 3.6: Normalized heat transfer coefficient (Nu/Nu_0) vs. non-dimensional oscillation frequency (f^*) at selected small amplitudes for the AR = 21.3 cylinder

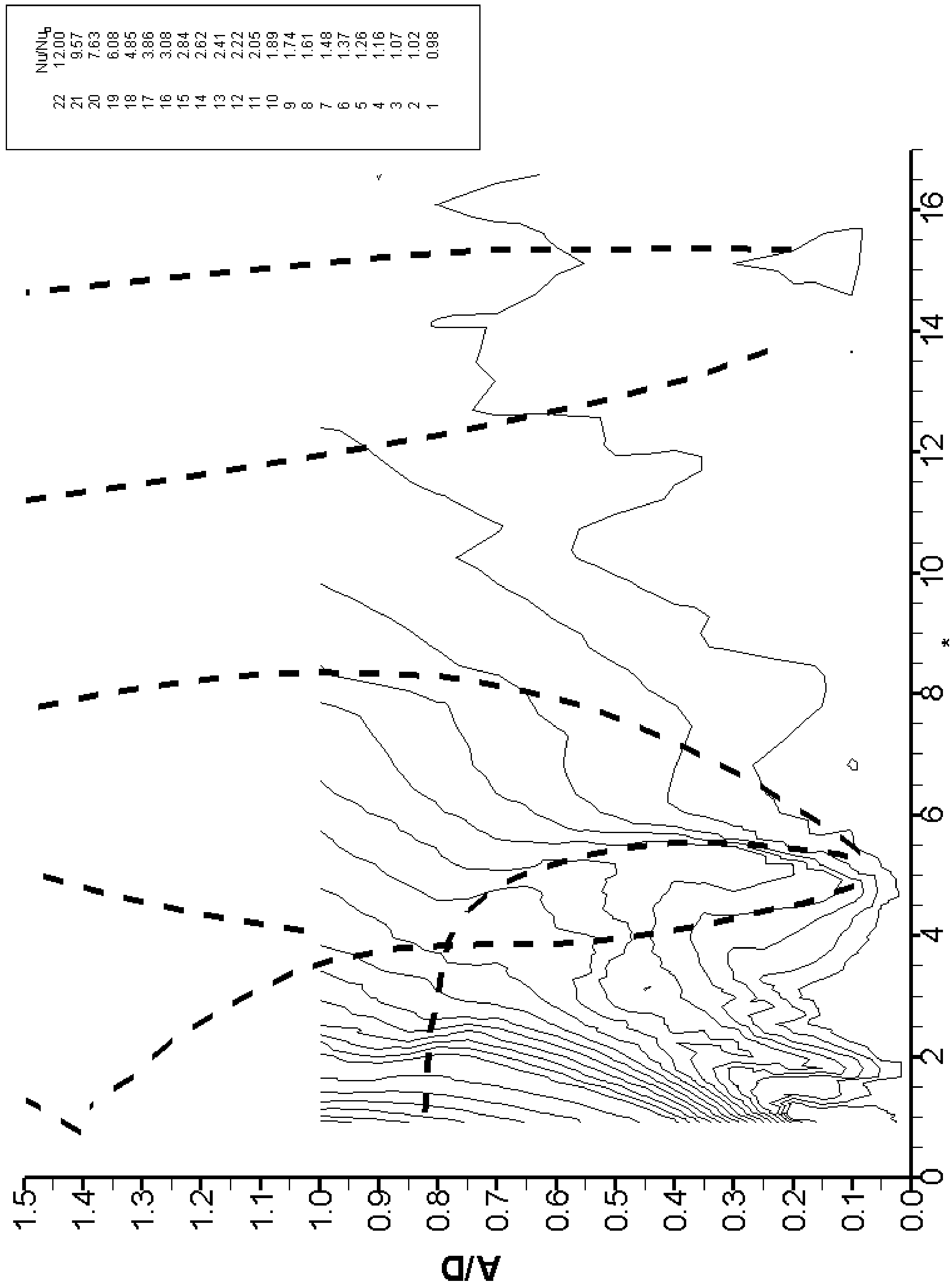

Figure 3.7: Contours of normalized heat transfer coefficient (Nu/Nu_0) for the AR = 14.2 cylinder with wake mode boundaries from Williamson and Roshko (1988) superimposed

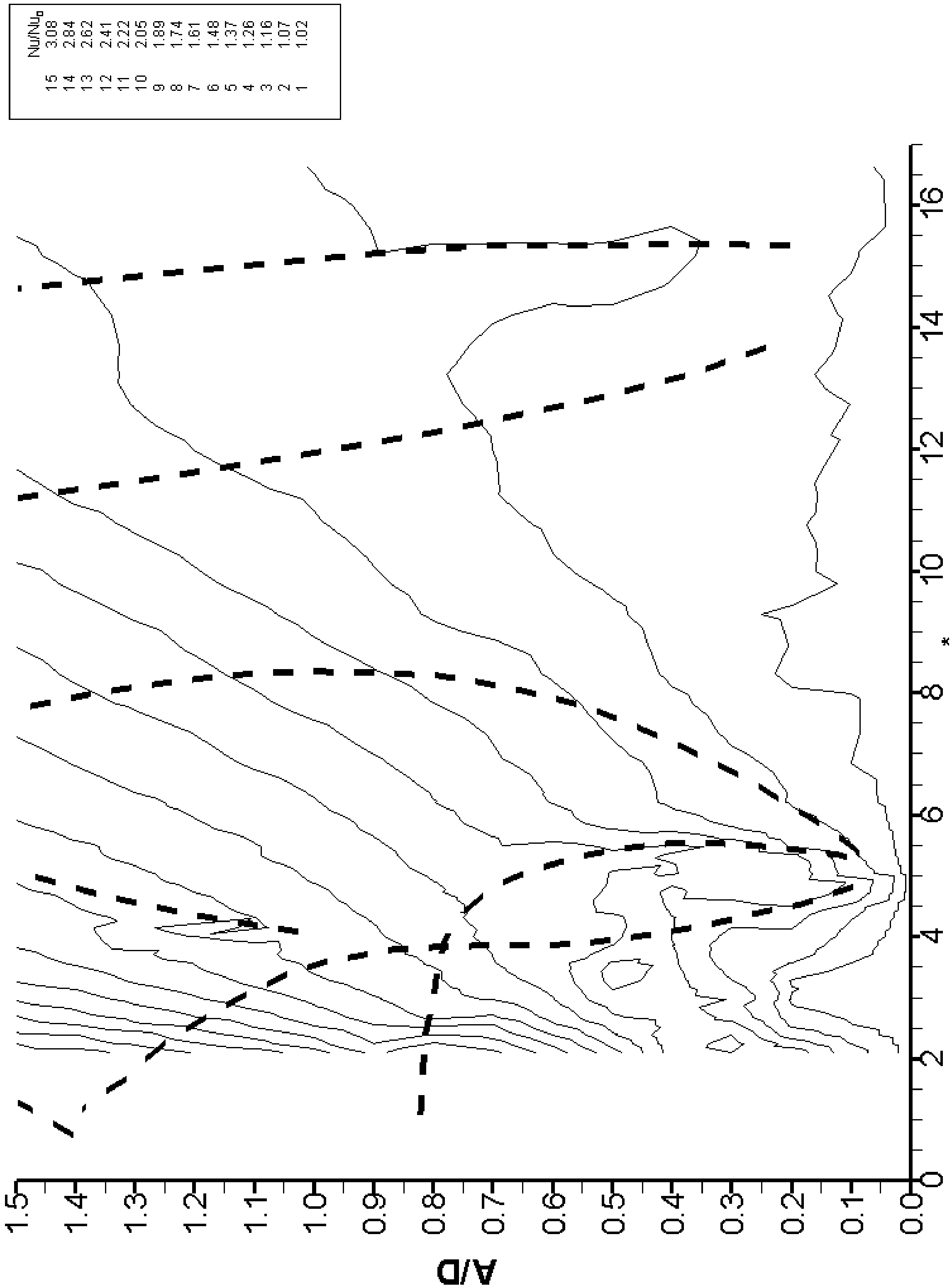

Figure 3.8: Contours of normalized heat transfer coefficient (Nu/Nu_0) for the AR = 21.3 cylinder with wake mode boundaries from Williamson and Roshko (1988) superimposed

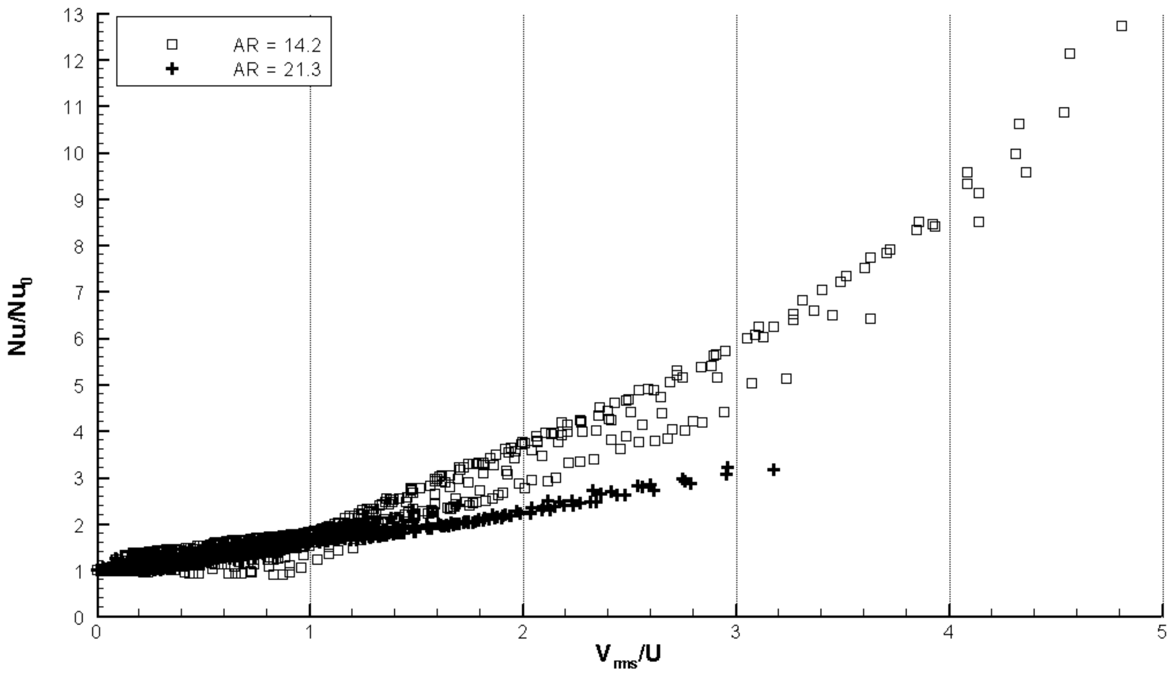

Figure 3.9: Normalized heat transfer coefficient (Nu/Nu_0) vs. non-dimensional rms transverse cylinder velocity (V_{rms}/U) for both cylinders

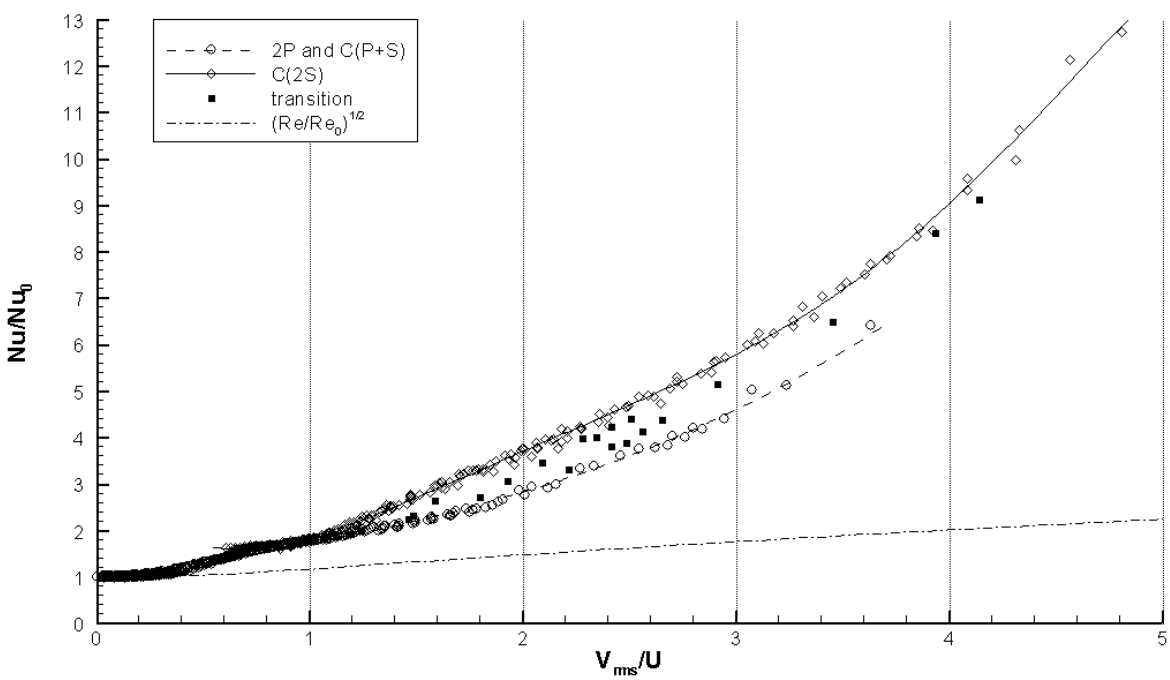

Figure 3.10: Normalized heat transfer coefficient (Nu/Nu_0) vs. non-dimensional rms transverse cylinder velocity (V_{rms}/U) for AR = 14.2 cylinder with wake modes identified and data near harmonic synchronizations removed; curves are least-squares polynomial fits to the data

4 Wake mode transitions and the mode-switching phenomenon

4.1 Introduction

In §3.5.3, the apparent existence of continuous transitions between distinct wake modes was noted. Broad transition regions were observed to exist in the heat transfer coefficient data, while for unheated cylinders transitions between wake modes are abrupt, though they may exhibit hysteresis. This suggests that the heating of the cylinder is somehow changing the wake formation process. Identifying the nature of this change would expose part of the dynamics of wake formation in general.

In the present chapter, these transition regions are explored in greater detail. It will be shown that the smooth transition regions actually consist of cases where the wake is repeatedly switching between distinct modes, a new phenomenon that is not observed for unheated cylinders. A qualitative model describing the mechanism for this mode-switching will be proposed. The implications of this discovery for understanding wake modes in general will also be discussed.

4.2 Time-dependent analysis of data from earlier experiments

The analysis of data in Chapter 3, using the model described in Appendix B, assumes that the cylinder's heat transfer coefficient is steady. While this assumption is in fact true for the vast majority of the cases considered, it is not correct for all cases. Certain cases in wake mode transition regions exhibit highly unsteady, and possibly periodic, behavior.

Figure 4.1 shows thermocouple temperature time series for 15 cases spanning the 2S/2P transition at amplitude ratios near 0.35. The arrangement of the subplots corresponds to ($1/f^*$,A/D) coordinates such that those subplots on the left side represent cases in the 2S wake mode region, and the subplots on the right correspond to cases in the 2P wake mode region. The 2S cases have a steady thermocouple temperature of about 41.3°C, while the 2P cases have steady temperatures over 43°C. The cases in the middle, however, do not have a steady temperature. Instead, they appear to repeatedly move between the temperature levels associated with the 2S and 2P wake modes. While the variations are not periodic, there does appear to be a dominant timescale. For the particular cases shown, the period of the switching is on the order of 30 to 40 seconds. The period of switching varies from cases to case and is generally shorter for the large aspect ratio cylinder. The timescale of these temperature variations will be examined in §4.4. Repetition of cases indicates that the large temperature variations consistently occur at the same conditions, and the timescales of the switching are repeatable, as well.

As noted in §3.5.3, the heat transfer coefficient, and consequently the cylinder core temperature, depends primarily on the wake mode in this region of the parameter space. The variation in cylinder core temperature therefore suggests that the wake mode for these cases is in fact switching repeatedly between the 2S and 2P modes. Such a phenomenon, which will be referred to as mode-switching, has not been observed to occur for unheated cylinders undergoing forced sinusoidal oscillations. The only similar phenomenon is a one-time switch from the 2P mode to the 2S mode related to startup conditions observed by Carberry et al. (2001). Later sections of this chapter focus on determining if mode-switching is actually occurring and on understanding the mechanism of the mode-switching.

The smooth wake mode transitions described in §3.5.3 can now be interpreted. The temperature used to determine the Nusselt number for each case was the average of a 200-second time series containing 100 to 1500 cylinder oscillations and, for cases with mode-switching, 4 to 14 cycles of mode-switching. For cases undergoing mode-switching, the average of the time series will correspond to some value in between the temperatures associated with the two modes being switched between. This will lead to an apparent smooth transition between the two modes in the heat transfer data.

It is desirable to have a single quantity that can be used to identify whether mode-switching occurred for a particular case. The first quantity considered was the uncertainty in the normalized heat transfer coefficient attributable to the standard deviation in the thermocouple temperature time series

$$\sigma_{Nu/Nu_0} \equiv \sqrt{\left(\frac{\partial(Nu/Nu_0)}{\partial T_{tc}}\right)^2}\,\sigma_{T_{tc}} = \frac{Nu/Nu_0}{T_{surf} - T_\infty}\,\sigma_{T_{tc}} \,. \tag{4.1}$$

This did not perform well for identifying mode-switching because it is too heavily weighted by the heat transfer coefficient. The direct dependence on the heat transfer coefficient was therefore removed to form a normalized quantity

$$\frac{\sigma_{Nu/Nu_0}}{Nu/Nu_0} = \frac{\sigma_{T_{tc}}}{T_{surf} - T_\infty}\,, \tag{4.2}$$

which performed significantly better. Contours of this normalized standard deviation are plotted in Figure 4.2 and Figure 4.3.

It is evident that mode-switching is confined to particular areas of the ($1/f^*$,A/D) plane. In Figure 4.4 and Figure 4.5, the Williamson and Roshko (1988) wake mode boundaries are superimposed on the standard deviation contours.

Mode-switching is particularly strong along the 2S/2P boundary, and it is also significant along the C(2S)/C(P+S) boundary. There is also evidence that mode-switching occurs in the region where the 2P, P+S and C(P+S) modes come together. However, mode-switching does not occur at all wake mode boundaries.

Switching also occurs around the harmonics of the Strouhal frequency. In these cases, the switching is not between distinct modes, but rather between wake structures that are synchronized with the harmonic frequency and structures that are not synchronized with the harmonic.

The regions of mode-switching occur at the same non-dimensional conditions for both of the cylinders used in this study. These conditions correspond to significantly different dimensional frequencies and amplitudes, which indicates that the mode-switching is a real fluid mechanical phenomenon related to the wake structure, not a spurious noise signal.

4.3 Verification of wake mode-switching

In order to verify that the presumed switching between wake modes is taking place, DPIV and thermocouple data were acquired simultaneously for an oscillation condition known to exhibit the signs of wake mode-switching. The condition $1/f^* = 5.60$, $A/D = 0.35$ was chosen because it had the highest value of $\sigma_{Nu/Nu_0}/(Nu/Nu_0)$ observed in the initial parameter space survey. This condition lies in the 2S/2P transition region.

DPIV data was acquired using the same setup as used for DPIT/V (described in §2.7), but the color content was not calibrated so no temperature information was obtained. Synchronization of the images with the thermocouple data was accomplished by recording the light sheet timing signal along with the thermocouple data. In order to resolve the timing signal, both signals were sampled at 500 samples per second. The DPIV data rate corresponded to 12.4 image pairs per cycle.

Figure 4.6 shows the recorded thermocouple signal as a function of time. If the hypothesis that the temperature fluctuations are caused by changes in wake mode is correct, there should a 2S wake mode when $dT_{tc}/dt < 0$, and there should be a 2P wake mode when $dT_{tc}/dt > 0$. The portions of Figure 4.6 that are marked with heavy lines are the times chosen to examine the wake mode. The times when the temperature was near its minimum and maximum values were not included because of a possible time lag between the actual mode-switching and the temperature signal.

The DPIV data corresponding to the indicated times was divided into two groups by the sign of the temperature slope. The negative slope group contained 31.5 cycles of the cylinder motion, and the positive slope group contained 19.4 cycles. The vorticity fields for each group were phase averaged with respect to the motion of the cylinder. The cylinder motion was divided into 16 equally sized phase "bins," and all of the flow snapshots in a bin were averaged together.

The resulting phase averaged vorticity fields are shown in Figure 4.7 and Figure 4.8. Eight of the 16 phases of the cylinder motion are shown, with every other phase being omitted. As predicted, the negative temperature slope vorticity fields exhibit a 2S wake mode, while the positive temperature slope vorticity fields show a 2P wake mode. This confirms that wake mode-switching is taking place.

4.4 Connection between temperature and wake mode

In order to determine the mechanism behind the observed mode-switching, the timescale of the switching was compared to a number of possible sources. Table 4.1 lists several known timescales in the flow. None of these timescales is on the same order as the observed timescale of the mode-switching. There is also no apparent correlation between the oscillation frequency and the mode-switching frequency.

There is one additional timescale present in the experiment due to the manner in which the cylinder is heated. As described in §2.3 and §2.6, the power input to the cylinder is held constant and the heat transfer coefficient then determines the resulting cylinder core temperature. If the heat transfer coefficient of the cylinder changes, there will be some amount of time required before the cylinder core reaches its new equilibrium temperature. It is possible that this cylinder thermal timescale is related to the mode-switching. However, the cylinder thermal timescale is not known and must be modeled.

In designing this set of experiments, it was assumed that the cylinder's heat transfer coefficient for a particular oscillation condition was steady. If this were the case, the only effect of the cylinder thermal timescale would be on the length of time required for the system to reach steady state. A rough estimate of the cylinder time scale was considered sufficient to estimate the necessary delay to allow the transient behavior to pass before recording data. In the unsteady cases, it is desirable to know the thermal time scale more accurately.

In order to determine the cylinder thermal time constant, a time-varying version of the internal heat transfer model was developed. It was constructed to simulate the cylinder's thermal response to a step change in the heat transfer coefficient at $t = 0$. The details of the unsteady model derivation can be found in Appendix C. The time constant for each cylinder was found to depend only on h_f, the heat transfer coefficient for $t \geq 0$. The calculated thermal time constants for various Nusselt numbers are shown in Figure 4.9. These time constants are of the same order as the observed mode-switching timescales. Variations in the observed timescale follow the trend of the model values, with shorter timescales corresponding to higher heat transfer coefficients.

This agreement between the timescale of mode-switching and the thermal time constant of the cylinder suggests that the observed temperature fluctuations are setting the period of the wake mode-switching. This implies that some type of feedback loop exists between the wake mode and the cylinder temperature. Of particular significance, this means that temperature is not a passive scalar in this flow.

A simulation was carried out using a simple hysteresis model in order to verify that a coupling between temperature and wake mode can produce the observed variations in cylinder core temperature. In the model, once the cylinder oscillations begin, the heat transfer coefficient can take on two possible values, h_1 or h_2. The heat transfer coefficient is determined by the cylinder surface temperature and the current state of the heat transfer coefficient as shown by the hysteresis loop in Figure 4.10. This model makes no attempt to identify the specific mechanism by which temperature affects the wake mode. The unsteady model of internal heat transfer developed in Appendix B was modified to allow h_f to take on the proper value according to this hysteresis loop.

Figure 4.11 shows the resulting temperature history on the cylinder using an initial condition corresponding to the stationary cylinder, h_1 equaling a typical value for the 2S mode, h_2 having a value typical of the 2P mode, and the properties of the AR = 14.2 cylinder. The switching temperatures, T_1 andT_2, were chosen to give approximately the observed variation in cylinder core temperature. While this model results in a periodic solution after the first mode-switch and not the quasi-periodic behavior observed in the experiments, the general features agree quite well. The timescale for the mode-switching is off by a factor of only 1.5. It is not surprising that such a simple model, which ignores all of the physics of the mode-switching mechanism, does not agree with the experiments in every detail. In fact, the high degree of similarity to the experimental results indicates that an abrupt change in the heat transfer coefficient induced by a change in surface temperature is a fairly good model of the mode-switching phenomenon.

4.5 Mode-switching mechanism model

The timescale of the observed mode-switching indicates that the cylinder temperature affects the cylinder wake structure but does not reveal the mechanism by which the temperature acts. That mechanism must be inferred indirectly. Temperature induced changes in the kinematic viscosity in a portion of the attached boundary layer are believed to be the means by which the temperature affects the wake structure.

Any plausible mechanism for mode-switching must allow for an incompatibility between the cylinder wake mode and the surface temperature it leads to. In addition, this incompatibility must drive the system towards a change in wake mode for some conditions. More specifically, it is necessary that in the mode-switching cases, the steady-state cylinder surface temperature corresponding to a particular wake mode causes the wake to switch out of that mode and in to a different mode. Such an incompatibility between wake structure and cylinder temperature may not always lead to mode-switching. For example, in the 2P mode the magnitude of the circulation of the leading and trailing vortices in a pair can be nearly equal or vastly different. Also, in Chapter 3 it was shown that the heat transfer coefficient varies more gradually within a wake mode than across mode boundaries. If the distribution of vorticity in the wake can adjust to the cylinder temperature sufficiently to reach either a limit cycle or equilibrium without changing wake mode, then no mode-switching will occur and no large fluctuations will appear in the temperature time series. Mode-switching is only observed to occur at particular oscillation conditions, so in the majority of cases the mechanism must lead the wake structure and the temperature to converge to either an equilibrium state or to a limit cycle entirely within one mode.

Temperature does not explicitly appear in the equations of motion describing this flow. However, temperature does enter indirectly through material properties. Of particular importance are density and viscosity. Temperature induced density differences will result in buoyancy forces on the fluid. Care was taken in designing the experiments to make sure that these buoyancy forces are not significant compared to inertial forces, so this is not considered as a possible mechanism. Viscosity differences, on the other hand, may be significant. While the density changes by only 0.3%, the kinematic viscosity of fluid at the cylinder surface is up to 20% lower than in the freestream. This can have a substantial effect on the flow near the cylinder. Therefore, temperature induced variations in the viscosity are thought to be the connection between wake mode and temperature.

Figure 4.12 shows the proposed model to explain the observed wake mode-switching phenomenon. The cylinder surface temperature sets the temperature profile of the thermal boundary layer, which then determines the viscosity in that layer. This will have an effect on the boundary layer velocity profile, which is also a function of the outer flow and of the existing wake. The influence of the existing wake allows hysteresis to enter the model. The boundary layer velocity profile and the outer flow determine the flux of vorticity and kinetic energy into the free shear layers. Following the ideas of Jeon and Gharib (2003), the kinetic energy of the fluid elements carrying the vorticity flux into the wake determines when a vortex pinches-off from the free shear layers, thereby determining the resulting wake mode. The cylinder surface temperature, therefore, is one factor that controls the distribution of vorticity in the wake, or the wake mode. As was demonstrated in §3.5.3, the wake mode is one of the factors that determine the cylinder heat transfer coefficient, which will set the surface temperature if the power input is constant. The loop is closed, and it is possible for feedback between the temperature and the wake structure to exist.

This mechanism is not equivalent to fluctuations in Reynolds number caused by temperature variations, though there is some similarity. The effect of varying cylinder temperature is not the same as if the freestream temperature is changed becasue the temperature is not uniform across the thermal boundary layer, and the thermal boundary layer is much thinner than the velocity boundary layer at the Prandtl number in this experiment. However, an analogy to a Reynolds number effect is useful. As mentioned in §1.2.1, the locations of wake mode boundaries depend on the Reynolds number and exhibit hysteresis. For a fixed oscillation frequency and amplitude, a change in Reynolds number due to a change in the fluid viscosity may, under the proper conditions, cause a wake mode boundary to move past the oscillation state. Due to hysteresis, there would be a finite difference in the Reynolds number at which switching occurs depending on the current wake mode. This would require a time delay and a temperature difference between successive mode-switches.

One significant implication of this model for the mechanism is that the sign of the derivative of kinematic viscosity with respect to temperature, $d\nu/dT$, is critical in determining if mode-switching occurs. This is related to the requirements for a plausible mechanism previously described. Had these experiments been conducted in air or in another fluid for which kinematic viscosity increases with increasing temperature, the conditions in this set of experiments that resulted in mode-switching would have presumably driven the wake mode boundary away from the oscillation state instead of towards it. The Prandtl number and its derivative may also play a role in determining the conditions for which mode switching occurs.

This proposed mechanism also implies that the heat transfer coefficient produced by a particular oscillation condition will depend on the cylinder input power or temperature. This is one possible way to test the model. Another way to test the model would be to perform detailed numerical simulations of the flow and heat transfer including explicit dependence of viscosity on temperature.

4.6 Conclusion

A new phenomenon was discovered in which the wake structure repeatedly switches between distinct wake modes or between variations of a single wake mode. The mechanism of this mode-switching is believed to be temperature induced variations in the fluid viscosity resulting in changes to the flux of vorticity and kinetic energy into the wake.

By highlighting the possible role of viscosity and of the separated shear layer fluxes in the determination of wake mode, this discovery may lead to improved understanding of the vortex formation and pinch-off processes in wakes in general, not just in heat transfer applications.

Additional investigations into mode-switching are necessary. Determining criteria for the occurrence of mode-switching would reveal a great deal about wake formation processes in general. This requires that the proposed model of the mode-switching mechanism be tested and made quantitative. To this end, numerical simulations in which the temperature dependence of viscosity can be prescribed or eliminated would be useful.

Tables and figures for Chapter 4

Table 4.1: Known timescales present in the flow

Source / phenomenon	Timescale (sec)
Cylinder oscillations	0.14 – 2.2
Water tunnel pumps	0.13 – 0.20
Water tunnel sloshing	~3
Water tunnel recirculation	~120

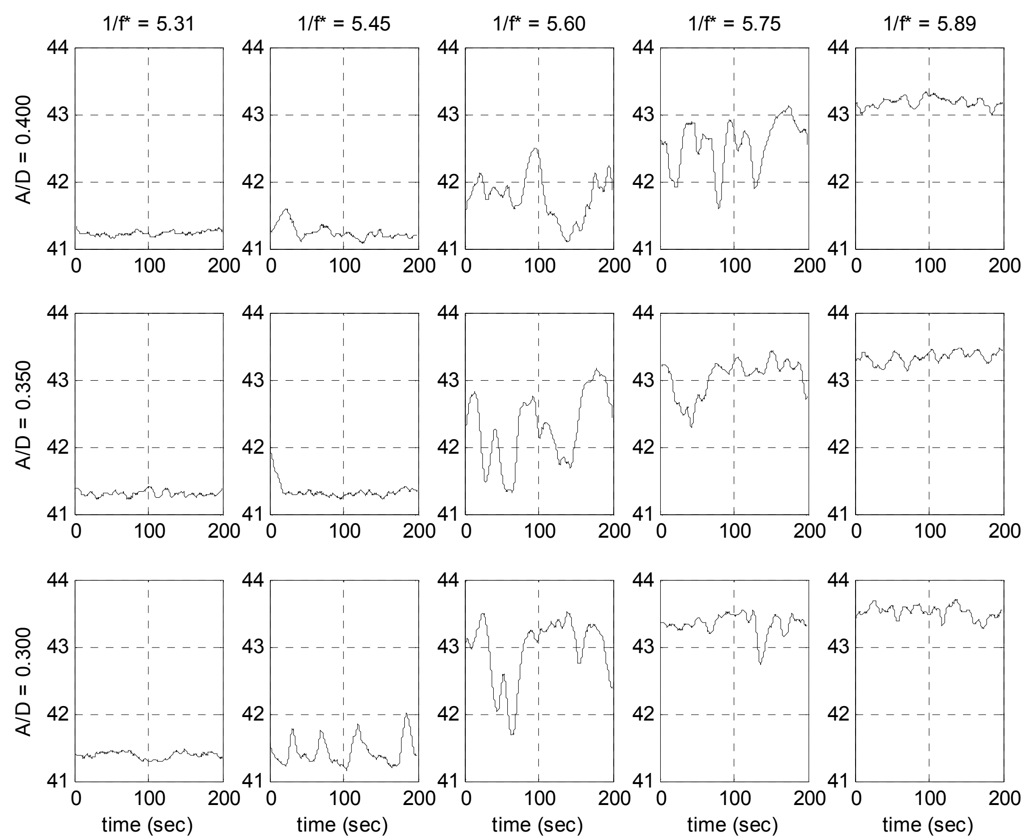

Figure 4.1: Time series of thermocouple temperature for several oscillation conditions near the 2S/2P transition using the AR = 14.2 cylinder

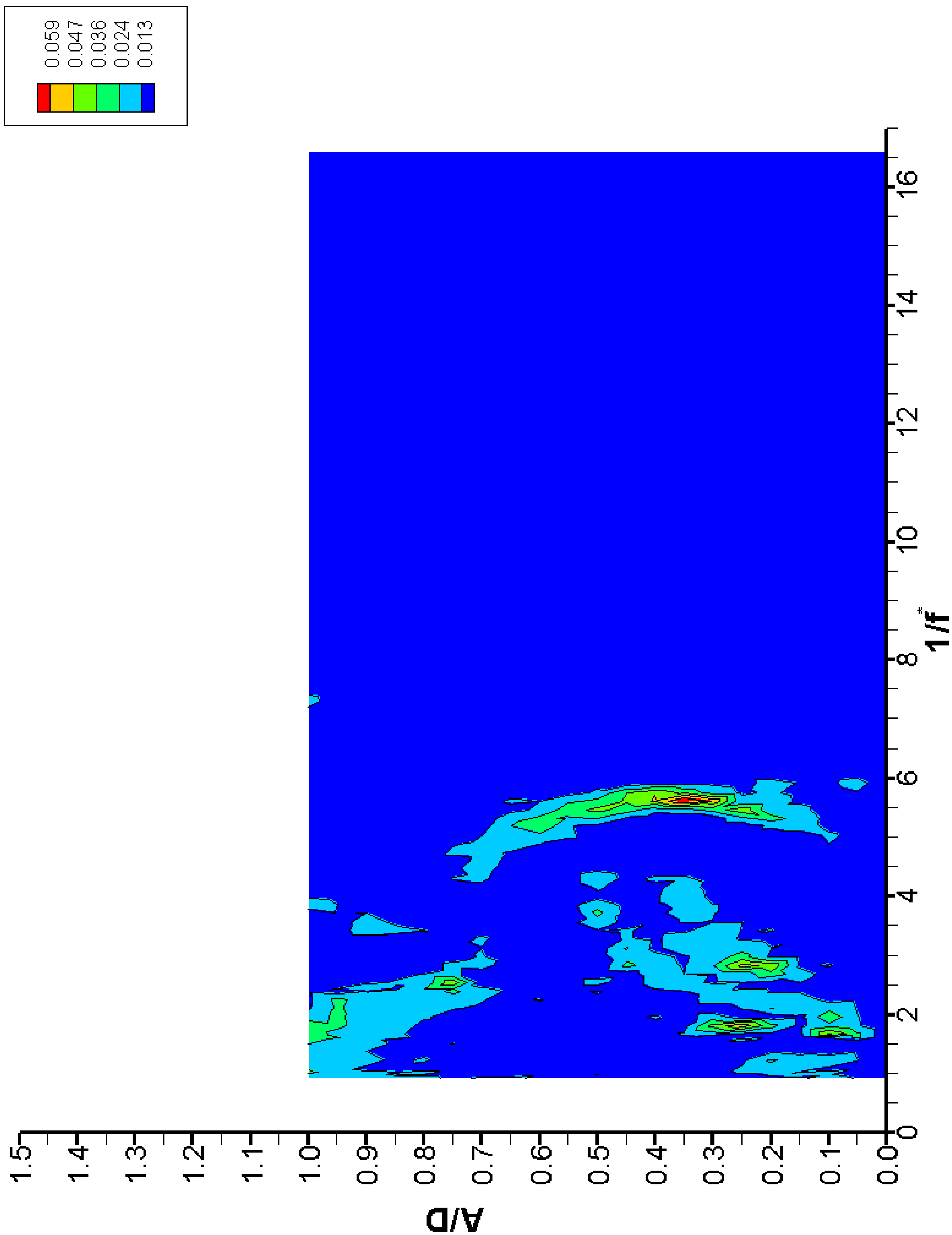

Figure 4.2: Contours of normalized standard deviation of heat transfer coefficient time series ($\sigma_{Nu/Nu_0}/(Nu/Nu_0)$) for the AR = 14.2 cylinder

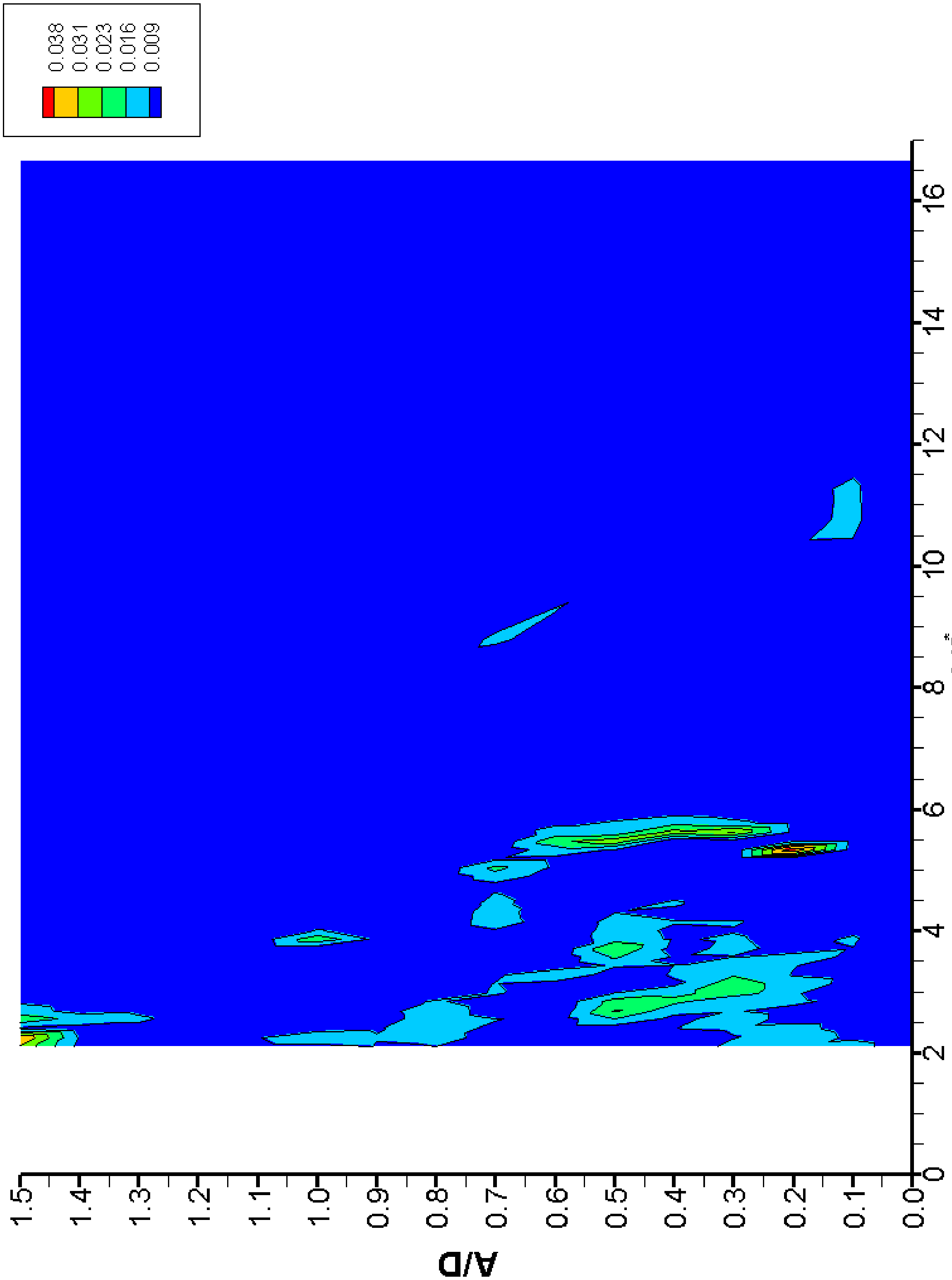

Figure 4.3: Contours of normalized standard deviation of heat transfer coefficient time series ($\sigma_{Nu/Nu_0}/(Nu/Nu_0)$) for the AR = 21.3 cylinder

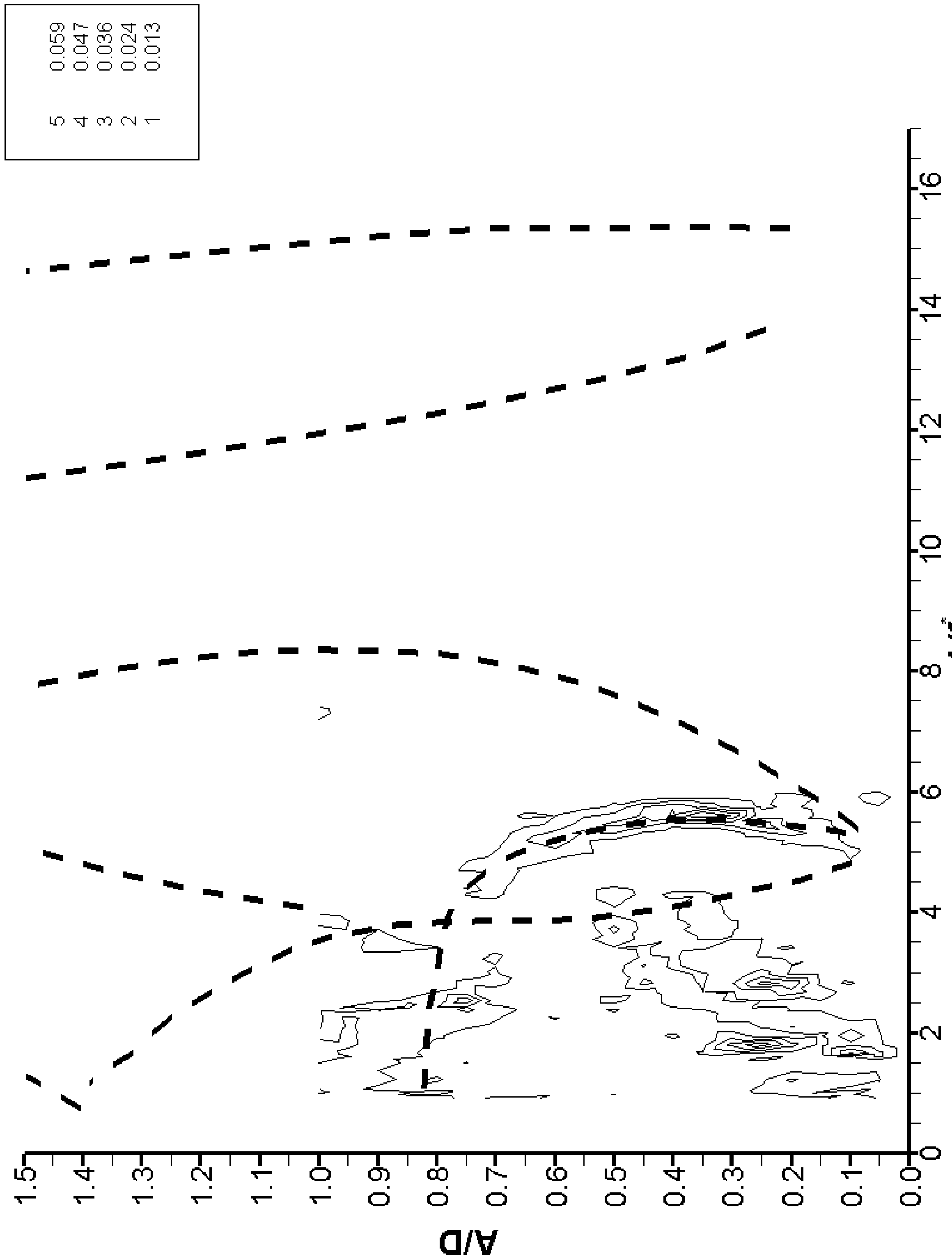

Figure 4.4: Contours of normalized standard deviation of heat transfer coefficient time series ($\sigma_{Nu/Nu_0}/(Nu/Nu_0)$) for the AR = 14.2 cylinder with wake mode boundaries from Williamson and Roshko (1988) superimposed

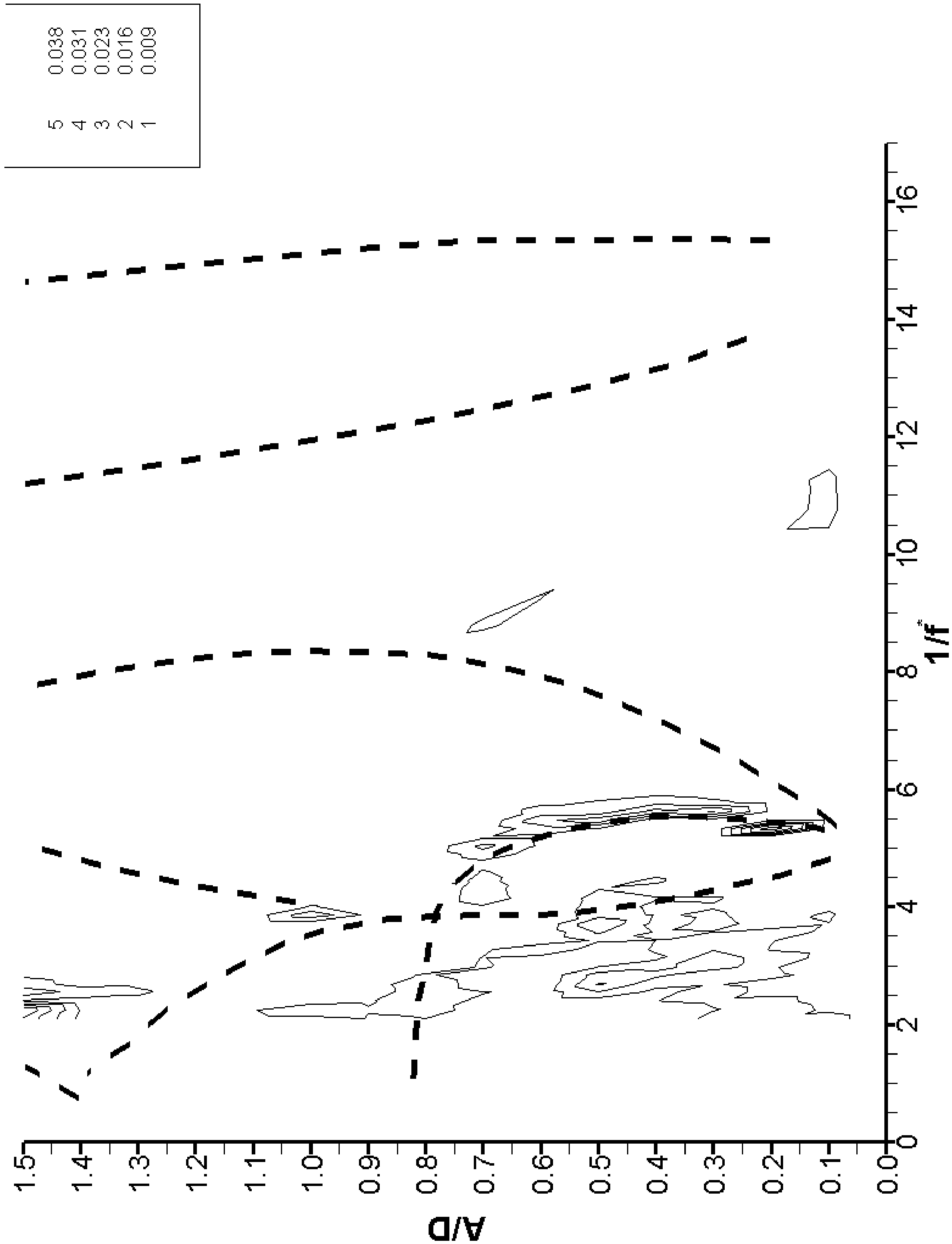

Figure 4.5: Contours of normalized standard deviation of heat transfer coefficient time series ($\sigma_{Nu/Nu_0}/(Nu/Nu_0)$) for the AR = 21.3 cylinder with wake mode boundaries from Williamson and Roshko (1988) superimposed

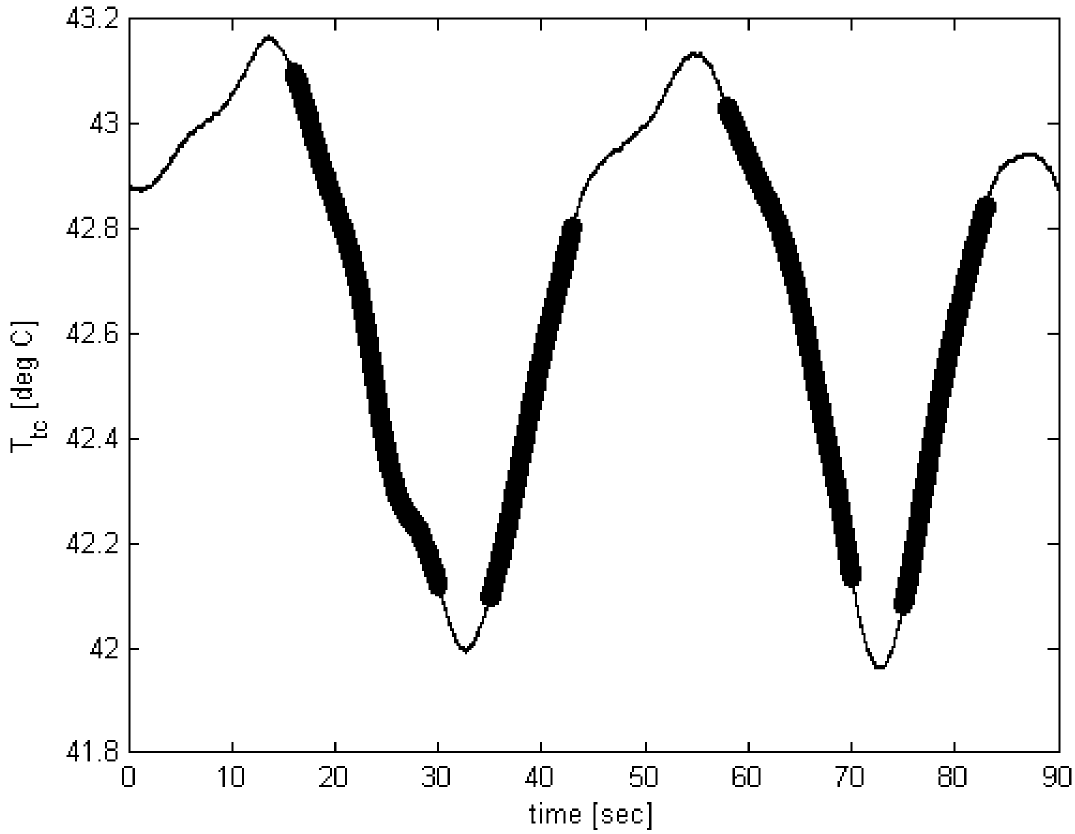

Figure 4.6: Time series of thermocouple temperature for data set synchronized with DPIV using AR = 14.2 cylinder oscillating at $1/f^*$ = 5.60, A/D = 0.35; times represented by heavy lines are included in the phase averaged DPIV data

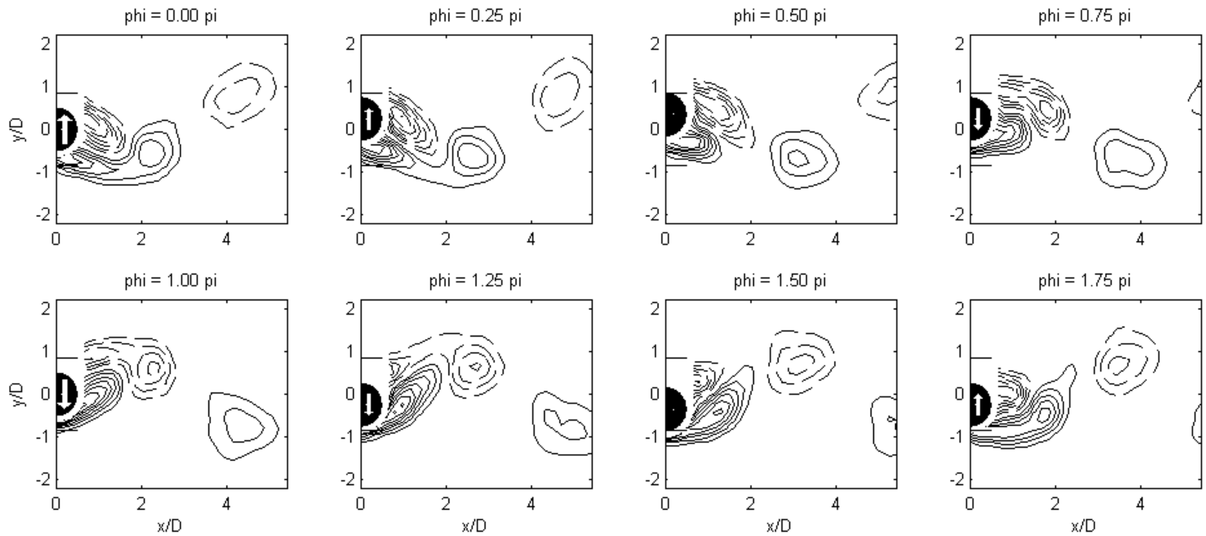

Figure 4.7: Phase averaged non-dimensional vorticity ($\omega D/U$) for $dT_{tc}/dt < 0$; cylinder motion divided into 16 phase bins, every other bin shown; positive vorticity contours are solid, negative vorticity contours are dashed; minimum contour levels = ± 0.33, contour spacing = 0.33

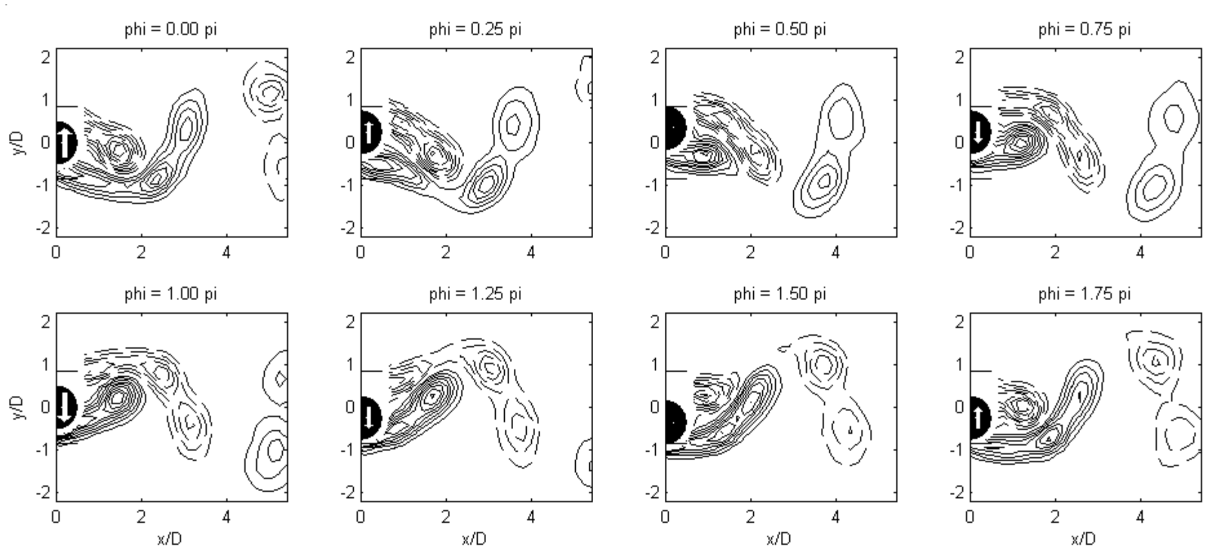

Figure 4.8: Phase averaged non-dimensional vorticity ($\omega D/U$) for $dT_{tc}/dt > 0$; cylinder motion divided into 16 phase bins, every other bin shown; positive vorticity contours are solid, negative vorticity contours are dashed; minimum contour levels = ± 0.33, contour spacing = 0.33

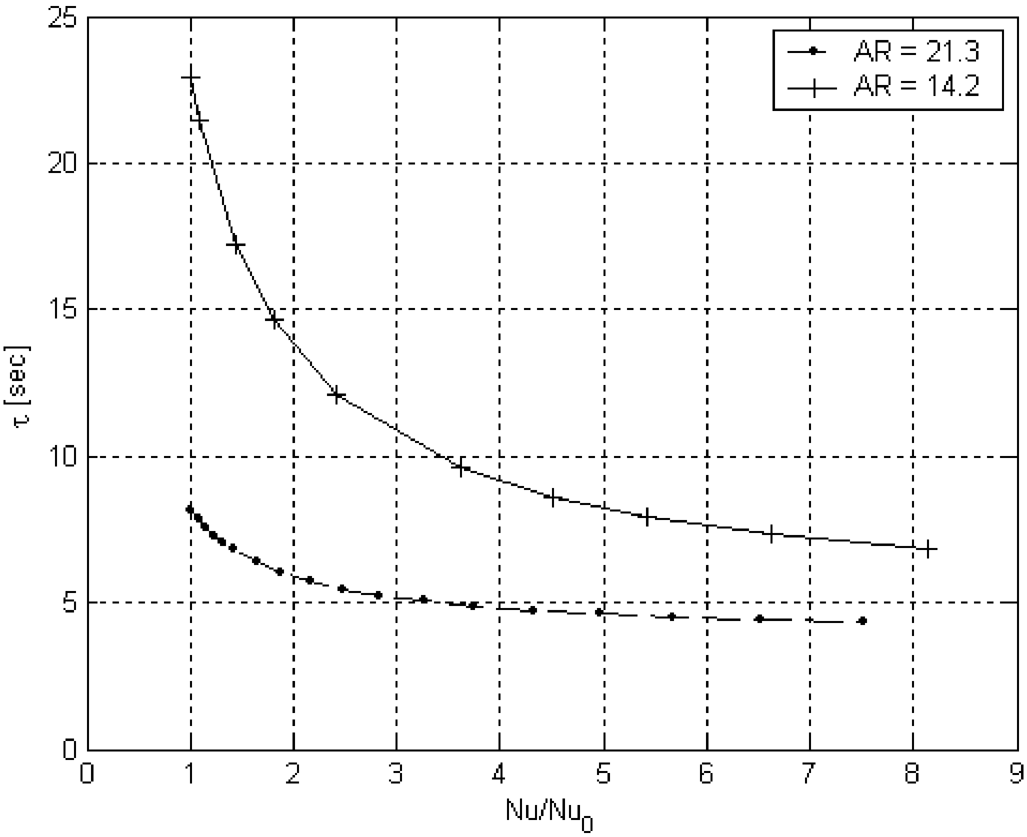

Figure 4.9: Cylinder thermal time constant (τ) as a function of normalized heat transfer coefficient (Nu/Nu_0)

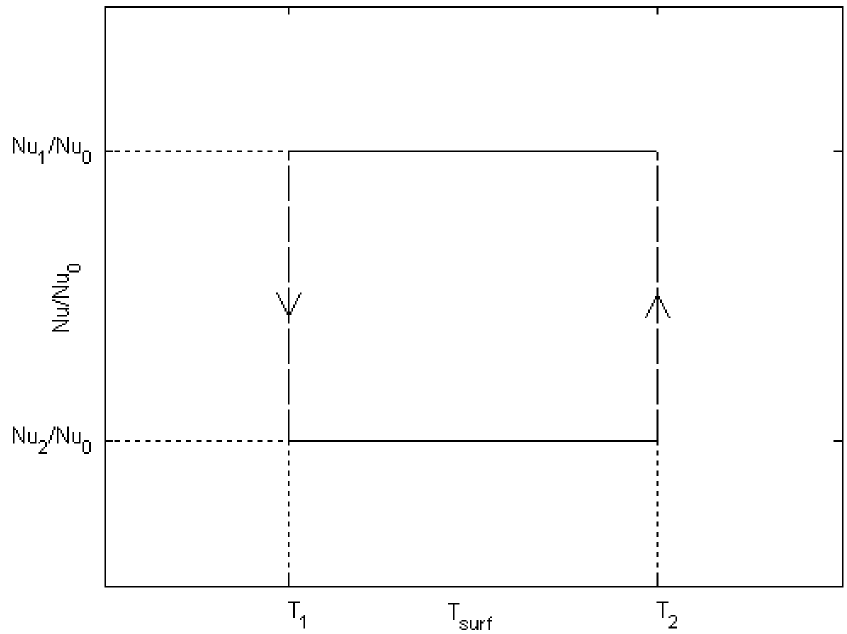

Figure 4.10: Hysteresis loop used to in simulation to represent the unknown mode-switching mechanism

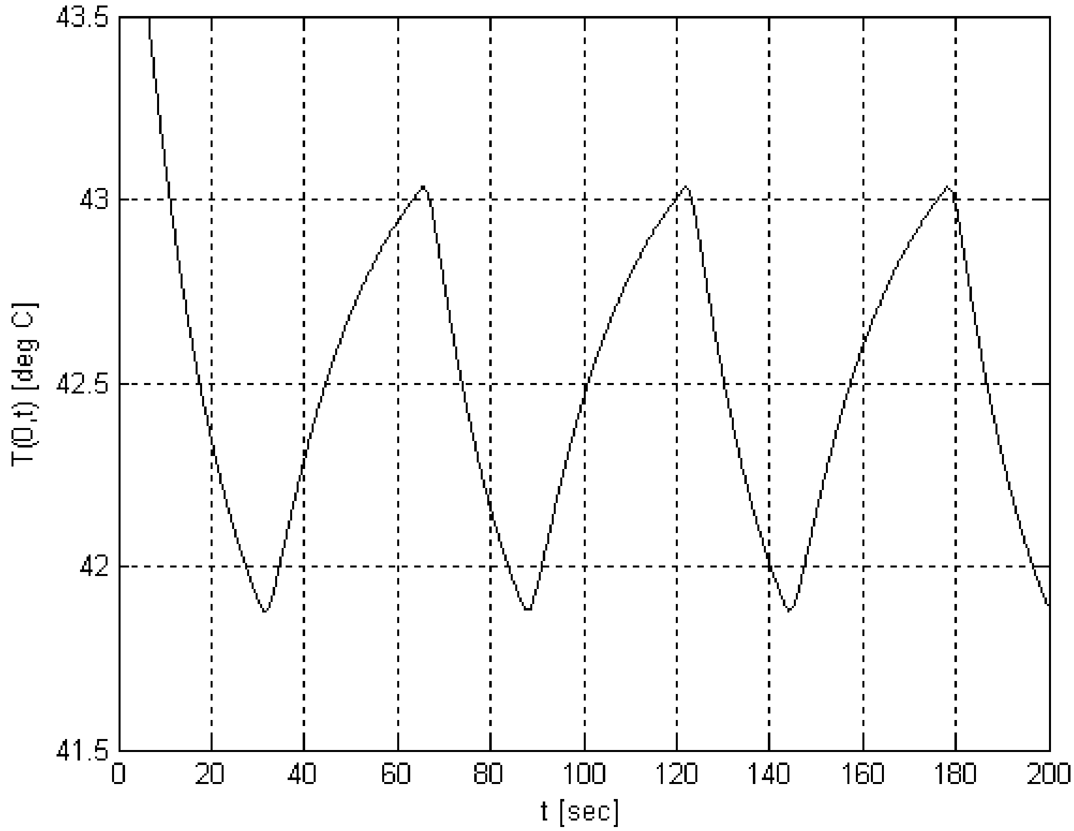

Figure 4.11: Temperature on cylinder axis vs. time for simulation based on hysteresis model of mode-switching; properties of AR = 14.2 cylinder were used with typical values of Nu/Nu_0 for the 2S and 2P modes; switching temperatures T_1 and T_2 were 0.4°C above the steady 2S surface temperature and 0.2°C below the steady 2P surface temperature

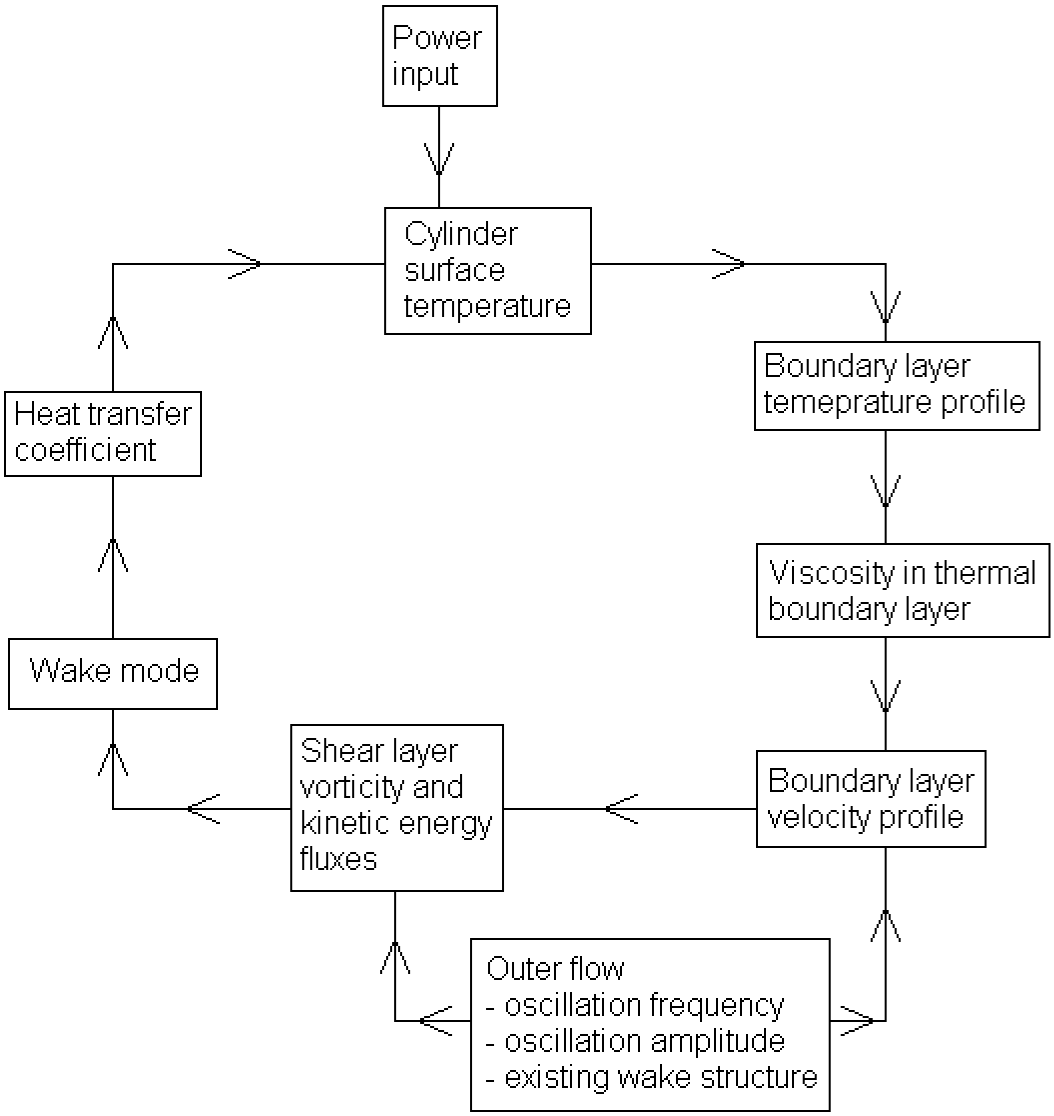

Figure 4.12: Model of the mode-switching mechanism

5 Wake structure and convective heat transfer coefficient

5.1 Introduction

In this chapter, results of experiments using DPIT/V to measure the temperature and velocity fields in the wake of heated oscillating cylinders are presented. These experiments were conducted in order to determine how wake structure affects heat transfer. Several new mechanisms were revealed, including the vortex dynamics during roll-up and the spacing between shed vortices. The effects of transverse cylinder velocity and cylinder aspect ratio were also identified.

5.2 Experimental conditions

A total of 44 different cases were investigated in the DPIT/V experiments on wake structure. This includes two non-oscillating cases and several cases that overlap in oscillation amplitude and frequency, though not in aspect ratio. The specific cases chosen are indicated in Figure 5.1 and in Table 5.1 and Table 5.2. The two different symbols in the figure indicate the two different aspect ratios of cylinders that were used in the experiments. The non-oscillating cases are shown in Figure 5.1 for reference at the natural shedding frequency and zero amplitude.

The cases were chosen to be representative of the full range of wake structures accessible with the experimental setup. Experiments were conducted in each wake mode region and at all of the Strouhal frequency harmonics evident in the data presented in Chapter 3. It was necessary to use the low aspect ratio cylinder to access high non-dimensional frequencies and to use the higher aspect ratio cylinder to achieve large amplitude ratios. Both cylinders were used in the areas where significant discrepancy between the two data sets existed, corresponding to the $\frac{1}{3}$ and $\frac{2}{3}$ sub-harmonics of the Strouhal frequency.

In several areas of the parameter space, clusters of cases were investigated. This allowed unusual features of Figure 3.3 and Figure 3.4—such as near $1/f^* \approx 4$, $A/D \approx 1.1$—to be studied more closely. Clusters of cases were also used to investigate the role of transverse velocity in determining the heat transfer coefficient within a wake mode.

In order to distinguish between cases, each case was assigned a letter and number. The letter S indicates the smaller aspect ratio (or short) cylinder, and L indicates the larger aspect ratio (or long) cylinder. For both cylinders, case 0 is the non-oscillating case. All oscillating cases are numbered in order of decreasing frequency, i.e, from left to right in Figure 5.1, for that cylinder. For cases with the same frequency, the smaller amplitude case has the lower number. The numbers corresponding to each oscillation condition are shown in Figure 5.2 and Figure 5.3.

5.3 Experimental setup and procedures

These experiments were carried out using the experimental setup described in Chapter 2. The details of the DPIT/V setup are located in §2.7, along with many of the procedures for acquiring and processing the data.

Data was acquired for this set of experiments in two separate runs, one for each of the two different aspect ratio cylinders used. Each run consisted of preparing the water tunnel, acquiring simultaneous DPIT/V and thermocouple data for each of the cases, and acquiring DPIT calibration data.

In order to obtain the best possible temperature data, it was necessary to thoroughly clean and properly prepare the water tunnel before the experiments. The cleaning was necessary to remove TLC particles that were used in the tunnel previously because they have a different color-temperature relationship than the newly added particles. The day prior to a run, the water tunnel was drained and all of the accessible surfaces were cleaned with a soft brush. Next, the honeycomb and screens were removed from the upstream section and cleaned using a brush and mild soap, then rinsed thoroughly. The tunnel was refilled with filtered water, run at high speed to stir up any loose particles, then drained again. Finally, the tunnel was filled with filtered water, the honeycomb and screens were replaced, and the filter and temperature control loop were left running overnight.

Before being added to the water tunnel, the TLC particles were heated past their blue clearing temperature. The calibration curve of the TLC can shift after the particles are exposed to temperatures above the blue clearing point. If this were to happen during the experiment, the calibration would be incorrect. Therefore, the particles were pre-heated so that any shift took place before the experiments began. Approximately 40 mL of TLC slurry was diluted in 1000 mL of de-ionized water. The particles were then heated and mixed using a hot plate/stirrer until the blue clearing temperature was exceeded. This process took about 25 minutes.

The TLC particles were then added to the water tunnel through a sieve with 75 μm openings. This removed any large particles or clumps of particles that would either fail to follow the flow or produce over-saturated images. The resulting particle loading of the tunnel was about 0.02% by volume. Approximately 30 minutes, or 15 tunnel re-circulation times, was allowed for the TLC particles to mix with the water in the tunnel. This time also allowed for an equilibrium amount of water to penetrate the protein encapsulation of the TLC particles.

Acquisition of DPIT/V and thermocouple data was automated to allow the set of cases to be investigated in a period of time over which the TLC color-temperature relationship remains fairly constant. The basic program was a modified version of the LabVIEW program described in §3.3. Additional code was added so that the program triggered the light sheet pulsing and the acquisition of video images. This resulted in synchronized DPIT/V and thermocouple data for each case. The number of cylinder oscillation cycles recorded for each case are listed in Table 5.1 and Table 5.2.

After data was acquired for each case in the run, DPIT calibration data was acquired. First, the water tunnel temperature control loop was set to a temperature just below the red clearing temperature for the TLC particles. As the water was cooling down, the cylinder was removed from the tunnel, and the RTD probe for the reference thermometer was moved to a location in the contraction immediately upstream of the test section. The procedure for acquiring calibration images described in §2.7 was then followed.

During the acquisition of data and calibration images, the water tunnel temperature was monitored using a reference thermometer. Between the two runs of data acquisition for this part of the study, the original reference thermometer (Fluke 2180A) stopped working properly. A new reference thermometer (Omega DP41-RTD) was therefore used for the large aspect ratio cases. There is fixed offset between the two thermometers of 0.2°C, though temperature differences were measure to a precision of 0.02°C for each. All temperatures measured with the new thermometer were referenced back to the original thermometer.

However, the offset was initially misidentified, and this resulted in the large aspect ratio cases being run with a freestream temperature of 25.4°C instead of 25.8°C. This does not significantly affect the Reynolds number and was accounted for in the computation of Nusselt number. The major effect of this is that the large aspect ratio cases were run at a freestream temperature where the relationship between temperature and hue for the TLC particles is not monotonic. This means that a portion of the range of the TLC is lost, and only the highest temperatures are reliably known. Therefore, the temperature data for these 14 cases was disregarded. Temperature data will only be considered for the 31 small aspect ratio cases.

After processing each pair of data images for a particular case, averaging of the data was performed. Several types of averaging were used: phase-averaging, balanced full-cycle averaging, and unbalanced averaging of the full data set. For phase-averaging, snapshots of the flow were grouped by the phase of the cylinder motion and the mean and rms of the groups were computed as

$$\begin{aligned} \langle q_b \rangle &\equiv \frac{1}{N_b}\sum_n q_{bn} \\ q_{bn}^* &\equiv q_{bn} - \langle q_b \rangle \\ q_{b,rms} &\equiv \sqrt{\frac{1}{N_b}\sum_n {q_{bn}^*}^2} = \sqrt{\frac{1}{N_b}\sum_n q_{bn}^2 - \langle q_b \rangle^2} \end{aligned} \quad . \qquad (5.1)$$

In these definitions, q is some property of the flow such as a velocity component, the temperature or the vorticity, b is the index indicating the phase bin, N_b is the number of snapshots in bin b, and n is the index of snapshots in bin b. In some cases, where the flow was expected to vary on a time scale of several oscillation cycles, the phase groupings extended over that number of oscillation cycles.

The balanced full-cycle averaging was intended to represent the overall mean and rms of the flow with each phase of the oscillation cycle equally represented. The balanced average and rms were therefore defined as

$$\begin{aligned} q_{mean} &\equiv \frac{1}{B}\sum_b \langle q_b \rangle \\ q_{rms} &\equiv \sqrt{\frac{1}{B}\sum_b \left(q_{b,rms}^2 + \langle q_b \rangle^2\right) - q_{mean}^2} \end{aligned}, \tag{5.2}$$

where B is the number of phase bins. This form of averaging was used for all of the oscillating cases.

For the non-oscillating cases, there is no oscillation phase with which to synchronize. It is possible to define a phase based on the velocity fluctuations in the wake, as was done by Park (1998). However, this was not found to aid in interpreting the data. For these cases, the individual snapshots were all averaged together to determine the mean and rms values

$$\begin{aligned} q_{mean} &\equiv \frac{1}{N}\sum_n q_n \\ q_n' &\equiv q_n - q_{mean} \\ q_{rms} &\equiv \sqrt{\frac{1}{N}\sum_n q_n'^2} = \sqrt{\frac{1}{N}\sum_n q_n^2 - q_{mean}^2} \end{aligned}. \tag{5.3}$$

Here, N is the total number of snapshots.

For phase-averaged quantities, values are presented in lab coordinates, so the cylinder is fixed in the x direction and moves in the y direction. When considering the mean flow, all quantities are presented in a coordinate system fixed with respect to the cylinder. This is so that it is evident how features of the flow would affect the heat transfer from the cylinder.

5.4 Results

A typical pair of data images, taken from case S19, is shown in Figure 5.4. The instantaneous normalized velocity, vorticity and temperature fields corresponding to this image pair are shown in Figure 5.5, Figure 5.6 and Figure 5.7. The gray rectangle in the velocity and vorticity plots indicates data that is not reliable because of the cylinder's image and shadow. In the plot of the temperature field, the dotted line indicates the streamwise location upstream of which the temperature range of the TLC particles was not sufficiently large to be useful.

Certain results are summarized for each case in Table 5.1 and Table 5.2, including the normalized Nusselt number, its standard deviation and the observed wake mode. The wake mode abbreviations are mainly taken from Williamson and Roshko (1988). The abbreviation NS indicates that no synchronization with the cylinder motion was observed. Two modes separated by a forward slash, /, indicates that mode-switching between those two modes was observed. Other abbreviations follow the scheme of Williamson and Roshko, with number-letter combinations indicating the number of single vortices or pairs of vortices shed per cycle.

Beginning with Figure 5.8 and continuing through Figure 5.141, various plots for each case are presented. For all cases, the mean and rms velocity and vorticity fields are presented. For the oscillating cases, the phase-averaged vorticity fields are also included. For the small aspect ratio cases, the phase-averaged temperature fields are also shown.

5.5 Discussion

5.5.1 Uncertainty

Before beginning a detailed discussion of uncertainty, a comment must be made about the temperature field. For cases S1 through about S20, the measured temperature is aberrantly high in the middle-bottom region of every snapshot. This effect becomes smaller for each case in this range. This is believed to be caused by a shift in the TLC color-temperature relationship over the course of the experiment. It is not clear why the effect is limited to this region. Because the calibration was carried out at the end of the run, the temperatures in this region for the later cases are accurate, while the earlier cases are inaccurate. This suggests that shorter runs, consisting of fewer cases, should be used in future DPIT/V studies.

The temperatures measured using DPIT/V in this experiment are limited to a resolution of about ±0.1°C. For most of the cases examined in this experiment, this resolution is sufficient to observe the significant temperature variations in the cylinder wake. However, for cases with very high heat transfer coefficients, the actual temperature differences are much smaller than this. At the highest heat transfer coefficients seen in this experiment, the cylinder surface temperature is only 0.7°C hotter than the freestream fluid. In addition, over the entire range of heat transfer coefficients observed, the temperatures in the wake are closer to the freestream temperature than to the cylinder surface temperature—typical maximum values of $(T-T_\infty)/(T_{surf}- T_\infty)$ are around 0.5. It is therefore beyond the capabilities of the present implementation of DPIT/V to measure the temperature field in the wake of certain cases with very high heat transfer coefficients. Data was still taken for these cases so that the velocity field could be measured. Cases S2, S3, S4 and S6 (Figure 5.14, Figure 5.17, Figure 5.20 and Figure 5.30) yield no useful temperature field information. Some information can be extracted from cases S10 and S13 (Figure 5.50 and Figure 5.63), but the signal to noise ratio is low.

5.5.2 Identifying wake mode

The wake mode for each case was identified in order to compare with the wake mode boundaries identified by Williamson and Roshko (1988) and the features of Figure 3.3 and Figure 3.4. The observed modes are tabulated in Table 5.1 and Table 5.2. For most cases, the mode is easily identifiable from the phase-averaged vorticity plots. However, the modes for some cases are more difficult to identify.

For cases S2, S3, S4 and S6 (Figure 5.12 to Figure 5.20, and Figure 5.28 to Figure 5.30) the wake mode is not obvious. The contours of vorticity are very irregular, and the temperature field cannot be resolved (see §5.5.1). The best indicators of mode in these cases are in fact the mean velocity and vorticity fields. The mean velocity field is essentially symmetric about the x-axis, and the vorticity field is anti-symmetric. Therefore, the wake mode must be a symmetric mode. The specific mode was identified as C(2S) by comparing the mean and phase-averaged fields to the C(P+S) cases S10, L1, L2 and L3 (Figure 5.48 to Figure 5.50 and Figure 5.116 to Figure 5.121). The similarity of the plots to the single vortex side of the asymmetric mode indicated the nature of the mode for these cases.

For case S28 (Figure 5.106 to Figure 5.108), it is also not clear how to identify the mode. The phase-averaged vorticity plots are distinct, and the motion of individual vortices can be followed, indicating that the shedding is synchronized with the cylinder motion. On the other hand, the first two single vortices shed are much larger than the third and fourth. The mode is clearly not symmetric with respect to the cylinder motion, but it is in some way synchronized. It is not clear if this should be considered non-synchronized or 4S (four single vortices per cycle).

In general, the wake modes agree well with the modes expected based upon the Williamson and Roshko boundaries and the features of Figure 3.3 and Figure 3.4. The only significant exceptions are for several of the low frequency cases. Cases S25, S27, S29, and possibly S28 (Figure 5.97 to Figure 5.99 and Figure 5.103 to Figure 5.111), all exhibit wake structures that are synchronized with the flow. According to the Williamson and Roshko boundaries, these cases should all be non-synchronized. It is possible that the disagreement is due to DPIV being a more sensitive technique than the floating particle traces used by Williamson and Roshko. For cases L12 and L13 (Figure 5.138 to Figure 5.141), though the wake is synchronized with the cylinder motion, there does not appear to be significant pairing between opposite signed vortices. The wakes for these cases appear to be essentially Kármán Vortex Streets, with the shedding locked onto 3 times the oscillation frequency. For this reason, these cases are labeled as 6S, not 2P+2S.

5.5.3 Formation length

Park (1998) suggested that the vortex formation length, λ_f, significantly affects the heat transfer coefficient. The vortex formation length in turn depends on the oscillation conditions. According to Park, for highly synchronized cases the wake vortices form close to the cylinder base and are therefore effective at removing hot fluid from the base region. For cases that are not strongly synchronized, the vortex roll-up process occurs far downstream of the cylinder, and the resulting heat transfer is near that of the non-oscillating cylinder. The formation length can also be long for some synchronized cases, such as cases L12 and L13 (Figure 5.138 to Figure 5.141) near the 1/3 sub-harmonic of the Strouhal frequency.

In order to compare with Park's results, the formation length was determined for all cases in which the wake consists only of single vortices, not pairs. This restriction is necessary because of the methods by which the formation length was determined. The formation length was determined in two different ways.

The first method is that used by Park. Park defined the formation length as the distance from the cylinder to the end of the wake bubble, or closed wake, in the mean velocity field. This location was identified using the critical point analysis of Perry and Fairlie (1974). For two-dimensional, incompressible flow only one of the invariants used by Perry and Fairlie, defined for the mean velocity field as

$$Q \equiv \det\left(\nabla \underline{u_{mean}}\right), \tag{5.4}$$

can take on a non-zero value. This quantity can be defined at each point in the flow where velocity data exists. If $Q > 0$ at a particular point, fluid at that point is undergoing rotation and is in the neighborhood of a center. Values of $Q < 0$ indicate that the point is in a saddle region. For this experiment, the quantity Q was computed at each point for which velocity data existed along a line located slightly off ($y/D = -0.14$ for $AR = 14.2$ and $y/D = 0.08$ for $AR = 21.3$) of the mean centerline of the cylinder. Along this line, fluid inside the wake bubble is in the neighborhood of a center so Q > 0, while the end of the wake bubble is a saddle region where Q < 0. The formation length was therefore taken to be the streamwise distance from the cylinder base to the first point on this line with a value of Q < 0.The second method used to determine the formation length was based upon the rms vorticity field. The formation length was defined as the streamwise distance from the cylinder base to the location of the peak rms vorticity on the same line. While these definitions for the formation length generally agree with each other for wakes consisting of only single vortices, they do not perform well for wakes with paired vortices.

Normalized heat transfer coefficients are plotted versus formation length in Figure 5.142. The horizontal error bars in Figure 5.142 correspond to the DPIV grid spacing, and the vertical error bars are due to the uncertainty in the measured heat transfer coefficient.

The present data supports Park's conclusion that short formation length corresponds to enhanced heat transfer. The large number of cases in the present study clarifies the relationship between formation length and heat transfer. While Park's data was consistent with a linear relationship between these two factors, the present data indicates that some type of threshold effect occurs. For λ_f > ~1.5, there is no significant change in Nu/Nu_0 for different formation lengths. For λ_f < ~1.5, there is significant heat transfer enhancement, but the value of Nu/Nu_0 varies widely over a small range of formation lengths. This suggests that formation length is not the only factor that determines the heat transfer coefficient. It appears that a short formation length is necessary for significant heat transfer enhancement, but the magnitude of the enhancement is determined by other details of the wake structure.

5.5.4 Streamwise spacing between vortices

A comparison of cases S14, S17 and S20 (Figure 5.64 to Figure 5.66, Figure 5.73 to Figure 5.75 and Figure 5.82 to Figure 5.84) reveals that the spacing between shed vortices plays a role in determining the heat transfer for 2S mode cases. The vortex spacing is a function of the vortex convective speed and the vortex shedding frequency, which in synchronized cases is equal to the oscillation frequency. While the formation process of the vortices prior to pinch-off appears almost identical for these three cases, the spacing of the shed vortices differ considerably. In these three cases, larger vortex spacing corresponds to higher heat transfer enhancement.

The reason for this correspondence is not clear, but it is believed that the heat transfer coefficient depends on the ability of the forming vortices to entrain freestream temperature fluid into the cylinder base region. A nearby vortex with the same sense of rotation would reduce the entrainment of outer flow fluid at the downstream side of the forming vortex by inducing a velocity directed away from the centerline. Figure 5.143 (case S14), Figure 5.144 (case S17) and Figure 5.145 (case S20) demonstrate this. In these figures, vector plots of the phase-averaged velocity are shown along with contours of the phase-averaged normalized temperature field in the region close to the cylinder base. It is evident that larger vortex spacing corresponds to more entrainment of freestream fluid by the near-wake. This entrainment has the effect of bending the temperature contours, thereby creating a steeper temperature gradient in the cylinder base region. This results in a higher local heat transfer coefficient for the cylinder base. A similar effect may exist for other modes consisting of single vortices, but an insufficient number of cases were investigated in these modes in order to make that determination.

5.5.5 Wake mode and heat transfer

Vortex spacing and entrainment may also explain why the heat transfer coefficient depends so strongly on wake mode. The most striking example of this dependence is the abrupt change in heat transfer coefficient across the 2S/2P boundary. Comparing case S20 (2S mode; Figure 5.82 to Figure 5.84 and Figure 5.145) with case S23 (2P mode; Figure 5.91 to Figure 5.93 and Figure 5.146), the role of the vortex formation process in affecting heat transfer is identifiable. Entrainment in the near-wake is very different for the two modes, as illustrated by Figure 5.145 and Figure 5.146. For the 2S case, entrainment occurs between each successive vortex close to the cylinder base. In the 2P case, the extended shear layers—consisting of closely spaced forming vortices with the same sense of rotation—shift the entrainment further downstream, so the cool freestream fluid has less impact on the cylinder base region.

In some sense, this is simply another manifestation of Park's formation length idea. The 2P mode always has extended shear layers, so the formation length is inherently longer than for the 2S mode. However, this is not the complete story. Unlike the wake of a non-oscillating cylinder, where the majority of the roll-up of vorticity occurs in a compact region located well downstream of the cylinder, in the 2P shear layers, the vortices begin to roll-up very close to the cylinder. Comparing the 2S and 2P roll-up processes, while the vortices begin to roll-up at about the same downstream position, they achieve very different maximum circulation at very different locations. For the 2S case, each vortex remains close to the cylinder base for almost half of the cycle, resulting in high circulation at that location and a relatively large separation between vortices. This leads to entrainment of freestream fluid to the base region. For the 2P case, though each vortex begins to roll up close to the cylinder, no vortex remains near the cylinder base as it grows. Instead, each vortex moves downstream as it grows, generating a series of closely spaced vortices that do not entrain a large amount of fluid. Most of the entrainment done by the vortices is farther downstream and is therefore ineffective at cooling the cylinder base region.

While the data shows a number of connections between wake structure and heat transfer coefficient, there is a notable exception. Cases L4, L5, L6 and L7 (Figure 5.122 to Figure 5.129) were investigated in order to understand a strange feature of Figure 3.4 near the region where the C(P+S), P+S and 2P wake modes come together. Though all four cases have 2P wakes, there are noticeable differences in the details of the wake structures. Cases L4 and L6 have similar wake structures to one another. Likewise, cases L5 and L7 have similar wake structures to each other. On the other hand, cases L4 and L7 have Nusselt numbers measurably higher than cases L5 and L6. It is not evident from the current data why this is so.

5.5.6 Transverse velocity

Transverse velocity appears to affect heat transfer enhancement in two ways. First, it increases the circulation of the forming vortices by increasing the vorticity flux in the shear layers. Second, it allows the vortices to affect a larger portion of the cylinder surface area.

The vorticity flux past a point on a boundary is a function of the outer flow velocity relative to that boundary. For the oscillating cylinders, the cylinder transverse velocity can therefore be a significant source of vorticity. This suggests that for cases with the same basic wake structure, higher transverse velocity should lead to higher circulation in the wake vortices. For a particular vortex roll-up distance and process, the circulation of the vortices is expected to determine the entrainment and mixing in the cylinder base region and should therefore determine the heat transfer enhancement.

The second effect of high transverse velocity is to expose a larger portion of the cylinder surface area to the high velocities and mixed fluid generated by forming vortices. As the cylinder moves transversely, the wake turns so as to be somewhat aligned with the instantaneous direction of the flow relative to the cylinder. The higher the transverse velocity, the greater the angle through which the wake turns. For conditions where the vortices roll-up close to the cylinder, heat transfer is primarily enhanced for the cylinder base region due to the proximity of the vortices. By moving the vortices over a larger portion of the cylinder base, higher transverse velocities should result in increased heat transfer enhancement for a particular wake mode.

These two effects can be seen in cases S13, S18, S22 and S23 (Figure 5.61 to Figure 5.63, Figure 5.76 to Figure 5.78 and Figure 5.88 to Figure 5.93). These are all 2P wakes with the leading vortex in each pair containing approximately twice the circulation of the trailing member of the pair. The four cases have different transverse velocities, and the heat transfer coefficient increases with increasing transverse velocity, as shown in Figure 5.147. The line in Figure 5.147 is a linear least-squares fit to the data intended to highlight the trend and does not indicate a functional relationship.

For each case, the circulation

$$\Gamma = \oint \underline{u} \cdot d\vec{s} = \iint \omega dA \tag{5.5}$$

of each pinched-off vortex was determined by summing the vorticity inside a contour at $\omega D/U = \pm 0.2$, multiplied by the area of the grid elements. Circulation is normalized as Γ/UD. These results are shown in Figure 5.148. As expected, the circulation of the vortices increases with increasing transverse velocity. The error bars indicate the difference between the absolute value of the measured circulation of the positive and negative vortices.

Figure 5.148 also shows the maximum angle, over the course of a cylinder oscillation cycle, between the freestream direction and a line connecting the center of the cylinder to the lead vortex in a pair while it was immediately adjacent to the cylinder. This angle, η, is defined as positive towards the side of the cylinder with the shear layer of opposite sense of rotation as the vortex. Therefore, a negative η indicates that the vortex remains on its original side of the cylinder while near the cylinder, and a positive η indicates that the vortex moves around the cylinder to the other side. Clearly, high transverse velocity causes the vortices to move over a large portion of the cylinder surface area.

5.5.7 Aspect ratio

In order to understand the aspect ratio effects described in §3.5.2 and §3.5.4, several cases were chosen with similar non-dimensional frequency and amplitude, but different aspect ratios. These cases are S0 and L0 (Figure 5.8 and Figure 5.115), S13 and L5 (Figure 5.61 to Figure 5.63, Figure 5.124 and Figure 5.125), S25 and L8 (Figure 5.97 to Figure 5.99, Figure 5.130 and Figure 5.131), and S26 and L9 (Figure 5.100 to Figure 5.102, Figure 5.132 and Figure 5.133).

A comparison of these cases reveals that the flow at the mid-span is nearly the same regardless of aspect ratio even though the measured heat transfer enhancement is different. This means that whatever is causing the difference in heat transfer enhancement is occurring near the ends of the cylinder, not near the mid-span. These end effects can occur either in the non-oscillating case or in the oscillating cases.

When the cylinder is oscillating, it has the effect of synchronizing the vortex shedding along the cylinder span. This tends to reduce the effects of aspect ratio on vortex shedding. It is therefore reasonable to suppose that aspect ratio has a more significant effect on the heat transfer for the non-oscillating cases than for the oscillating cases. This would imply that the difference in the observed heat transfer enhancement is primarily due to scaling by the non-oscillating cases. There may also be significant end effects for cases in which the wake is only weakly synchronized with the cylinder oscillations.

The model for determining heat transfer coefficient was calibrated to get the non-oscillating cylinder Nusselt number to match published values for each cylinder. If the actual Nusselt number for the non-oscillating cases were different than the predicted values due to aspect ratio effects, it would cause the Nusselt numbers determined for oscillating cases to be incorrect as well. Assuming that the actual non-oscillating case Nusselt numbers for a particular cylinder are smaller than the predicted values, then all of the Nusselt numbers determined for that cylinder are too large. If oscillations reduce the aspect ratio effects, this would cause the ratio Nu/Nu_0 to be too large for all of the oscillating cases. With the additional assumption that the aspect ratio effects are more significant for the small aspect ratio cylinder, this is consistent with the small aspect ratio data lying above the large aspect ratio data in Figure 3.9. However, because the model of heat transfer inside the cylinder is not linear in the measured temperature, it is not trivial to correct the data.

If aspect ratio is having a significant effect on the non-oscillating cylinder cases as suspected, the values of Nu/Nu_0 presented in this study cannot be considered reliable. However, the trends in Nu/Nu_0 and the mechanisms for heat transfer enhancement are still valid

5.6 Conclusion

Two new mechanisms by which wake structure affects heat transfer were identified. First, the streamwise spacing of shed vortices was correlated with heat transfer coefficient for the 2S mode. The physical mechanism resulting in this correlation is believed to be the effect of streamwise spacing on the entrainment of freestream temperature fluid by the forming vortices. Second, the motion of the vortices during roll-up was found to significantly affect the cylinder heat transfer coefficient by determining the location at which entrainment of freestream fluid occurs. This mechanism explains the dependence of heat transfer coefficient on wake mode. These new mechanisms are in addition to the effect of formation length discovered by Park (1998), which was also observed in the current study.

Transverse cylinder velocity was found to have two direct effects on heat transfer. First, the cylinder's transverse oscillations produce additional vorticity, which rolls up in the wake. The transverse velocity is therefore a factor in determining the circulation of the wake vortices. For a fixed wake structure, the circulation of the vortices determines their effectiveness at enhancing heat transfer. Second, high transverse velocity spreads the heat transfer enhancement due to vortices over a larger portion of the cylinder base by turning the wake with respect to the freestream.

The role of aspect ratio in determining the heat transfer coefficient appears to be limited mainly to non-oscillating cylinders, though it may also be important for some weakly synchronized oscillating cases. There were no significant differences in wake structure at the mid-span for equivalent non-dimensional oscillation conditions for the two aspect ratios used in this study. This implies that the observed heat transfer enhancement dependence on aspect ratio is due to end effects. One implication of this observation is that it may be possible to achieve the benefits of a high aspect ratio heat exchanger element using low aspect ratio oscillating elements. This idea requires further confirmation over a larger range of aspect ratios.

The existence of significant aspect ratio effects for the non-oscillating cases casts doubt on the calibration method for the model used to determine heat transfer coefficient from the thermocouple temperature. Even if the reported values of

Nu/Nu_0 are systematically too large, the trends in heat transfer coefficient and the mechanisms identified are still valid.

Tables and figures for Chapter 5

Table 5.1: Cases investigated with DPIT/V using the small aspect ratio (AR=14.2) cylinder

case	$1/f^*$	f^*	A/D	cycles	Nu/Nu_0	σ_{Nu/Nu_0}	$\frac{\sigma_{Nu/Nu_0}}{Nu/Nu_0}$	mode
S0	~4.76	~0.21	0.00	60.5	1.00	0.0088	0.0088	
S1	0.92	1.082	0.10	332.9	0.96	0.0085	0.0089	NS
S2	1.07	0.932	0.85	288.7	8.22	0.1379	0.0168	C(2S)
S3	1.37	0.729	0.70	228.4	4.88	0.0361	0.0074	C(2S)
S4	1.37	0.729	0.80	219.9	5.72	0.0351	0.0061	C(2S)
S5	1.81	0.553	0.10	171.5	1.20	0.0131	0.0109	C(2S)
S6	1.96	0.511	0.85	158.8	3.32	0.0563	0.0170	C(2S)
S7	2.10	0.476	0.30	147.3	1.47	0.0076	0.0052	C(2S)
S8	2.54	0.394	0.10	126.2	0.99	0.0076	0.0077	C(2S)
S9	2.68	0.373	0.20	115.4	1.02	0.0116	0.0114	C(2S)
S10	2.68	0.373	0.90	115.7	2.22	0.0167	0.0075	C(P+S)
S11	2.98	0.336	0.30	106.8	1.23	0.0516	0.0421	C(2S)
S12	3.13	0.320	0.45	100.2	1.37	0.0200	0.0146	C(2S)
S13	3.71	0.270	1.00	82.7	1.84	0.0081	0.0044	2P
S14	3.99	0.250	0.20	77.2	1.13	0.0060	0.0053	2S
S15	3.99	0.250	0.50	76.3	1.48	0.0365	0.0246	2S/C(2S)
S16	4.29	0.233	0.60	70.7	1.58	0.0071	0.0045	2S
S17	4.59	0.218	0.25	66.3	1.28	0.0113	0.0089	2S
S18	4.59	0.218	0.90	66.4	1.67	0.0080	0.0048	2P
S19	4.73	0.211	0.10	63.6	1.17	0.0083	0.0071	2S
S20	5.18	0.193	0.30	58.3	1.38	0.0071	0.0051	2S
S21	5.75	0.174	0.55	51.6	1.35	0.0287	0.0212	2S/2P
S22	5.75	0.174	0.65	52.9	1.30	0.0066	0.0050	2P
S23	5.90	0.169	0.30	52.0	1.08	0.0183	0.0169	2P
S24	6.20	0.161	0.55	48.8	1.18	0.0079	0.0067	2P
S25	7.80	0.128	0.30	35.4	1.01	0.0098	0.0097	2P
S26	7.80	0.128	0.90	37.0	1.23	0.0108	0.0088	2P
S27	9.75	0.103	0.90	29.9	1.11	0.0047	0.0043	2P
S28	10.24	0.098	0.30	29.8	1.00	0.0080	0.0080	NS or 4S
S29	11.70	0.085	0.60	25.0	1.00	0.0065	0.0065	2P
S30	15.11	0.066	0.20	19.8	1.00	0.0072	0.0073	6S

Table 5.2: Cases investigated with DPIT/V using the large aspect ratio (AR=21.3) cylinder

case	$1/f^*$	f^*	A/D	cycles	Nu/Nu_0	σ_{Nu/Nu_0}	$\frac{\sigma_{Nu/Nu_0}}{Nu/Nu_0}$	Mode
L0	~4.76	~0.21	0.00	87.1	1.00	0.0103	0.0103	
L1	2.39	0.418	1.20	173.3	2.52	0.0055	0.0022	C(P+S)
L2	2.39	0.418	1.30	173.3	2.59	0.0195	0.0076	C(P+S)
L3	2.84	0.352	1.20	146.0	2.11	0.0091	0.0043	C(P+S)
L4	3.86	0.259	1.20	107.4	1.79	0.0032	0.0018	2P
L5	4.01	0.249	1.00	103.3	1.69	0.0137	0.0081	2P
L6	4.15	0.241	1.20	99.9	1.72	0.0062	0.0036	2P
L7	4.45	0.225	1.20	93.3	1.78	0.0049	0.0027	2P
L8	7.83	0.128	0.30	53.0	1.06	0.0049	0.0046	2P
L9	7.83	0.128	0.90	53.0	1.29	0.0049	0.0038	2P
L10	11.73	0.085	0.50	50.7	1.05	0.0053	0.0050	NS or 2P
L11	13.22	0.076	1.20	50.9	1.11	0.0068	0.0061	2P+2S
L12	14.68	0.068	0.50	51.1	1.04	0.0058	0.0056	6S
L13	16.15	0.062	0.50	51.2	1.04	0.0055	0.0053	6S

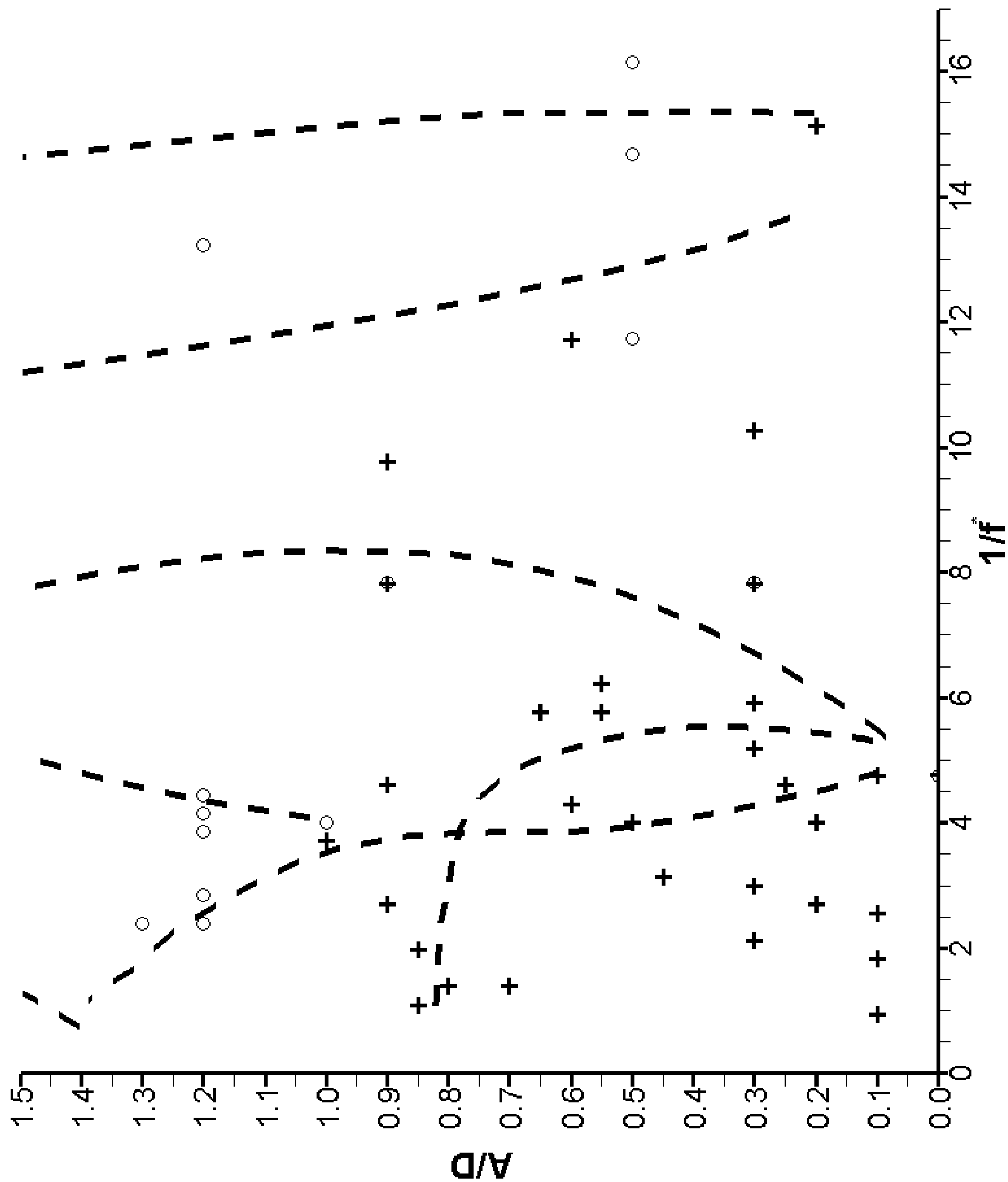

Figure 5.1: Cases investigated using DPIV/T; + symbol indicates AR = 14.2 cylinder, ○ symbol indicates AR = 21.3 cylinder

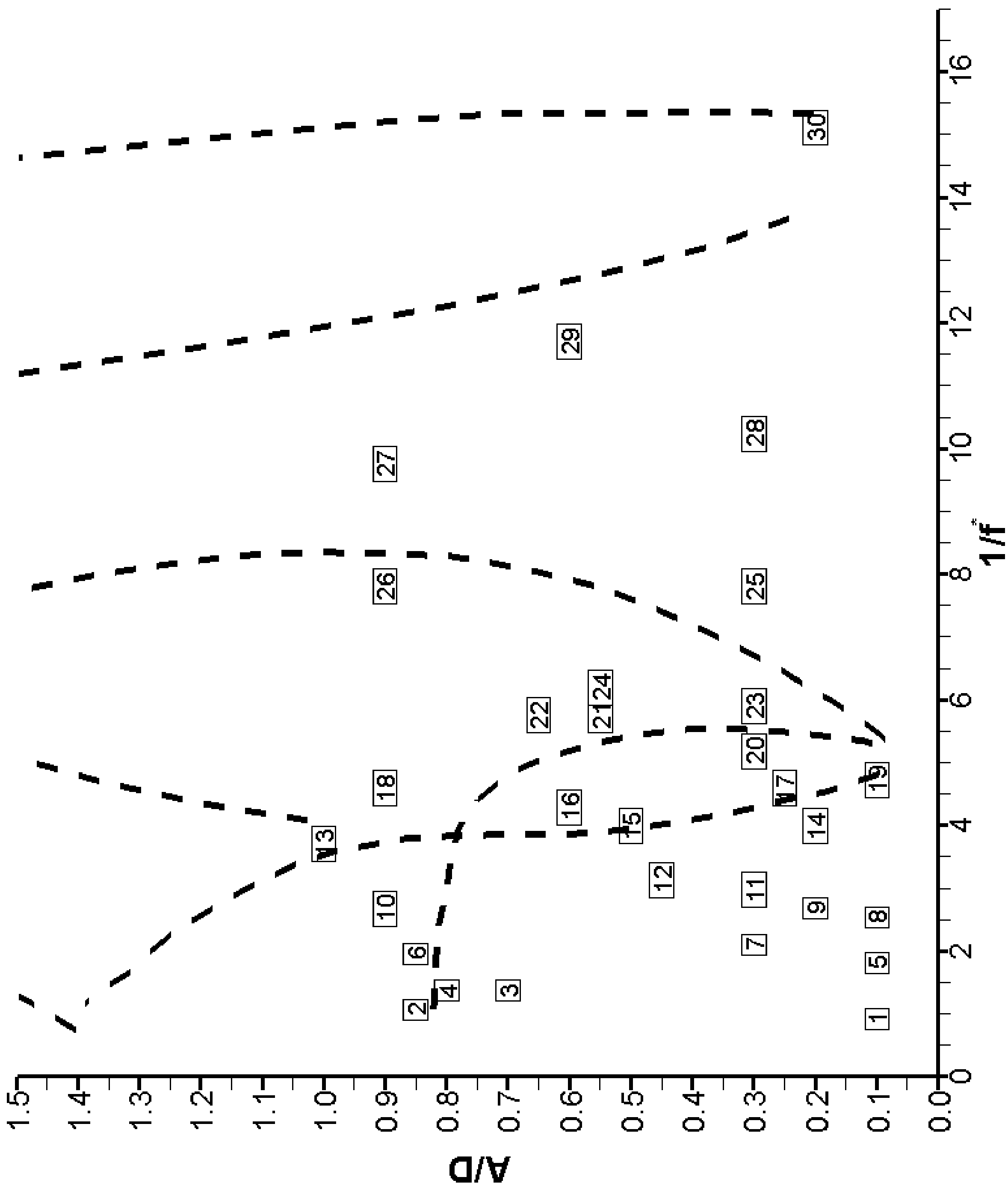

Figure 5.2: Oscillating cases investigated using DPIV/T for the AR = 14.2 cylinder (S), case numbers shown

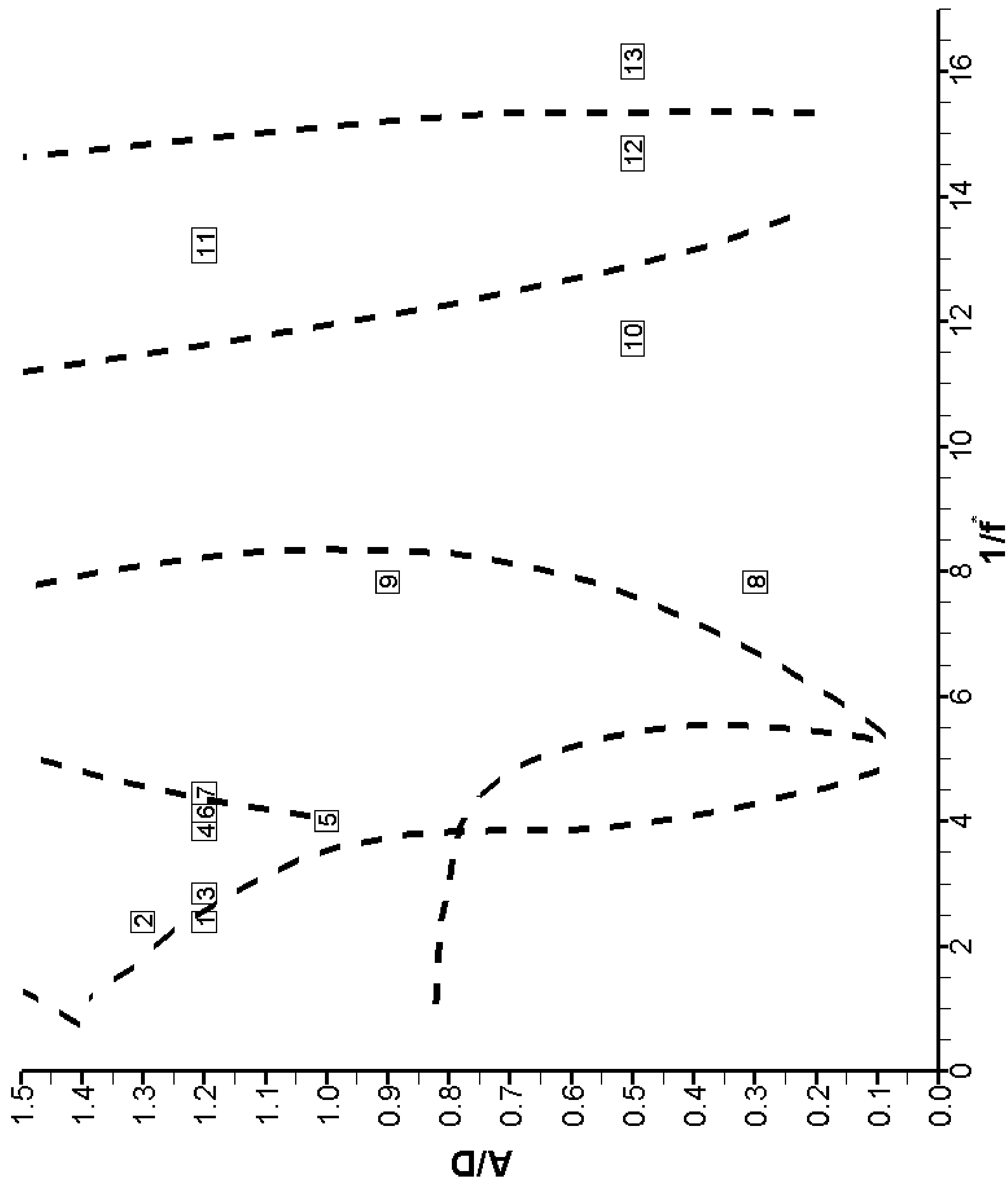

Figure 5.3: Oscillating cases investigated using DPIV/T for the AR = 21.3 cylinder (L), case numbers shown

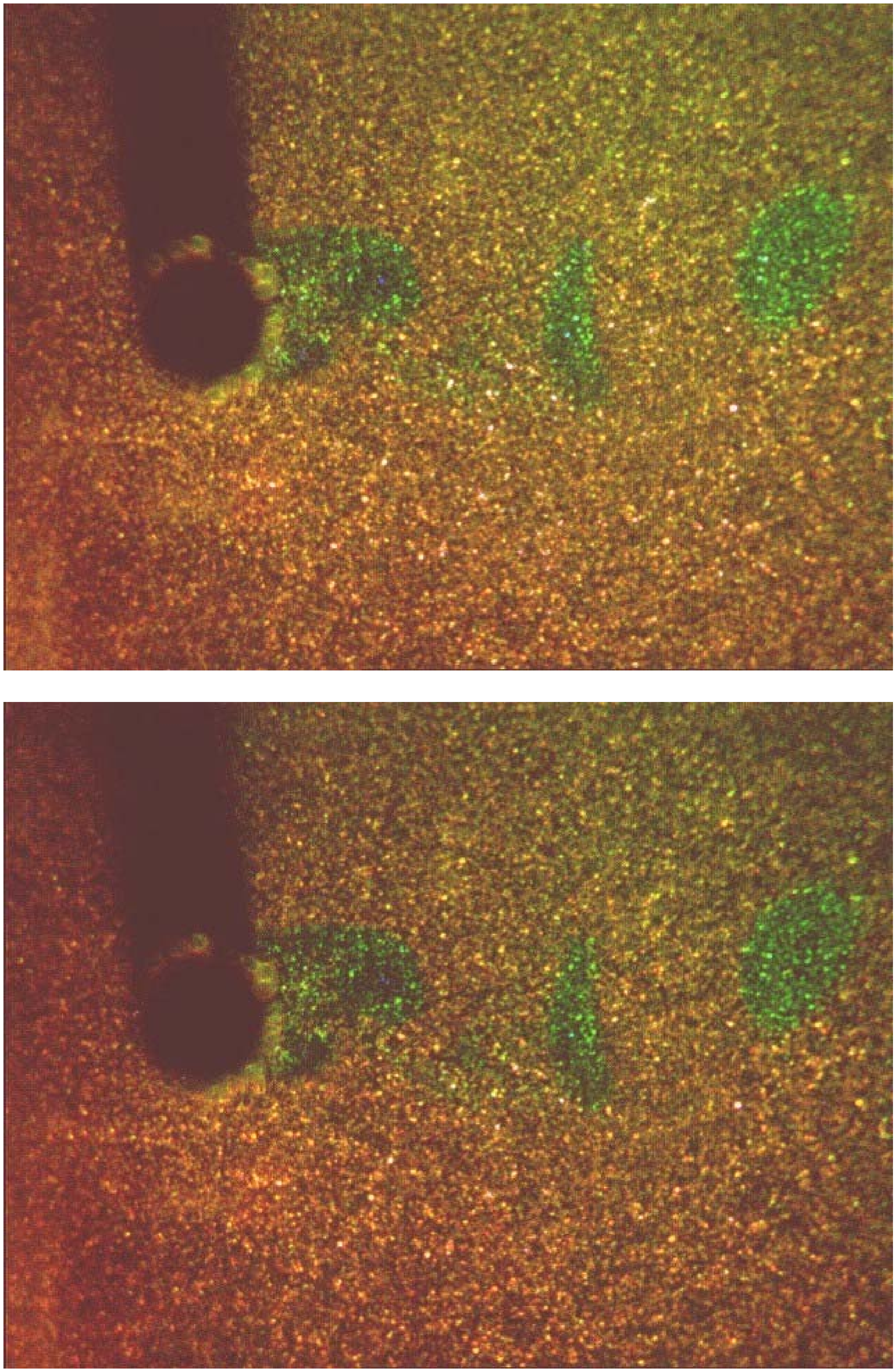

Figure 5.4: Sample image pair from case S19; color equalized and brightness increased to improve print quality

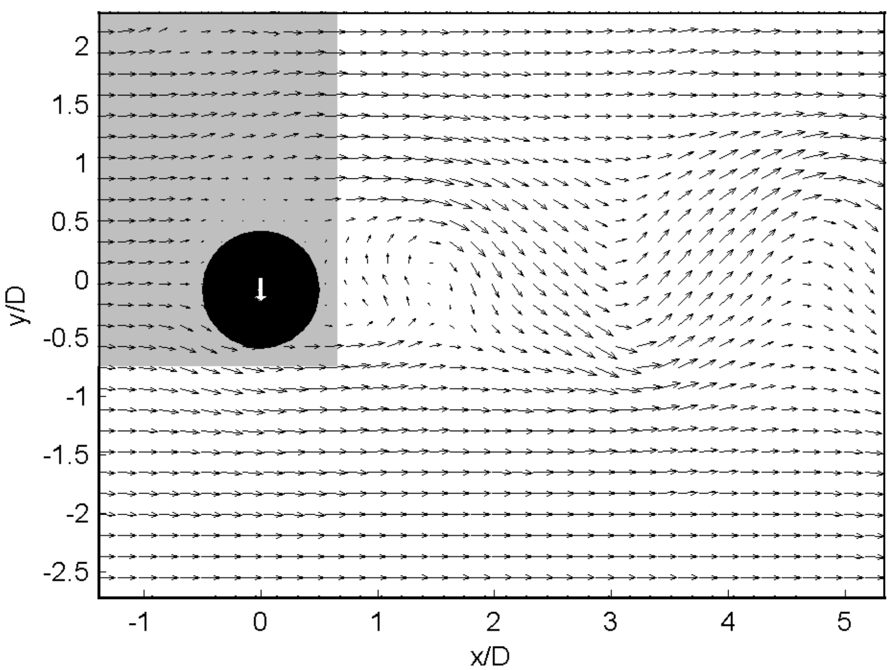

Figure 5.5: Velocity field determined from the pair of images in Figure 5.4

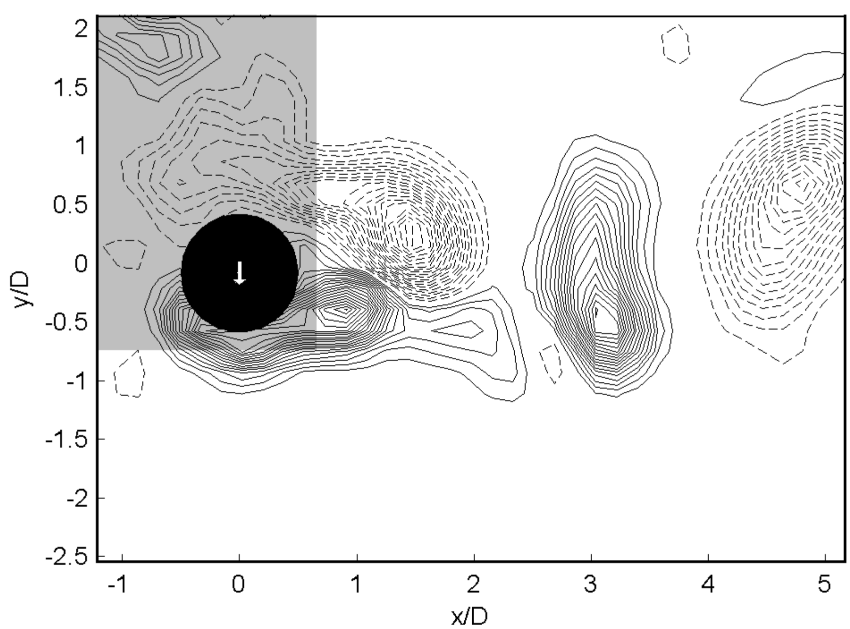

Figure 5.6: Normalized vorticity (ωD/U) field determined from the pair of images in Figure 5.4; contour spacing 0.2, positive contours solid, negative contours dashed

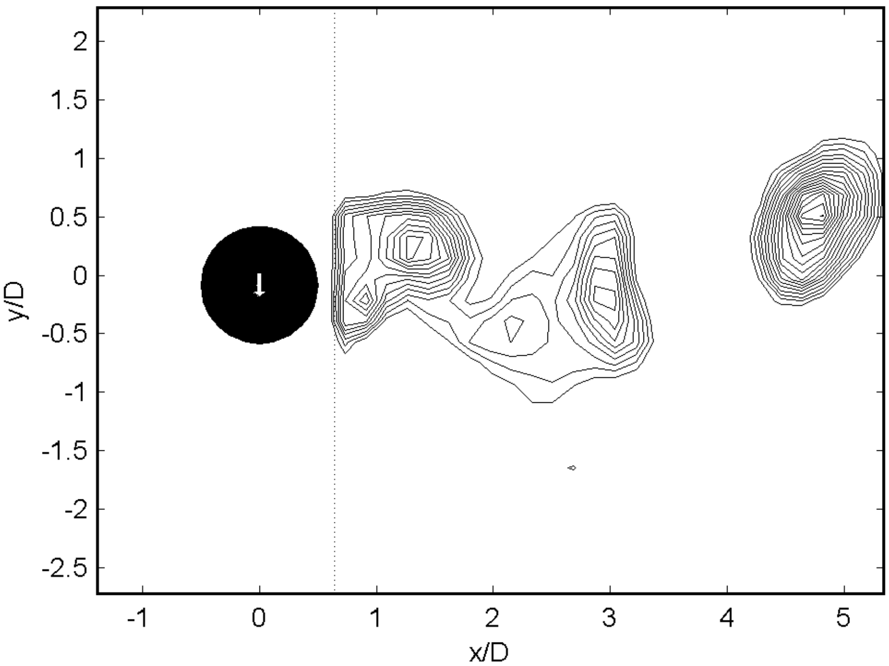

Figure 5.7: Normalized temperature ($(T-T_\infty)/(T_{surf}- T_\infty)$) field determined from the pair of images in Figure 5.4; minimum contour 0.015, contour spacing 0.005

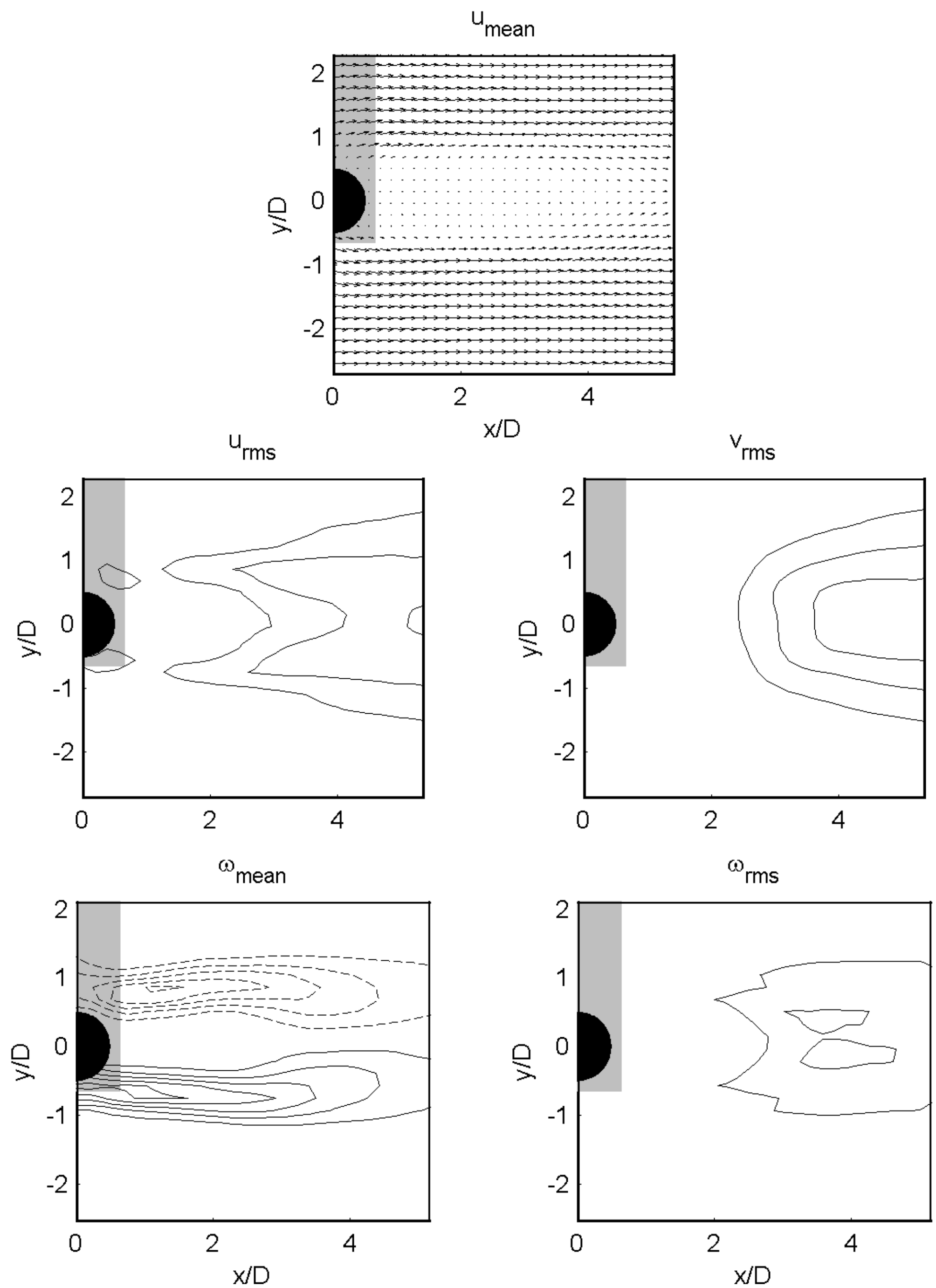

Figure 5.8: Mean and rms normalized velocity (u/U) and normalized vorticity (ωD/U) for case S0; rms velocity contours are at 0.1 intervals; vorticity contours are at 0.5 intervals, negative contours are dashed, positive contours are solid

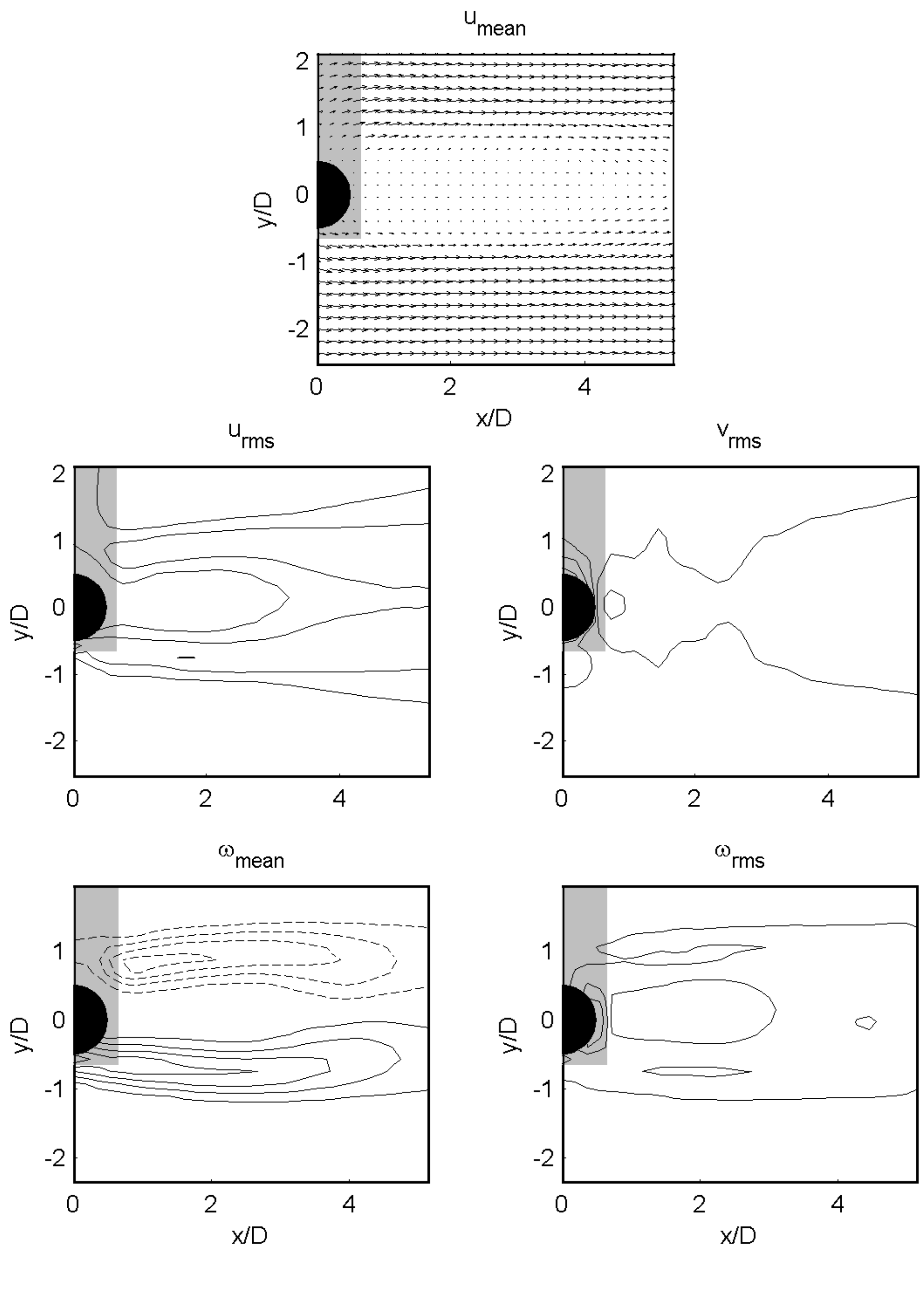

Figure 5.9: Mean and rms normalized velocity (u/U) and normalized vorticity (ωD/U) for case S1; rms velocity contours are at 0.1 intervals; vorticity contours are at 0.5 intervals, negative contours are dashed, positive contours are solid

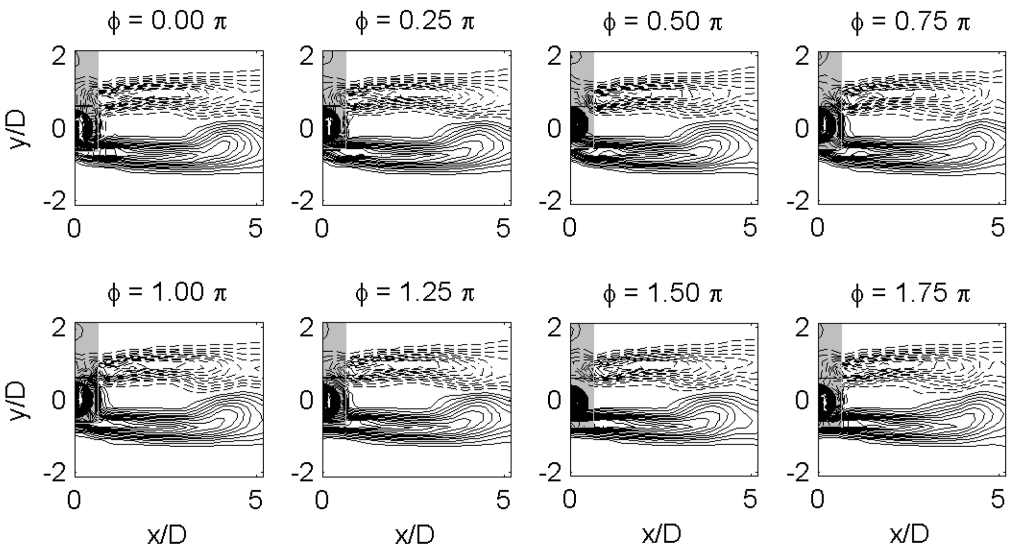

Figure 5.10: Phase-averaged normalized vorticity ($\omega D/U$) for case S1; 1 cycle divided into 16 bins, every other bin shown; minimum contours ±0.2, contour spacing 0.2, positive contours solid, negative contours dashed

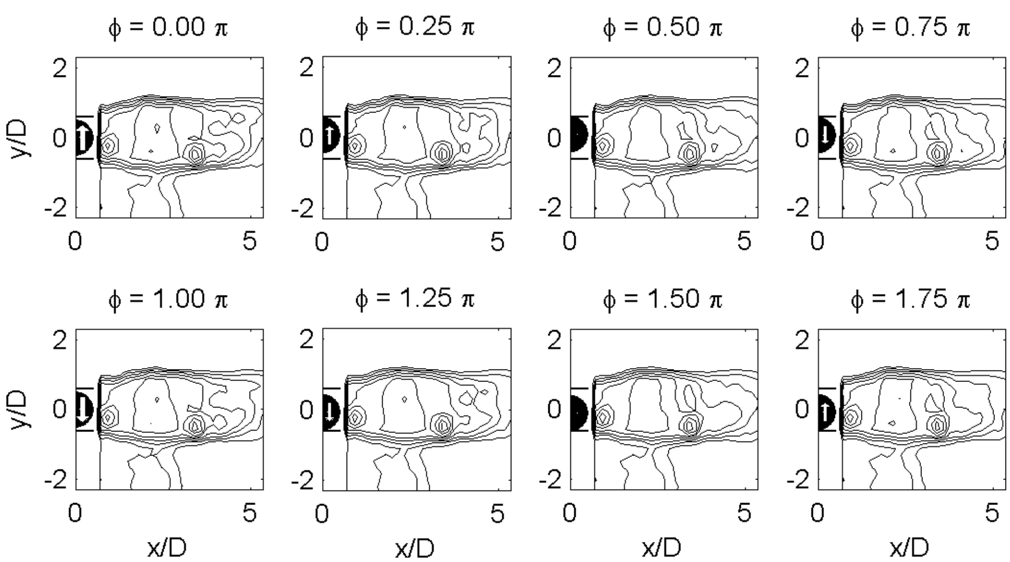

Figure 5.11: Phase-averaged normalized temperature ($(T-T_\infty)/(T_{surf}-T_\infty)$) for case S1; 1 cycle divided into 16 bins, every other bin shown; minimum contour 0.015, contour spacing 0.005

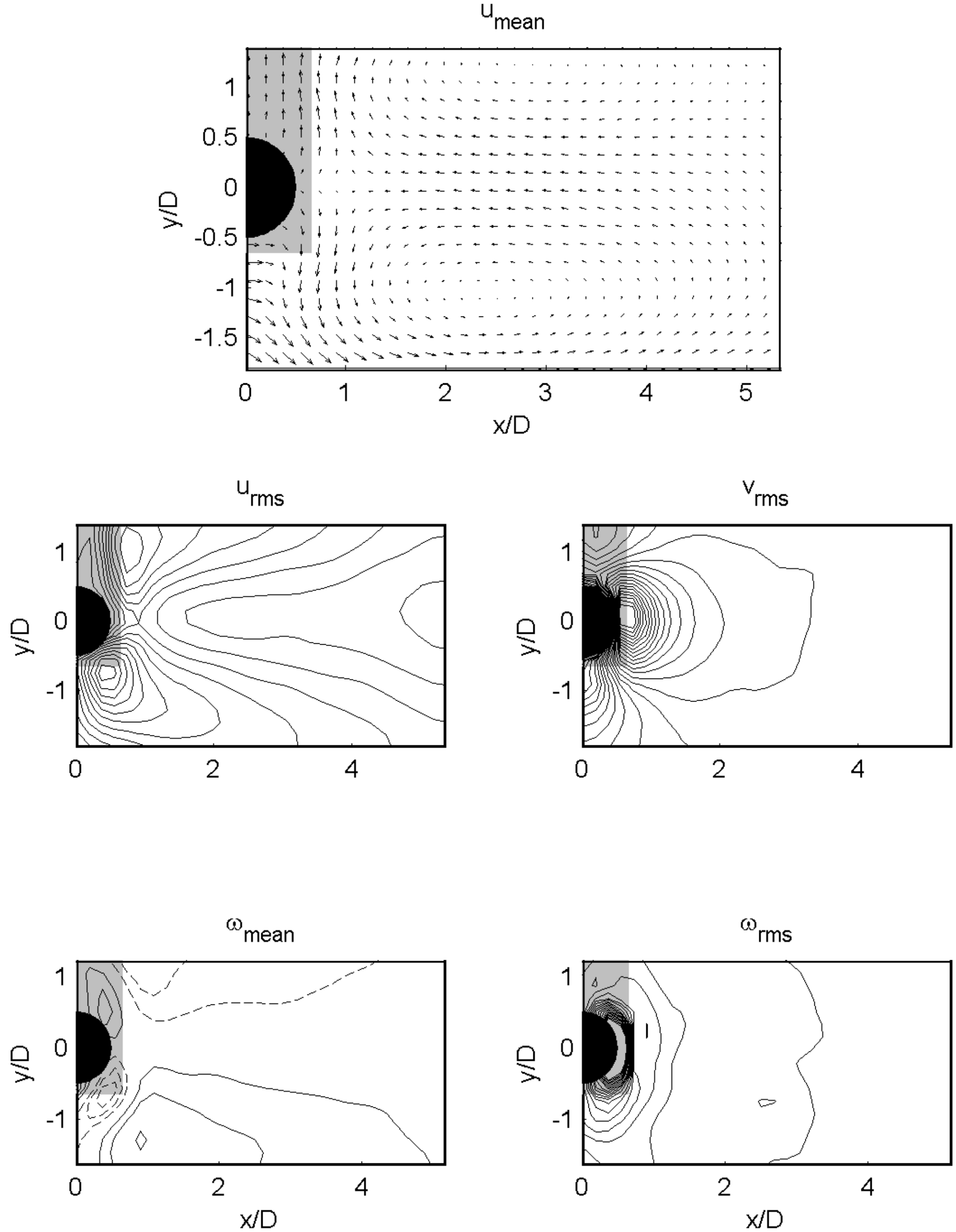

Figure 5.12: Mean and rms normalized velocity (u/U) and normalized vorticity (ωD/U) for case S2; rms velocity contours are at 0.1 intervals; vorticity contours are at 0.5 intervals, negative contours are dashed, positive contours are solid

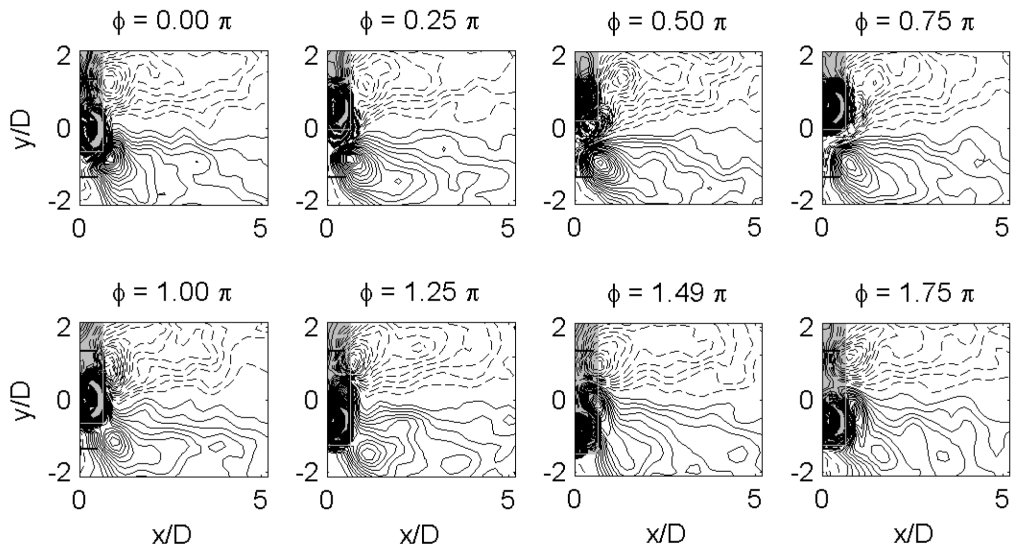

Figure 5.13: Phase-averaged normalized vorticity (ωD/U) for case S2; 1 cycle divided into 16 bins, every other bin shown; minimum contours ±0.2, contour spacing 0.2, positive contours solid, negative contours dashed

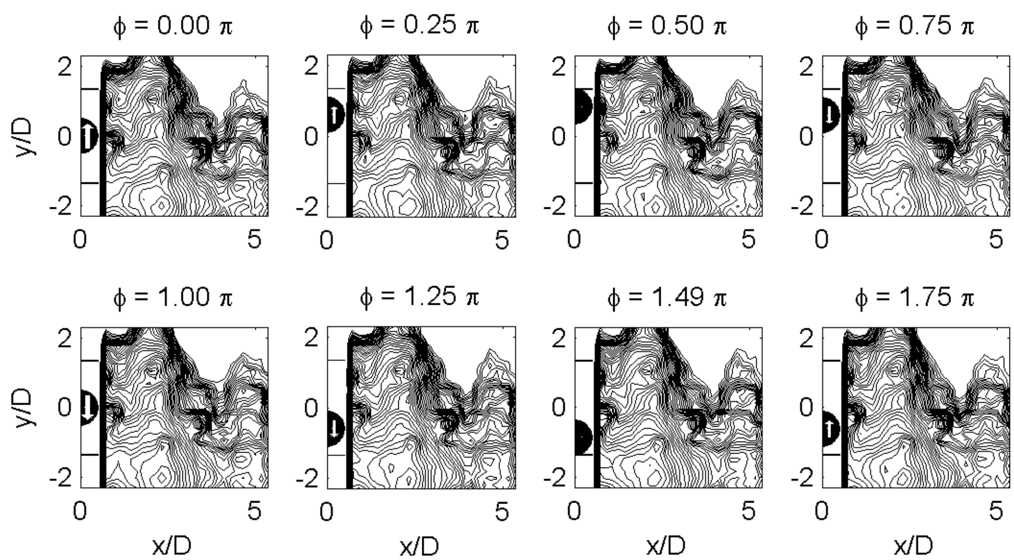

Figure 5.14: Phase-averaged normalized temperature ($(T-T_\infty)/(T_{surf}- T_\infty)$) for case S2; 1 cycle divided into 16 bins, every other bin shown; minimum contour 0.015, contour spacing 0.005

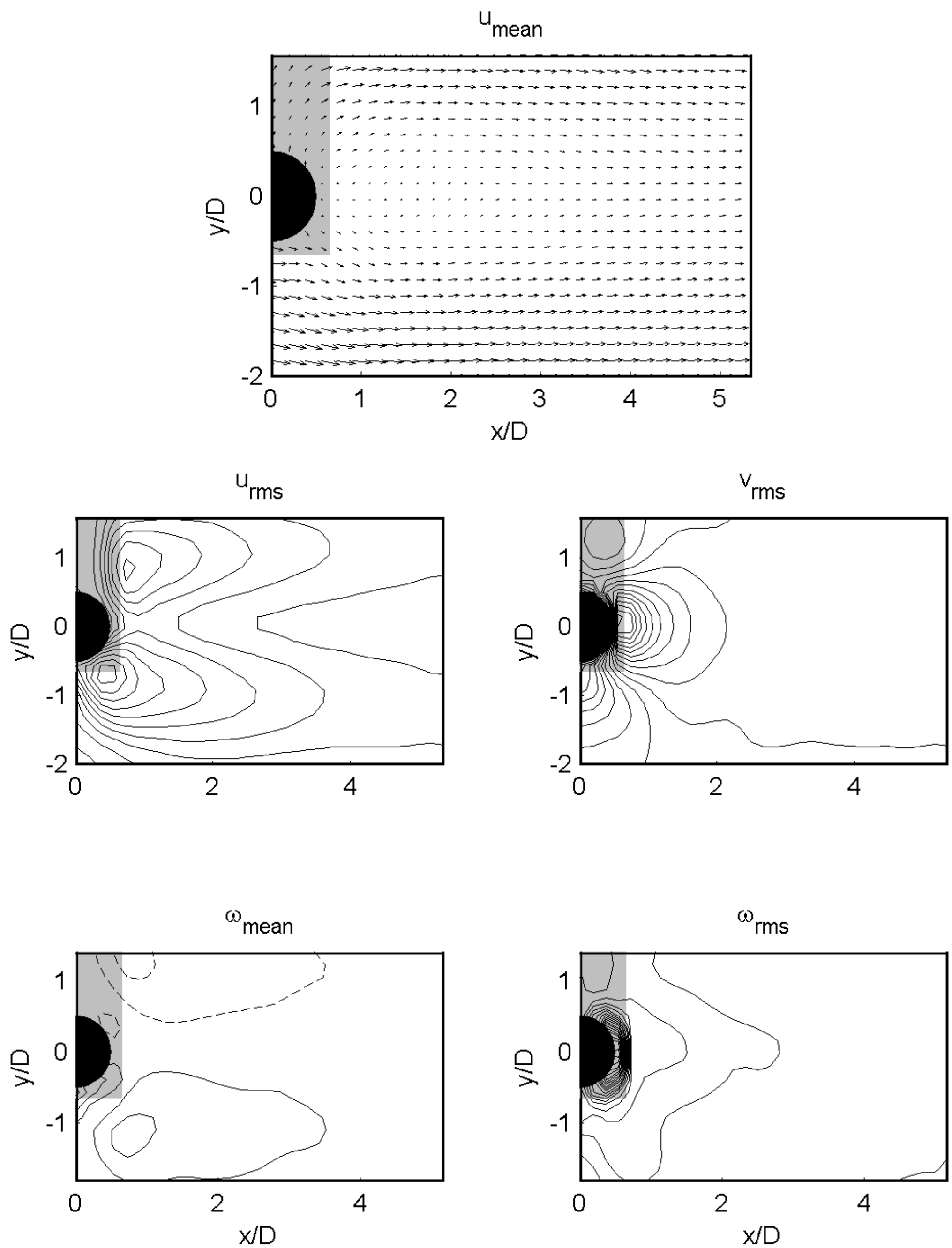

Figure 5.15: Mean and rms normalized velocity (u/U) and normalized vorticity (ωD/U) for case S3; rms velocity contours are at 0.1 intervals; vorticity contours are at 0.5 intervals, negative contours are dashed, positive contours are solid

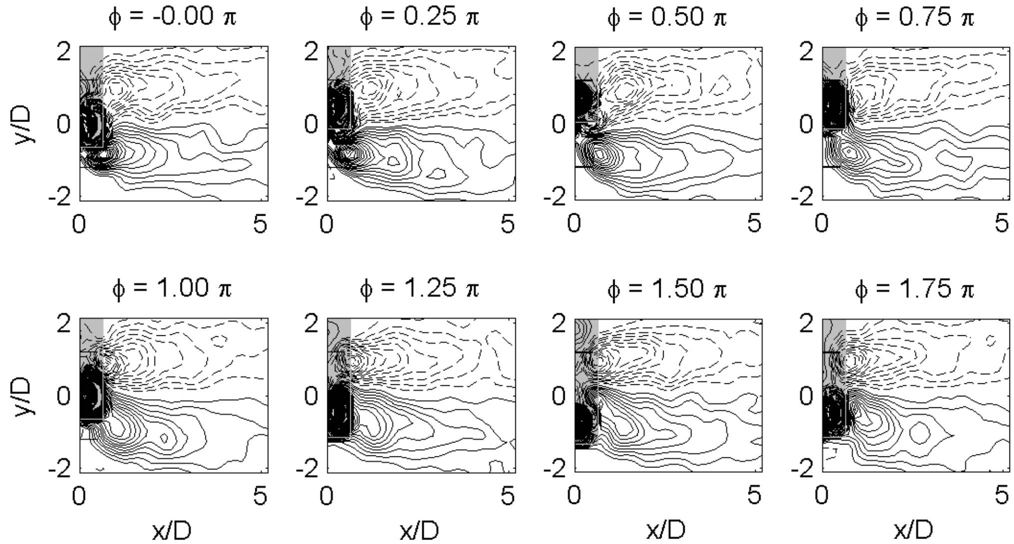

Figure 5.16: Phase-averaged normalized vorticity ($\omega D/U$) for case S3; 1 cycle divided into 16 bins, every other bin shown; minimum contours ±0.2, contour spacing 0.2, positive contours solid, negative contours dashed

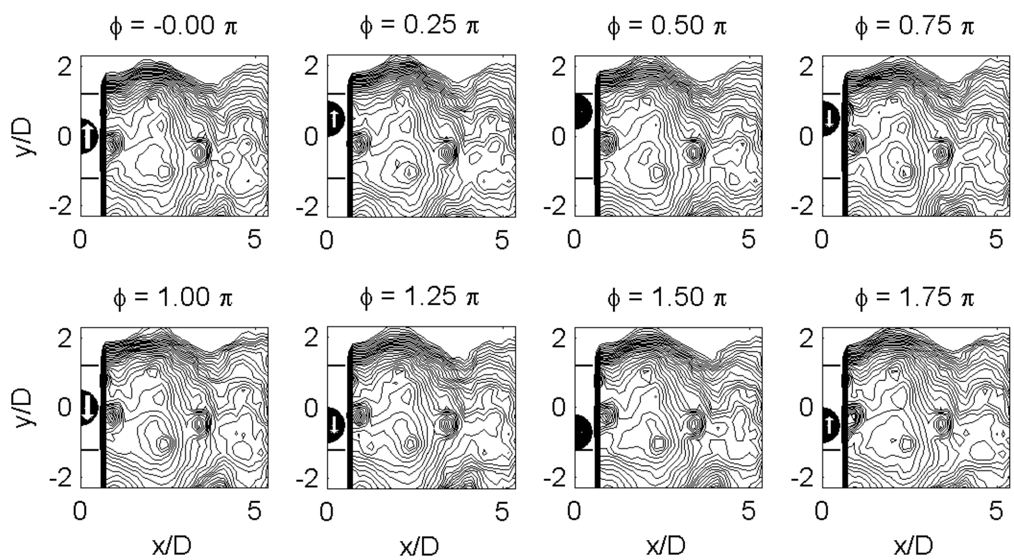

Figure 5.17: Phase-averaged normalized temperature ($(T-T_\infty)/(T_{surf}- T_\infty)$) for case S3; 1 cycle divided into 16 bins, every other bin shown; minimum contour 0.015, contour spacing 0.005

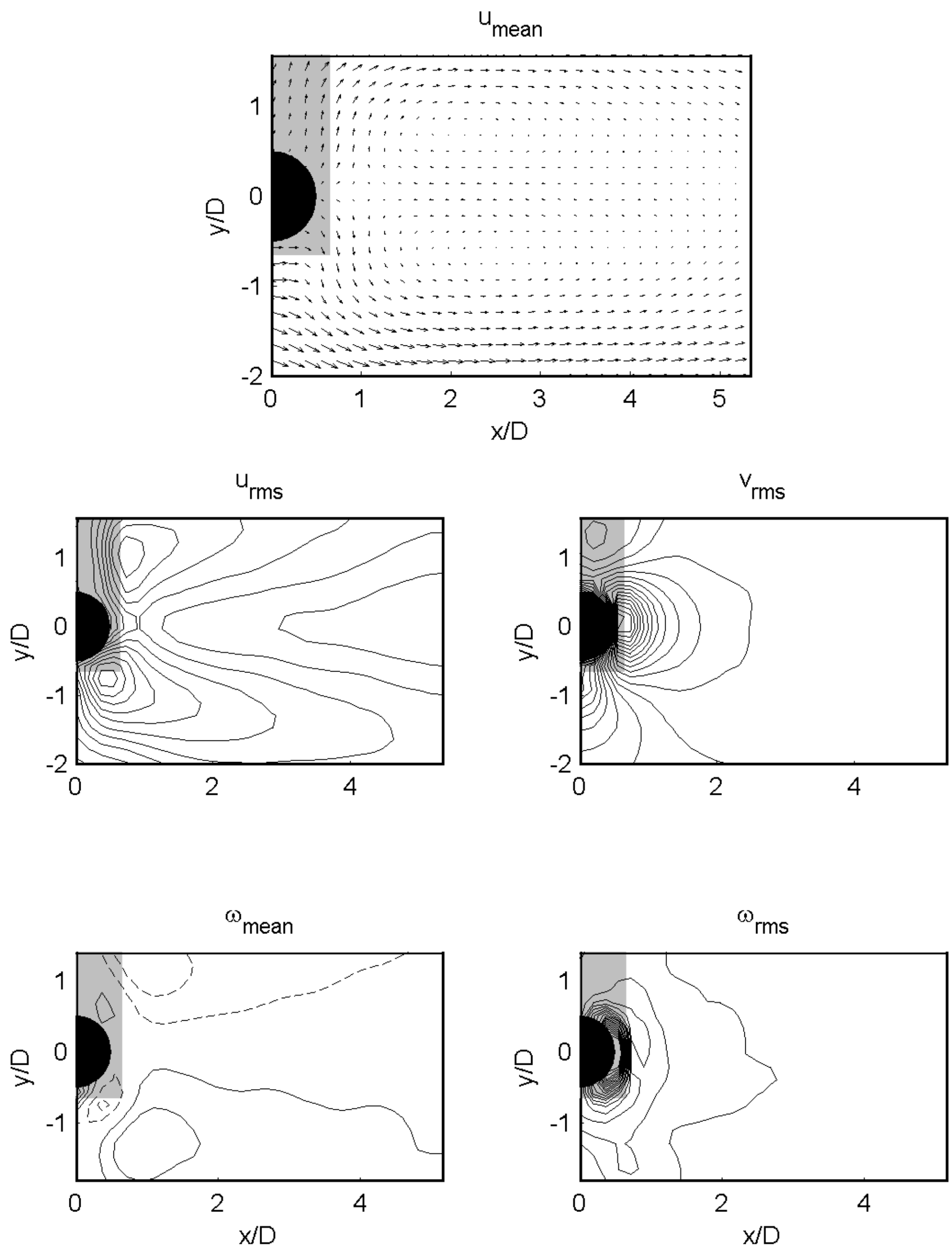

Figure 5.18: Mean and rms normalized velocity ($\underline{u}$/U) and normalized vorticity (ωD/U) for case S4; rms velocity contours are at 0.1 intervals; vorticity contours are at 0.5 intervals, negative contours are dashed, positive contours are solid

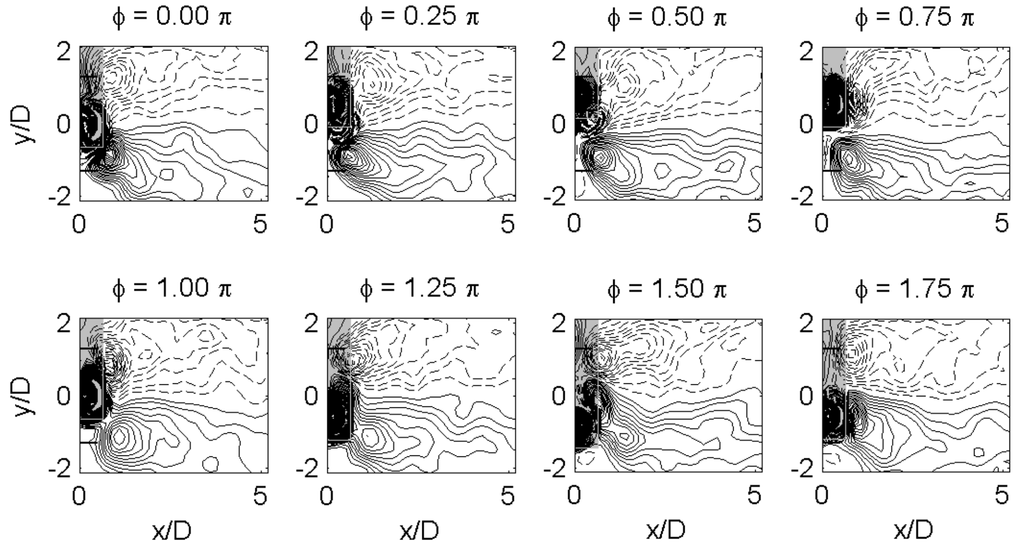

Figure 5.19: Phase-averaged normalized vorticity ($\omega D/U$) for case S4; 1 cycle divided into 16 bins, every other bin shown; minimum contours ±0.2, contour spacing 0.2, positive contours solid, negative contours dashed

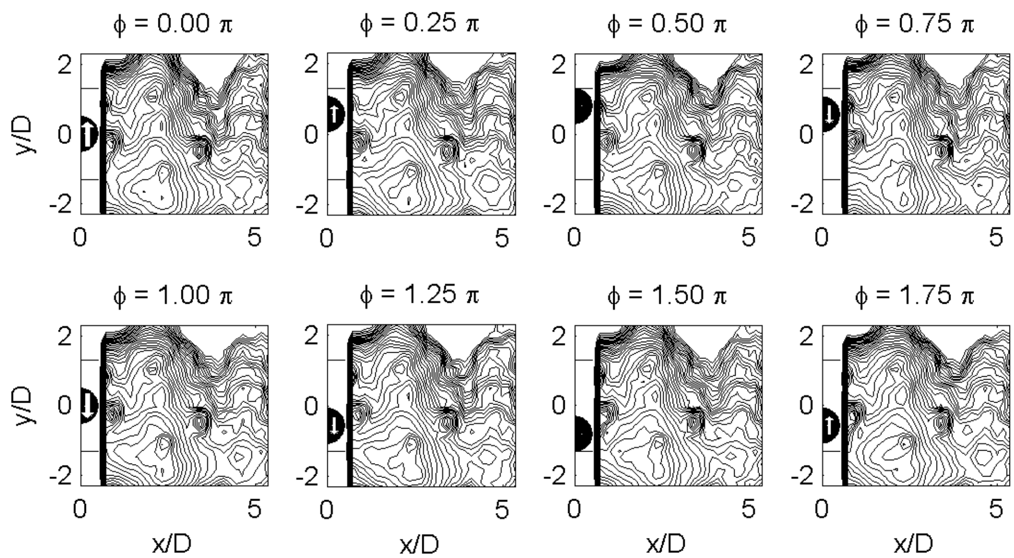

Figure 5.20: Phase-averaged normalized temperature ($(T-T_\infty)/(T_{surf}-T_\infty)$) for case S4; 1 cycle divided into 16 bins, every other bin shown; minimum contour 0.015, contour spacing 0.005

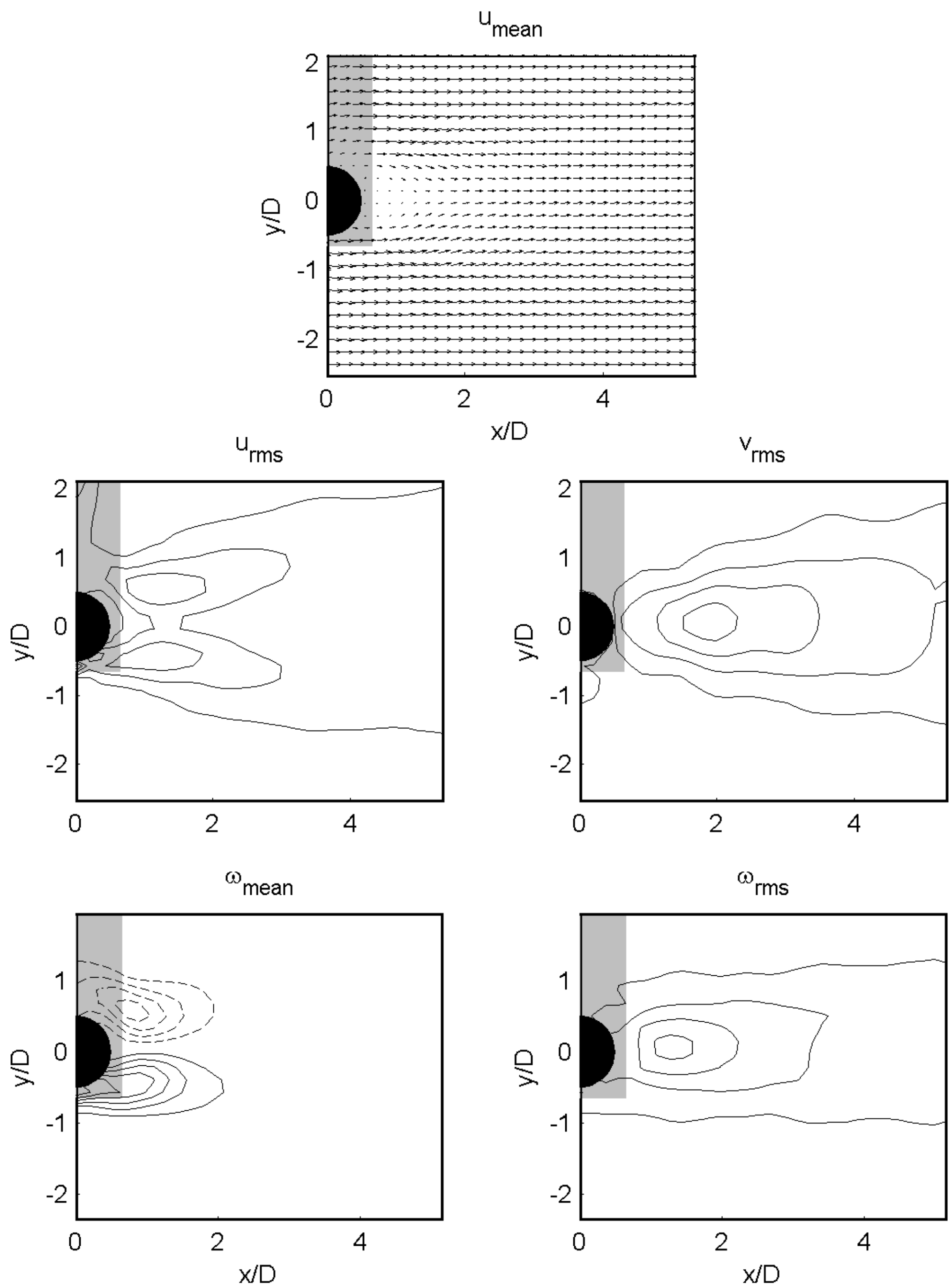

Figure 5.21: Mean and rms normalized velocity (u/U) and normalized vorticity (ωD/U) for case S5; rms velocity contours are at 0.1 intervals; vorticity contours are at 0.5 intervals, negative contours are dashed, positive contours are solid

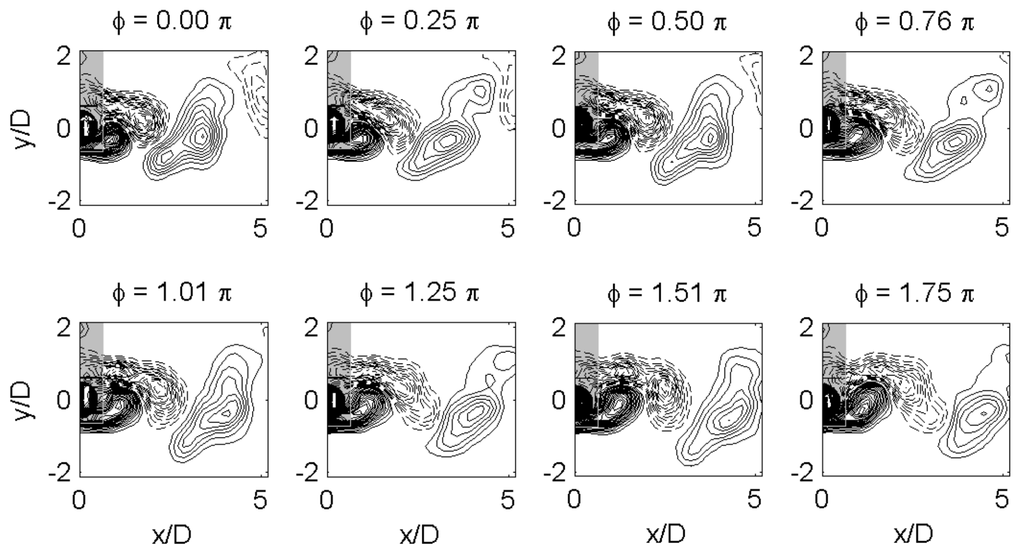

Figure 5.22: Phase-averaged normalized vorticity ($\omega D/U$) for case S5; 3 cycles divided into 48 bins, every other bin for 1st cycle shown; minimum contours ±0.2, contour spacing 0.2, positive contours solid, negative contours dashed

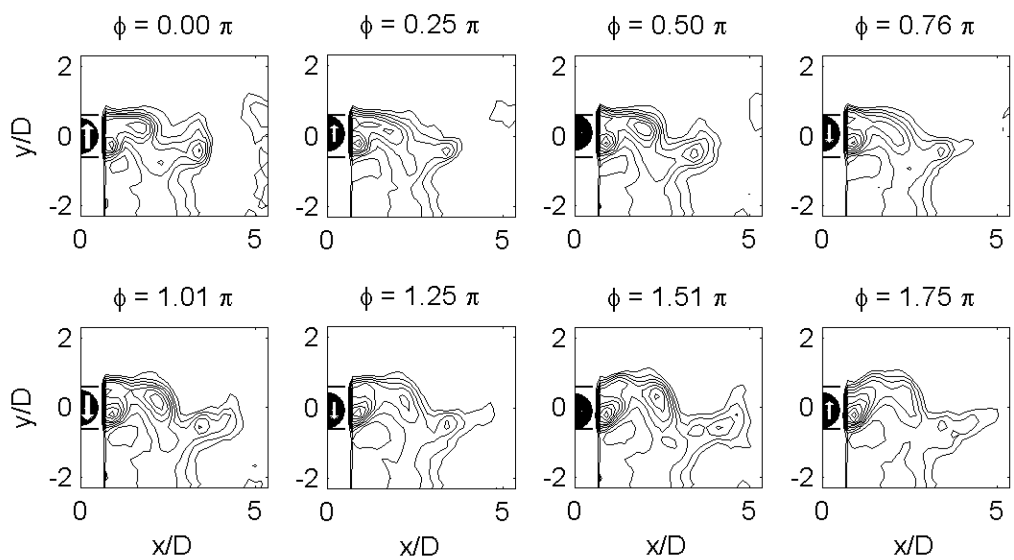

Figure 5.23: Phase-averaged normalized temperature ($(T-T_\infty)/(T_{surf}-T_\infty)$) for case S5; 3 cycles divided into 48 bins, every other bin for 1sr cycle shown; minimum contour 0.015, contour spacing 0.005

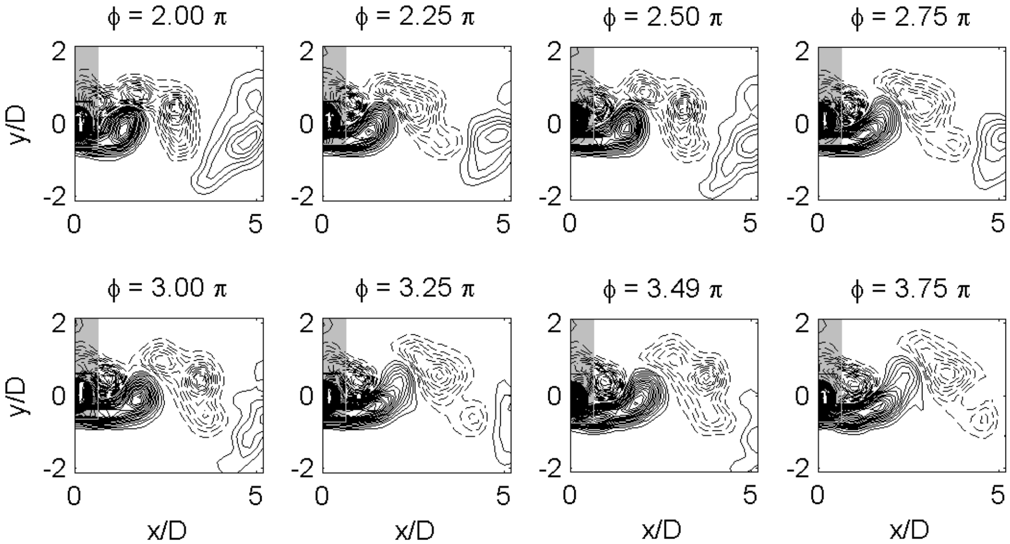

Figure 5.24: Phase-averaged vorticity (ωD/U) for case S5; 3 cycles divided into 48 bins, every other bin for 2nd cycle shown; minimum contours ±0.2, contour spacing 0.2, positive contours solid, negative contours dashed

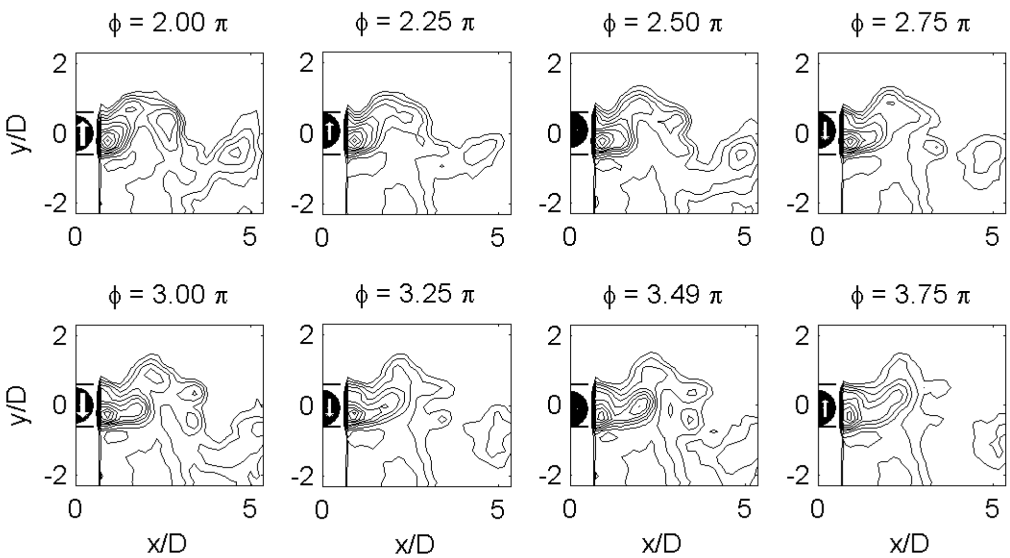

Figure 5.25: Phase-averaged normalized temperature ($(T-T_\infty)/(T_{surf}- T_\infty)$) for case S5; 3 cycles divided into 48 bins, every other bin for 2nd cycle shown; minimum contour 0.015, contour spacing 0.005

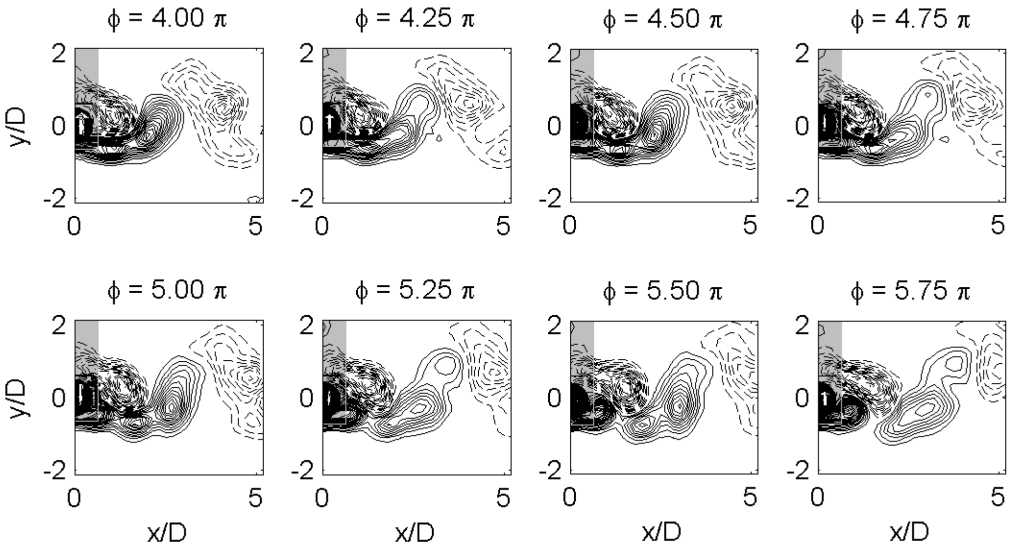

Figure 5.26: Phase-averaged normalized vorticity ($\omega D/U$) for case S5; 3 cycles divided into 48 bins, every other bin for 3rd cycle shown; minimum contours ±0.2, contour spacing 0.2, positive contours solid, negative contours dashed

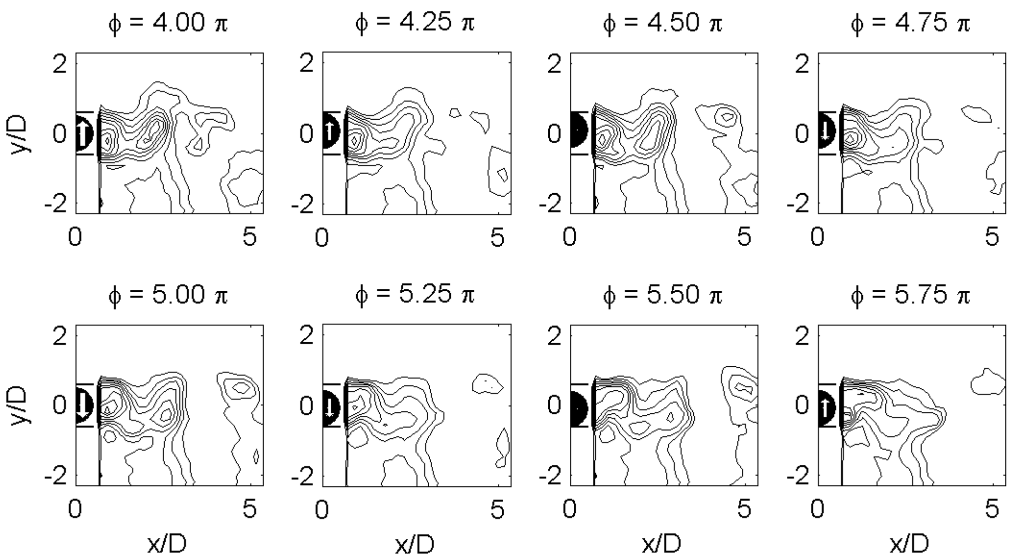

Figure 5.27: Phase-averaged normalized temperature ($(T-T_\infty)/(T_{surf}-T_\infty)$) for case S5; 3 cycles divided into 48 bins, every other bin for 3rd cycle shown; minimum contour 0.015, contour spacing 0.005

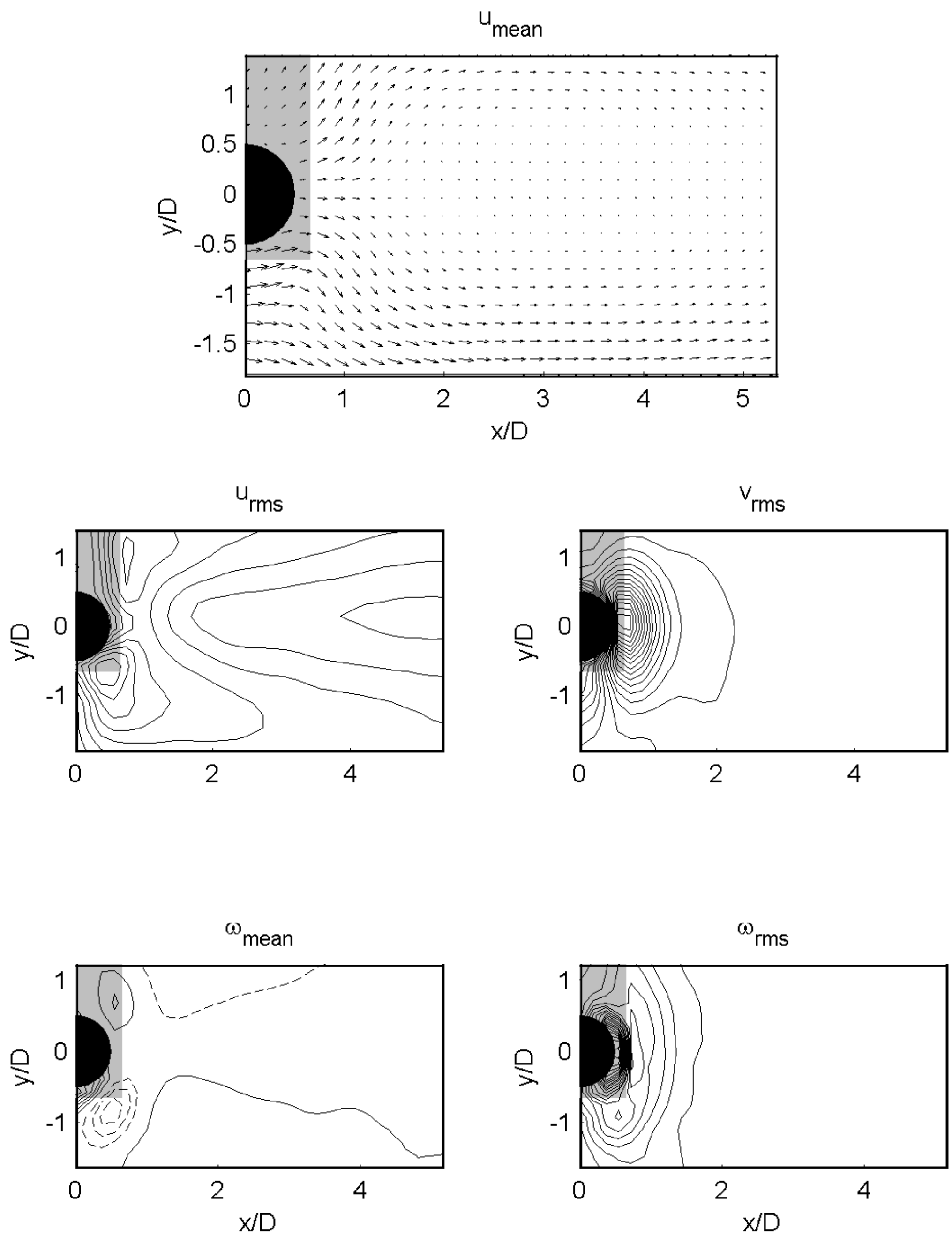

Figure 5.28: Mean and rms normalized velocity (u/U) and normalized vorticity (ωD/U) for case S6; rms velocity contours are at 0.1 intervals; vorticity contours are at 0.5 intervals, negative contours are dashed, positive contours are solid

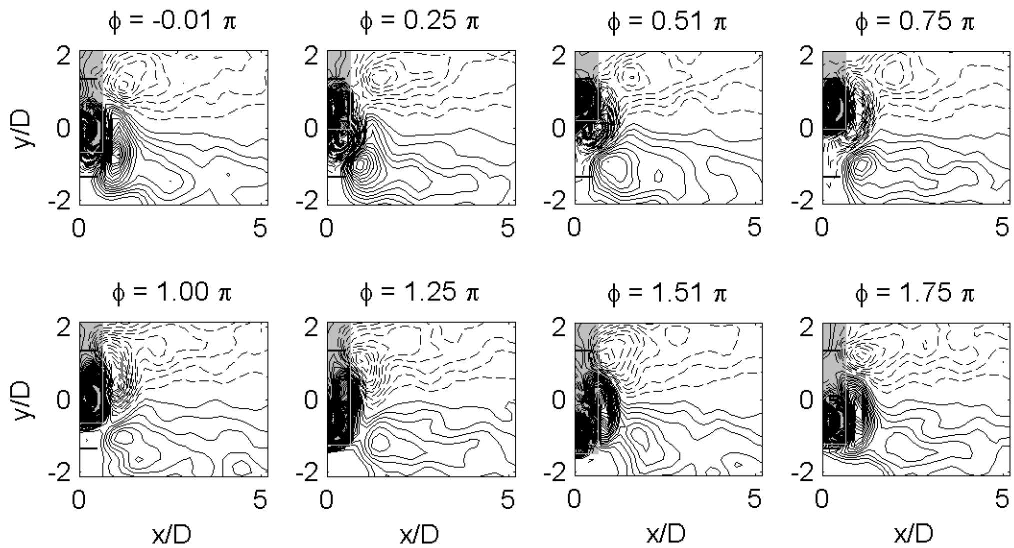

Figure 5.29: Phase-averaged normalized vorticity (ωD/U) for case S6; 1 cycle divided into 16 bins, every other bin shown; minimum contours ±0.2, contour spacing 0.2, positive contours solid, negative contours dashed

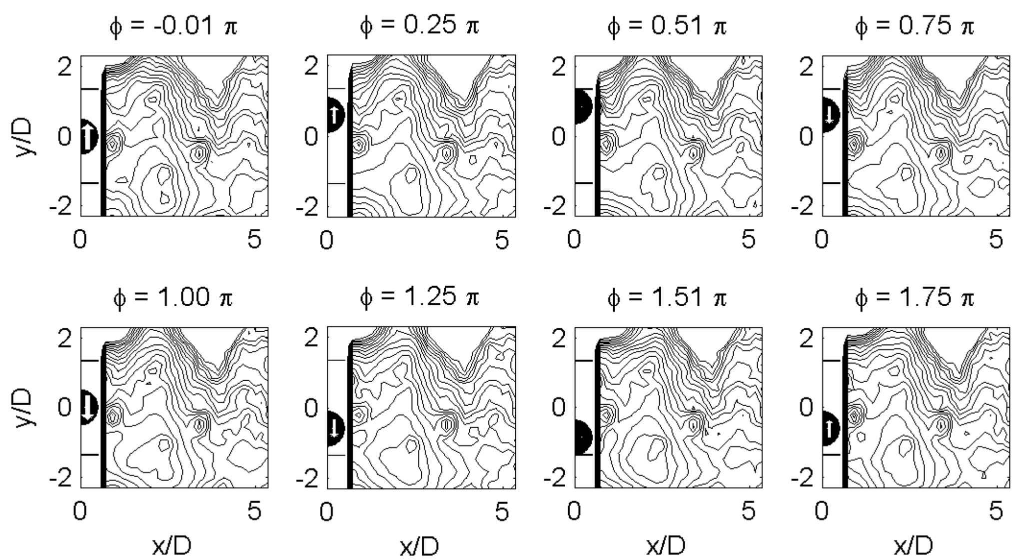

Figure 5.30: Phase-averaged normalized temperature ($(T-T_\infty)/(T_{surf}-T_\infty)$) for case S6; 1 cycle divided into 16 bins, every other bin shown; minimum contour 0.015, contour spacing 0.005

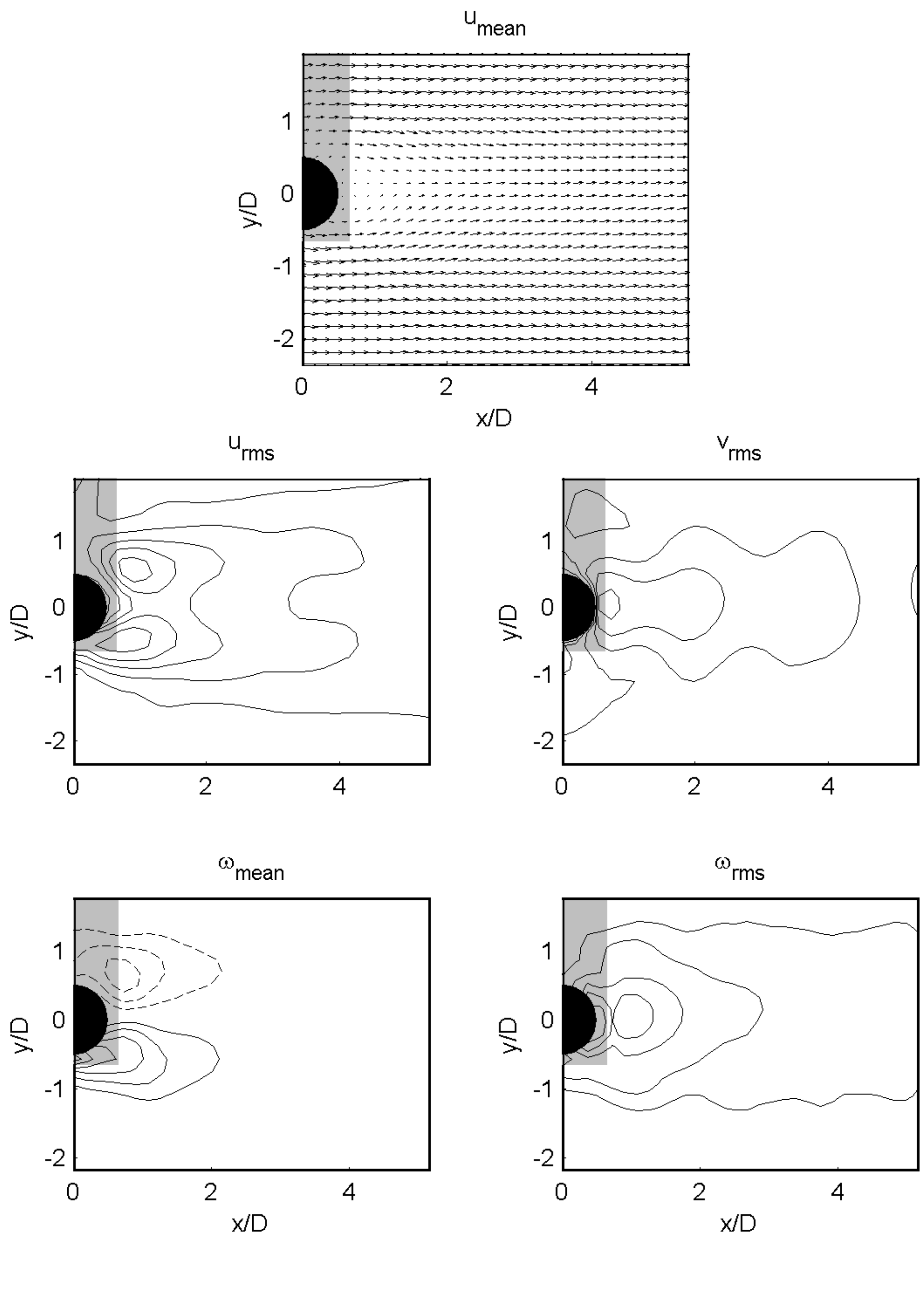

Figure 5.31: Mean and rms normalized velocity (u/U) and normalized vorticity (ωD/U) for case S7; rms velocity contours are at 0.1 intervals; vorticity contours are at 0.5 intervals, negative contours are dashed, positive contours are solid

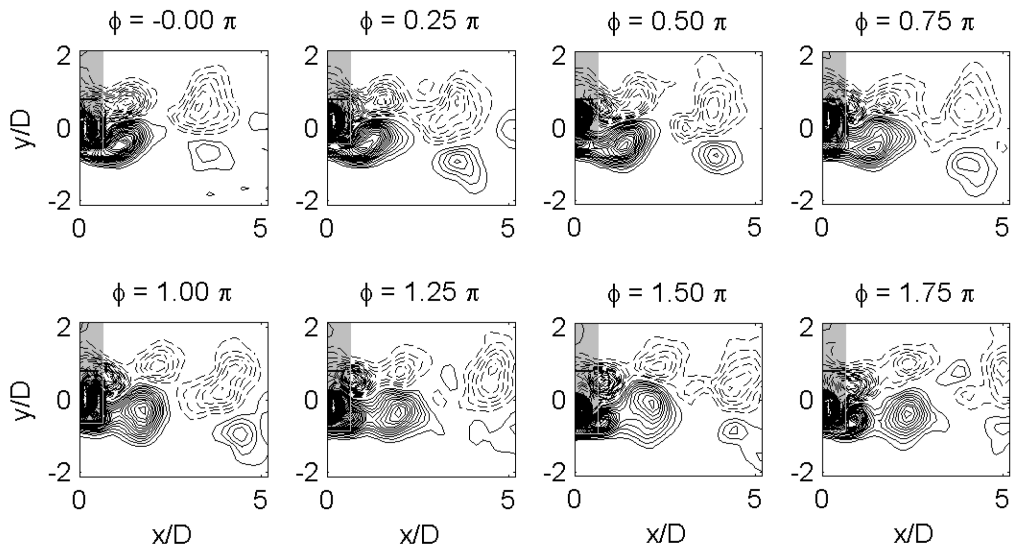

Figure 5.32: Phase-averaged normalized vorticity (ωD/U) for case S7; 3 cycles divided into 48 bins, every other bin for 1st cycle shown; minimum contours ±0.2, contour spacing 0.2, positive contours solid, negative contours dashed

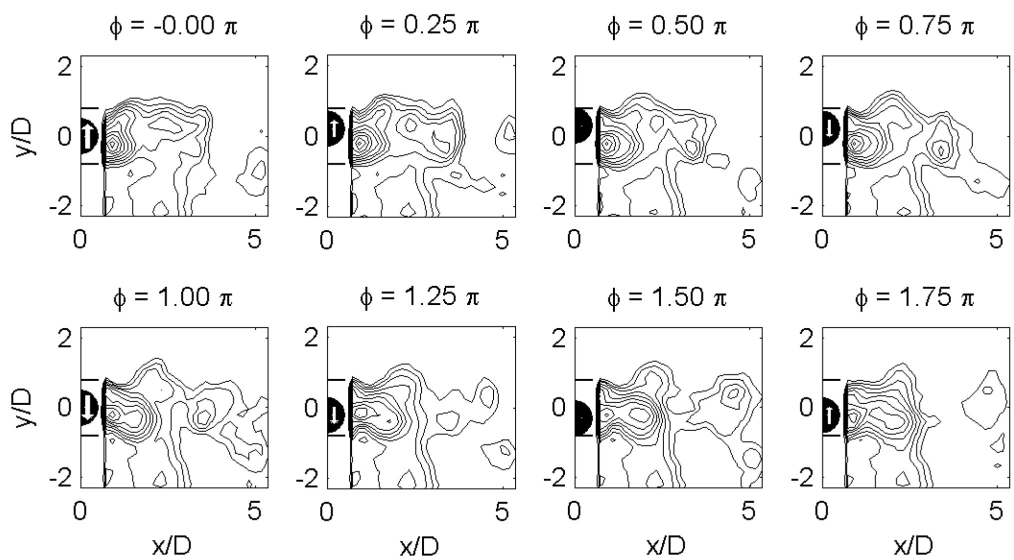

Figure 5.33: Phase-averaged normalized temperature ($(T-T_\infty)/(T_{surf}-T_\infty)$) for case S7; 3 cycles divided into 48 bins, every other bin for 1st cycle shown; minimum contour 0.015, contour spacing 0.005

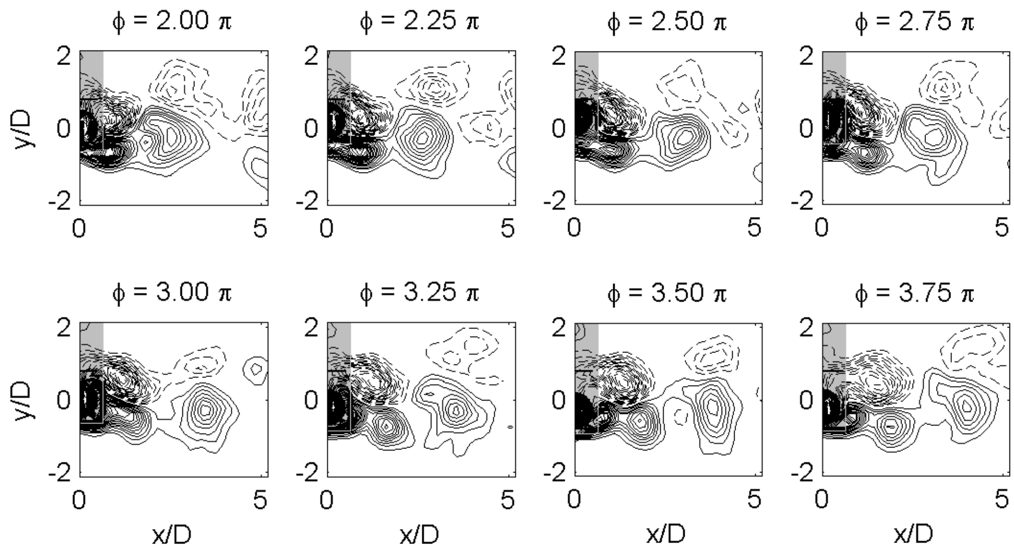

Figure 5.34: Phase-averaged vorticity (ωD/U) for case S7; 3 cycles divided into 48 bins, every other bin for 2nd cycle shown; minimum contours ±0.2, contour spacing 0.2, positive contours solid, negative contours dashed

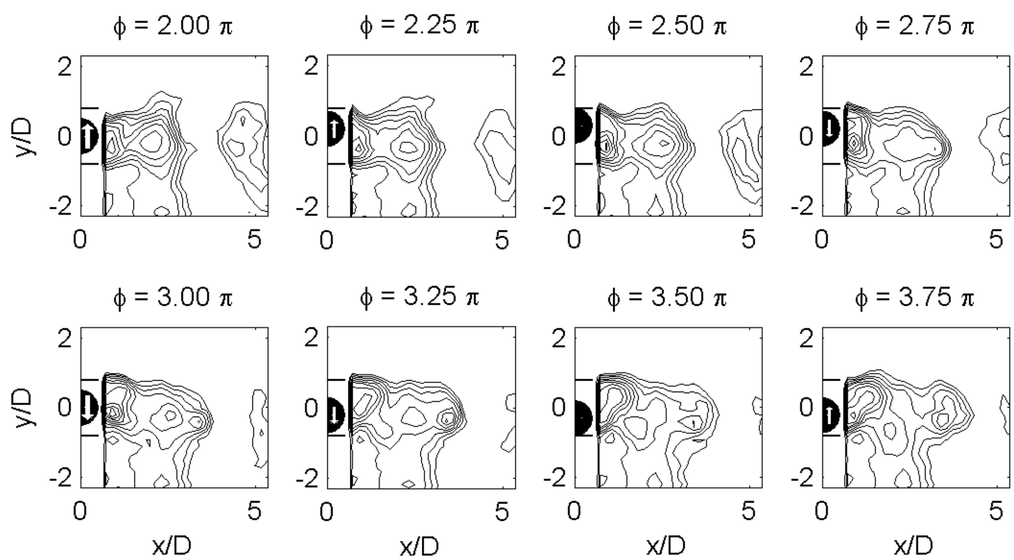

Figure 5.35: Phase-averaged normalized temperature ($(T-T_\infty)/(T_{surf}-T_\infty)$) for case S7; 3 cycles divided into 48 bins, every other bin for 2nd cycle shown; minimum contour 0.015, contour spacing 0.005

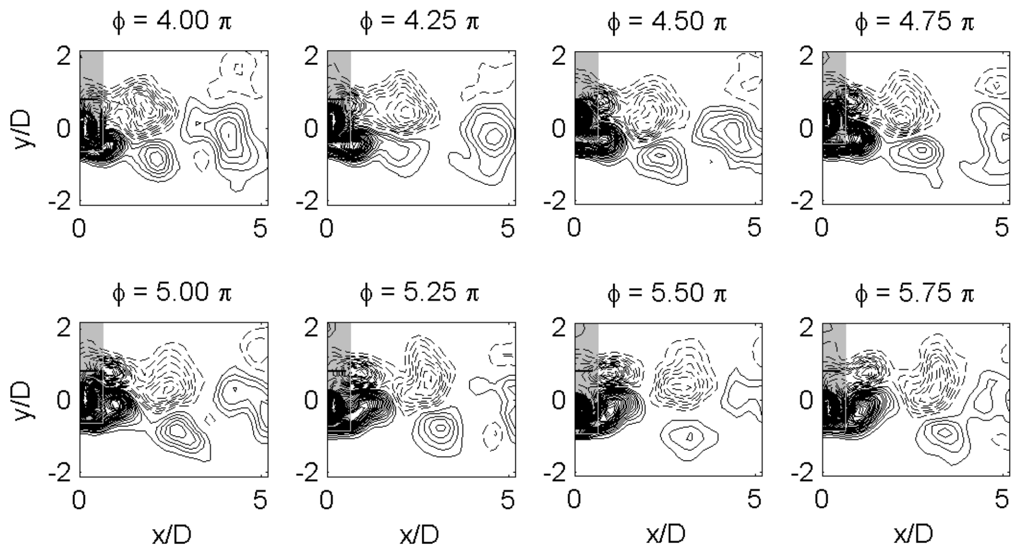

Figure 5.36: Phase-averaged normalized vorticity (ωD/U) for case S7; 3 cycles divided into 48 bins, every other bin for 3rd cycle shown; minimum contours ±0.2, contour spacing 0.2, positive contours solid, negative contours dashed

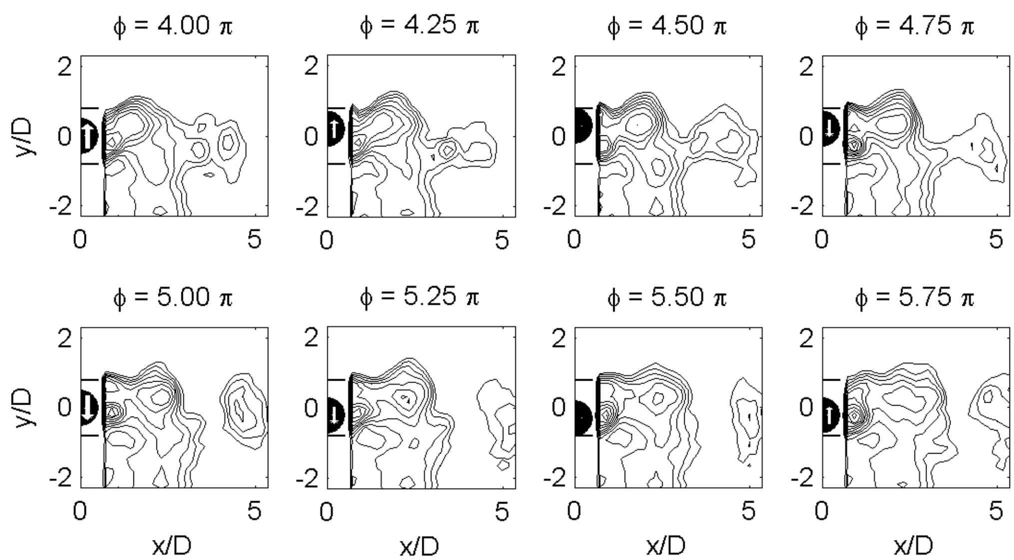

Figure 5.37: Phase-averaged normalized temperature ($(T-T_\infty)/(T_{surf}-T_\infty)$) for case S7; 3 cycles divided into 48 bins, every other bin for 3rd cycle shown; minimum contour 0.015, contour spacing 0.005

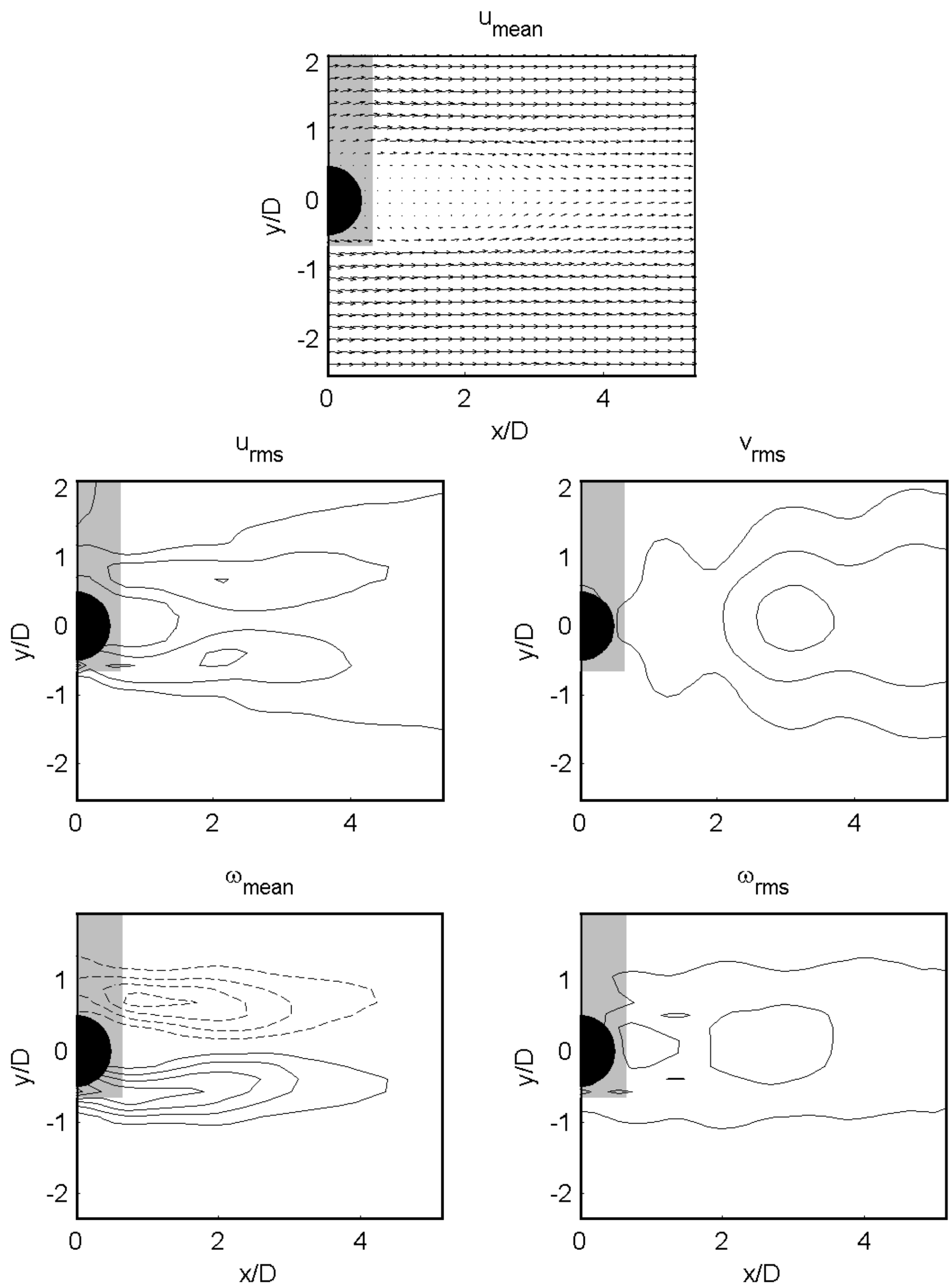

Figure 5.38: Mean and rms normalized velocity (u/U) and normalized vorticity (ωD/U) for case S8; rms velocity contours are at 0.1 intervals; vorticity contours are at 0.5 intervals, negative contours are dashed, positive contours are solid

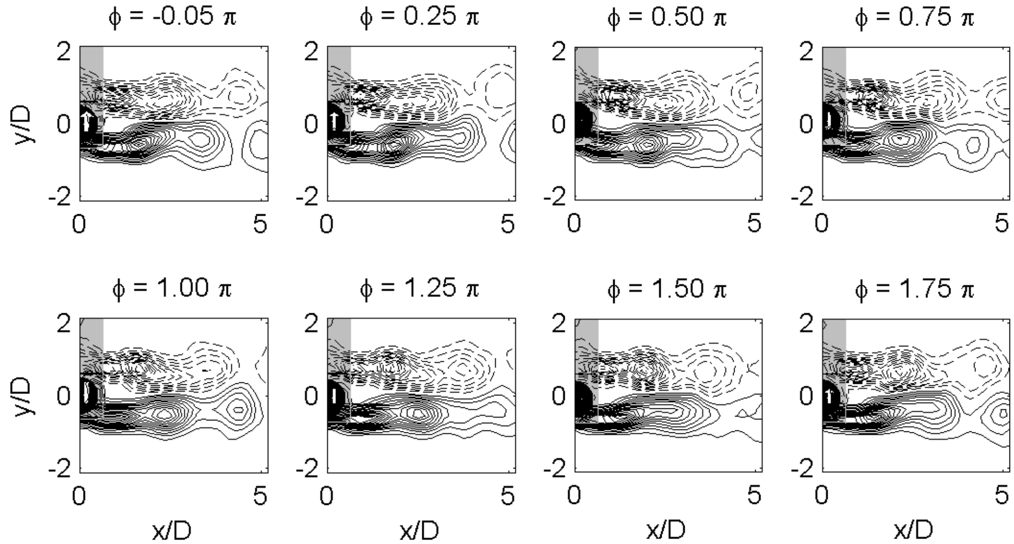

Figure 5.39: Phase-averaged normalized vorticity (ωD/U) for case S8; 2 cycles divided into 32 bins, every other bin for 1st cycle shown; minimum contours ±0.2, contour spacing 0.2, positive contours solid, negative contours dashed

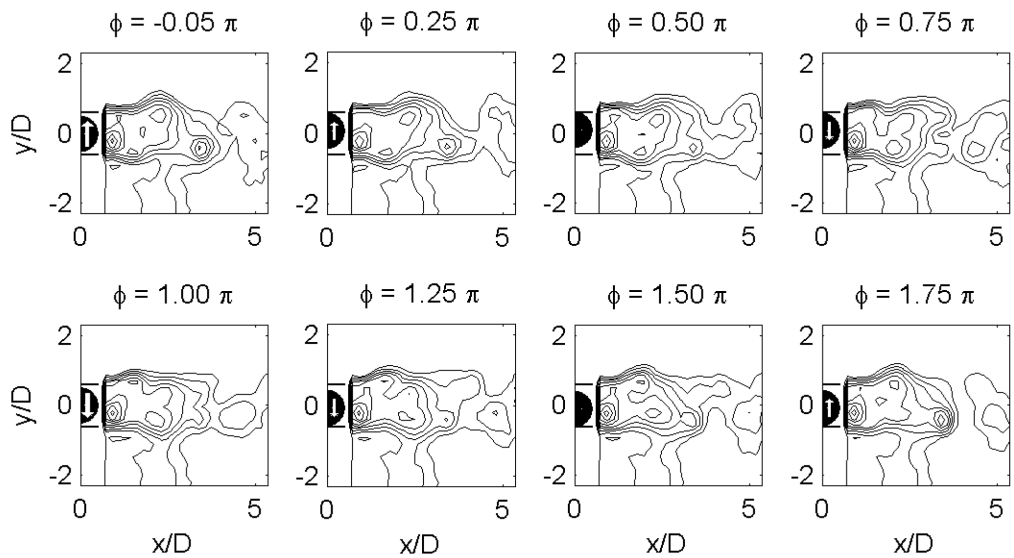

Figure 5.40: Phase-averaged normalized temperature ($(T-T_\infty)/(T_{surf}-T_\infty)$) for case S8; 2 cycles divided into 32 bins, every other bin for 1st cycle shown; minimum contour 0.015, contour spacing 0.005

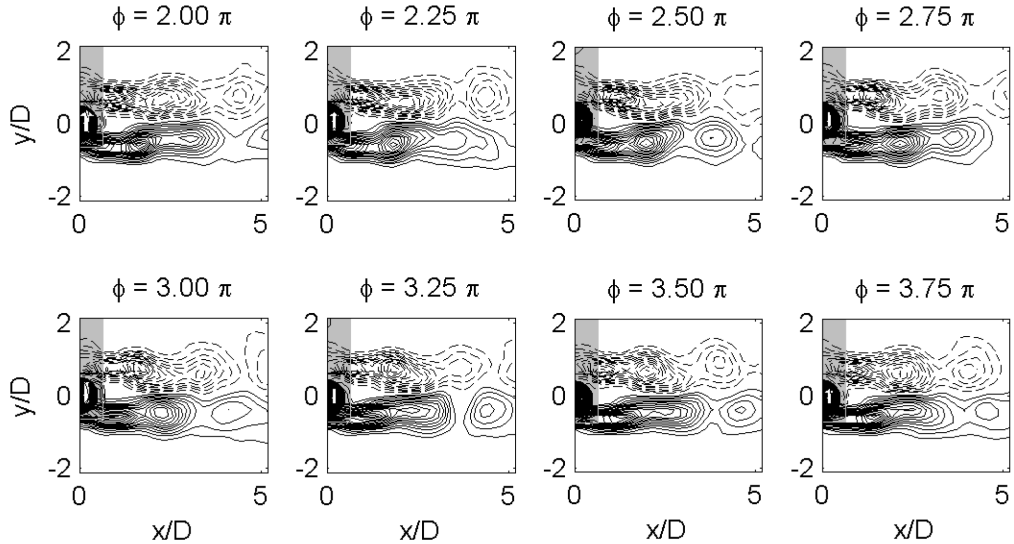

Figure 5.41: Phase-averaged vorticity ($\omega D/U$) for case S8; 2 cycles divided into 32 bins, every other bin for 2nd cycle shown; minimum contours ±0.2, contour spacing 0.2, positive contours solid, negative contours dashed

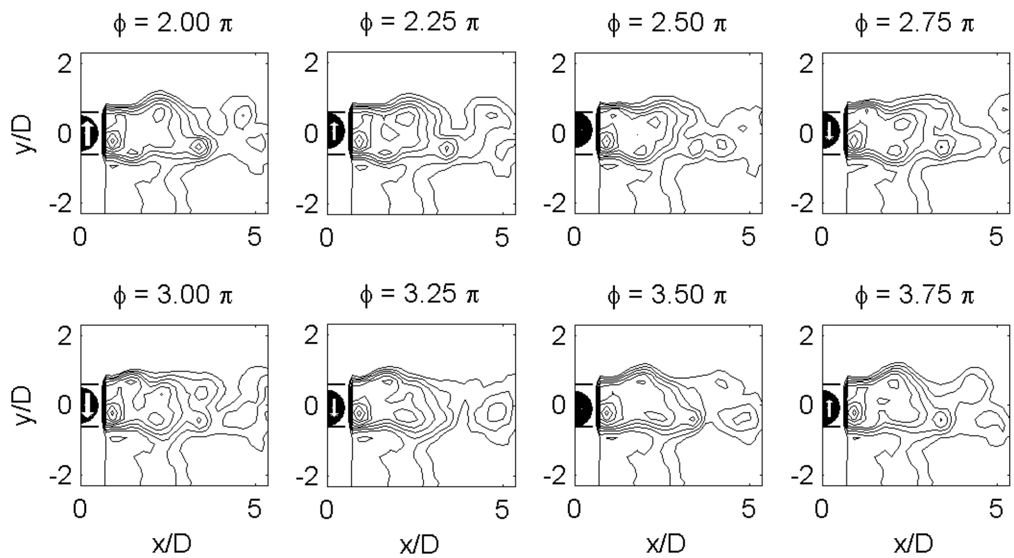

Figure 5.42: Phase-averaged normalized temperature ($(T-T_\infty)/(T_{surf}-T_\infty)$) for case S8; 2 cycles divided into 32 bins, every other bin for 2nd cycle shown; minimum contour 0.015, contour spacing 0.005

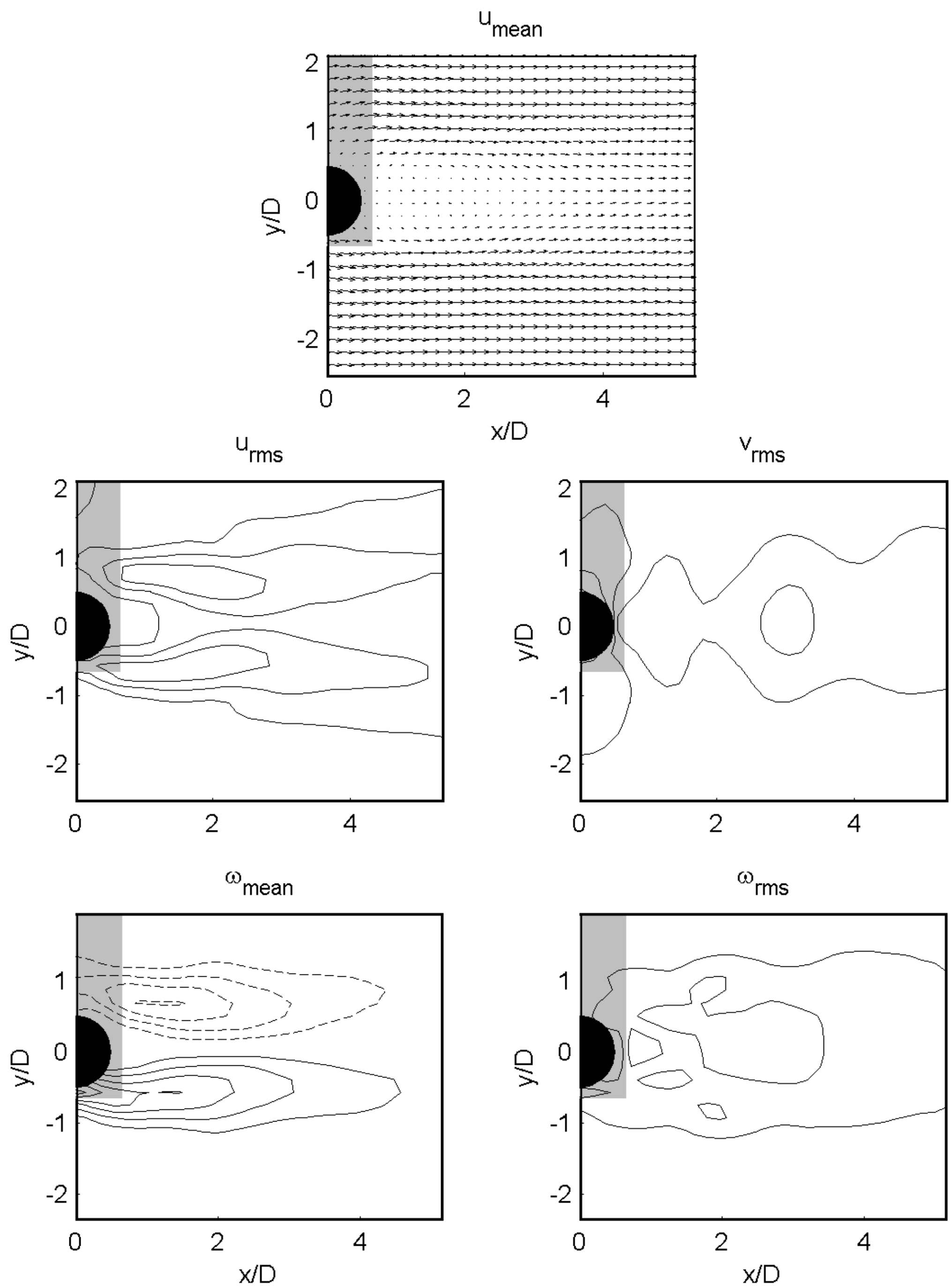

Figure 5.43: Mean and rms normalized velocity (u/U) and normalized vorticity (ωD/U) for case S9; rms velocity contours are at 0.1 intervals; vorticity contours are at 0.5 intervals, negative contours are dashed, positive contours are solid

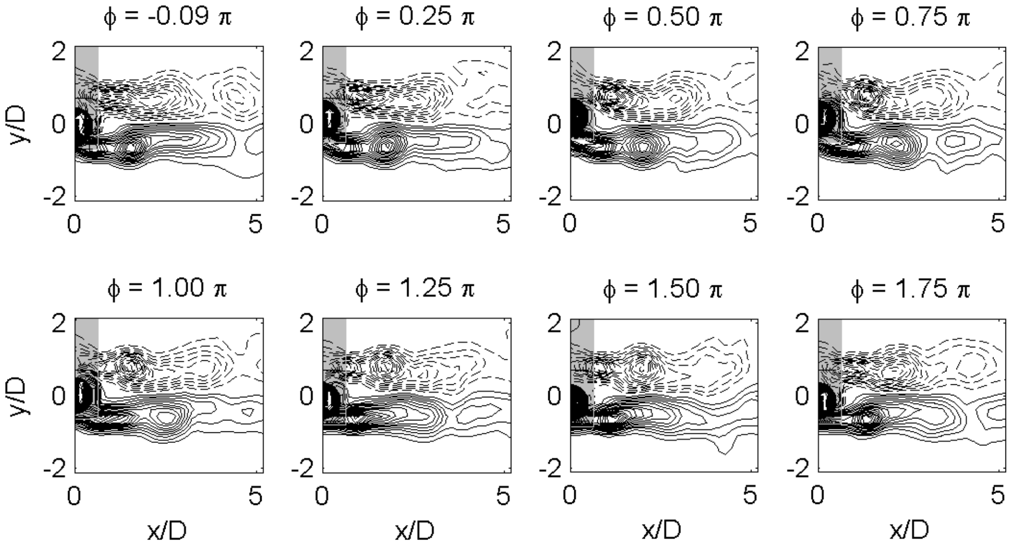

Figure 5.44: Phase-averaged normalized vorticity ($\omega D/U$) for case S9; 2 cycles divided into 32 bins, every other bin for 1st cycle shown; minimum contours ±0.2, contour spacing 0.2, positive contours solid, negative contours dashed

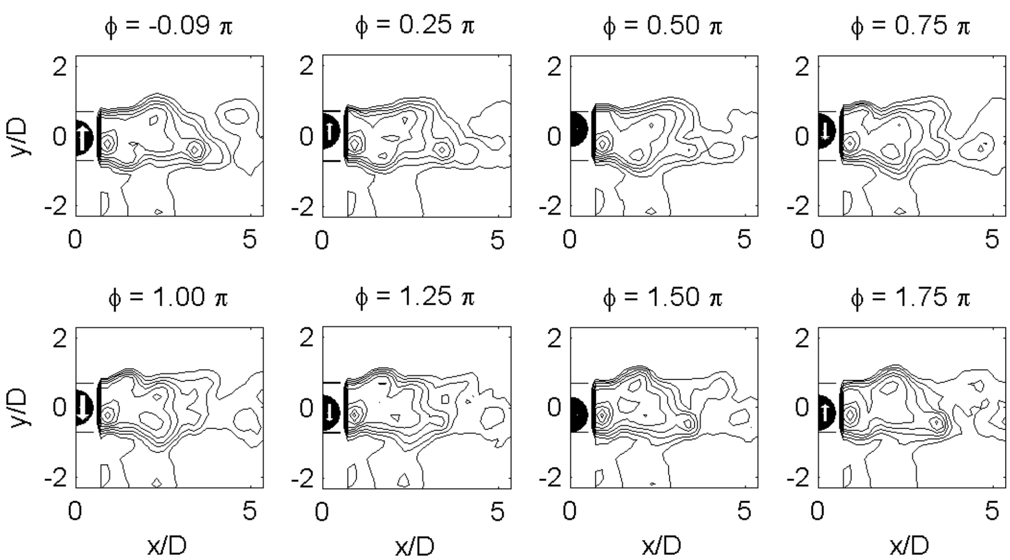

Figure 5.45: Phase-averaged normalized temperature ($(T-T_\infty)/(T_{surf}-T_\infty)$) for case S9; 2 cycles divided into 32 bins, every other bin for 1st cycle shown; minimum contour 0.015, contour spacing 0.005

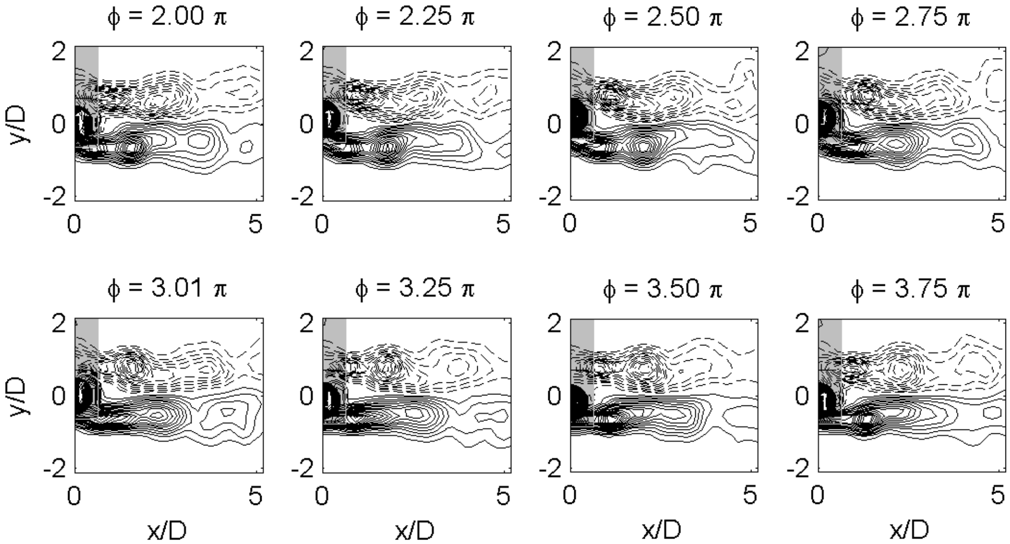

Figure 5.46: Phase-averaged normalized vorticity ($\omega D/U$) for case S9; 2 cycles divided into 32 bins, every other bin for 2nd cycle shown; minimum contours ±0.2, contour spacing 0.2, positive contours solid, negative contours dashed

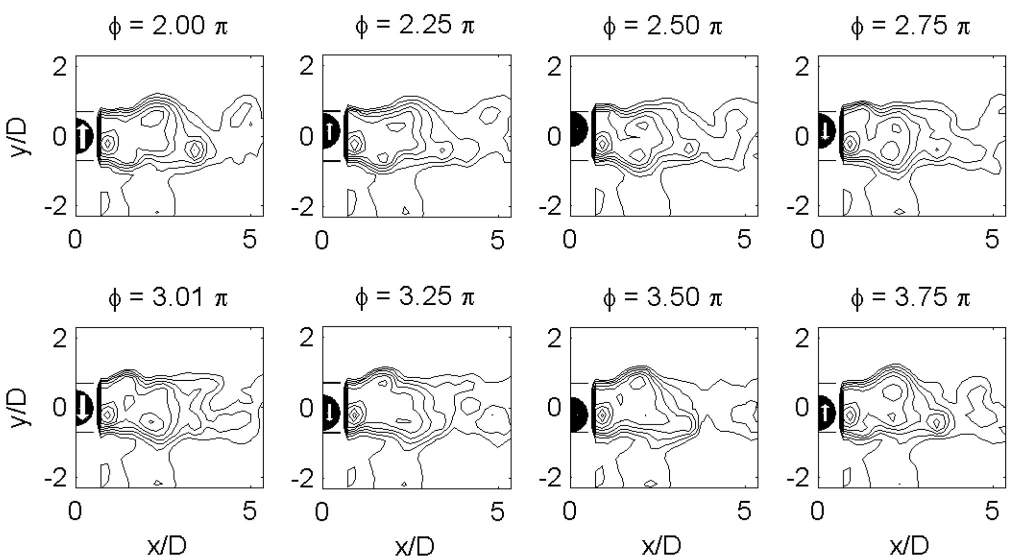

Figure 5.47: Phase-averaged normalized temperature ($(T-T_\infty)/(T_{surf}- T_\infty)$) for case S9; 2 cycles divided into 32 bins, every other bin for 2nd cycle shown; minimum contour 0.015, contour spacing 0.005

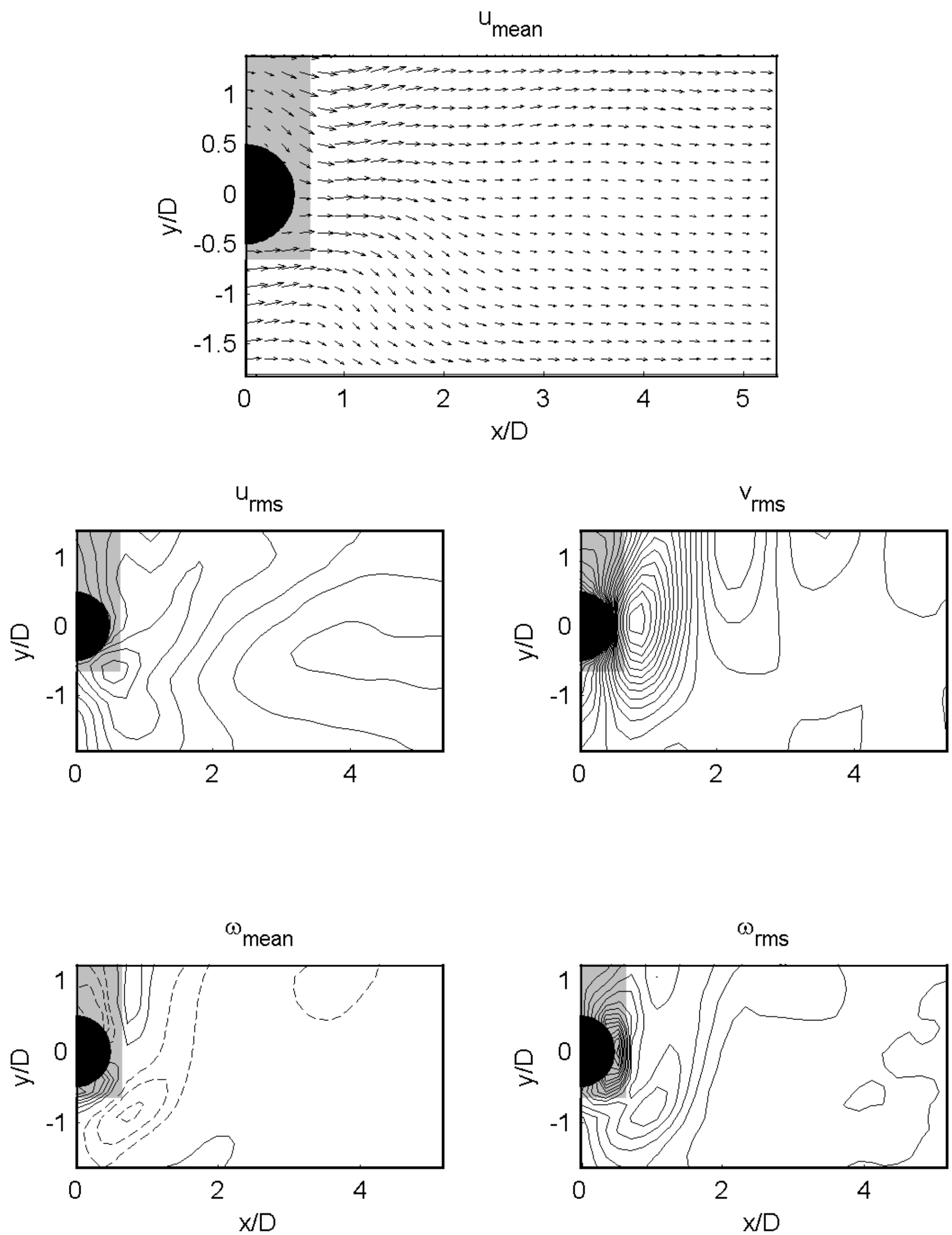

Figure 5.48: Mean and rms normalized velocity ($\underline{u}$/U) and normalized vorticity (ωD/U) for case S10; rms velocity contours are at 0.1 intervals; vorticity contours are at 0.5 intervals, negative contours are dashed, positive contours are solid

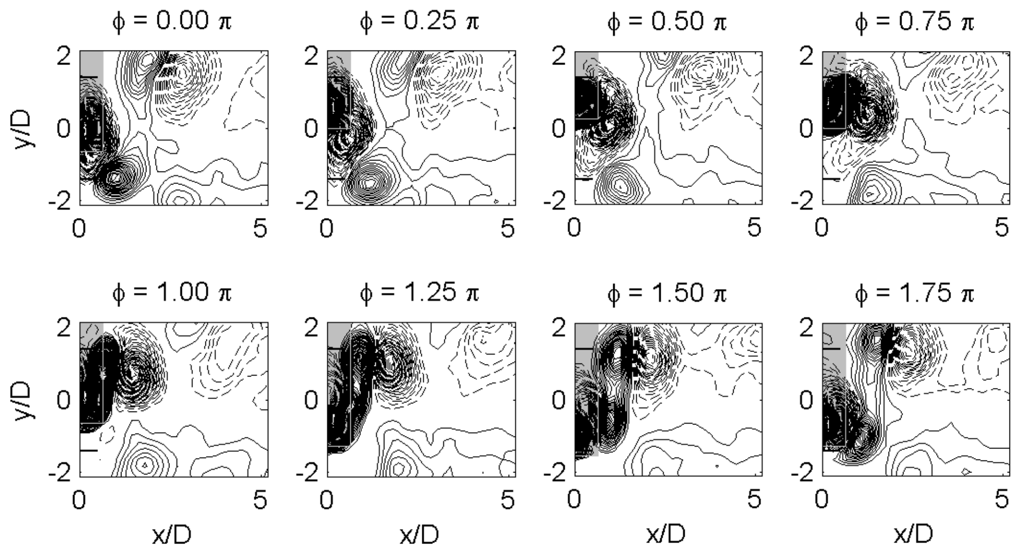

Figure 5.49: Phase-averaged normalized vorticity ($\omega D/U$) for case S10; 1 cycle divided into 16 bins, every other bin shown; minimum contours ±0.2, contour spacing 0.2, positive contours solid, negative contours dashed

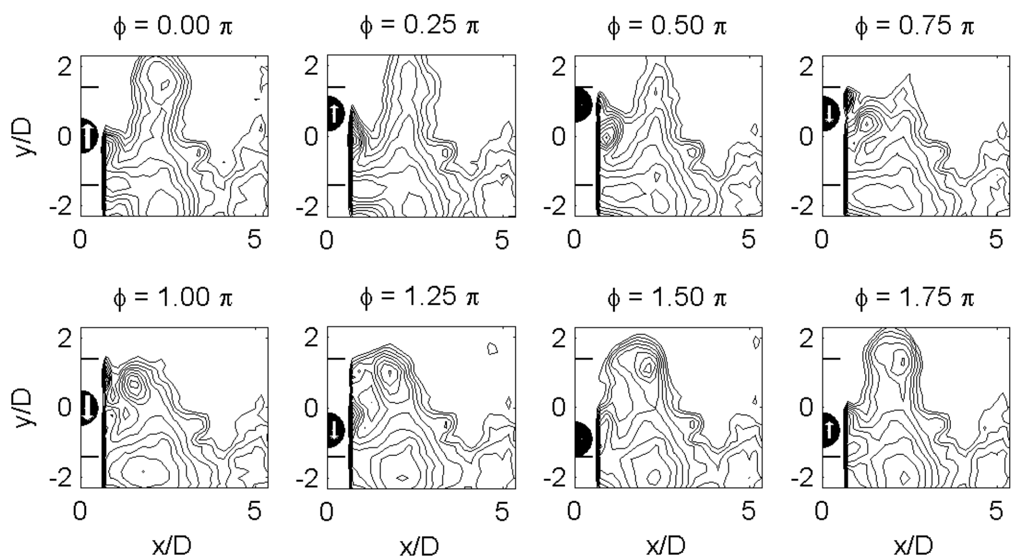

Figure 5.50: Phase-averaged normalized temperature ($(T-T_\infty)/(T_{surf}-T_\infty)$) for case S10; 1 cycle divided into 16 bins, every other bin shown; minimum contour 0.015, contour spacing 0.005

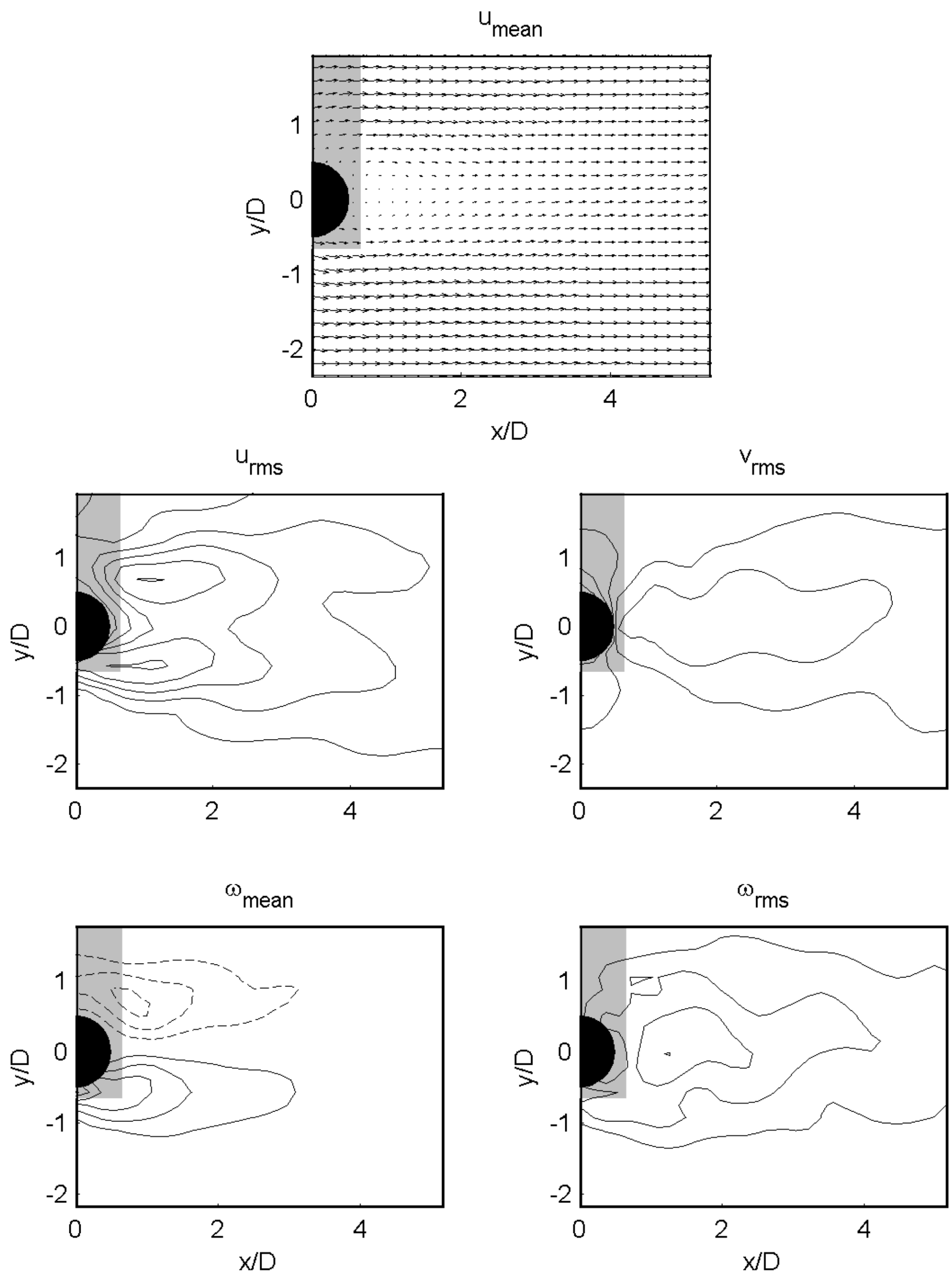

Figure 5.51: Mean and rms normalized velocity (u/U) and normalized vorticity (ωD/U) for case S11; rms velocity contours are at 0.1 intervals; vorticity contours are at 0.5 intervals, negative contours are dashed, positive contours are solid

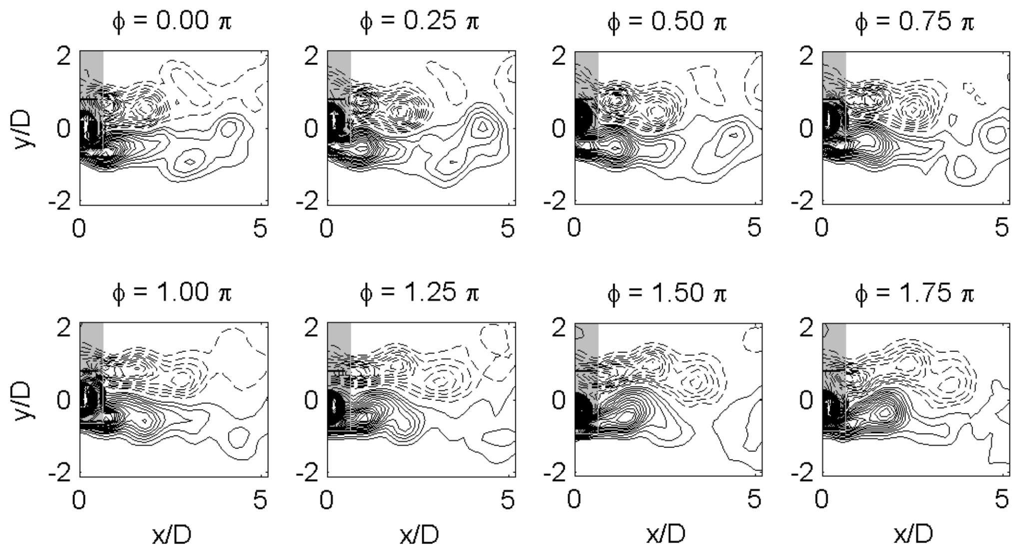

Figure 5.52: Phase-averaged normalized vorticity ($\omega D/U$) for case S11; 2 cycles divided into 32 bins, every other bin for 1st cycle shown; minimum contours ±0.2, contour spacing 0.2, positive contours solid, negative contours dashed

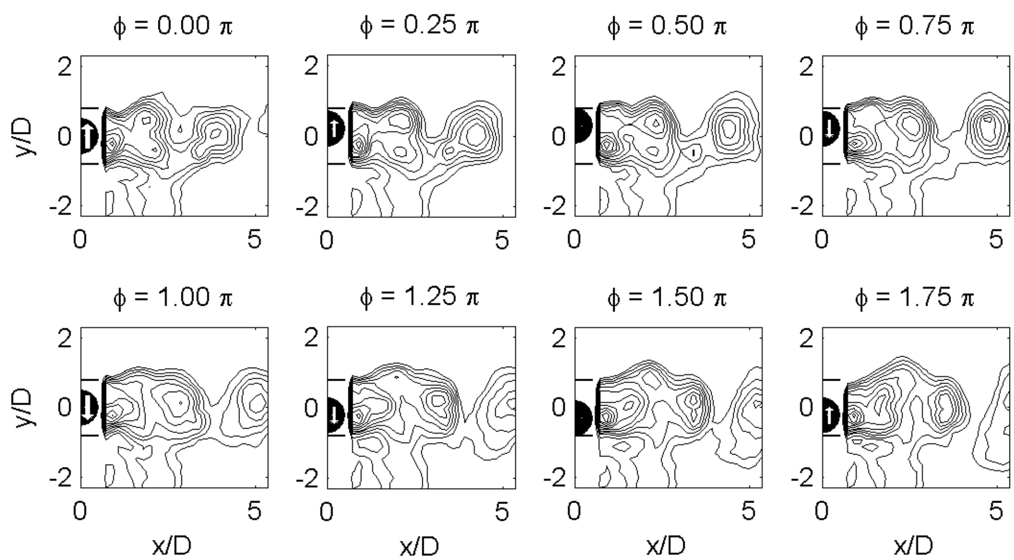

Figure 5.53: Phase-averaged normalized temperature ($(T-T_\infty)/(T_{surf}-T_\infty)$) for case S11; 2 cycles divided into 32 bins, every other bin for 1st cycle shown; minimum contour 0.015, contour spacing 0.005

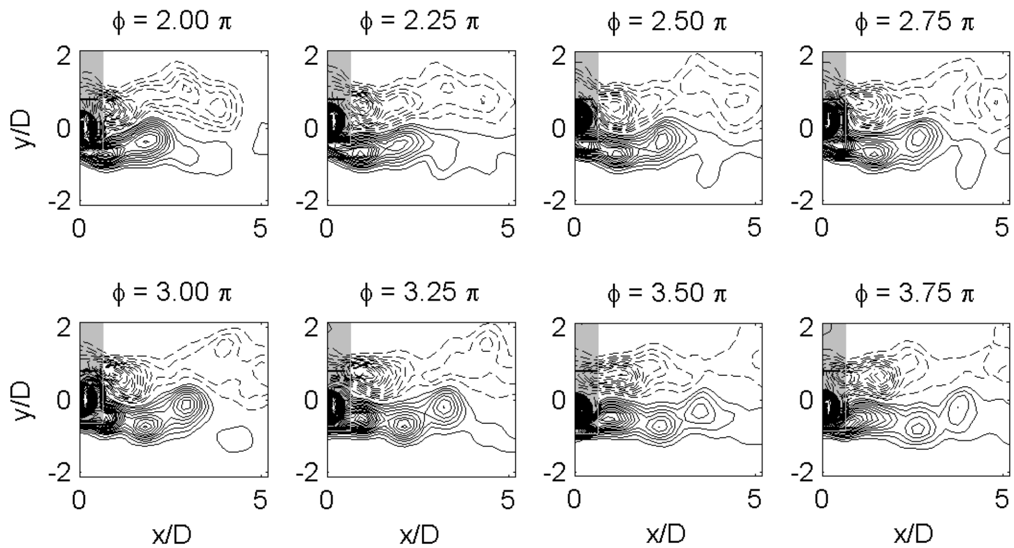

Figure 5.54: Phase-averaged normalized vorticity ($\omega D/U$) for case S11; 2 cycles divided into 32 bins, every other bin for 2nd cycle shown; minimum contours ±0.2, contour spacing 0.2, positive contours solid, negative contours dashed

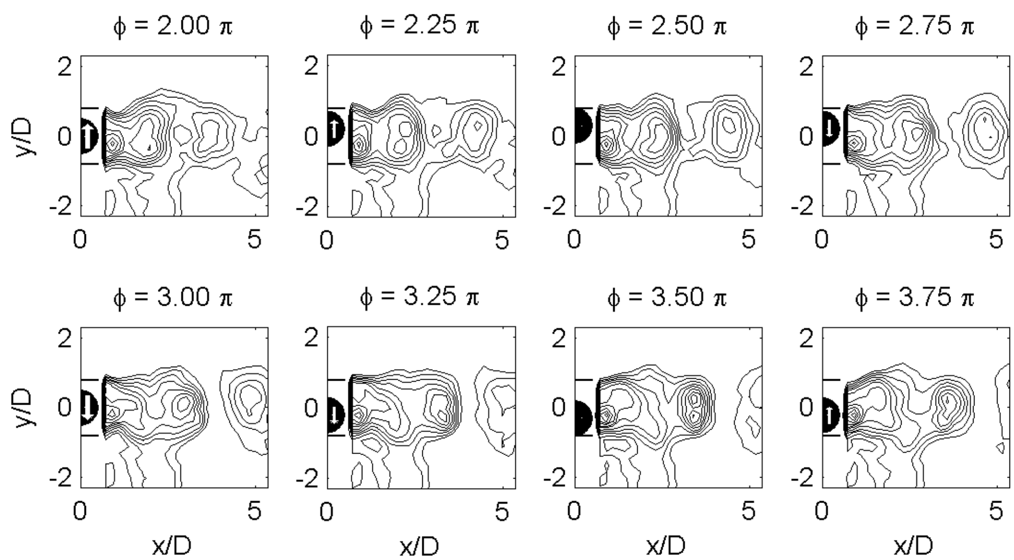

Figure 5.55: Phase-averaged normalized temperature ($(T-T_\infty)/(T_{surf}-T_\infty)$) for case S11; 2 cycles divided into 32 bins, every other bin for 2nd cycle shown; minimum contour 0.015, contour spacing 0.005

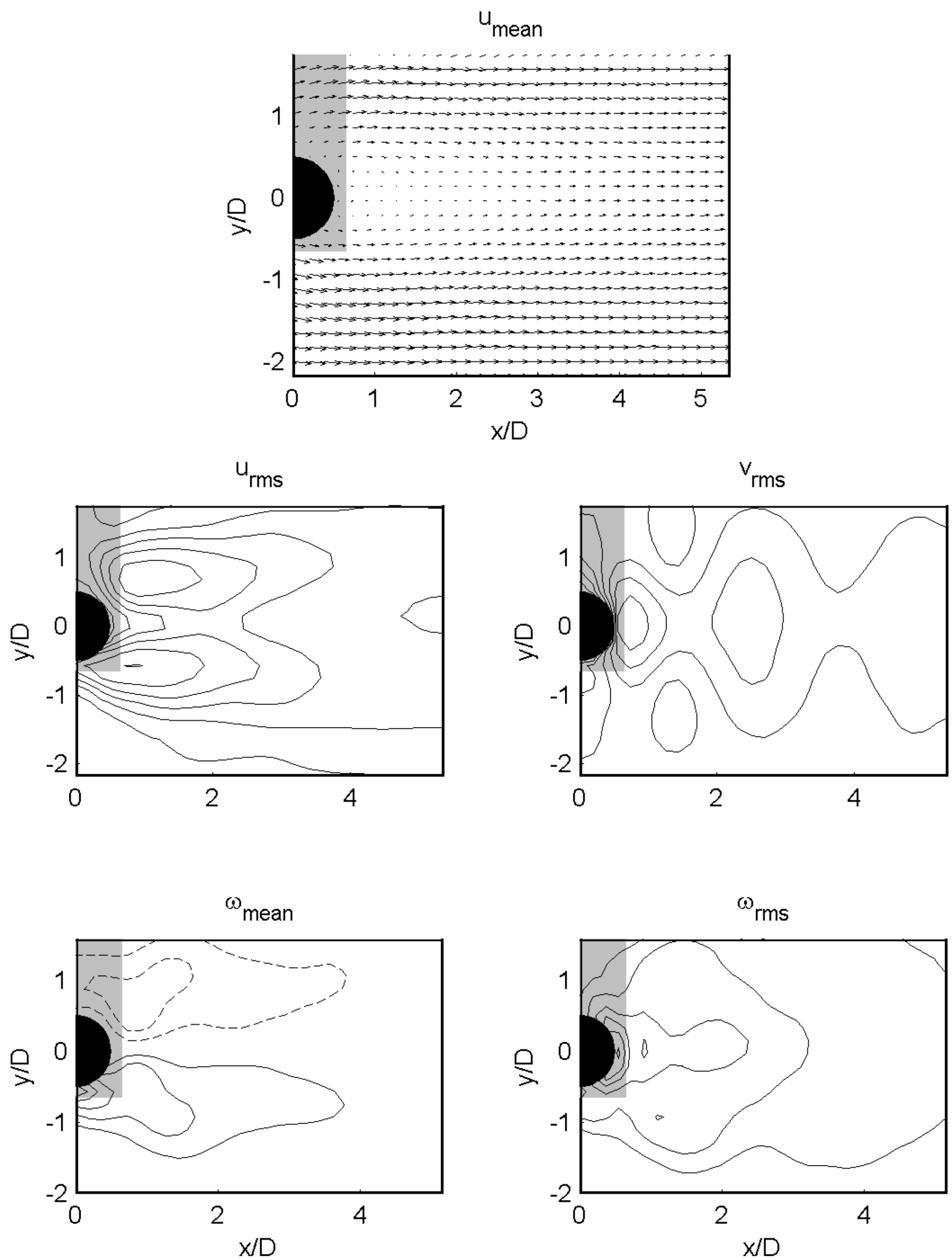

Figure 5.56: Mean and rms normalized velocity (u/U) and normalized vorticity (ωD/U) for case S12; rms velocity contours are at 0.1 intervals; vorticity contours are at 0.5 intervals, negative contours are dashed, positive contours are solid

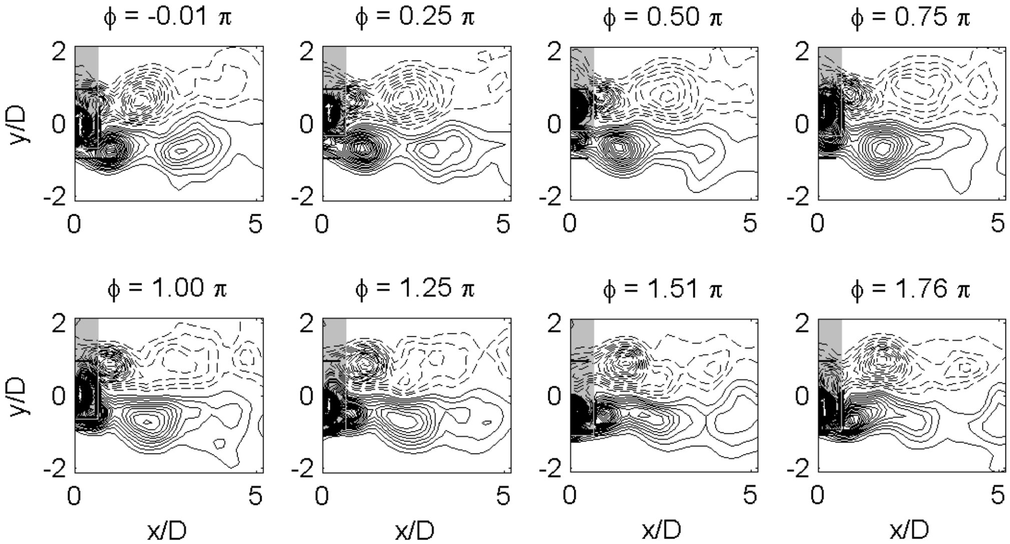

Figure 5.57: Phase-averaged normalized vorticity (ωD/U) for case S12; 2 cycles divided into 32 bins, every other bin for 1st cycle shown; minimum contours ±0.2, contour spacing 0.2, positive contours solid, negative contours dashed

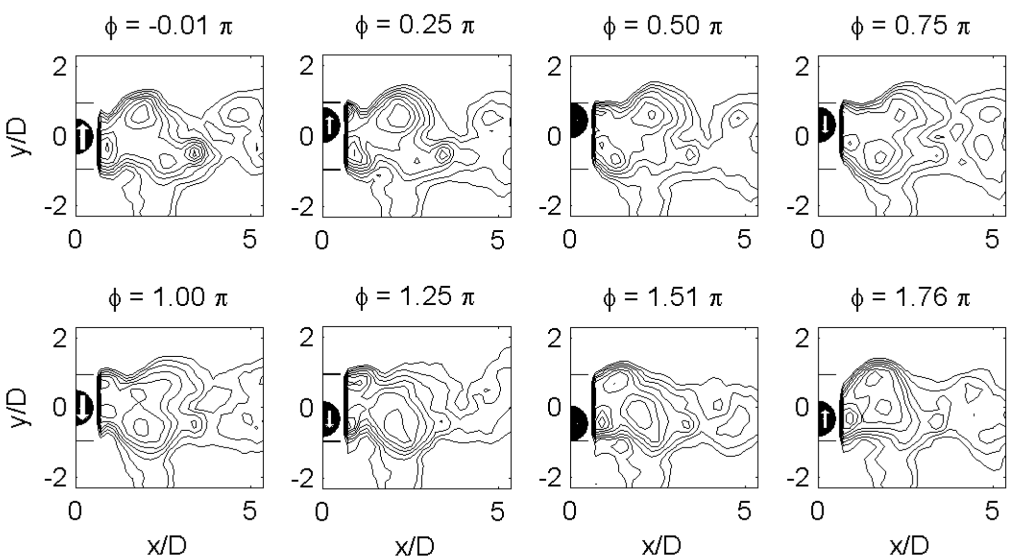

Figure 5.58: Phase-averaged normalized temperature ($(T-T_\infty)/(T_{surf}-T_\infty)$) for case S12; 2 cycles divided into 32 bins, every other bin for 1st cycle shown; minimum contour 0.015, contour spacing 0.005

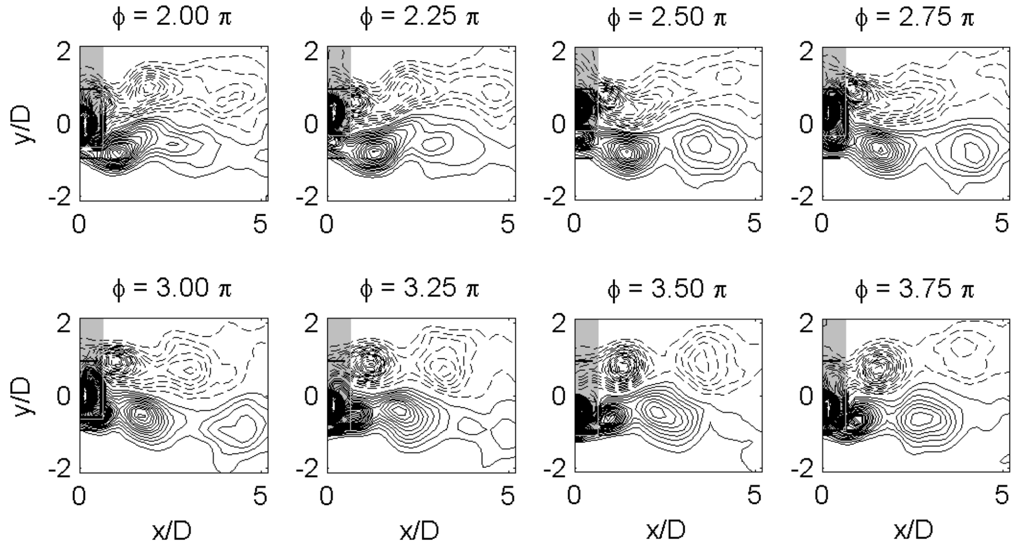

Figure 5.59: Phase-averaged normalized vorticity (ωD/U) for case S12; 2 cycles divided into 32 bins, every other bin for 2nd cycle shown; minimum contours ±0.2, contour spacing 0.2, positive contours solid, negative contours dashed

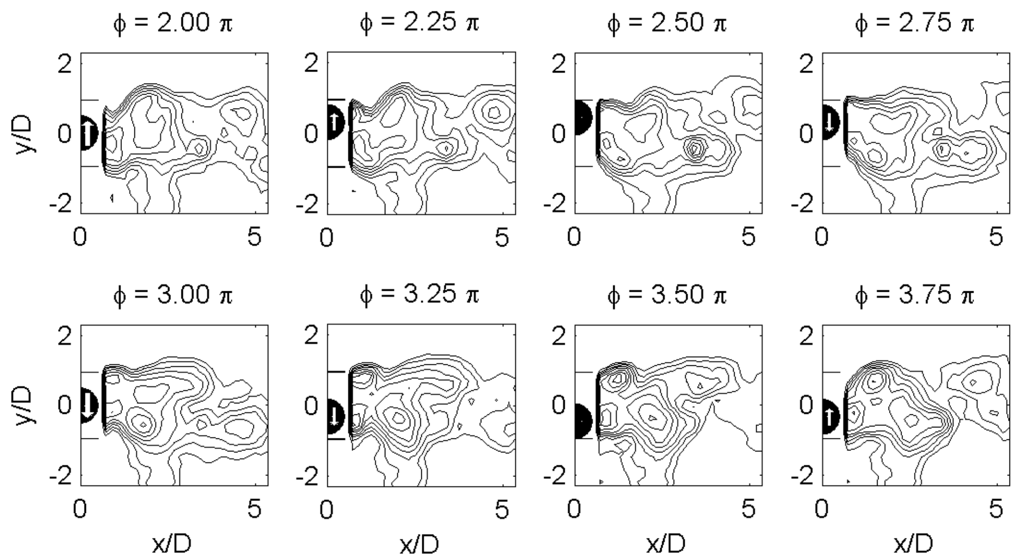

Figure 5.60: Phase-averaged normalized temperature ($(T-T_\infty)/(T_{surf}-T_\infty)$) for case S12; 2 cycles divided into 32 bins, every other bin for 2nd cycle shown; minimum contour 0.015, contour spacing 0.005

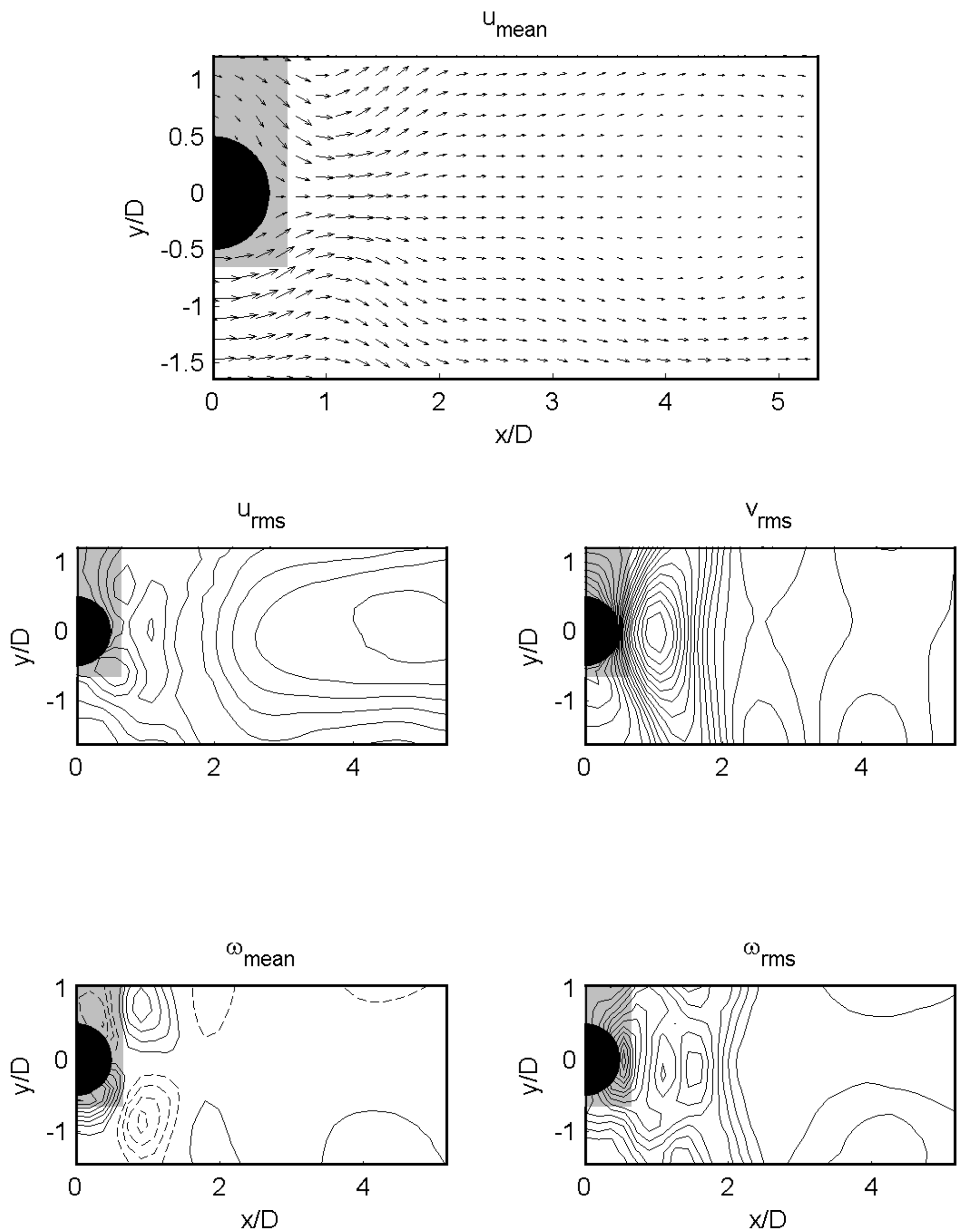

Figure 5.61: Mean and rms normalized velocity (<u>u</u>/U) and normalized vorticity (ωD/U) for case S13; rms velocity contours are at 0.1 intervals; vorticity contours are at 0.5 intervals, negative contours are dashed, positive contours are solid

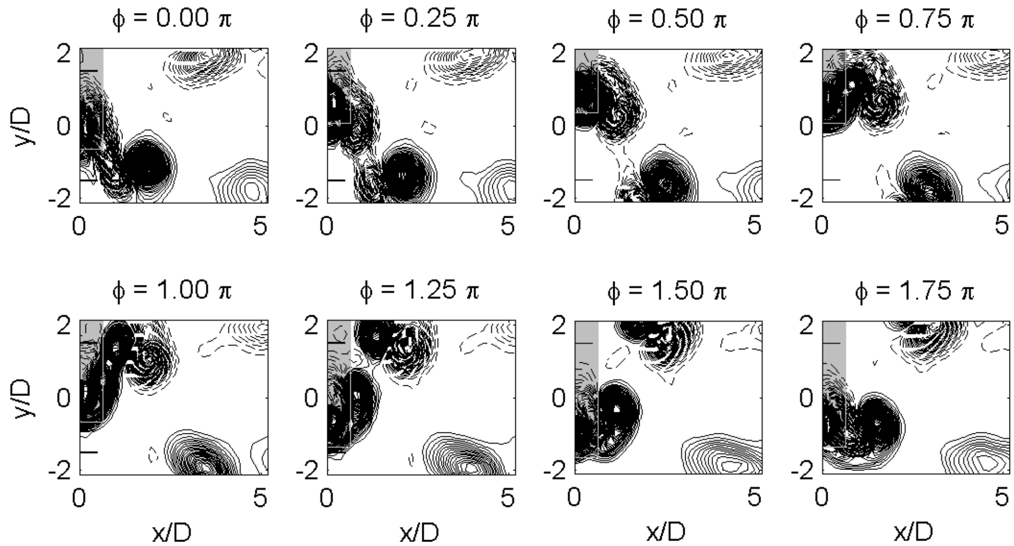

Figure 5.62: Phase-averaged normalized vorticity ($\omega D/U$) for case S13; 1 cycle divided into 16 bins, every other bin shown; minimum contours ±0.2, contour spacing 0.2, positive contours solid, negative contours dashed

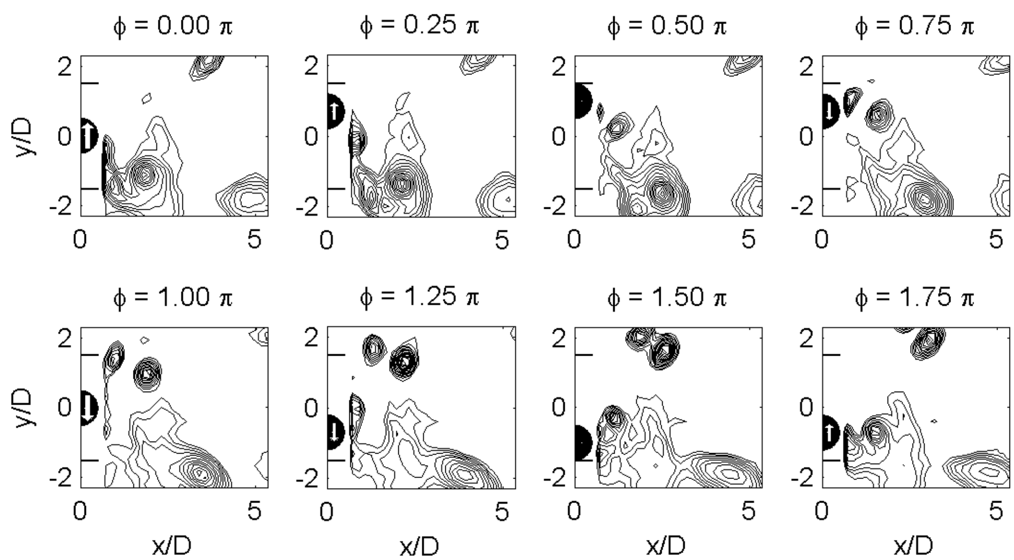

Figure 5.63: Phase-averaged normalized temperature ($(T-T_\infty)/(T_{surf}-T_\infty)$) for case S13; 1 cycle divided into 16 bins, every other bin shown; minimum contour 0.015, contour spacing 0.005

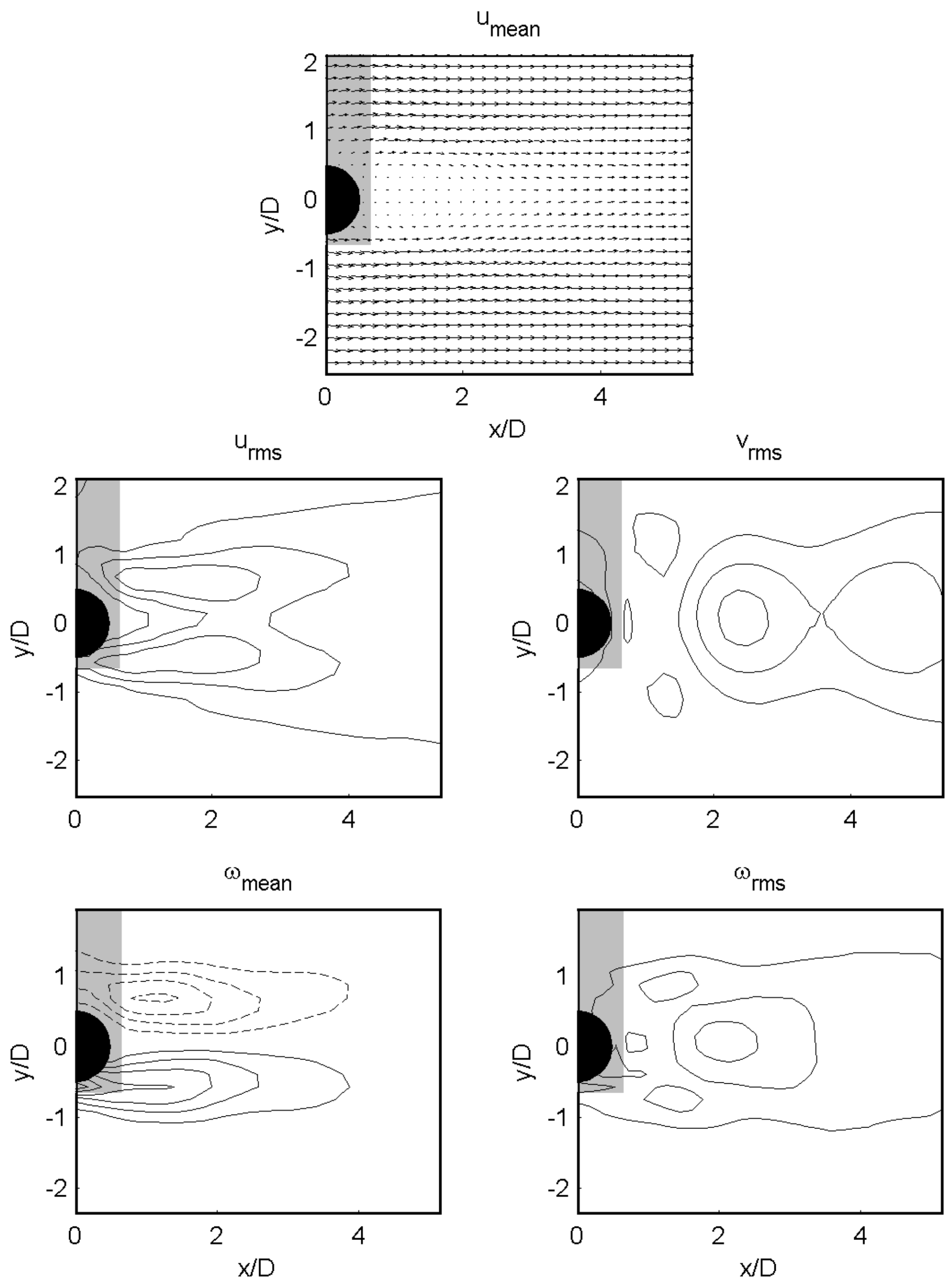

Figure 5.64: Mean and rms normalized velocity (u/U) and normalized vorticity (ωD/U) for case S14; rms velocity contours are at 0.1 intervals; vorticity contours are at 0.5 intervals, negative contours are dashed, positive contours are solid

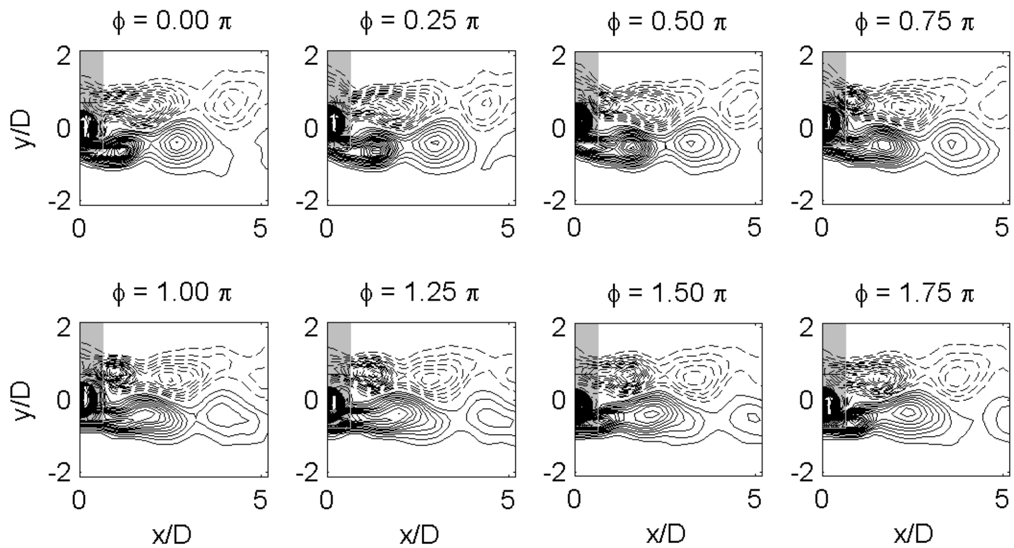

Figure 5.65: Phase-averaged normalized vorticity ($\omega D/U$) for case S14; 1 cycle divided into 16 bins, every other bin shown; minimum contours ±0.2, contour spacing 0.2, positive contours solid, negative contours dashed

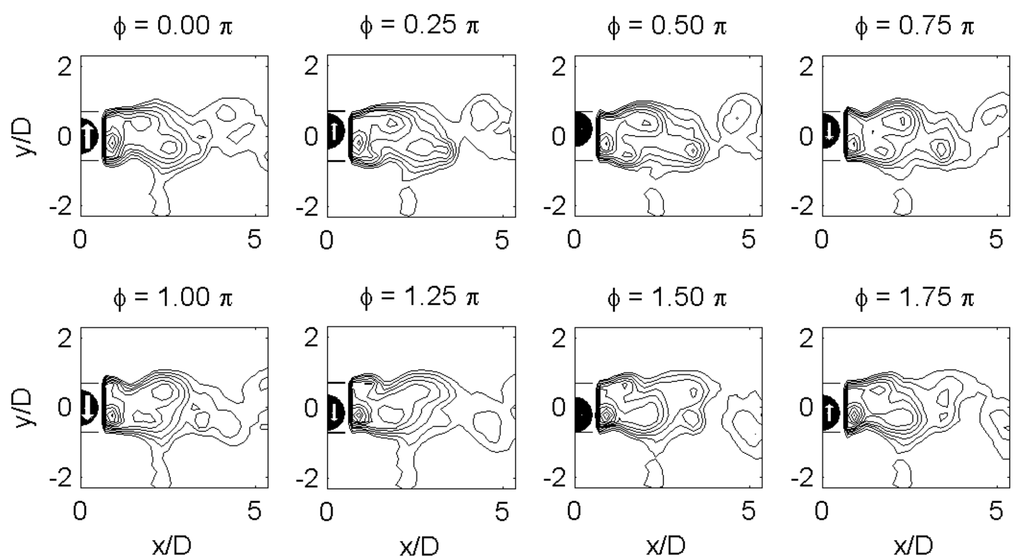

Figure 5.66: Phase-averaged normalized temperature ($(T-T_\infty)/(T_{surf}-T_\infty)$) for case S14; 1 cycle divided into 16 bins, every other bin shown; minimum contour 0.015, contour spacing 0.005

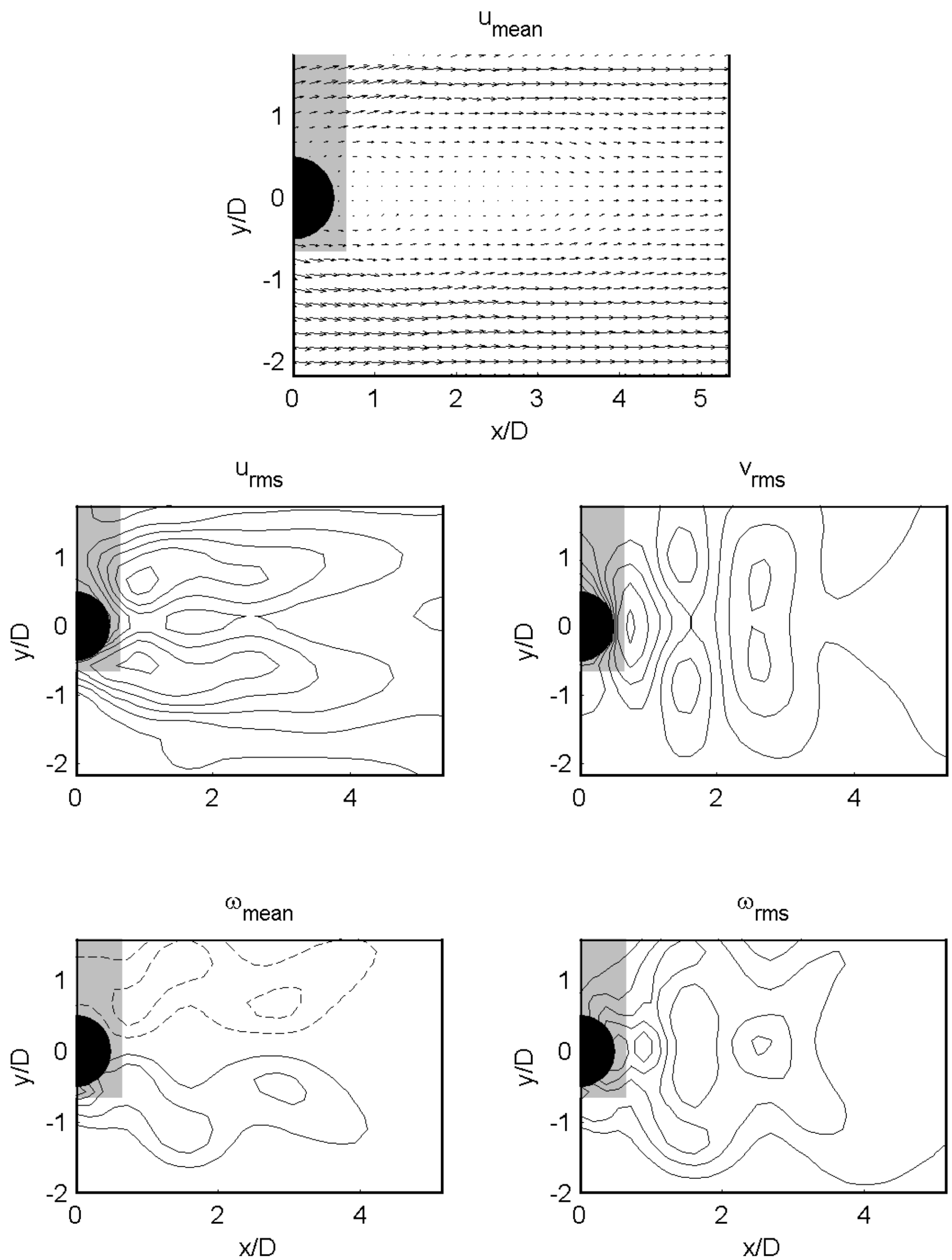

Figure 5.67: Mean and rms normalized velocity (u/U) and normalized vorticity (ωD/U) for case S15; rms velocity contours are at 0.1 intervals; vorticity contours are at 0.5 intervals, negative contours are dashed, positive contours are solid

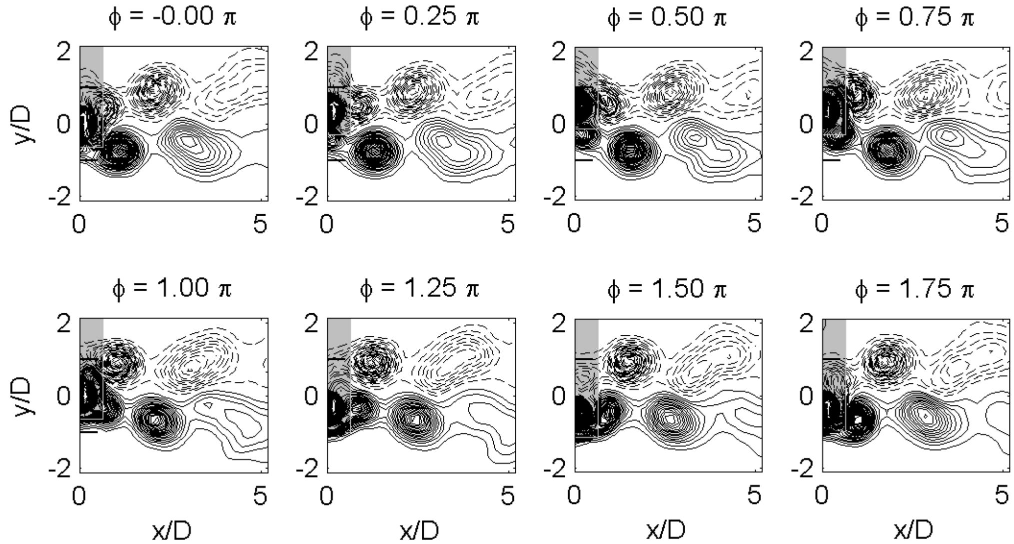

Figure 5.68: Phase-averaged normalized vorticity (ωD/U) for case S15; 1 cycle divided into 16 bins, every other bin shown; minimum contours ±0.2, contour spacing 0.2, positive contours solid, negative contours dashed

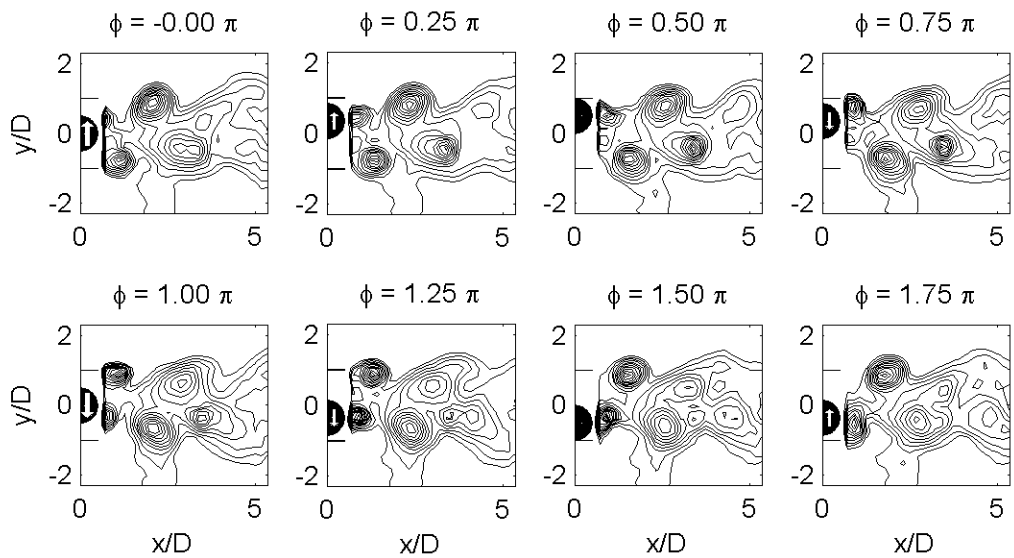

Figure 5.69: Phase-averaged normalized temperature ($(T-T_\infty)/(T_{surf}-T_\infty)$) for case S15; 1 cycle divided into 16 bins, every other bin shown; minimum contour 0.015, contour spacing 0.005

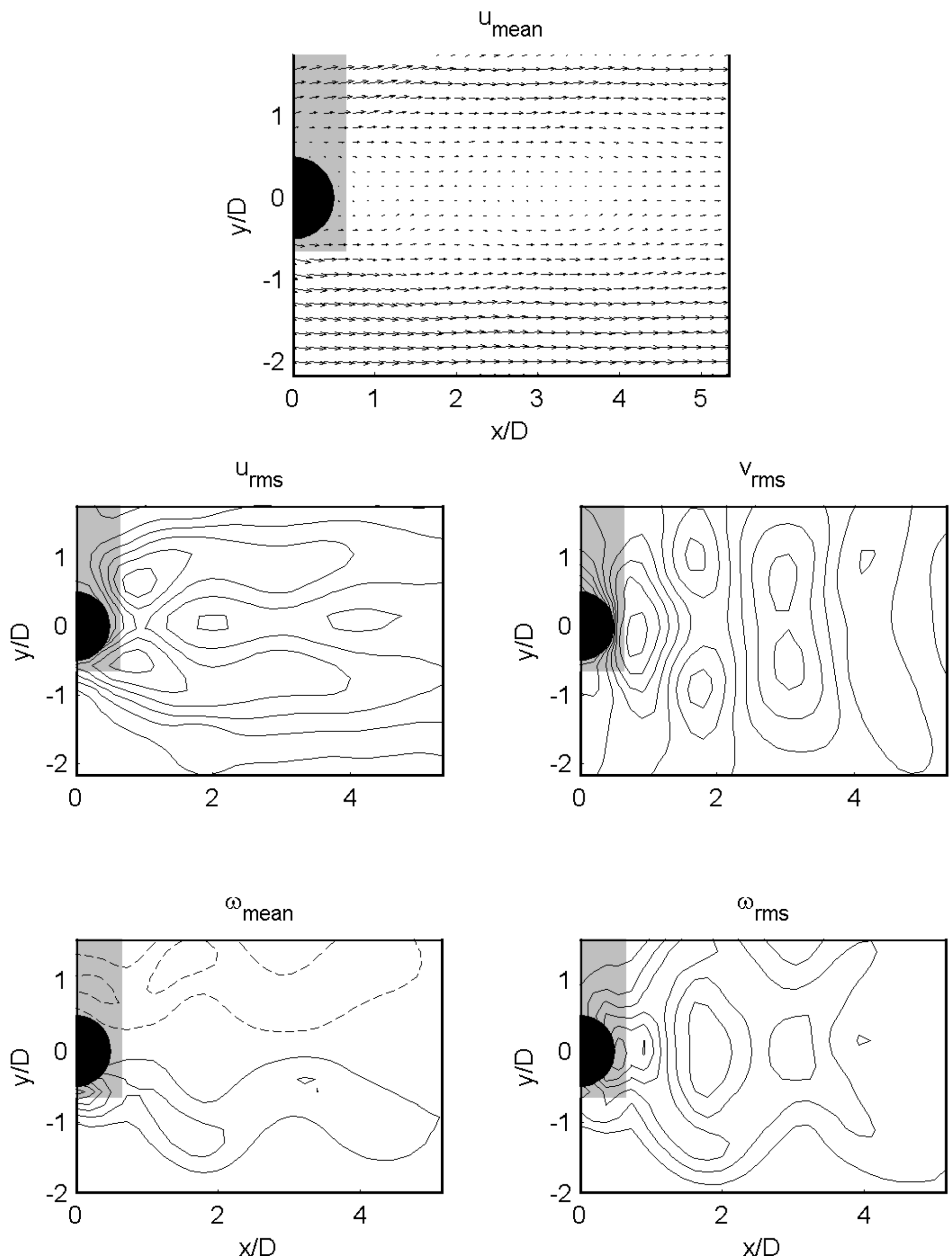

Figure 5.70: Mean and rms normalized velocity (u/U) and normalized vorticity (ωD/U) for case S16; rms velocity contours are at 0.1 intervals; vorticity contours are at 0.5 intervals, negative contours are dashed, positive contours are solid

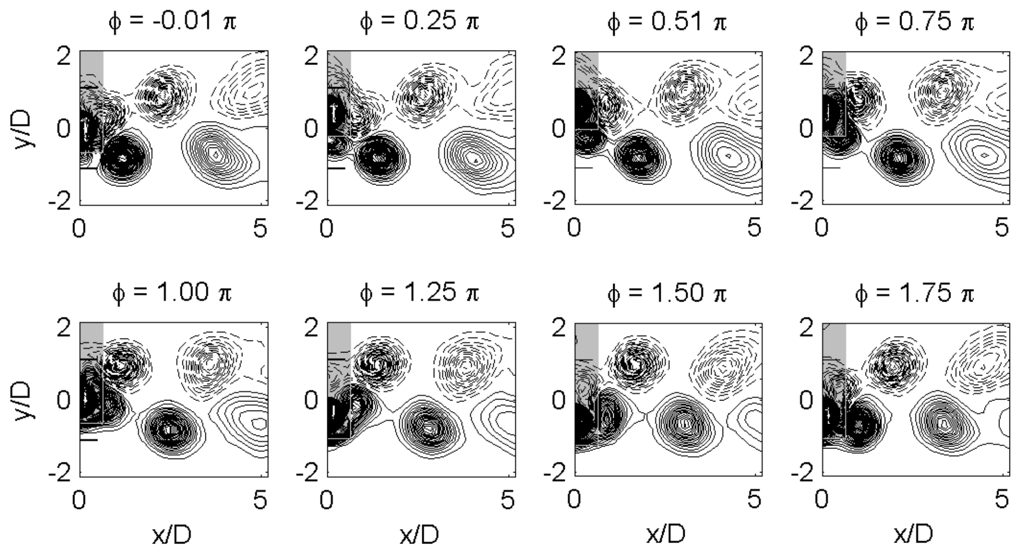

Figure 5.71: Phase-averaged normalized vorticity ($\omega D/U$) for case S16; 1 cycle divided into 16 bins, every other bin shown; minimum contours ±0.2, contour spacing 0.2, positive contours solid, negative contours dashed

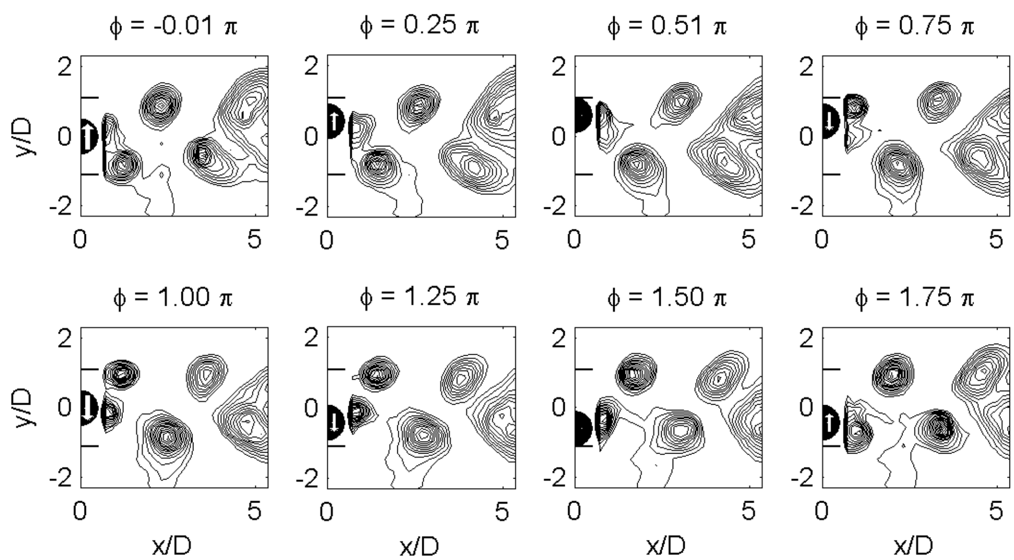

Figure 5.72: Phase-averaged normalized temperature ($(T-T_\infty)/(T_{surf}- T_\infty)$) for case S16; 1 cycle divided into 16 bins, every other bin shown; minimum contour 0.015, contour spacing 0.005

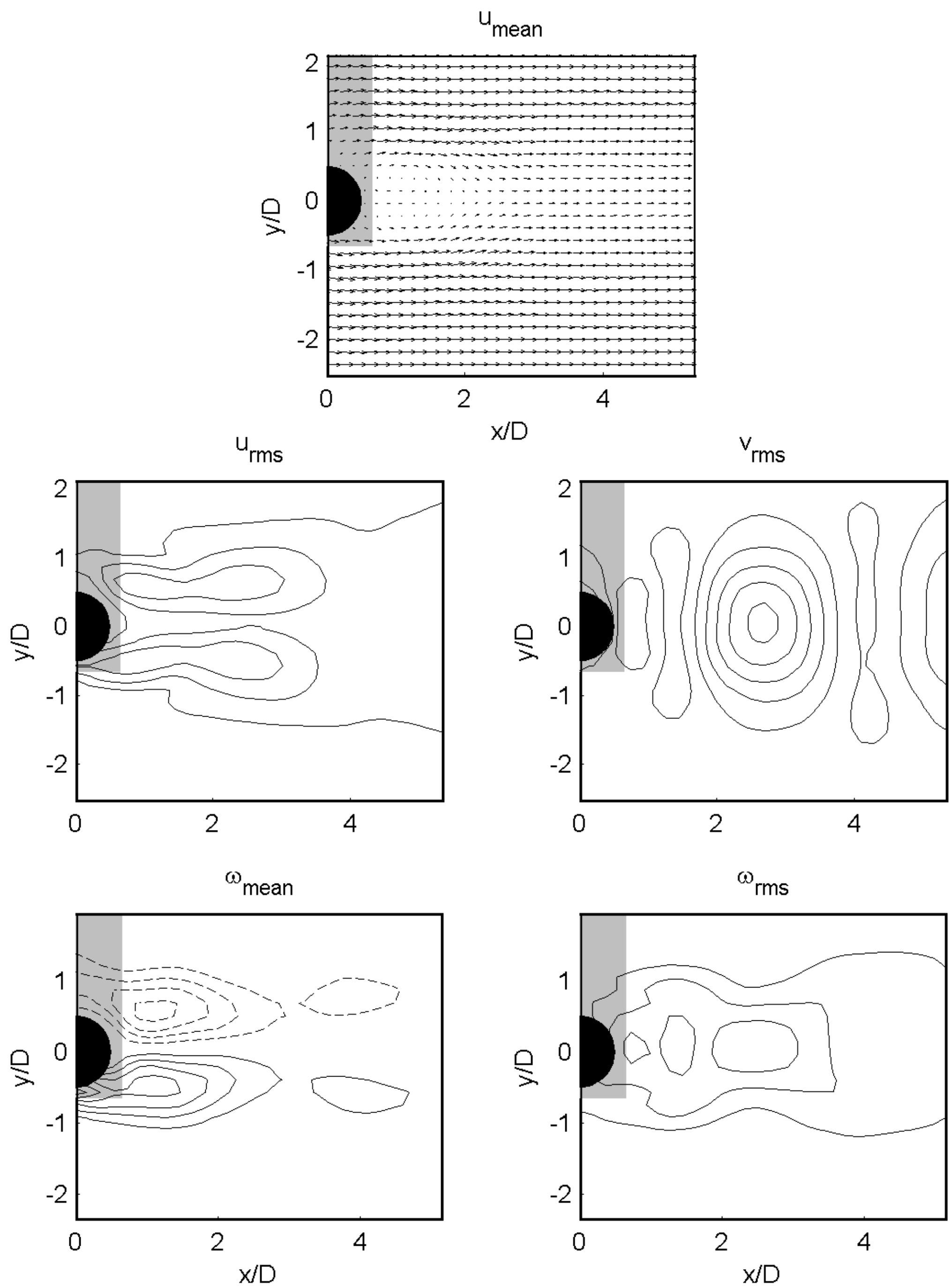

Figure 5.73: Mean and rms normalized velocity (u/U) and normalized vorticity (ωD/U) for case S17; rms velocity contours are at 0.1 intervals; vorticity contours are at 0.5 intervals, negative contours are dashed, positive contours are solid

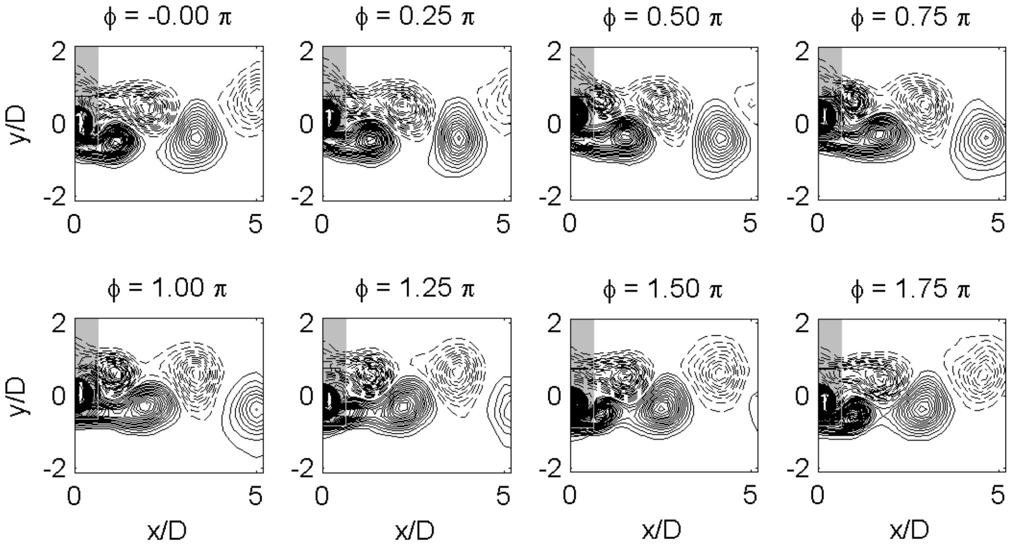

Figure 5.74: Phase-averaged normalized vorticity (ωD/U) for case S17; 1 cycle divided into 16 bins, every other bin shown; minimum contours ±0.2, contour spacing 0.2, positive contours solid, negative contours dashed

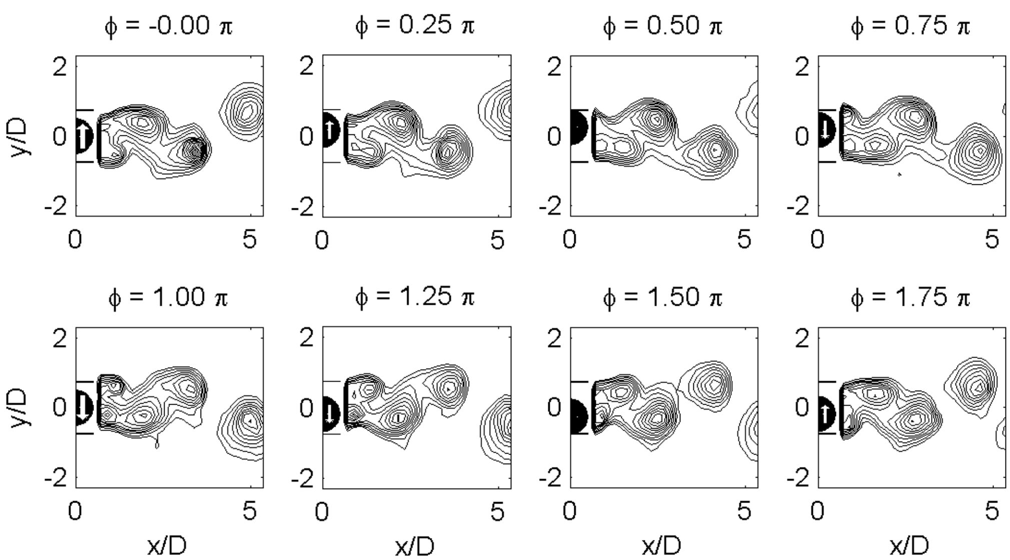

Figure 5.75: Phase-averaged normalized temperature ($(T-T_\infty)/(T_{surf}-T_\infty)$) for case S17; 1 cycle divided into 16 bins, every other bin shown; minimum contour 0.015, contour spacing 0.005

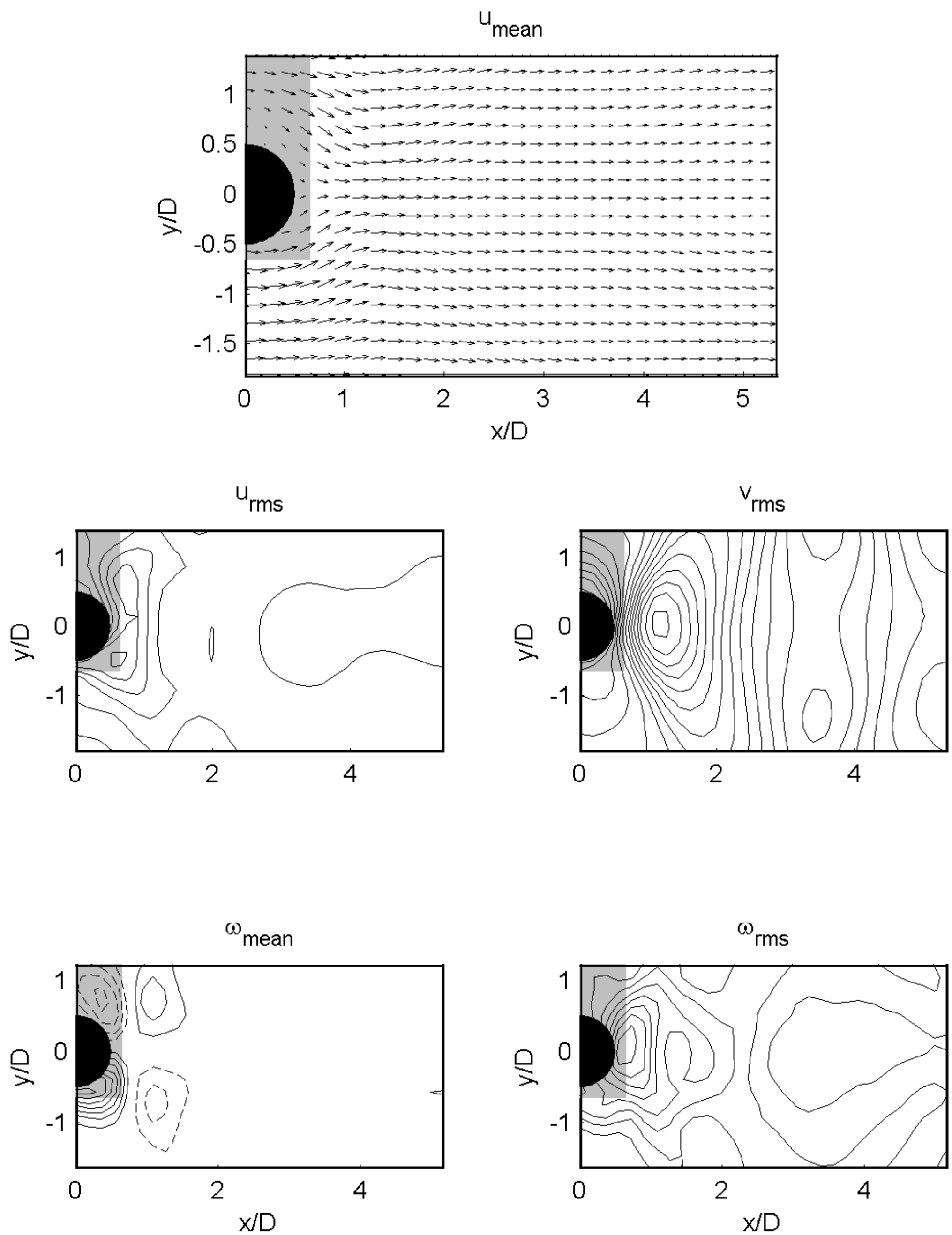

Figure 5.76: Mean and rms normalized velocity (u/U) and normalized vorticity (ωD/U) for case S18; rms velocity contours are at 0.1 intervals; vorticity contours are at 0.5 intervals, negative contours are dashed, positive contours are solid

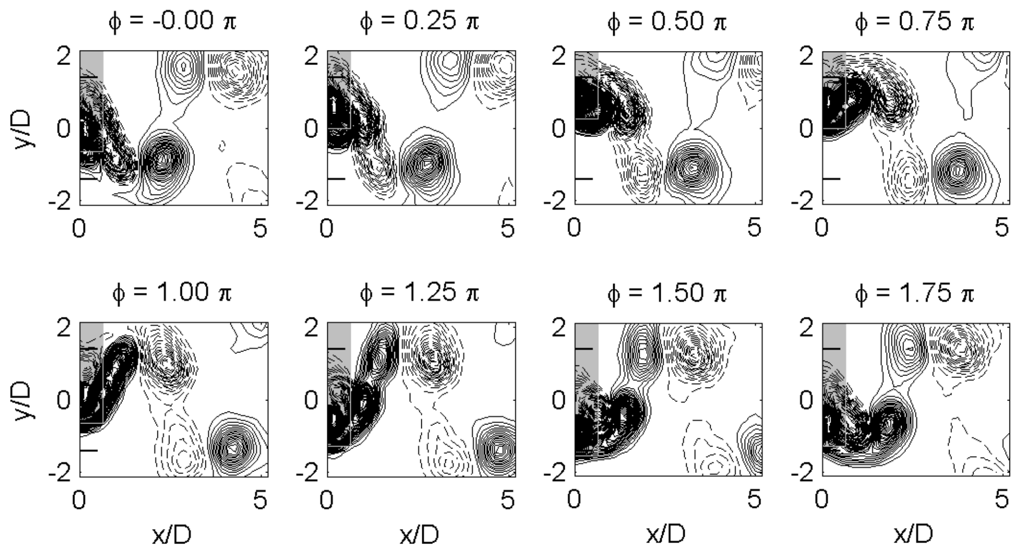

Figure 5.77: Phase-averaged normalized vorticity ($\omega D/U$) for case S18; 1 cycle divided into 16 bins, every other bin shown; minimum contours ±0.2, contour spacing 0.2, positive contours solid, negative contours dashed

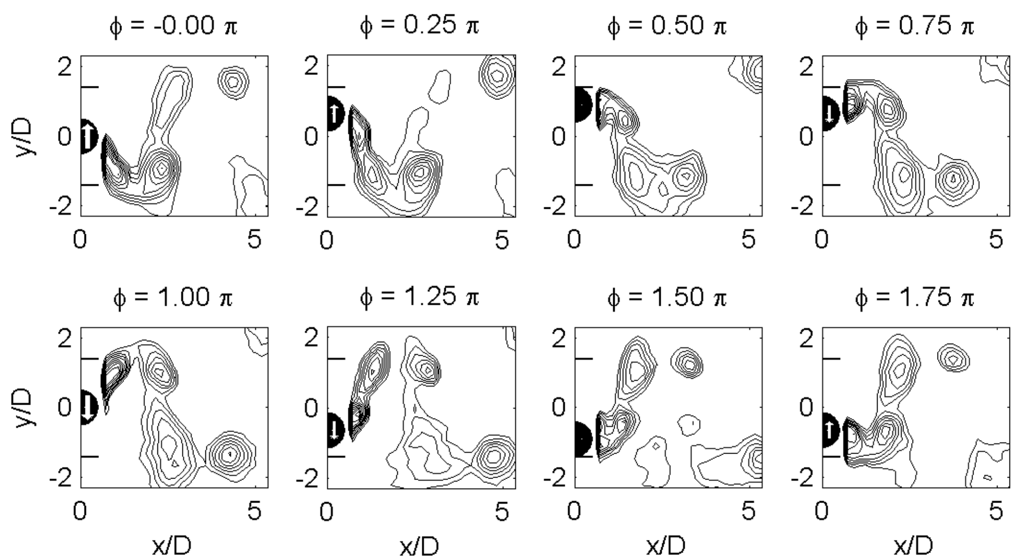

Figure 5.78: Phase-averaged normalized temperature ($(T-T_\infty)/(T_{surf}-T_\infty)$) for case S18; 1 cycle divided into 16 bins, every other bin shown; minimum contour 0.015, contour spacing 0.005

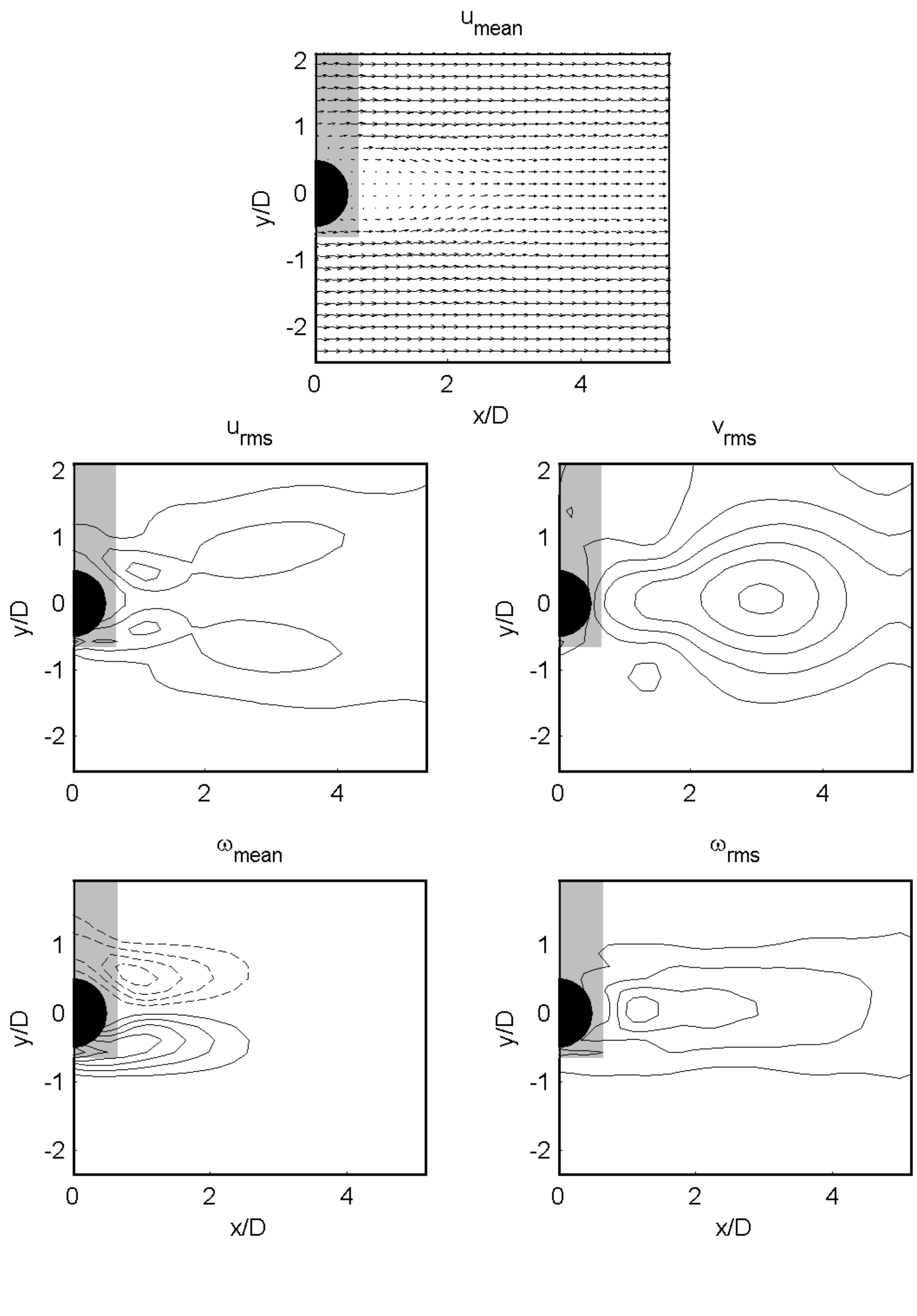

Figure 5.79: Mean and rms normalized velocity (u/U) and normalized vorticity (ωD/U) for case S19; rms velocity contours are at 0.1 intervals; vorticity contours are at 0.5 intervals, negative contours are dashed, positive contours are solid

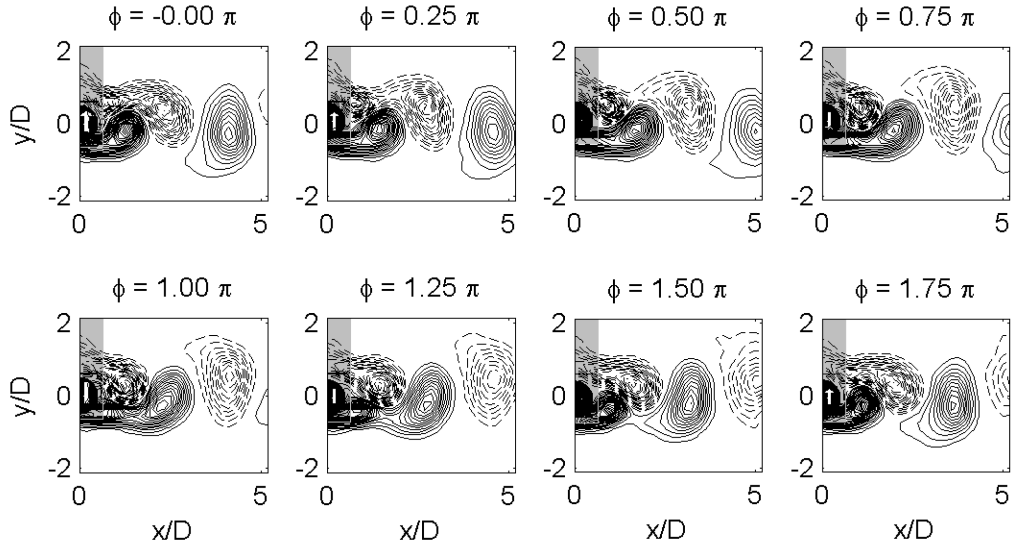

Figure 5.80: Phase-averaged normalized vorticity ($\omega D/U$) for case S19; 1 cycle divided into 16 bins, every other bin shown; minimum contours ±0.2, contour spacing 0.2, positive contours solid, negative contours dashed

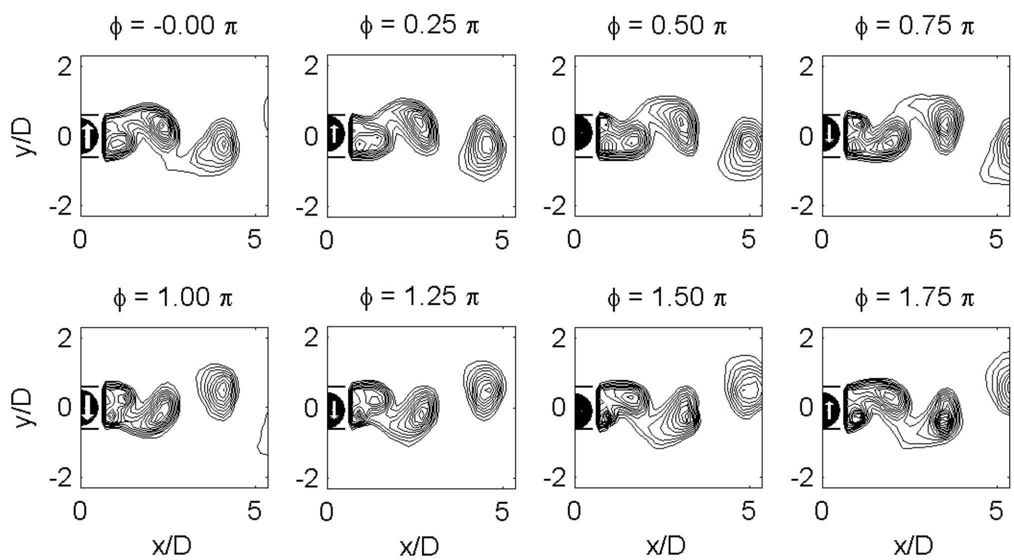

Figure 5.81: Phase-averaged normalized temperature ($(T-T_\infty)/(T_{surf}-T_\infty)$) for case S19; 1 cycle divided into 16 bins, every other bin shown; minimum contour 0.015, contour spacing 0.005

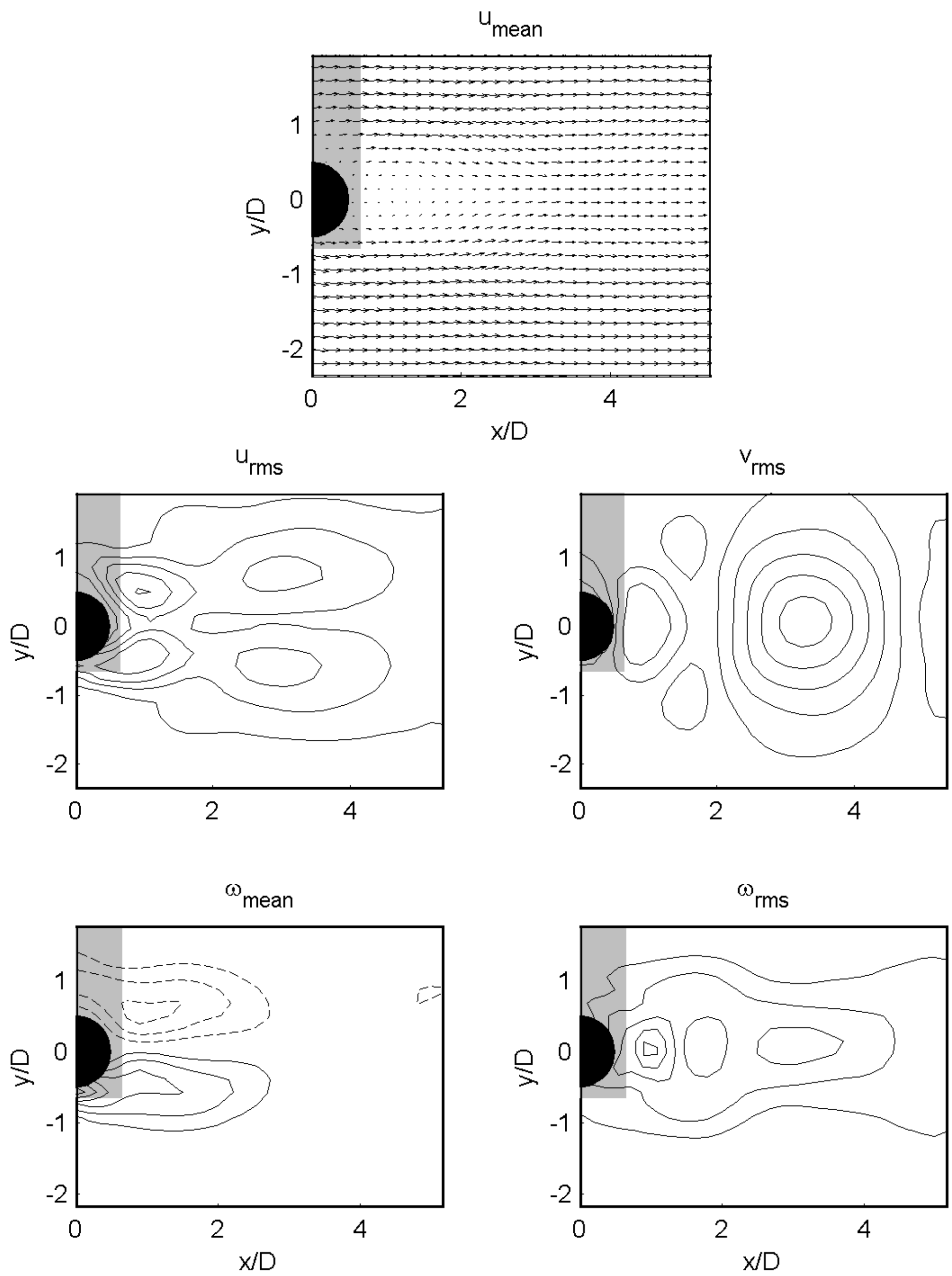

Figure 5.82: Mean and rms normalized velocity (u/U) and normalized vorticity (ωD/U) for case S20; rms velocity contours are at 0.1 intervals; vorticity contours are at 0.5 intervals, negative contours are dashed, positive contours are solid

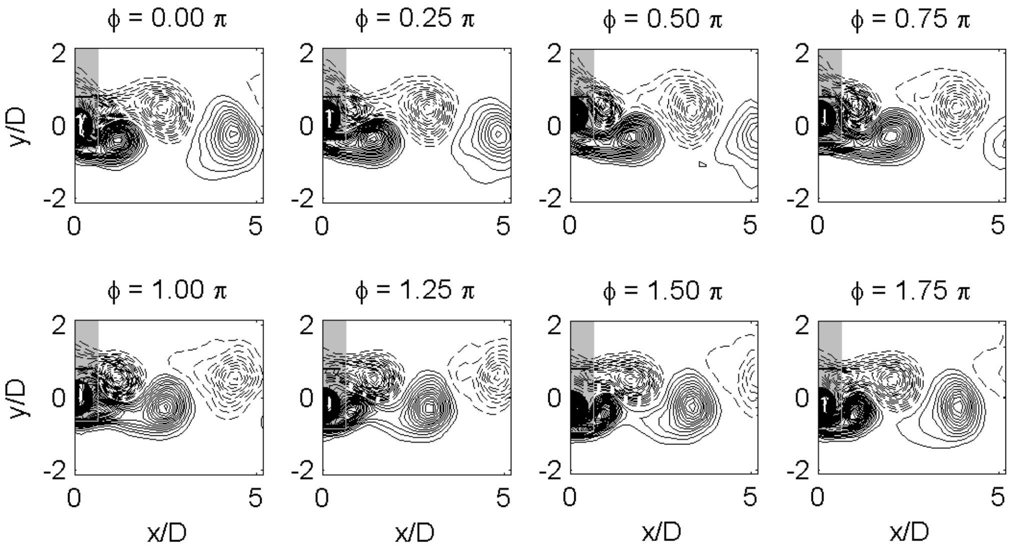

Figure 5.83: Phase-averaged normalized vorticity ($\omega D/U$) for case S20; 1 cycle divided into 16 bins, every other bin shown; minimum contours ±0.2, contour spacing 0.2, positive contours solid, negative contours dashed

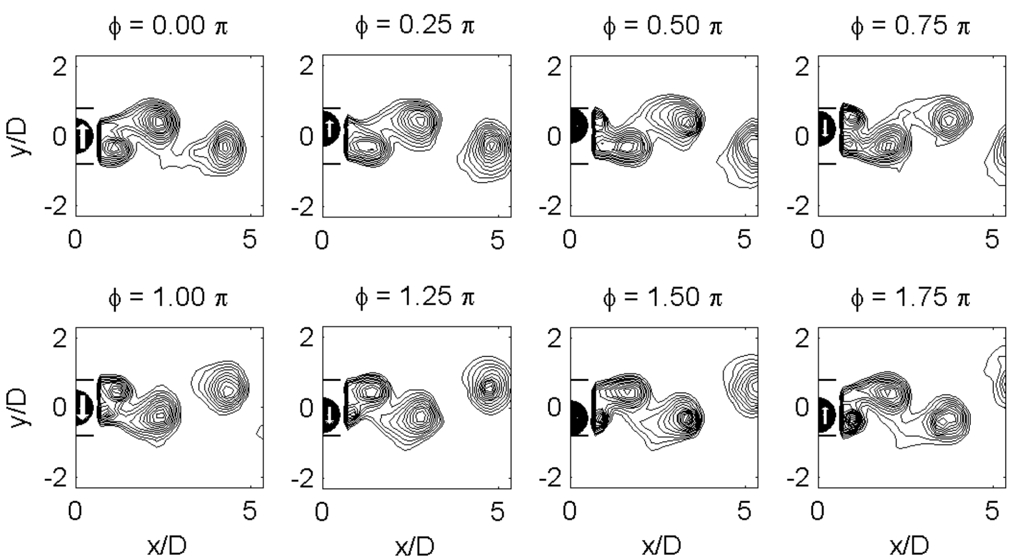

Figure 5.84: Phase-averaged normalized temperature ($(T-T_\infty)/(T_{surf}-T_\infty)$) for case S20; 1 cycle divided into 16 bins, every other bin shown; minimum contour 0.015, contour spacing 0.005

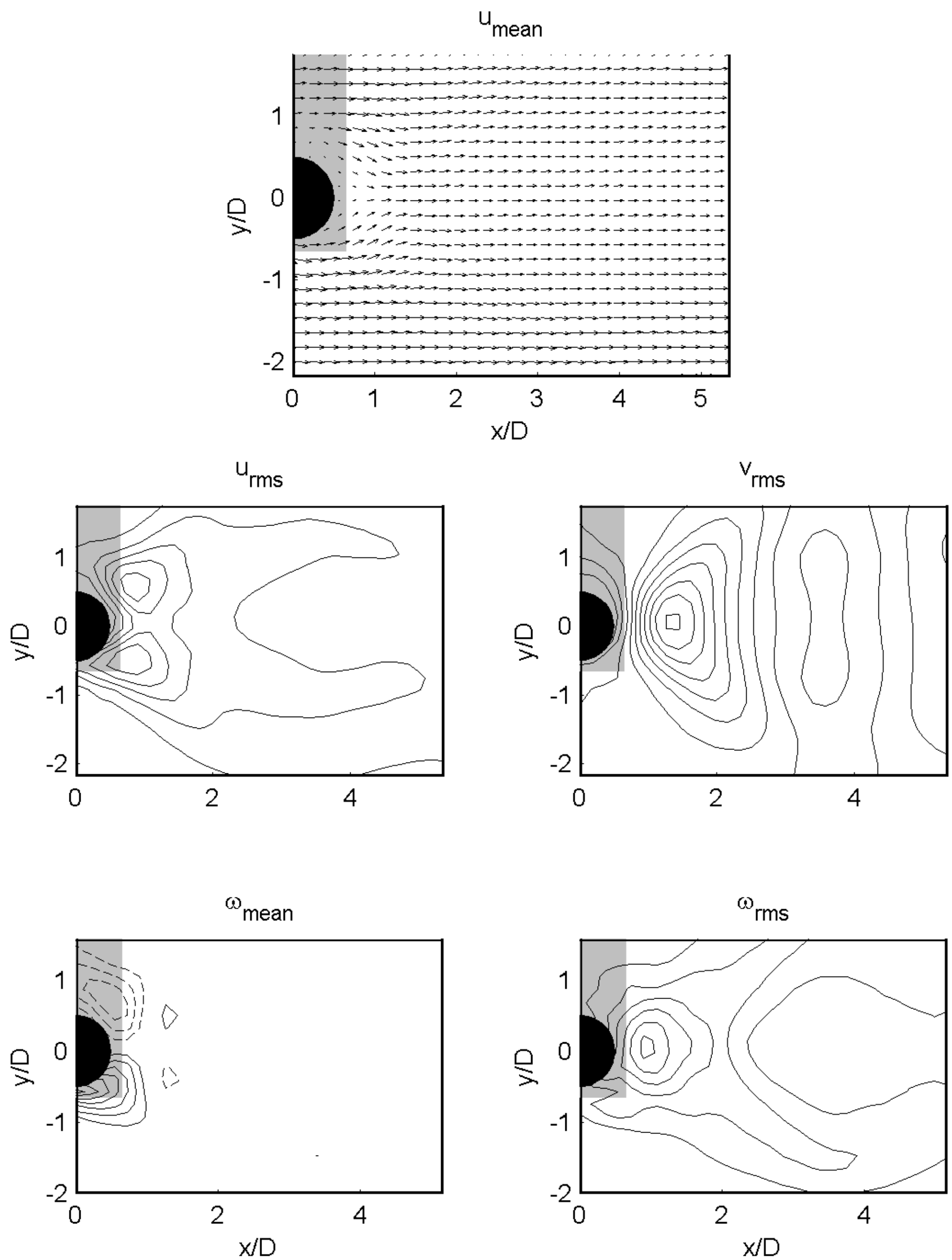

Figure 5.85: Mean and rms normalized velocity (u/U) and normalized vorticity (ωD/U) for case S21; rms velocity contours are at 0.1 intervals; vorticity contours are at 0.5 intervals, negative contours are dashed, positive contours are solid

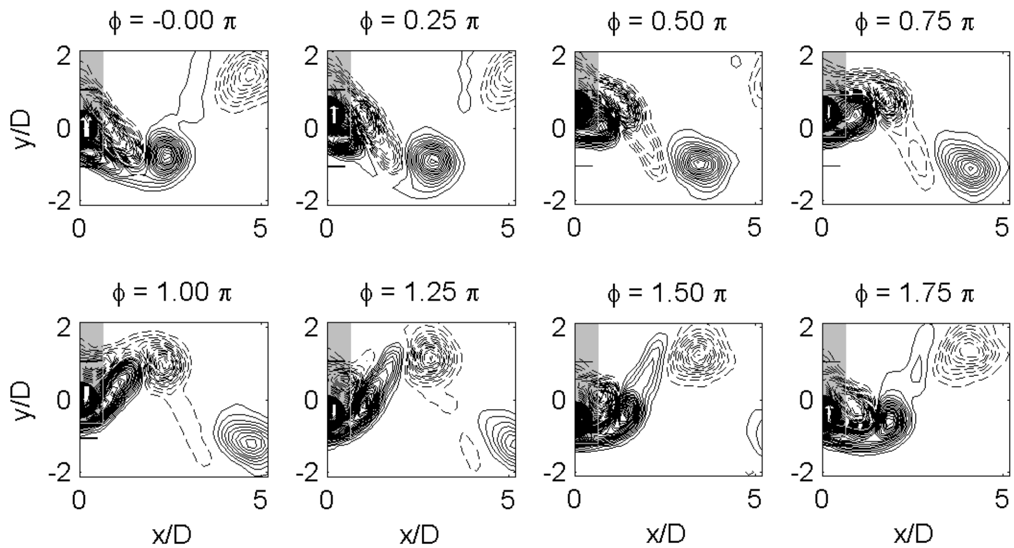

Figure 5.86: Phase-averaged normalized vorticity ($\omega D/U$) for case S21; 1 cycle divided into 16 bins, every other bin shown; minimum contours ±0.2, contour spacing 0.2, positive contours solid, negative contours dashed

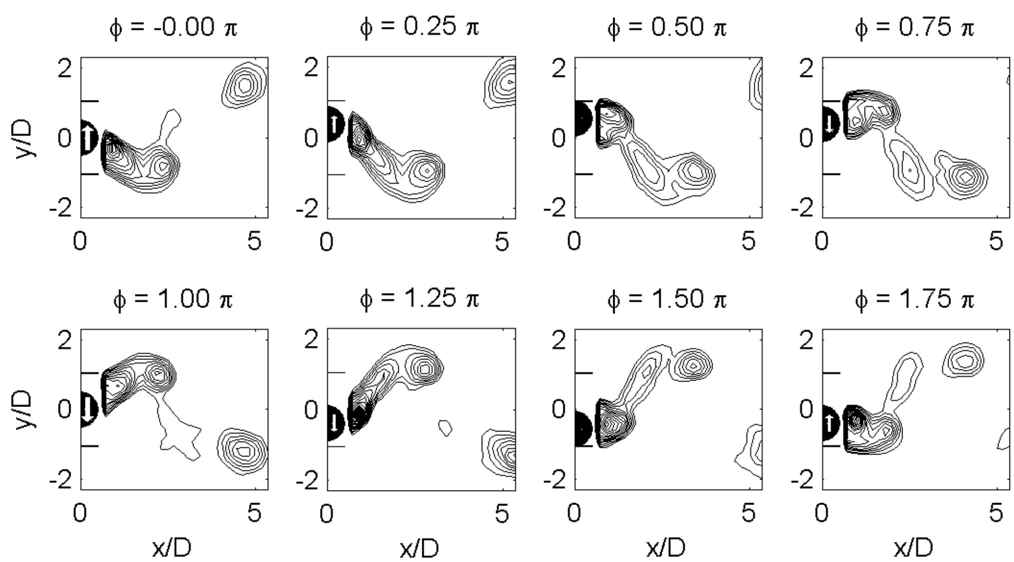

Figure 5.87: Phase-averaged normalized temperature ($(T-T_\infty)/(T_{surf}- T_\infty)$) for case S21; 1 cycle divided into 16 bins, every other bin shown; minimum contour 0.015, contour spacing 0.005

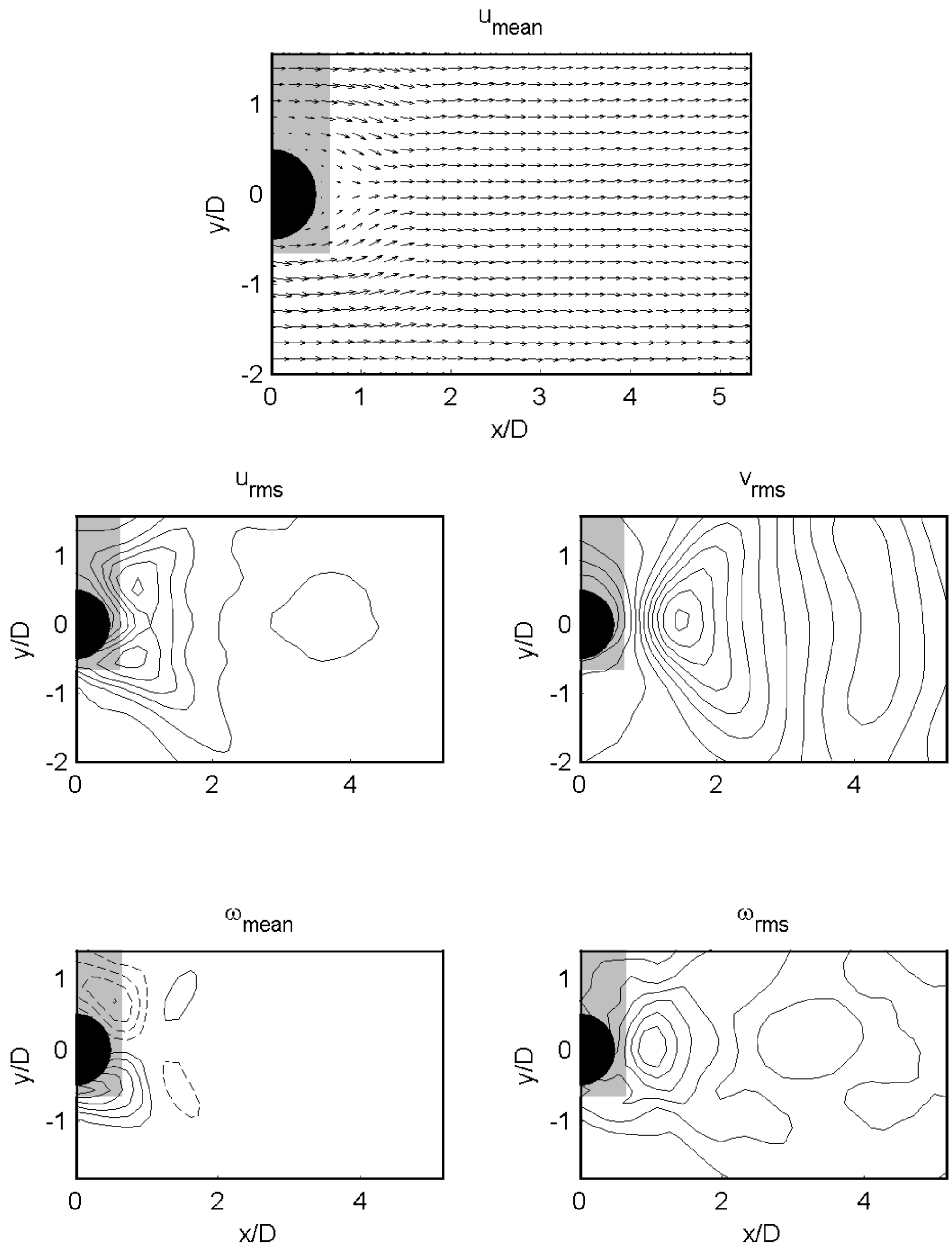

Figure 5.88: Mean and rms normalized velocity (u/U) and normalized vorticity (ωD/U) for case S22; rms velocity contours are at 0.1 intervals; vorticity contours are at 0.5 intervals, negative contours are dashed, positive contours are solid

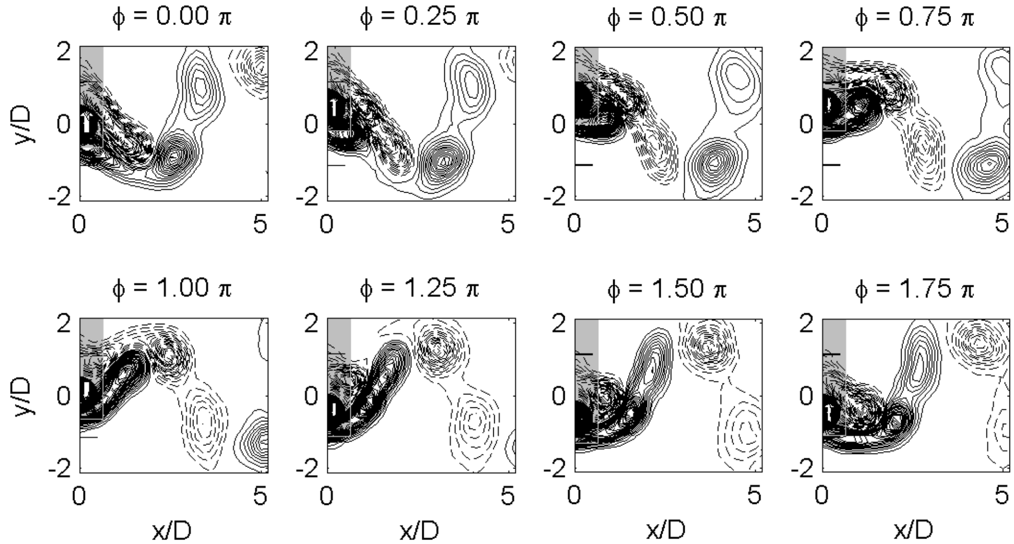

Figure 5.89: Phase-averaged normalized vorticity (ωD/U) for case S22; 1 cycle divided into 16 bins, every other bin shown; minimum contours ±0.2, contour spacing 0.2, positive contours solid, negative contours dashed

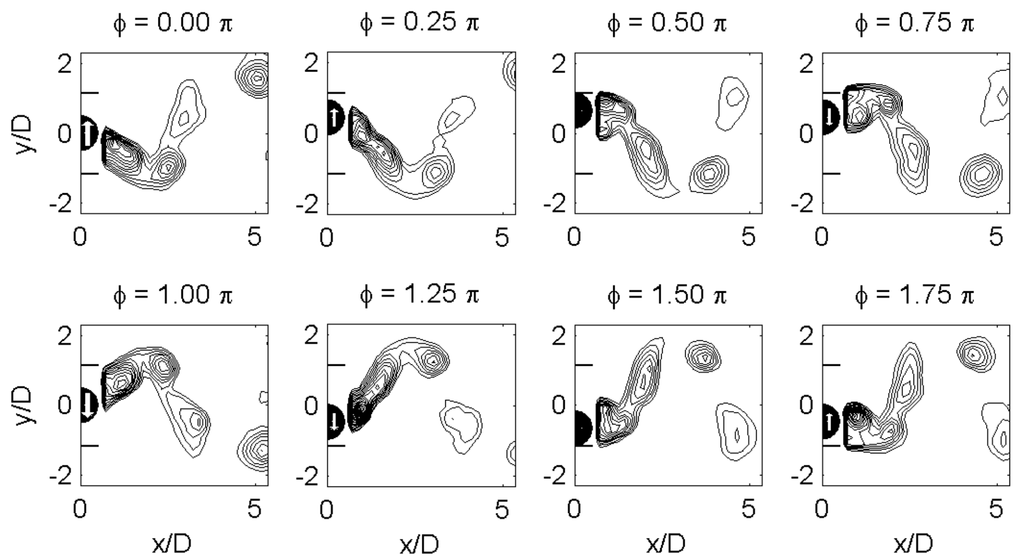

Figure 5.90: Phase-averaged normalized temperature ($(T-T_\infty)/(T_{surf}-T_\infty)$) for case S22; 1 cycle divided into 16 bins, every other bin shown; minimum contour 0.015, contour spacing 0.005

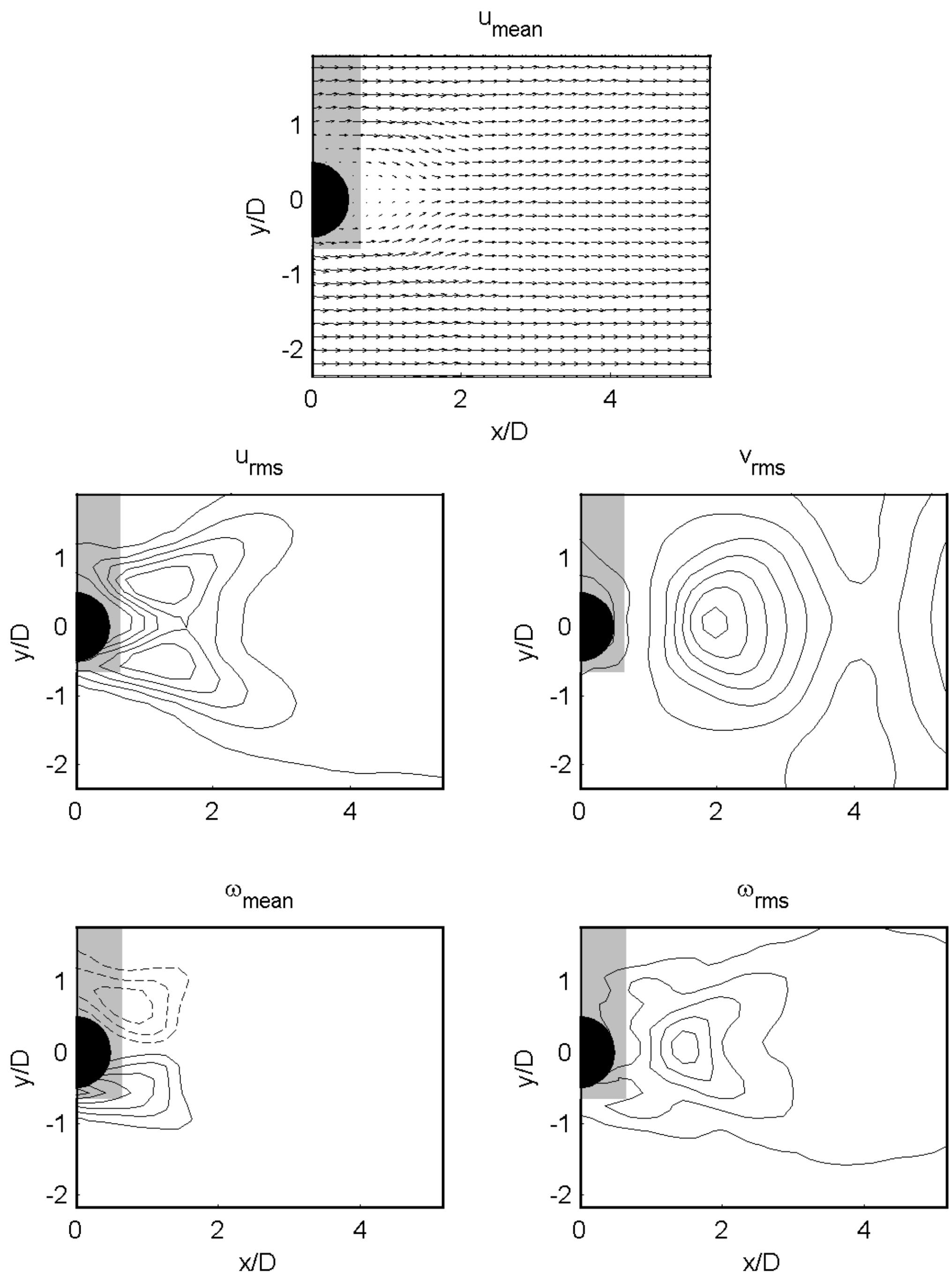

Figure 5.91: Mean and rms normalized velocity (u/U) and normalized vorticity (ωD/U) for case S23; rms velocity contours are at 0.1 intervals; vorticity contours are at 0.5 intervals, negative contours are dashed, positive contours are solid

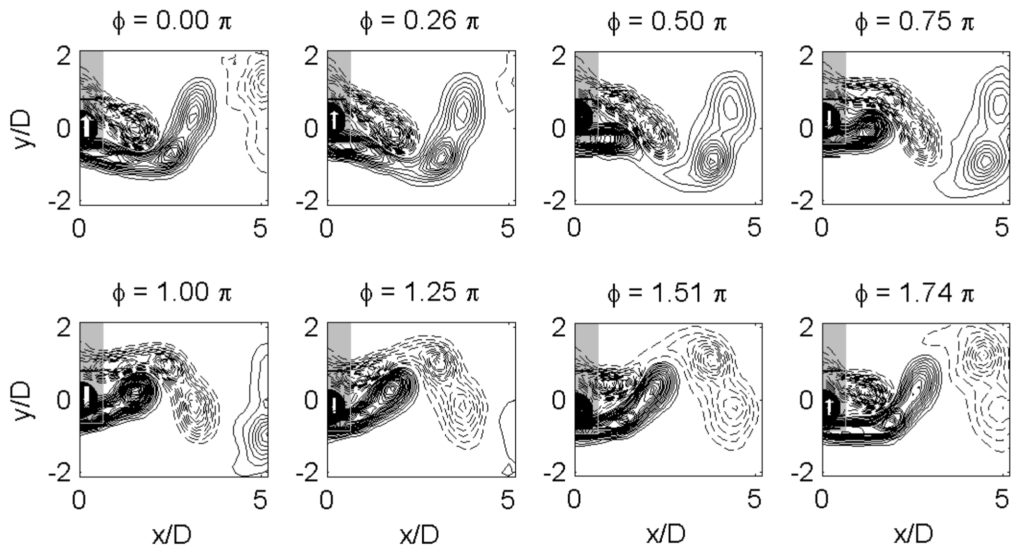

Figure 5.92: Phase-averaged normalized vorticity (ωD/U) for case S23; 1 cycle divided into 16 bins, every other bin shown; minimum contours ±0.2, contour spacing 0.2, positive contours solid, negative contours dashed

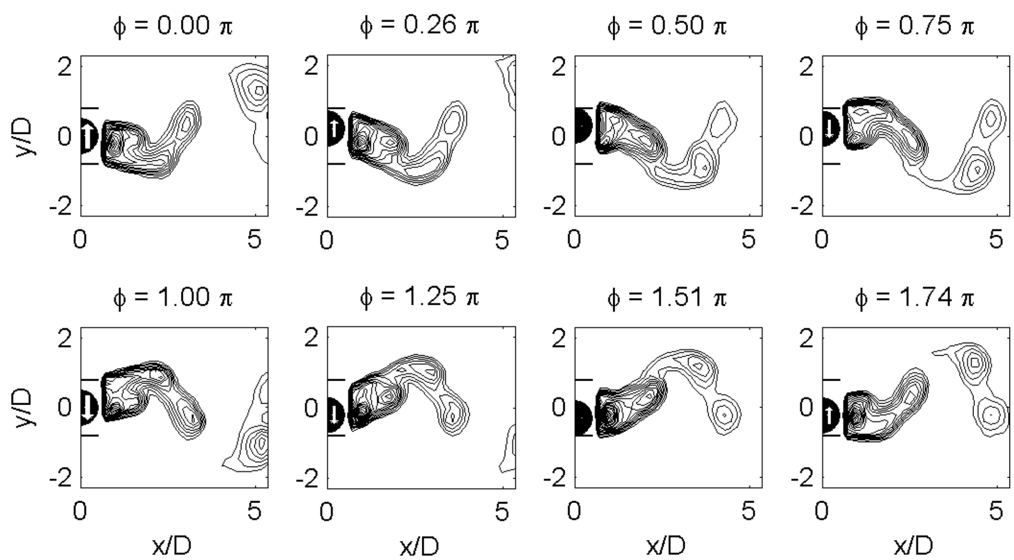

Figure 5.93: Phase-averaged normalized temperature ($(T-T_\infty)/(T_{surf}- T_\infty)$) for case S23; 1 cycle divided into 16 bins, every other bin shown; minimum contour 0.015, contour spacing 0.005

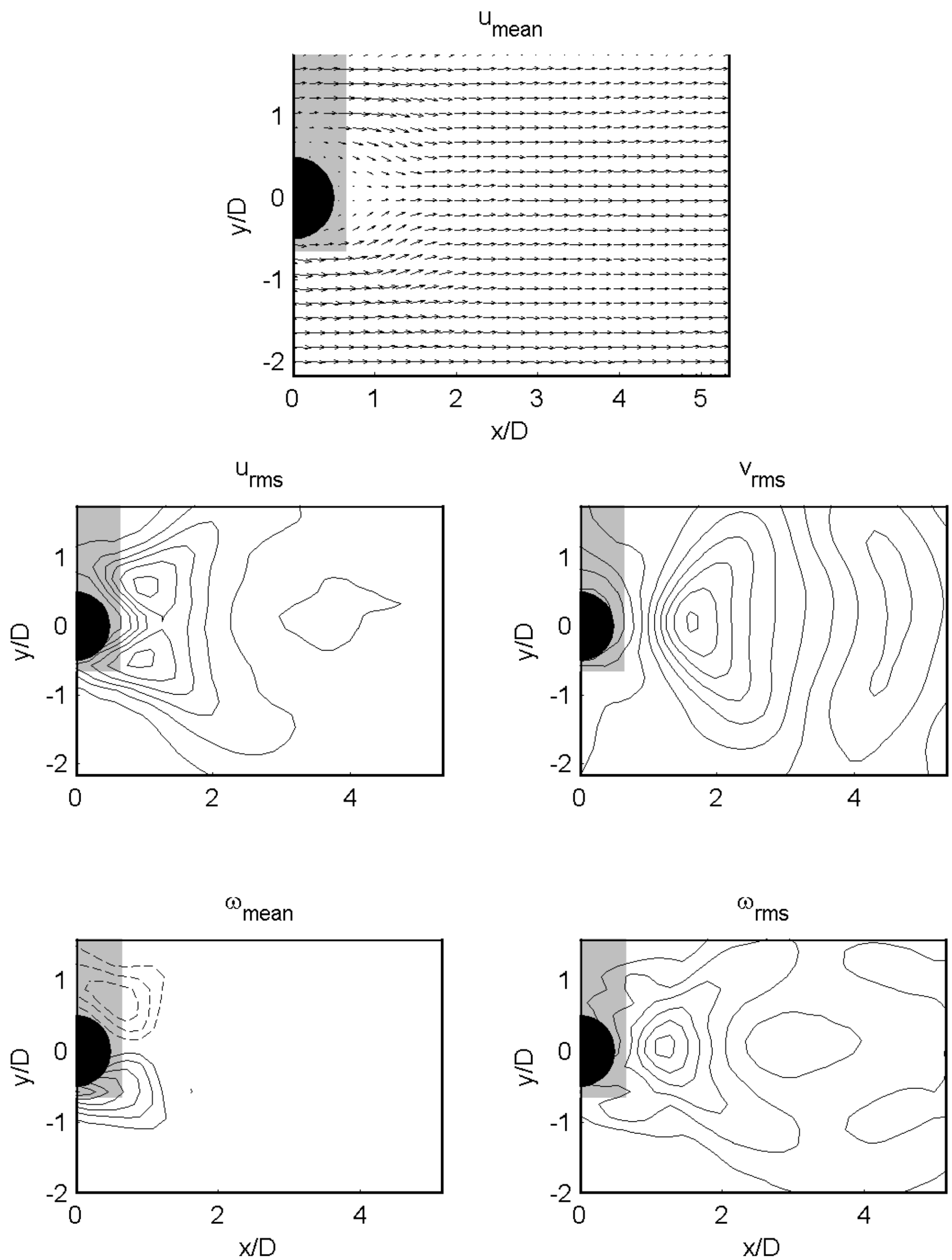

Figure 5.94: Mean and rms normalized velocity (u/U) and normalized vorticity (ωD/U) for case S24; rms velocity contours are at 0.1 intervals; vorticity contours are at 0.5 intervals, negative contours are dashed, positive contours are solid

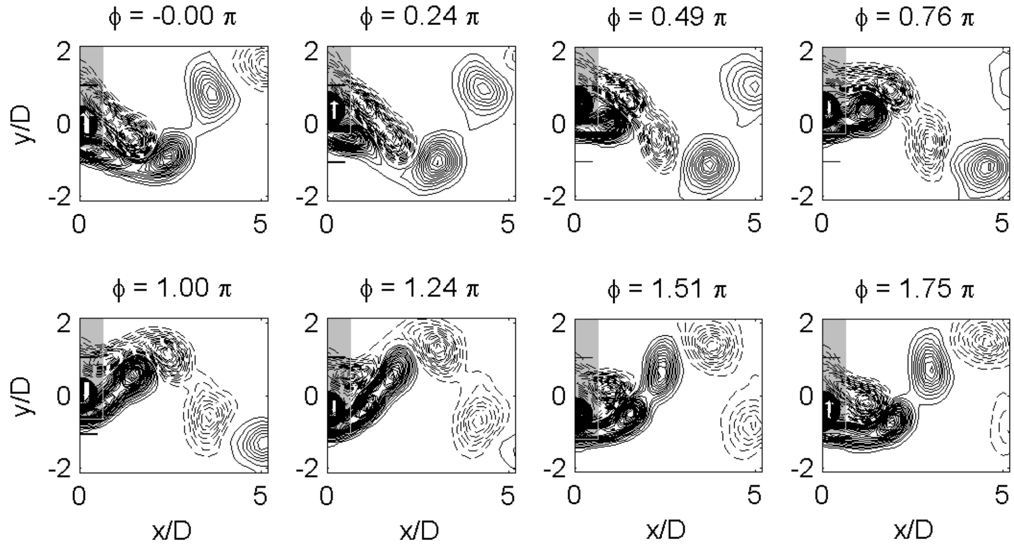

Figure 5.95: Phase-averaged normalized vorticity ($\omega D/U$) for case S24; 1 cycle divided into 16 bins, every other bin shown; minimum contours ±0.2, contour spacing 0.2, positive contours solid, negative contours dashed

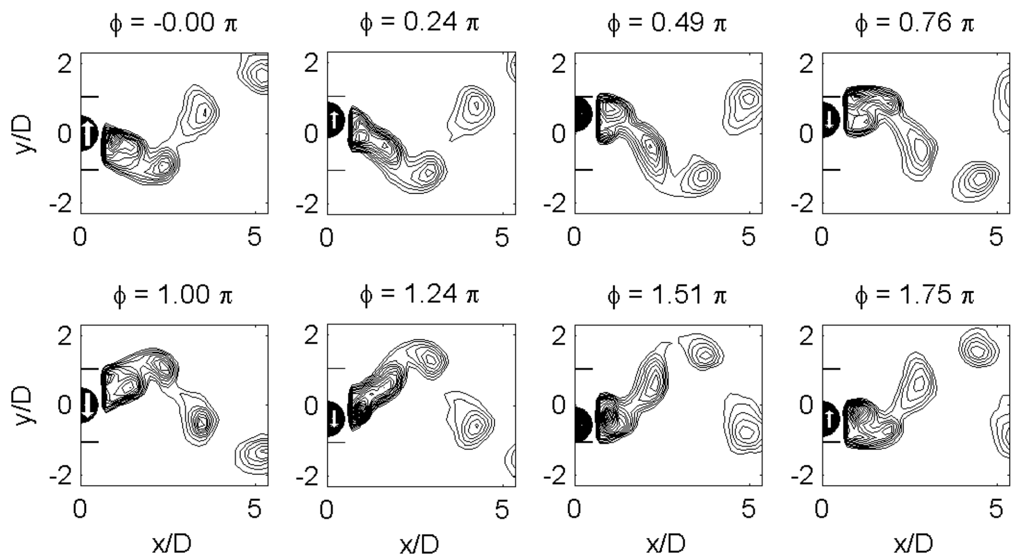

Figure 5.96: Phase-averaged normalized temperature ($(T-T_\infty)/(T_{surf}-T_\infty)$) for case S24; 1 cycle divided into 16 bins, every other bin shown; minimum contour 0.015, contour spacing 0.005

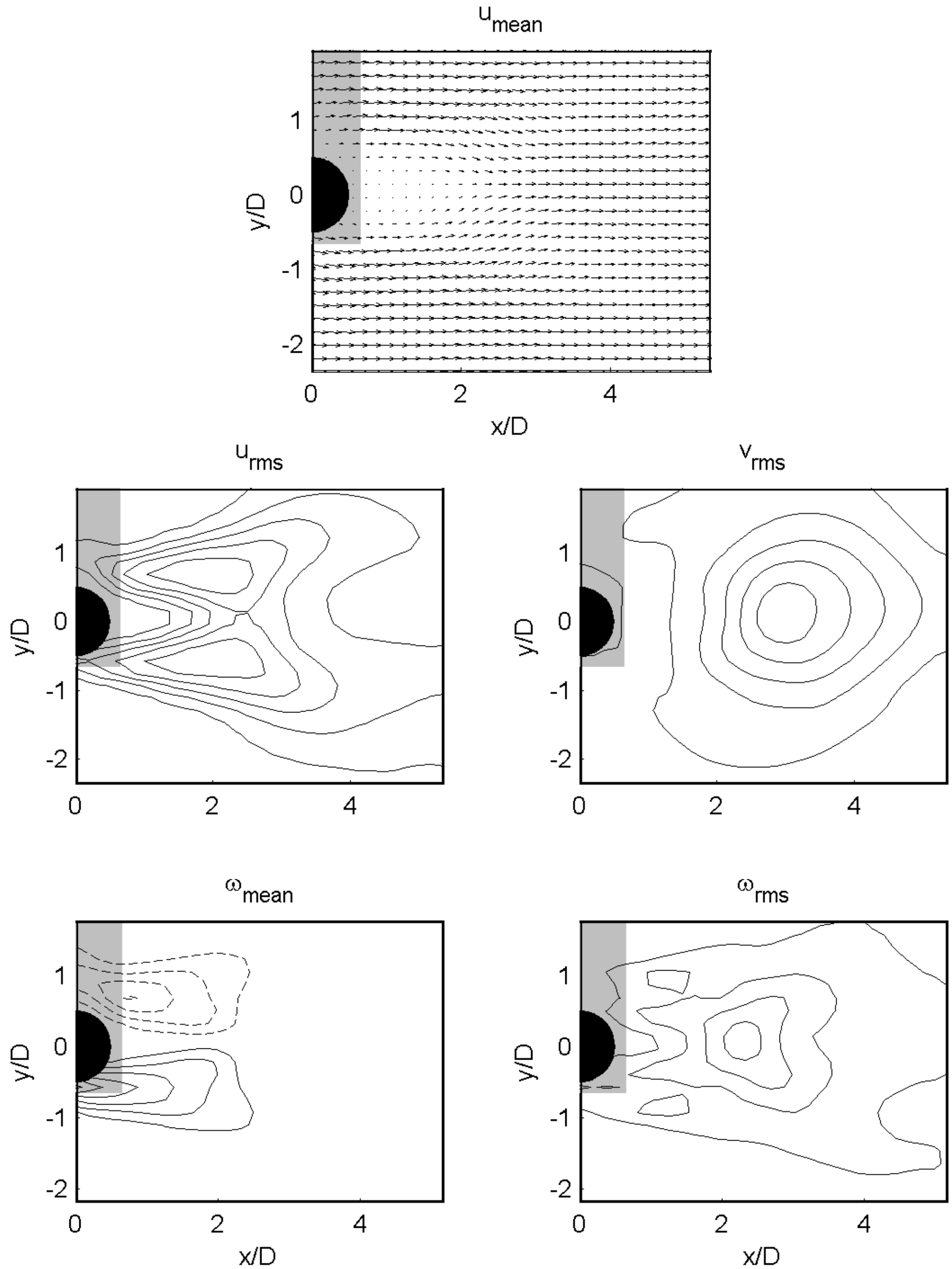

Figure 5.97: Mean and rms normalized velocity (u/U) and normalized vorticity (ωD/U) for case S25; rms velocity contours are at 0.1 intervals; vorticity contours are at 0.5 intervals, negative contours are dashed, positive contours are solid

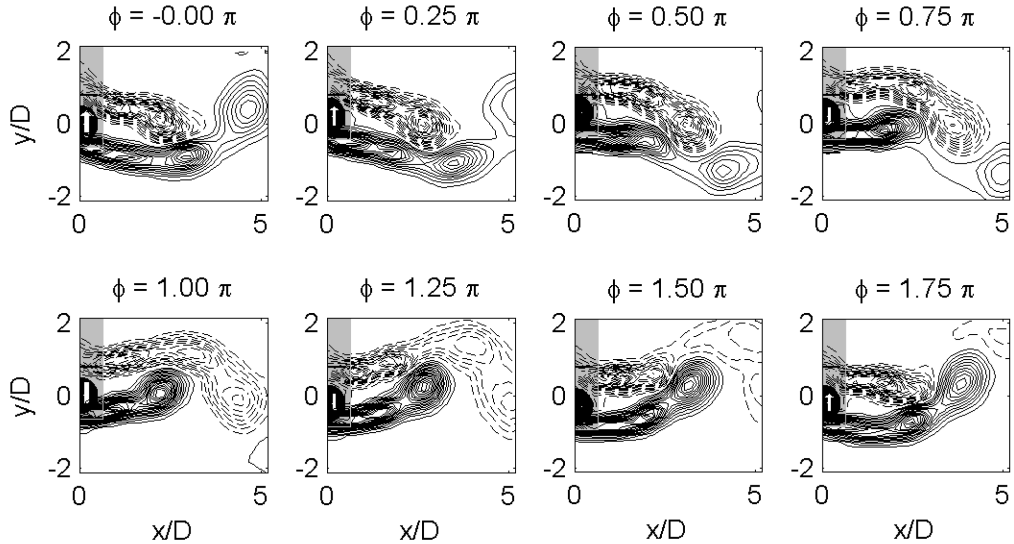

Figure 5.98: Phase-averaged normalized vorticity (ωD/U) for case S25; 1 cycle divided into 16 bins, every other bin shown; minimum contours ±0.2, contour spacing 0.2, positive contours solid, negative contours dashed

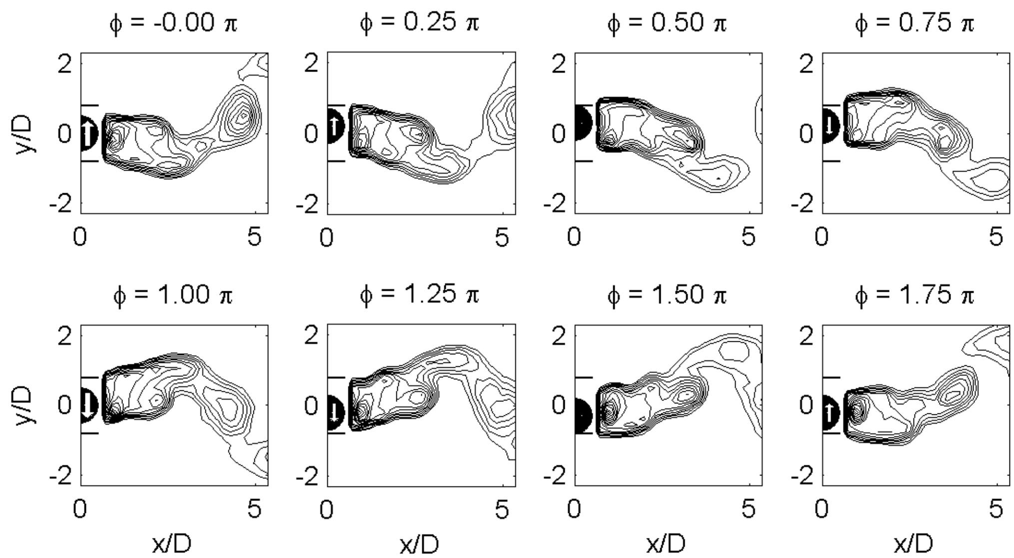

Figure 5.99: Phase-averaged normalized temperature ($(T-T_\infty)/(T_{surf}- T_\infty)$) for case S25; 1 cycle divided into 16 bins, every other bin shown; minimum contour 0.015, contour spacing 0.005

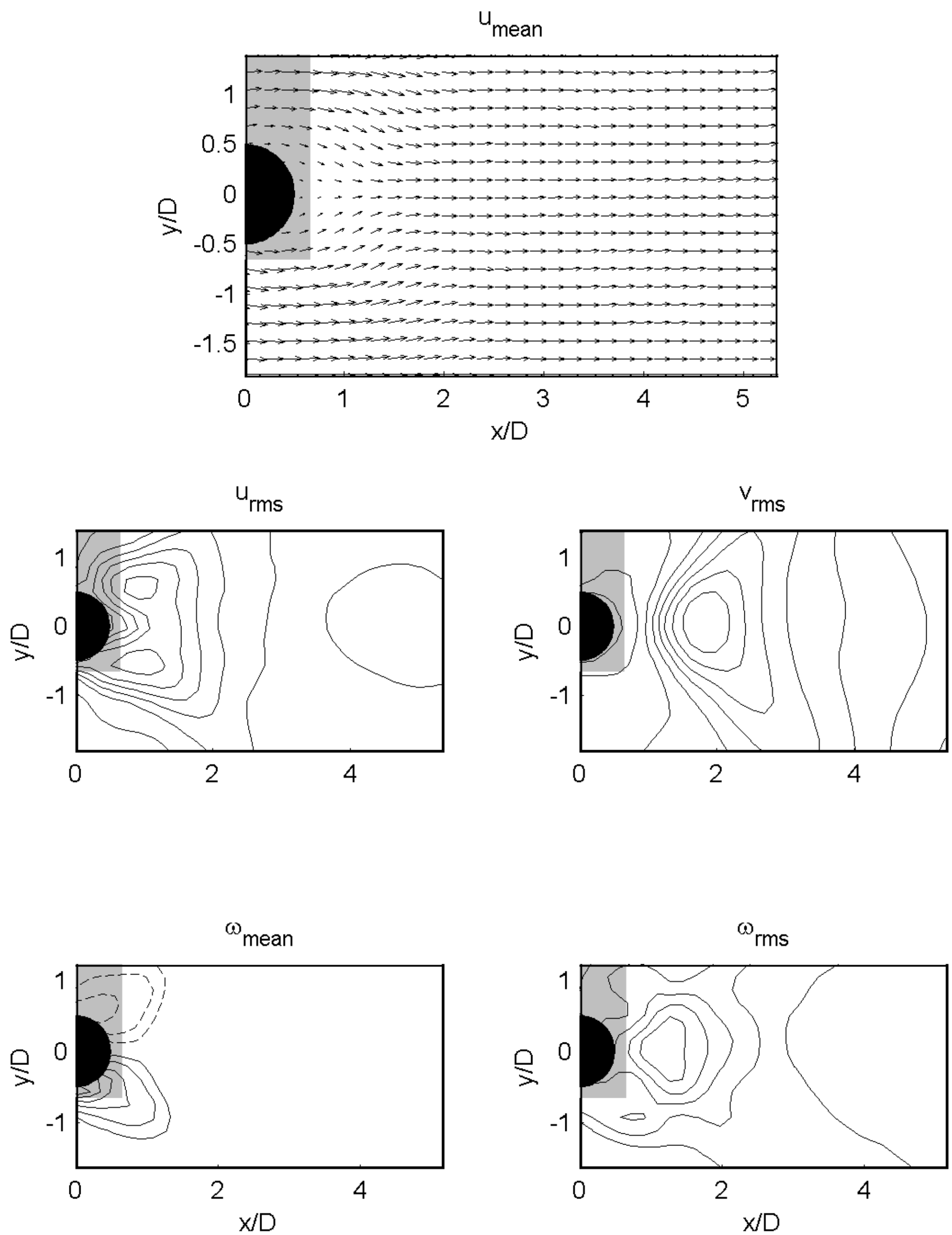

Figure 5.100: Mean and rms normalized velocity ($\underline{u}$/U) and normalized vorticity (ωD/U) for case S26; rms velocity contours are at 0.1 intervals; vorticity contours are at 0.5 intervals, negative contours are dashed, positive contours are solid

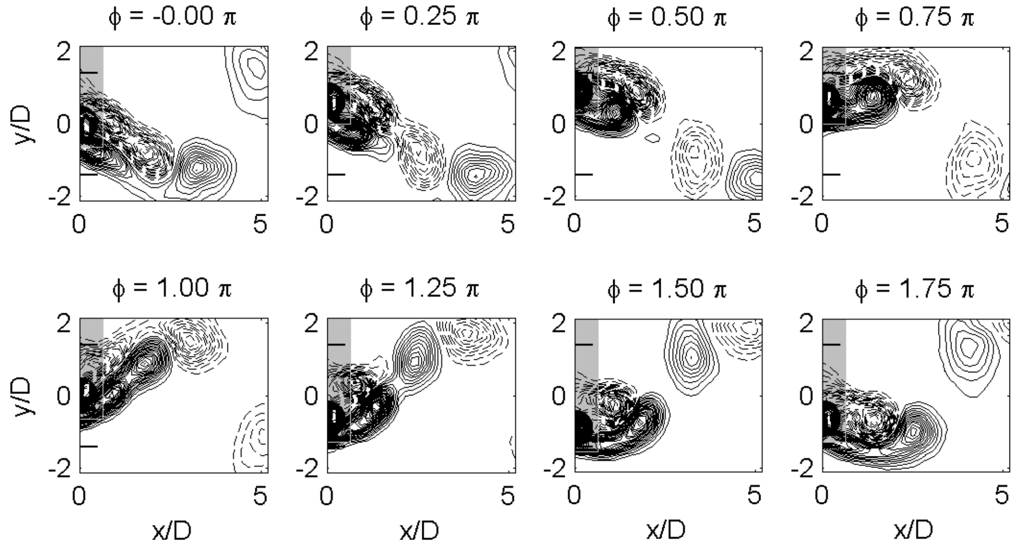

Figure 5.101: Phase-averaged normalized vorticity (ωD/U) for case S26; 1 cycle divided into 16 bins, every other bin shown; minimum contours ±0.2, contour spacing 0.2, positive contours solid, negative contours dashed

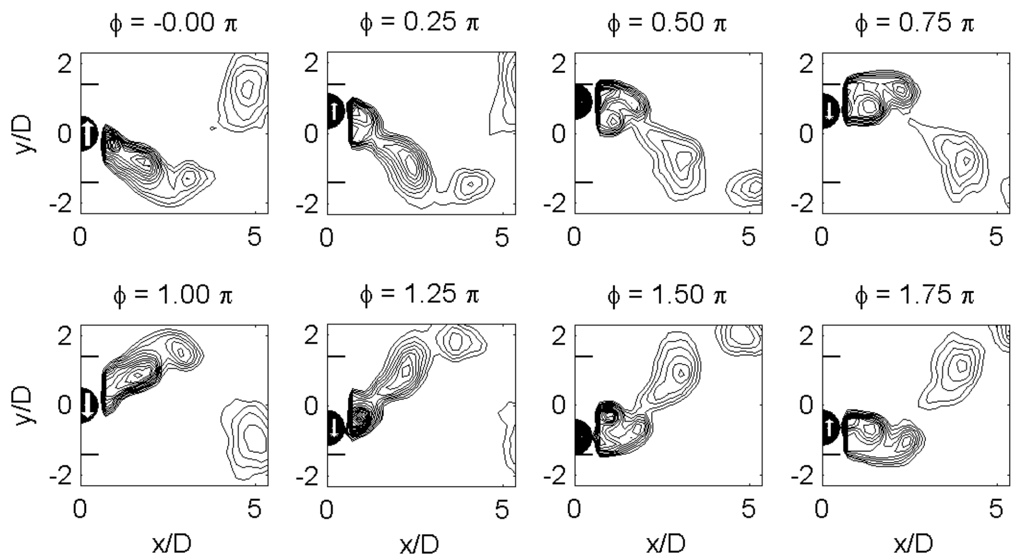

Figure 5.102: Phase-averaged normalized temperature ($(T-T_\infty)/(T_{surf}-T_\infty)$) for case S26; 1 cycle divided into 16 bins, every other bin shown; minimum contour 0.015, contour spacing 0.005

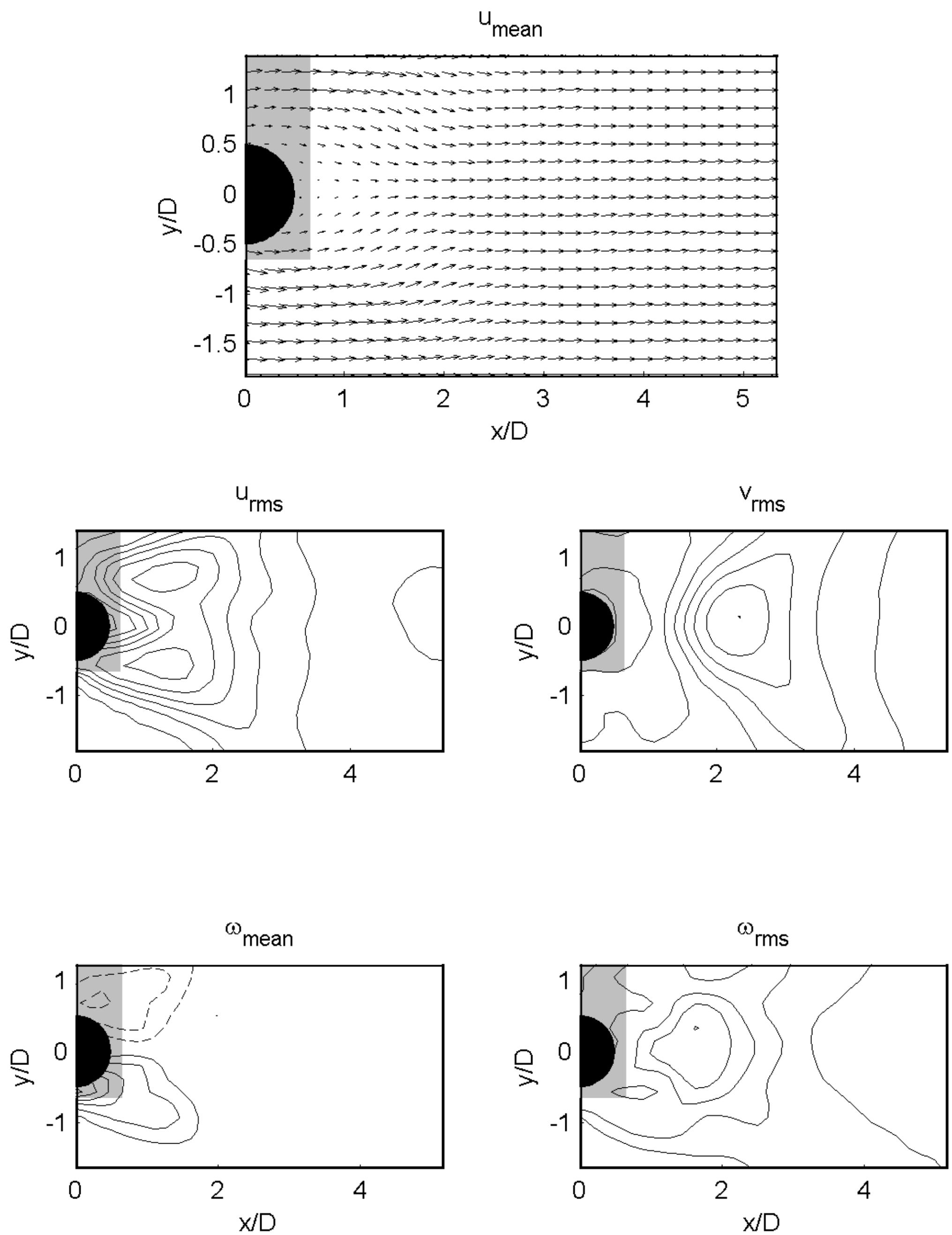

Figure 5.103: Mean and rms normalized velocity (u/U) and normalized vorticity (ωD/U) for case S27; rms velocity contours are at 0.1 intervals; vorticity contours are at 0.5 intervals, negative contours are dashed, positive contours are solid

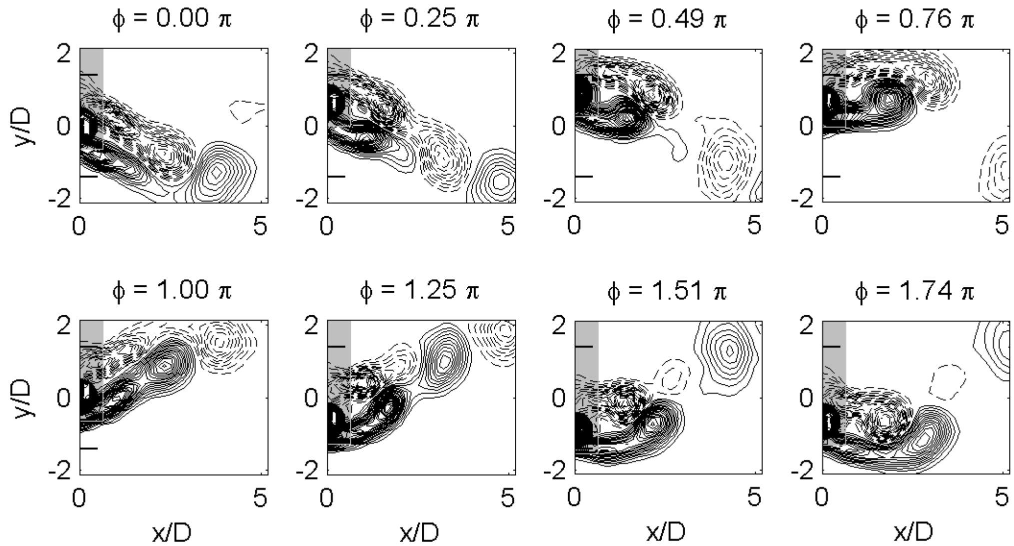

Figure 5.104: Phase-averaged normalized vorticity (ωD/U) for case S27; 1 cycle divided into 16 bins, every other bin shown; minimum contours ±0.2, contour spacing 0.2, positive contours solid, negative contours dashed

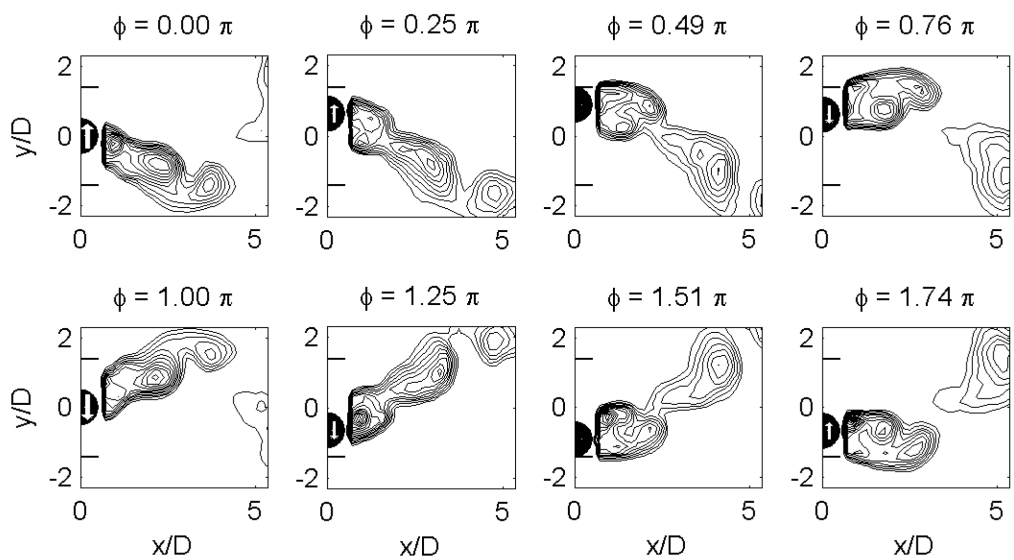

Figure 5.105: Phase-averaged normalized temperature ($(T-T_\infty)/(T_{surf}- T_\infty)$) for case S27; 1 cycle divided into 16 bins, every other bin shown; minimum contour 0.015, contour spacing 0.005

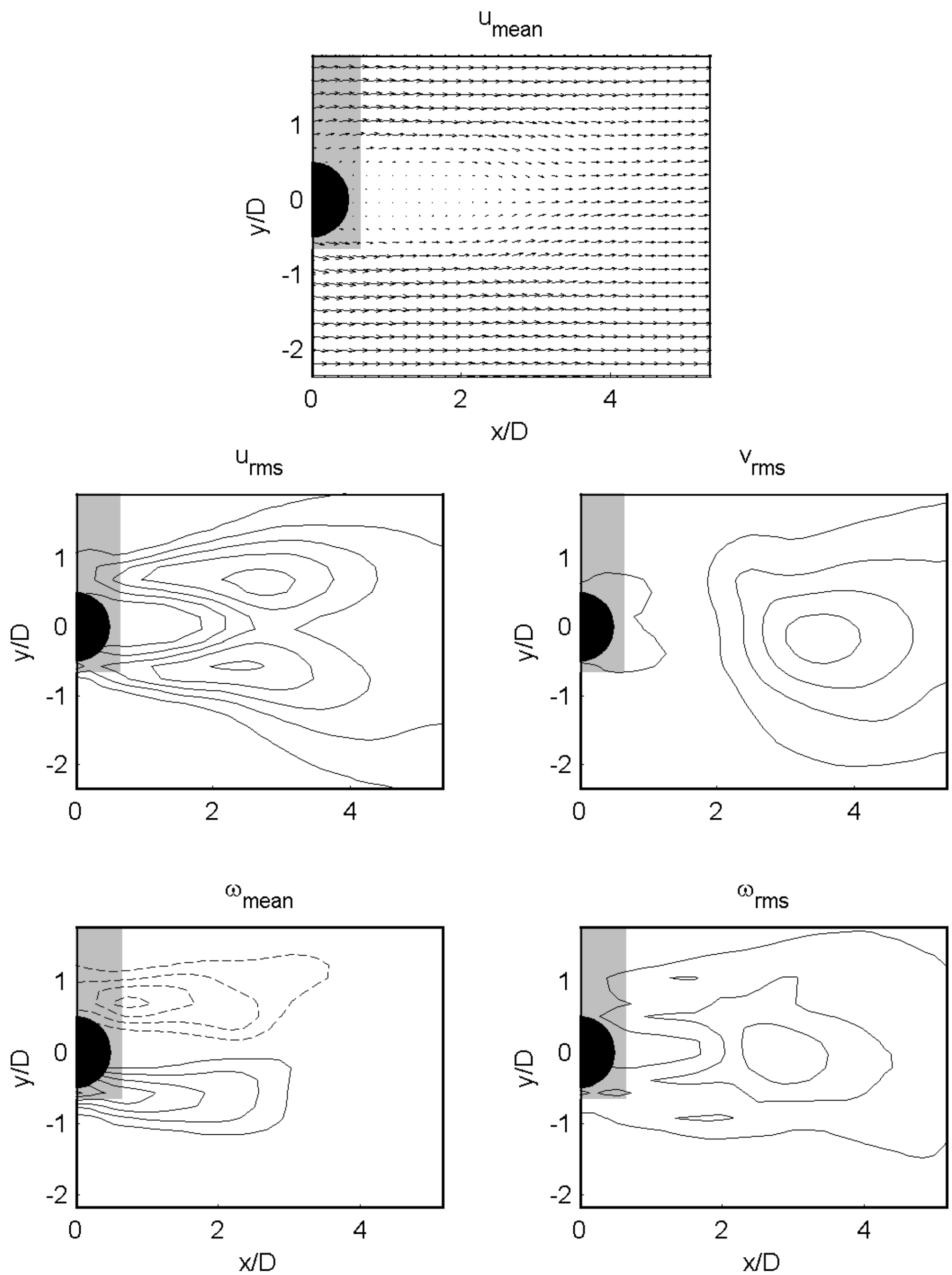

Figure 5.106: Mean and rms normalized velocity (u/U) and normalized vorticity (ωD/U) for case S28; rms velocity contours are at 0.1 intervals; vorticity contours are at 0.5 intervals, negative contours are dashed, positive contours are solid

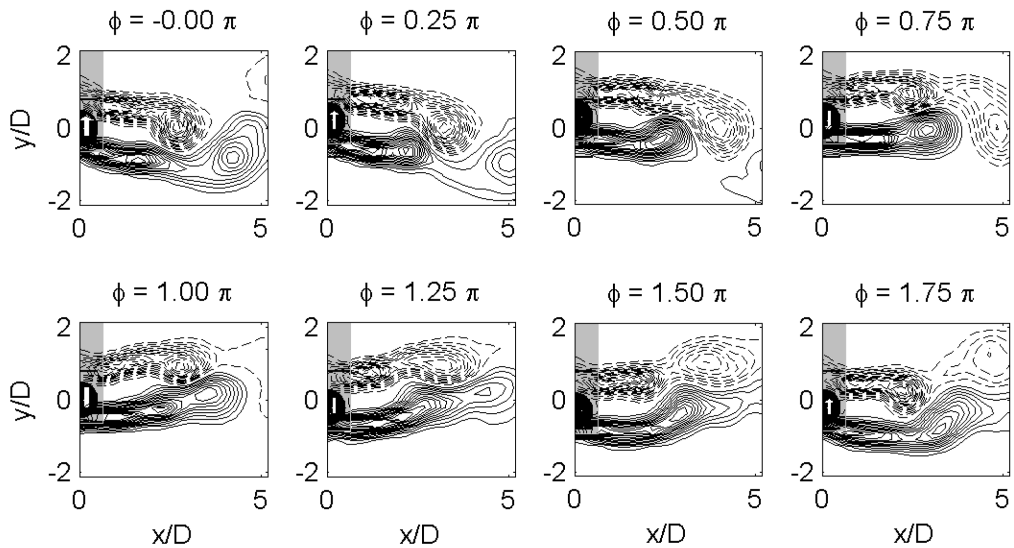

Figure 5.107: Phase-averaged normalized vorticity (ωD/U) for case S28; 1 cycle divided into 16 bins, every other bin shown; minimum contours ±0.2, contour spacing 0.2, positive contours solid, negative contours dashed

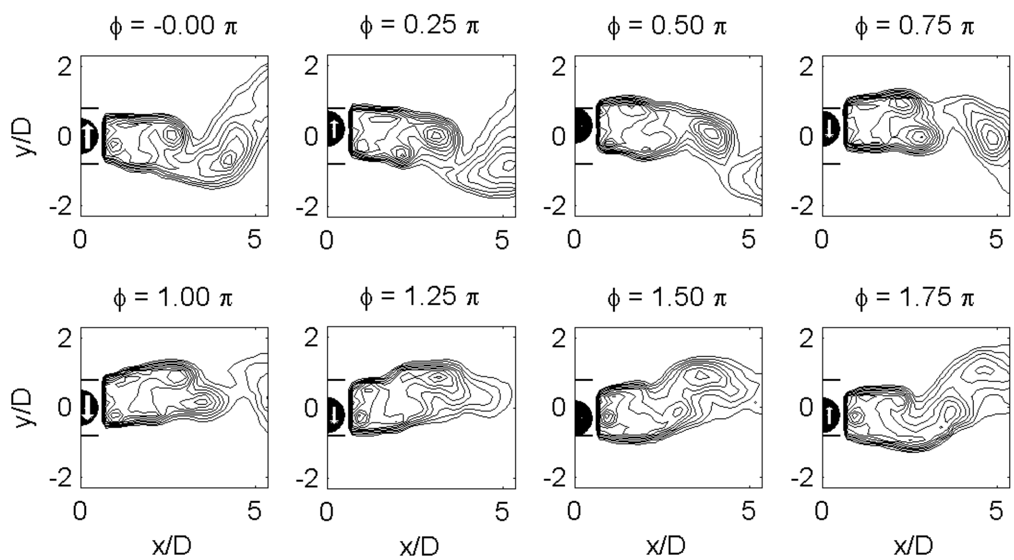

Figure 5.108: Phase-averaged normalized temperature ($(T-T_\infty)/(T_{surf}-T_\infty)$) for case S28; 1 cycle divided into 16 bins, every other bin shown; minimum contour 0.015, contour spacing 0.005

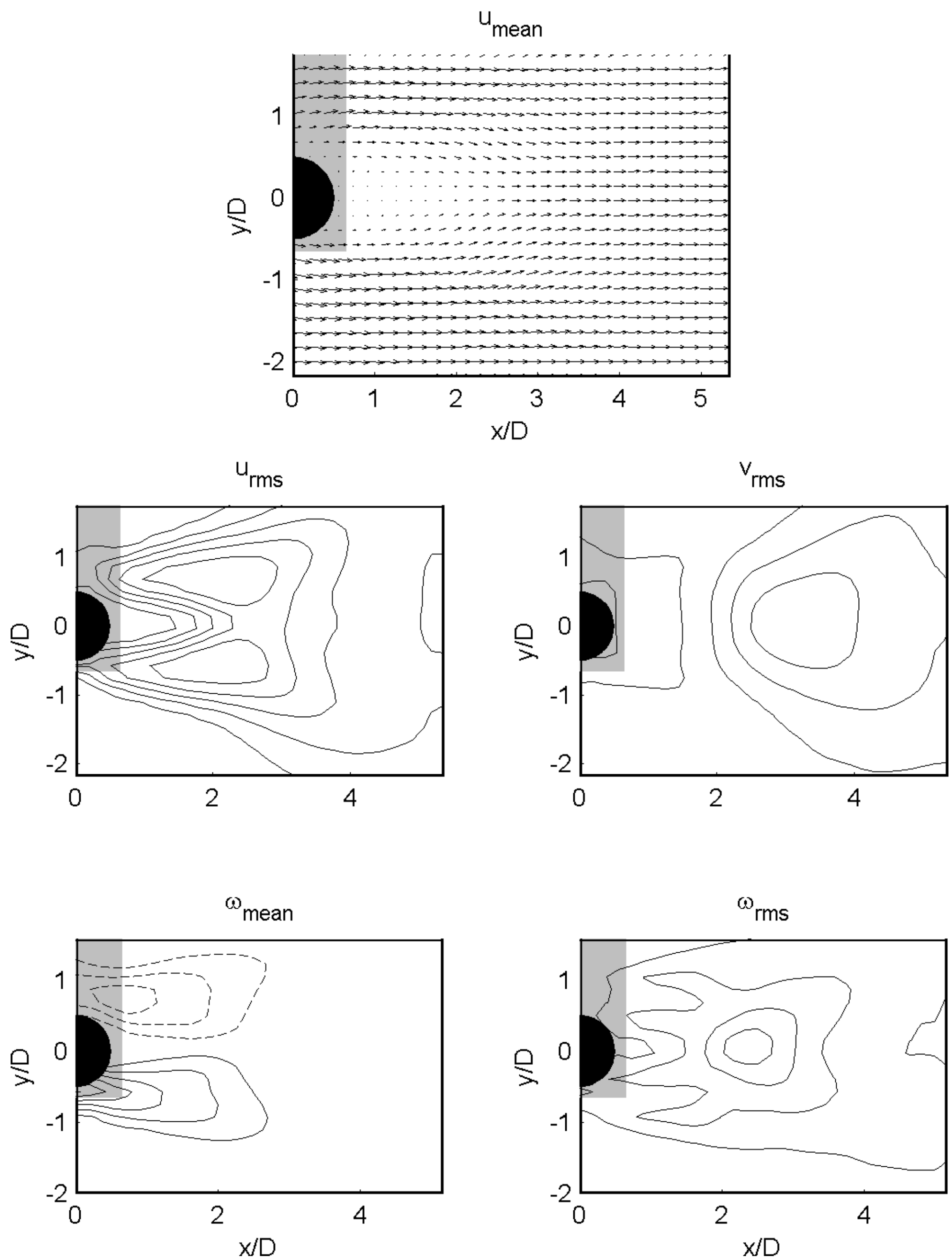

Figure 5.109: Mean and rms normalized velocity (u/U) and normalized vorticity (ωD/U) for case S29; rms velocity contours are at 0.1 intervals; vorticity contours are at 0.5 intervals, negative contours are dashed, positive contours are solid

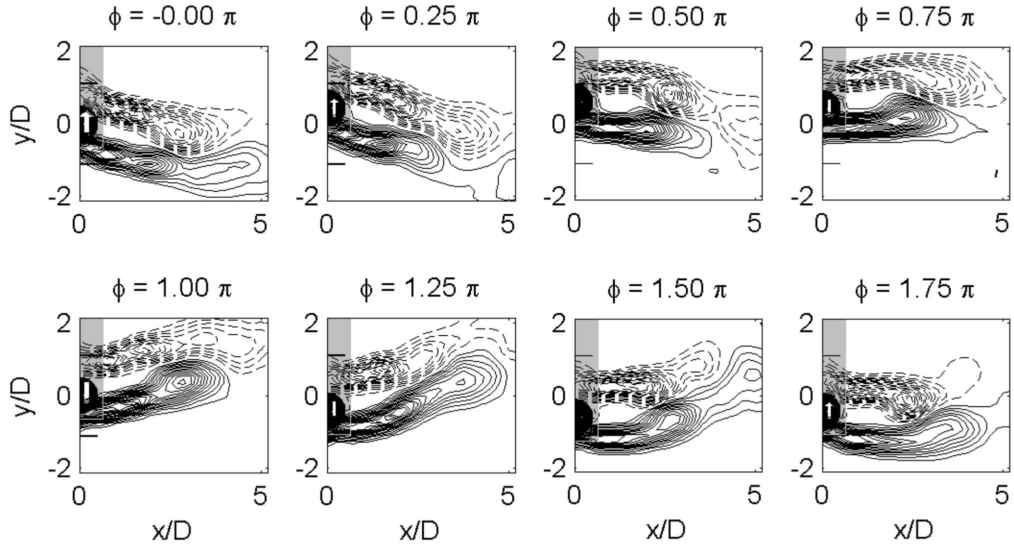

Figure 5.110: Phase-averaged normalized vorticity ($\omega D/U$) for case S29; 1 cycle divided into 16 bins, every other bin shown; minimum contours ±0.2, contour spacing 0.2, positive contours solid, negative contours dashed

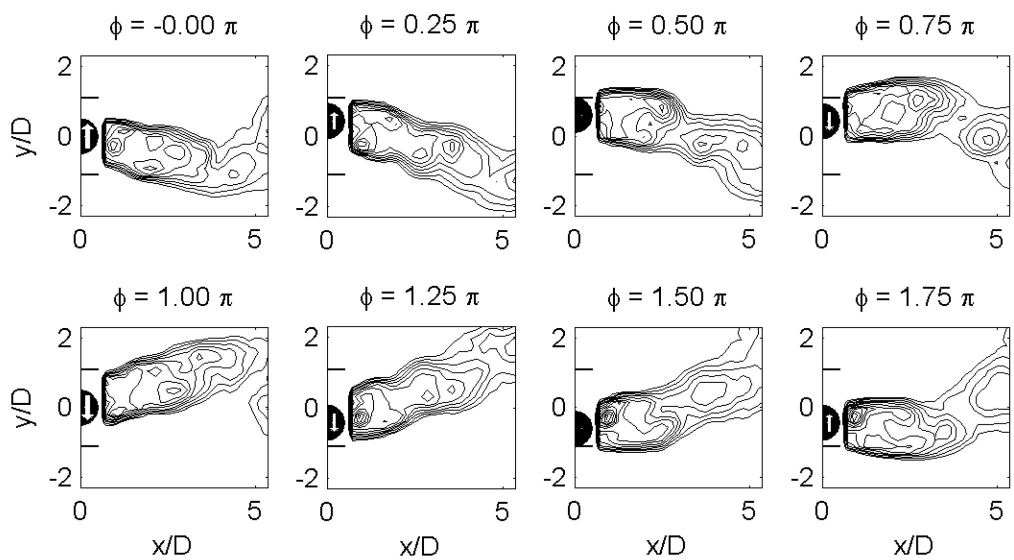

Figure 5.111: Phase-averaged normalized temperature ($(T-T_\infty)/(T_{surf}-T_\infty)$) for case S29; 1 cycle divided into 16 bins, every other bin shown; minimum contour 0.015, contour spacing 0.005

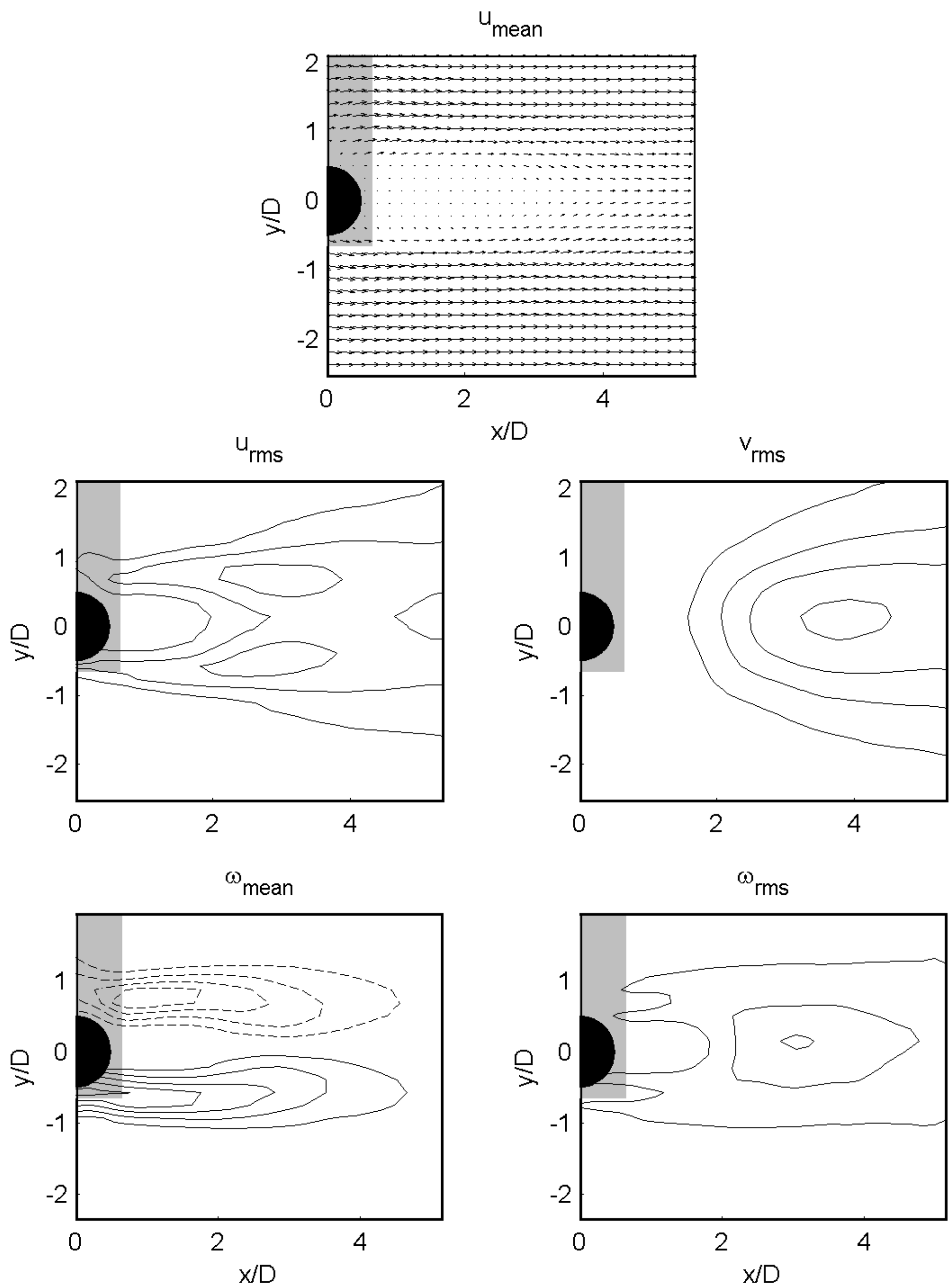

Figure 5.112: Mean and rms normalized velocity (u/U) and normalized vorticity (ωD/U) for case S30; rms velocity contours are at 0.1 intervals; vorticity contours are at 0.5 intervals, negative contours are dashed, positive contours are solid

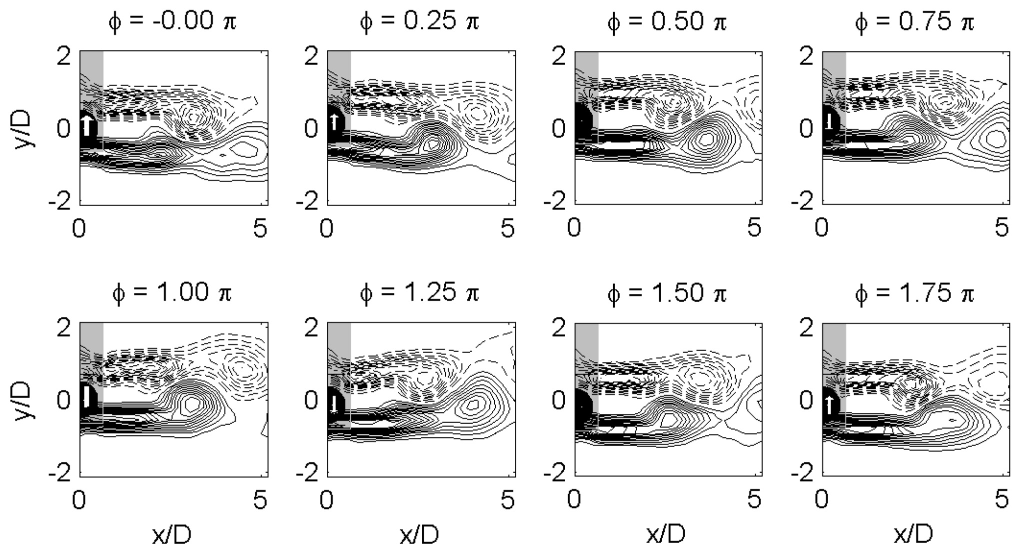

Figure 5.113: Phase-averaged normalized vorticity (ωD/U) for case S30; 1 cycle divided into 16 bins, every other bin shown; minimum contours ±0.2, contour spacing 0.2, positive contours solid, negative contours dashed

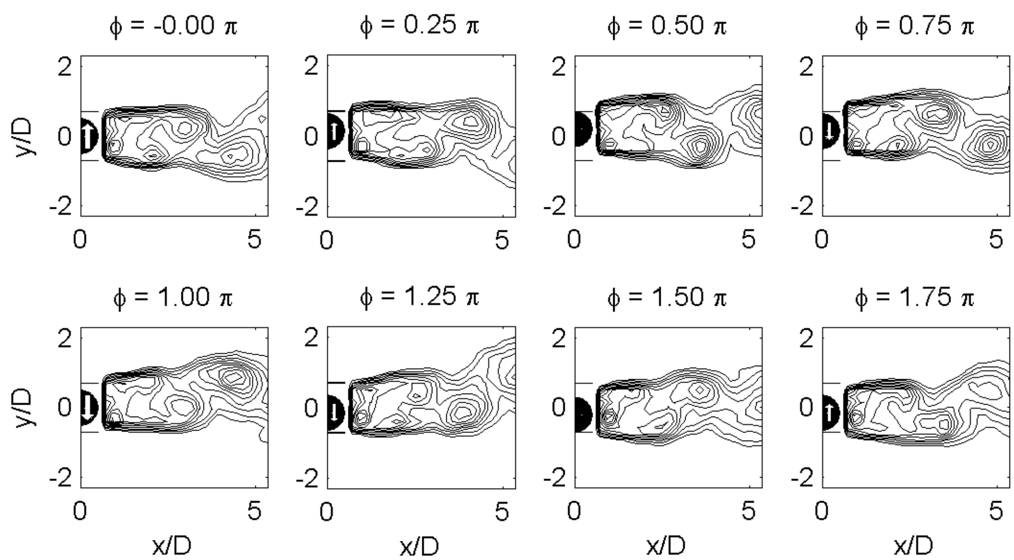

Figure 5.114: Phase-averaged normalized temperature ($(T-T_\infty)/(T_{surf}-T_\infty)$) for case S30; 1 cycle divided into 16 bins, every other bin shown; minimum contour 0.015, contour spacing 0.005

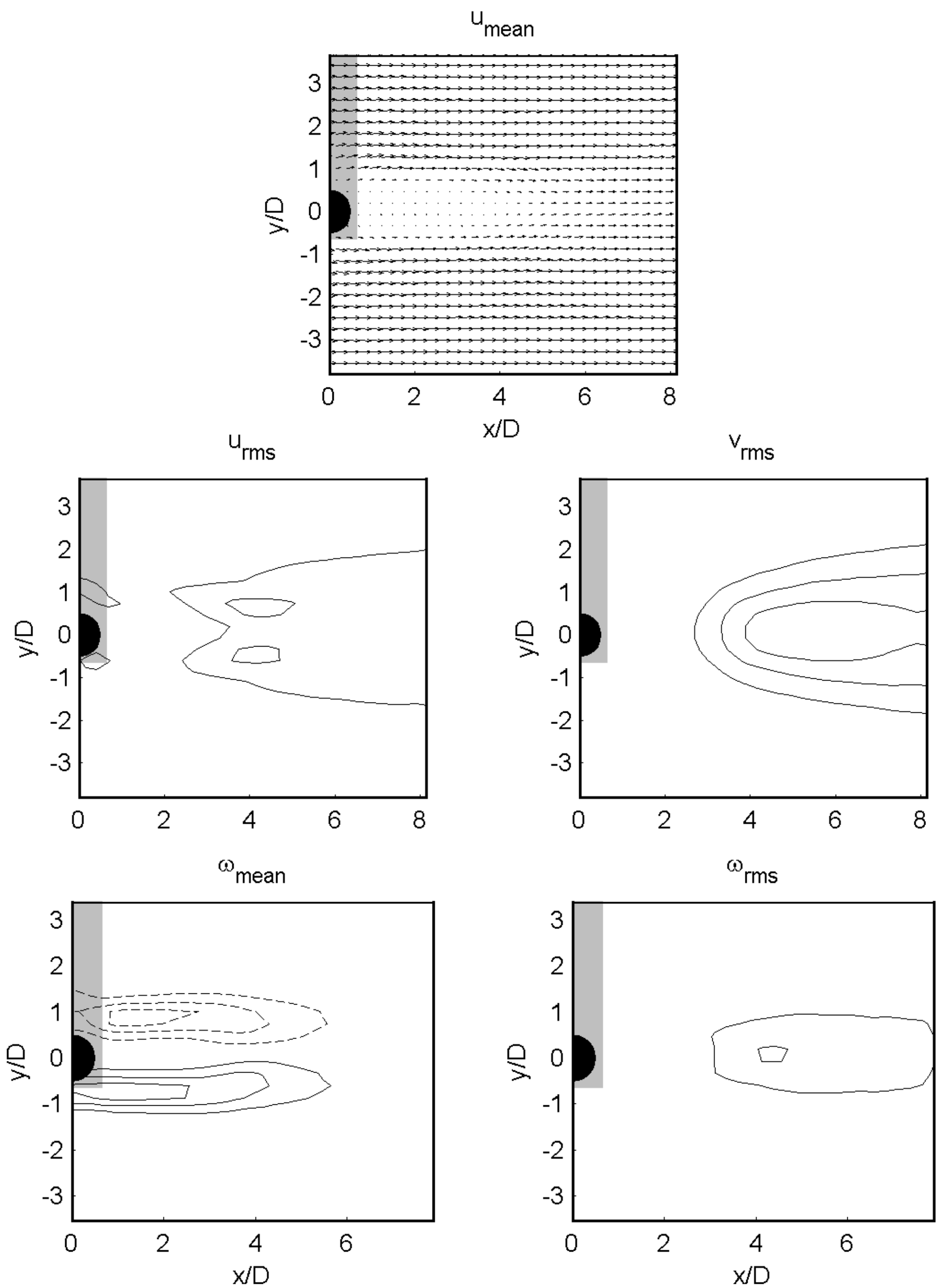

Figure 5.115: Mean and rms normalized velocity (u/U) and normalized vorticity (ωD/U) for case L0; rms velocity contours are at 0.1 intervals; vorticity contours are at 0.5 intervals, negative contours are dashed, positive contours are solid

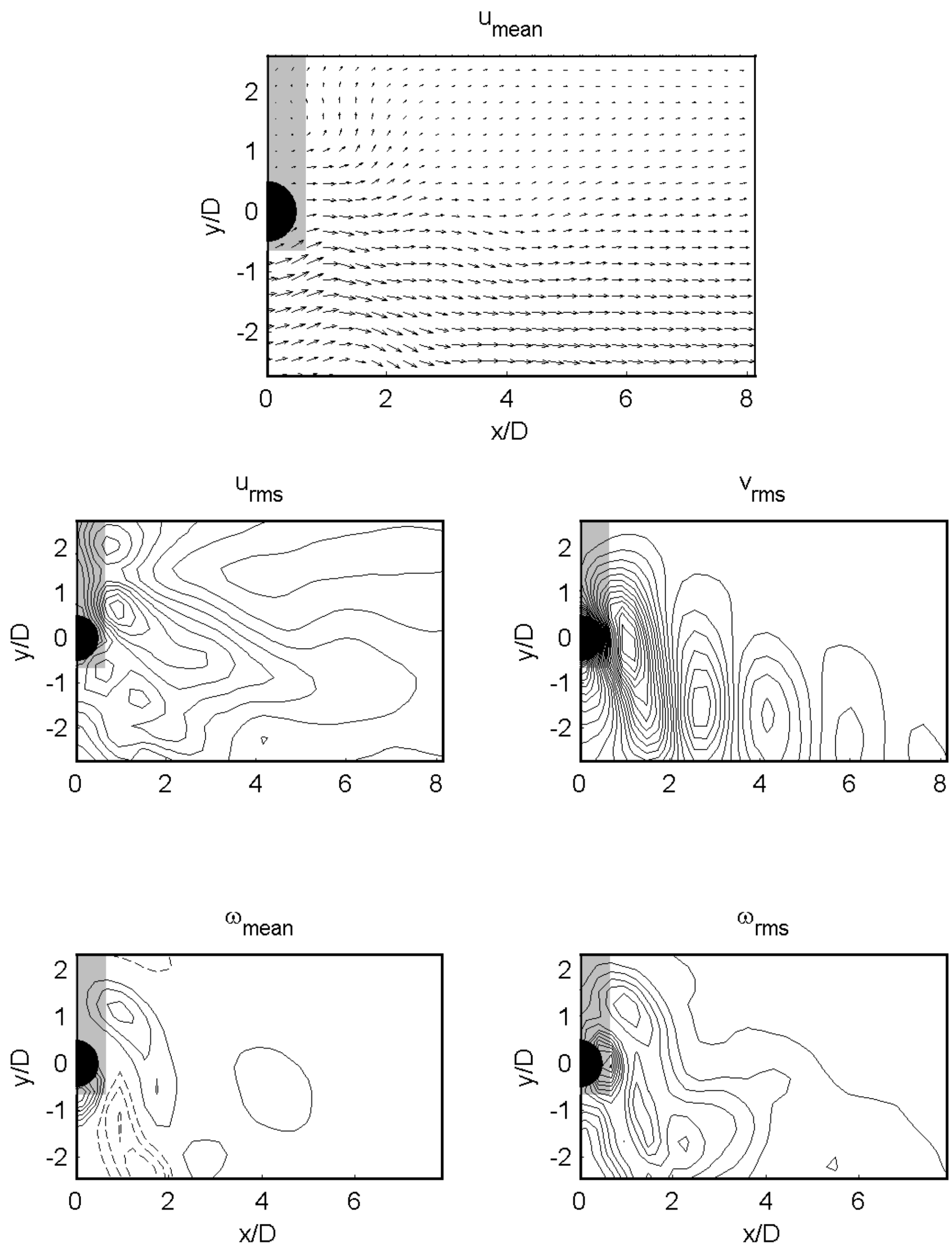

Figure 5.116: Mean and rms normalized velocity (u/U) and normalized vorticity (ωD/U) for case L1; rms velocity contours are at 0.1 intervals; vorticity contours are at 0.5 intervals, negative contours are dashed, positive contours are solid

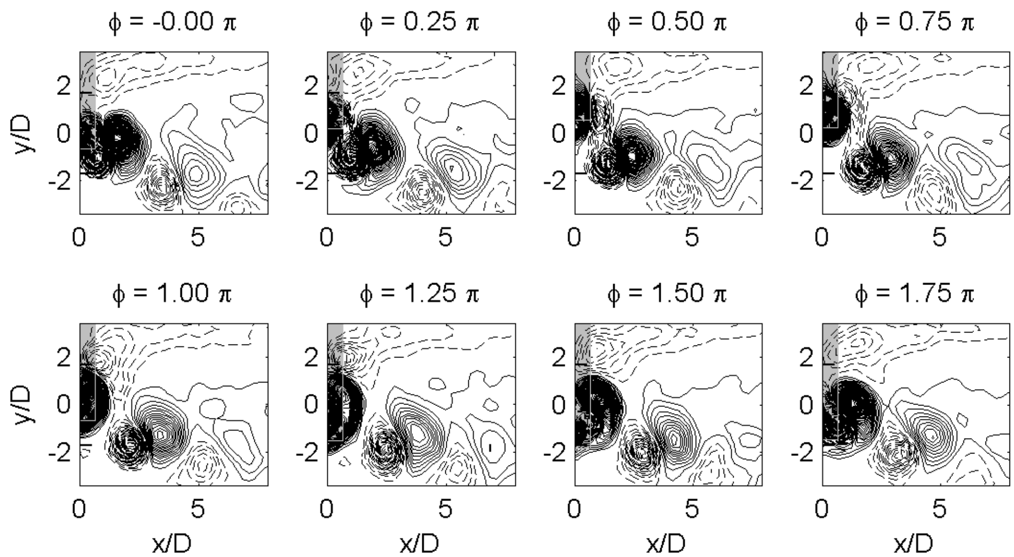

Figure 5.117: Phase-averaged normalized vorticity (ωD/U) for case L1; 1 cycle divided into 16 bins, every other bin shown; minimum contours ±0.2, contour spacing 0.2, positive contours solid, negative contours dashed

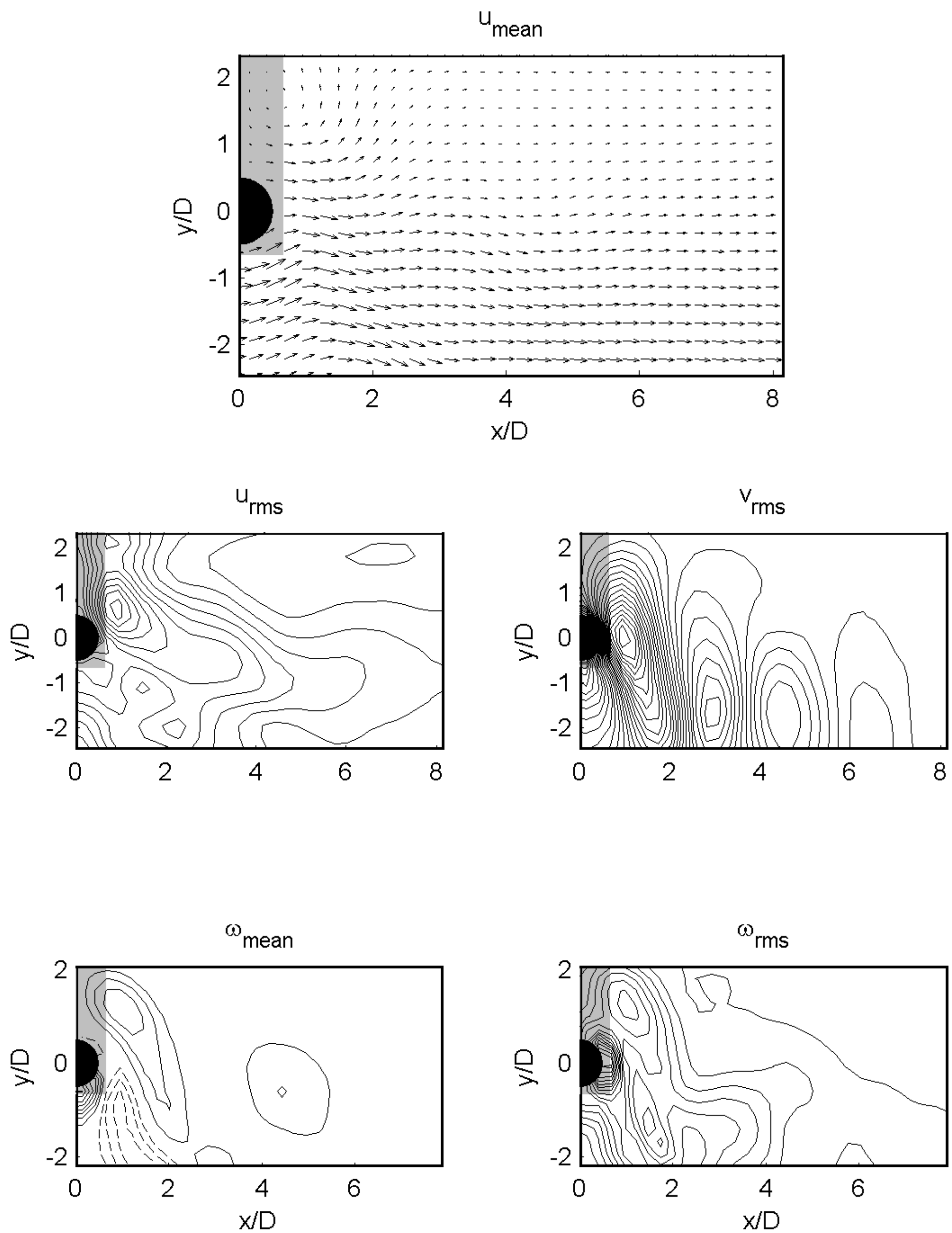

Figure 5.118: Mean and rms normalized velocity (u/U) and normalized vorticity (ωD/U) for case L2; rms velocity contours are at 0.1 intervals; vorticity contours are at 0.5 intervals, negative contours are dashed, positive contours are solid

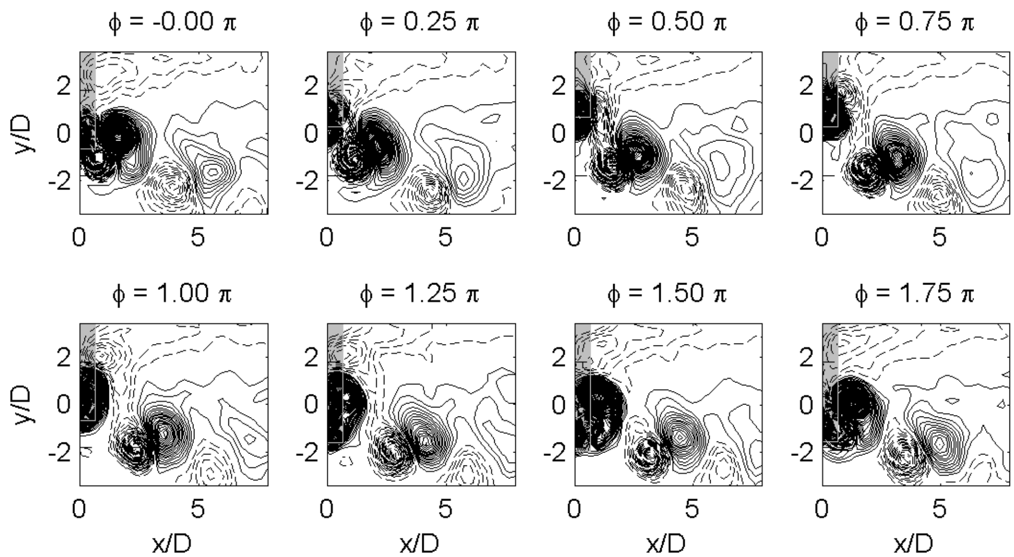

Figure 5.119: Phase-averaged normalized vorticity (ωD/U) for case L2; 1 cycle divided into 16 bins, every other bin shown; minimum contours ±0.2, contour spacing 0.2, positive contours solid, negative contours dashed

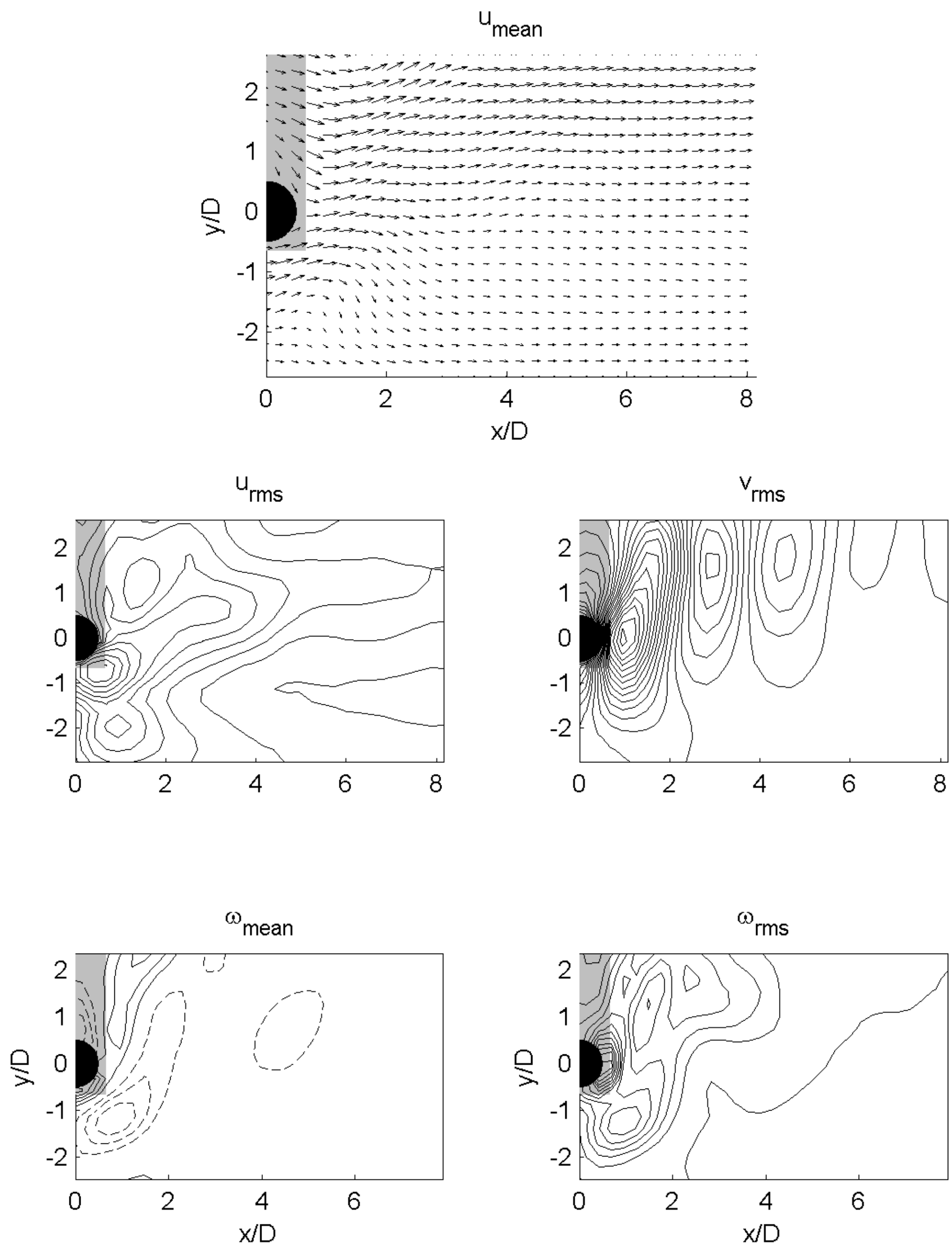

Figure 5.120: Mean and rms normalized velocity (u/U) and normalized vorticity (ωD/U) for case L3; rms velocity contours are at 0.1 intervals; vorticity contours are at 0.5 intervals, negative contours are dashed, positive contours are solid

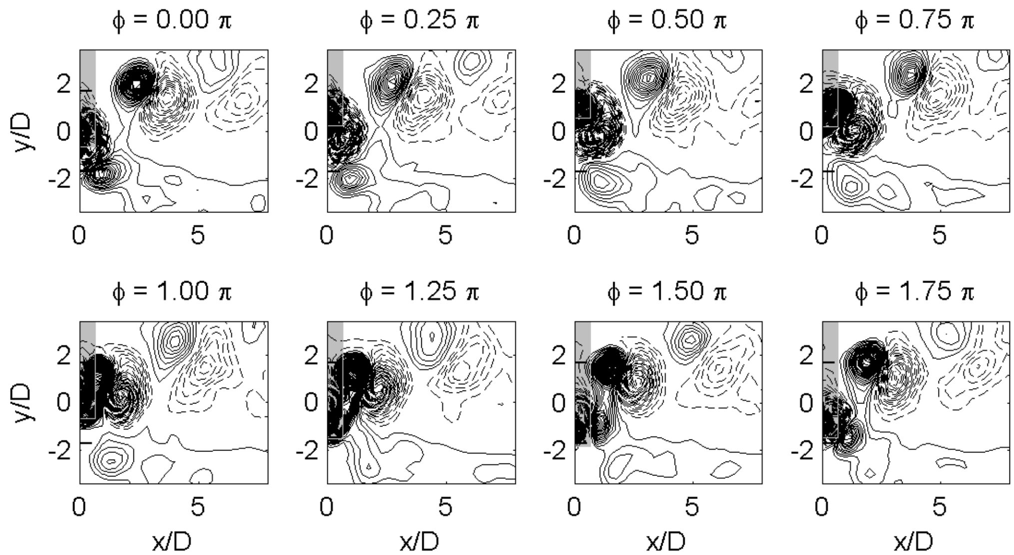

Figure 5.121: Phase-averaged normalized vorticity (ωD/U) for case L3; 1 cycle divided into 16 bins, every other bin shown; minimum contours ±0.2, contour spacing 0.2, positive contours solid, negative contours dashed

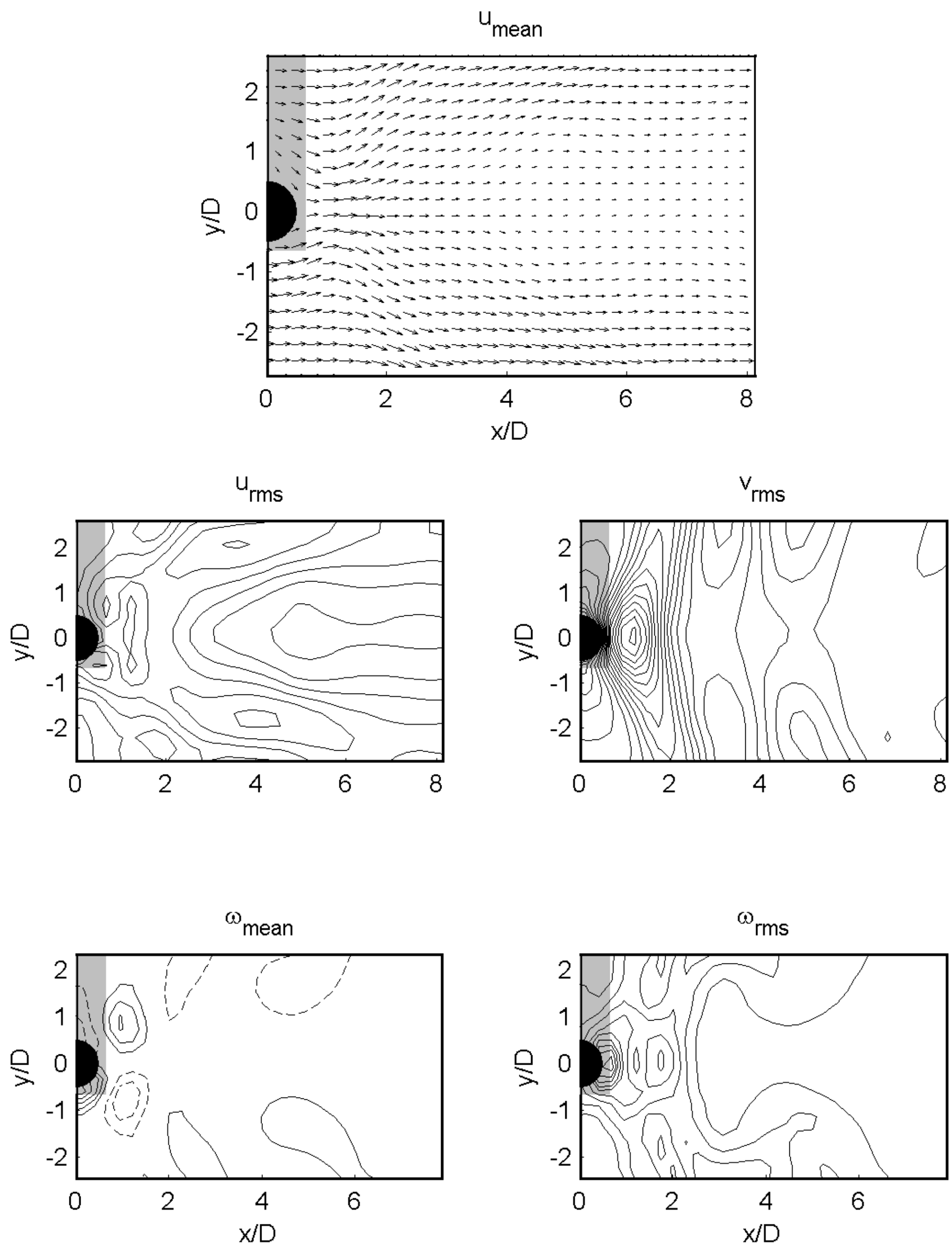

Figure 5.122: Mean and rms normalized velocity (u/U) and normalized vorticity (ωD/U) for case L4; rms velocity contours are at 0.1 intervals; vorticity contours are at 0.5 intervals, negative contours are dashed, positive contours are solid

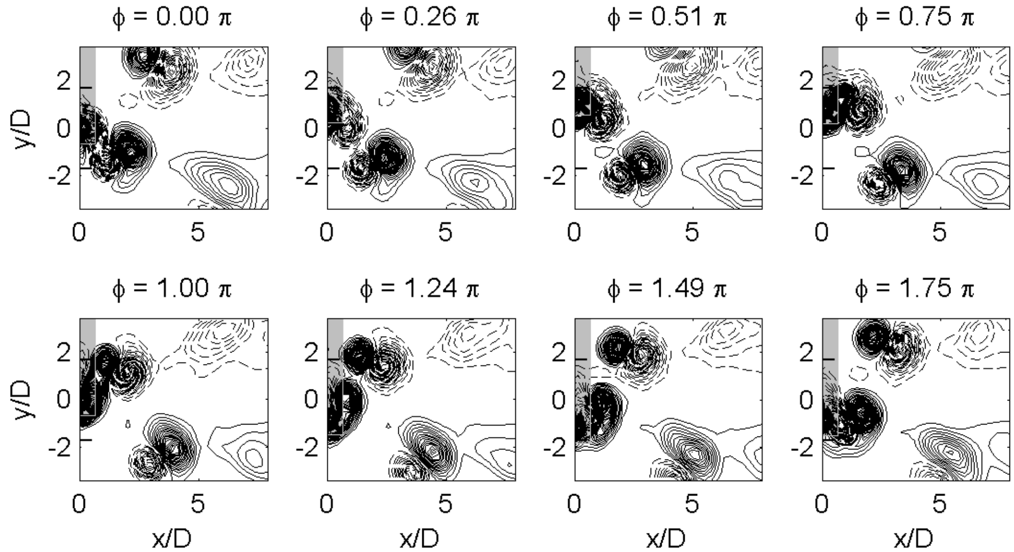

Figure 5.123: Phase-averaged normalized vorticity (ωD/U) for case L4; 1 cycle divided into 16 bins, every other bin shown; minimum contours ±0.2, contour spacing 0.2, positive contours solid, negative contours dashed

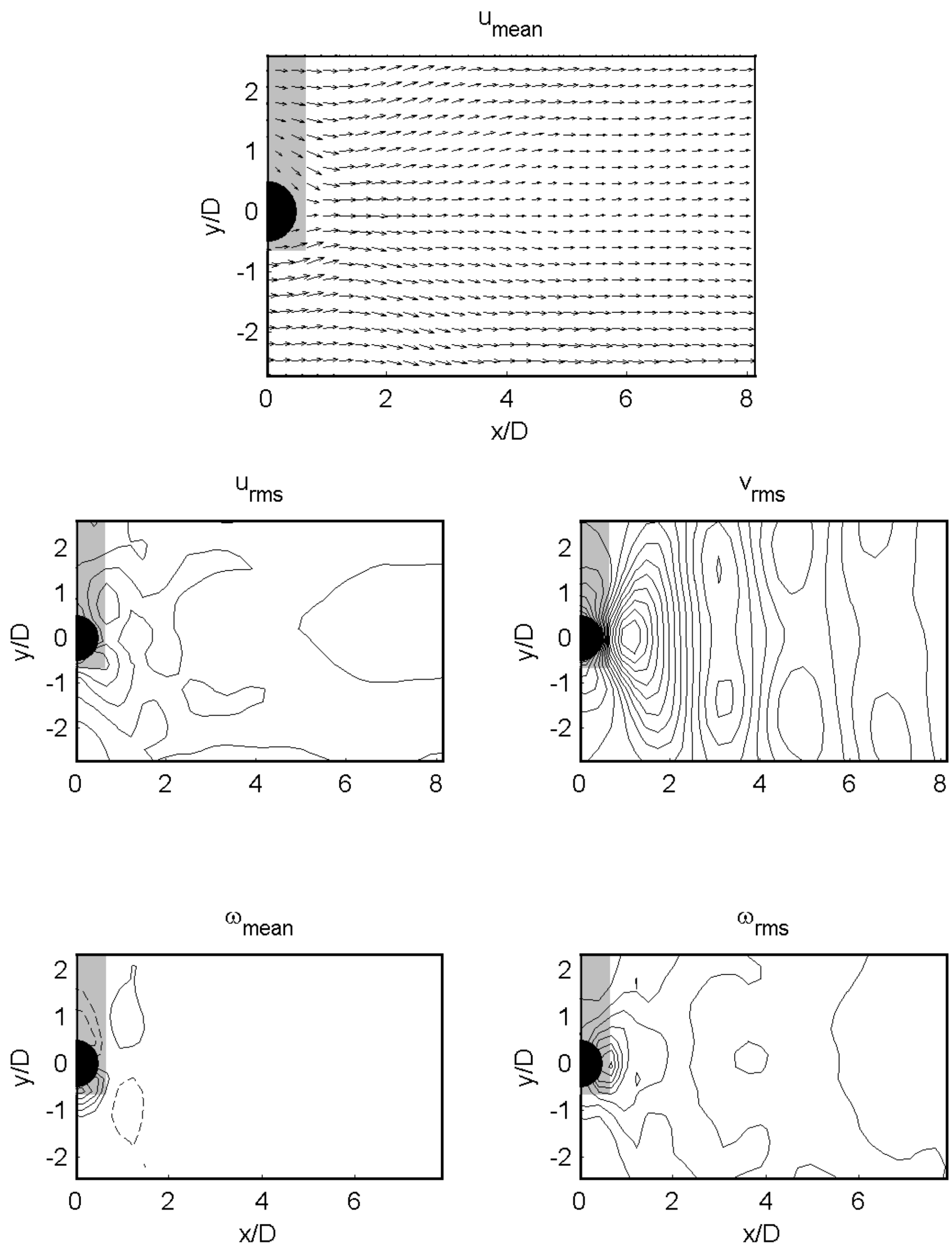

Figure 5.124: Mean and rms normalized velocity (u/U) and normalized vorticity (ωD/U) for case L5; rms velocity contours are at 0.1 intervals; vorticity contours are at 0.5 intervals, negative contours are dashed, positive contours are solid

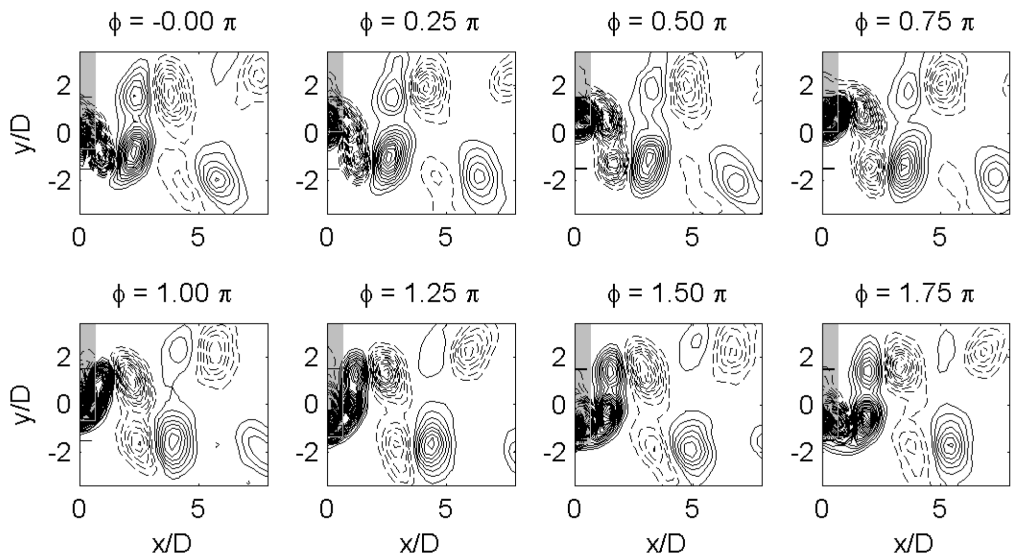

Figure 5.125: Phase-averaged normalized vorticity (ωD/U) for case L5; 1 cycle divided into 16 bins, every other bin shown; minimum contours ±0.2, contour spacing 0.2, positive contours solid, negative contours dashed

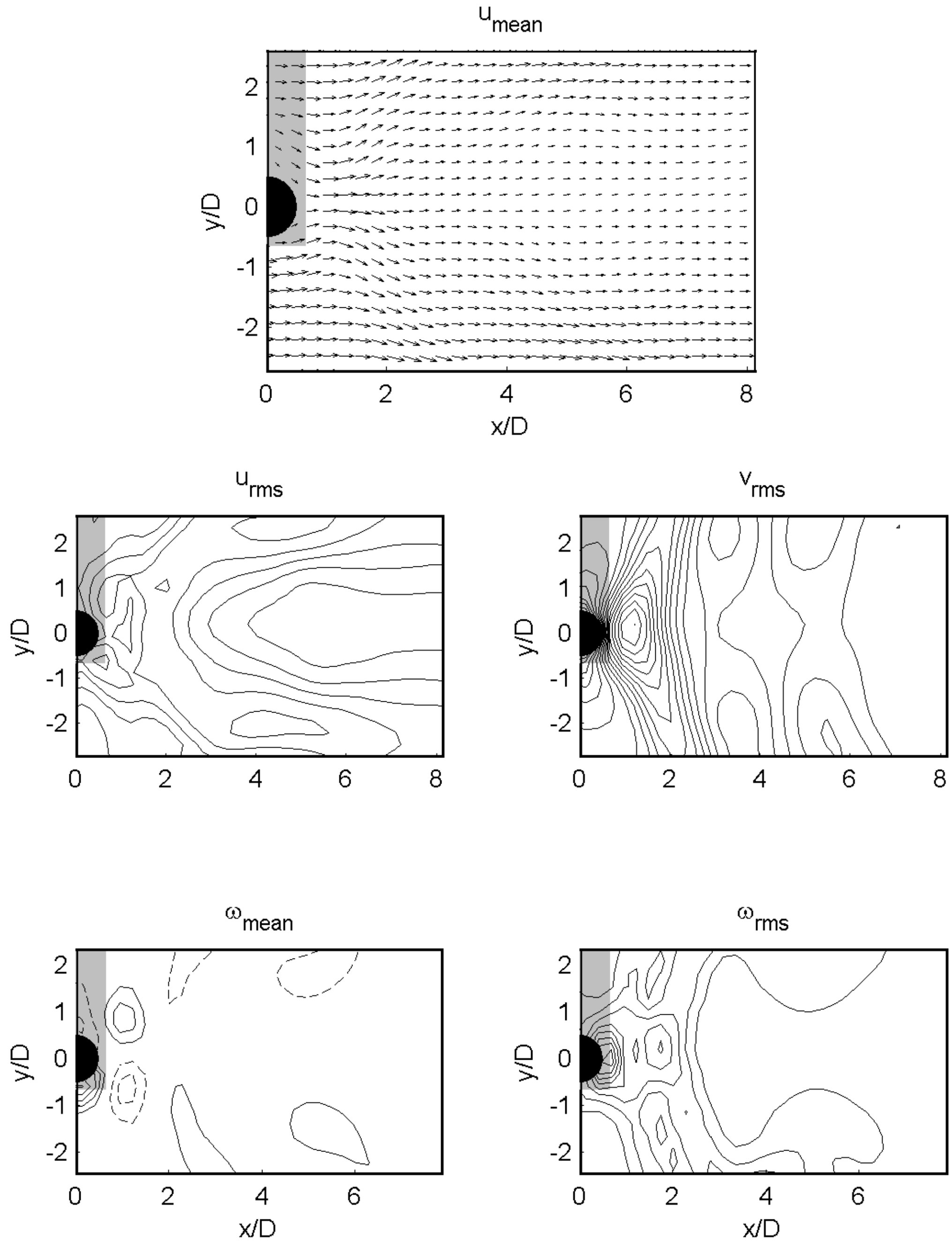

Figure 5.126: Mean and rms normalized velocity (u/U) and normalized vorticity (ωD/U) for case L6; rms velocity contours are at 0.1 intervals; vorticity contours are at 0.5 intervals, negative contours are dashed, positive contours are solid

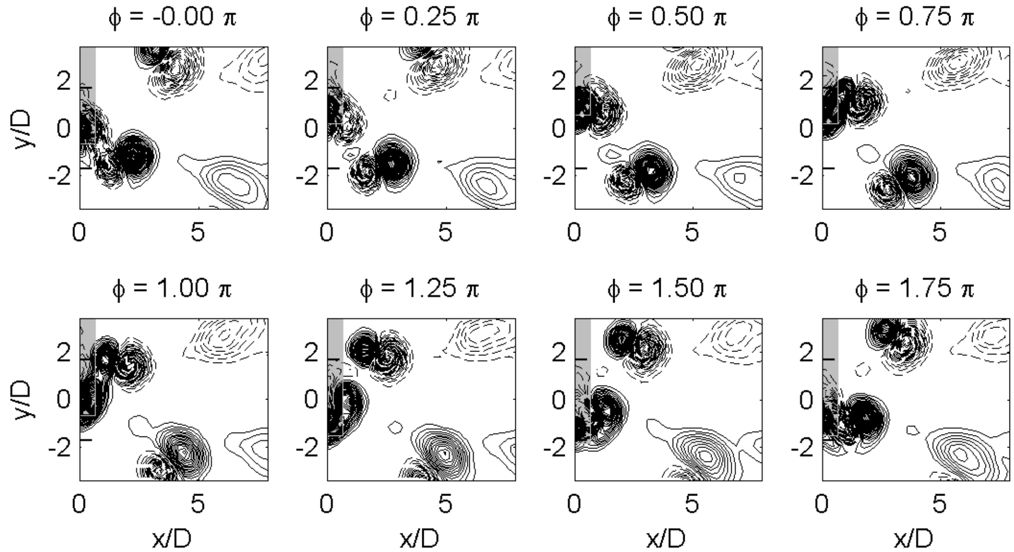

Figure 5.127: Phase-averaged normalized vorticity (ωD/U) for case L6; 1 cycle divided into 16 bins, every other bin shown; minimum contours ±0.2, contour spacing 0.2, positive contours solid, negative contours dashed

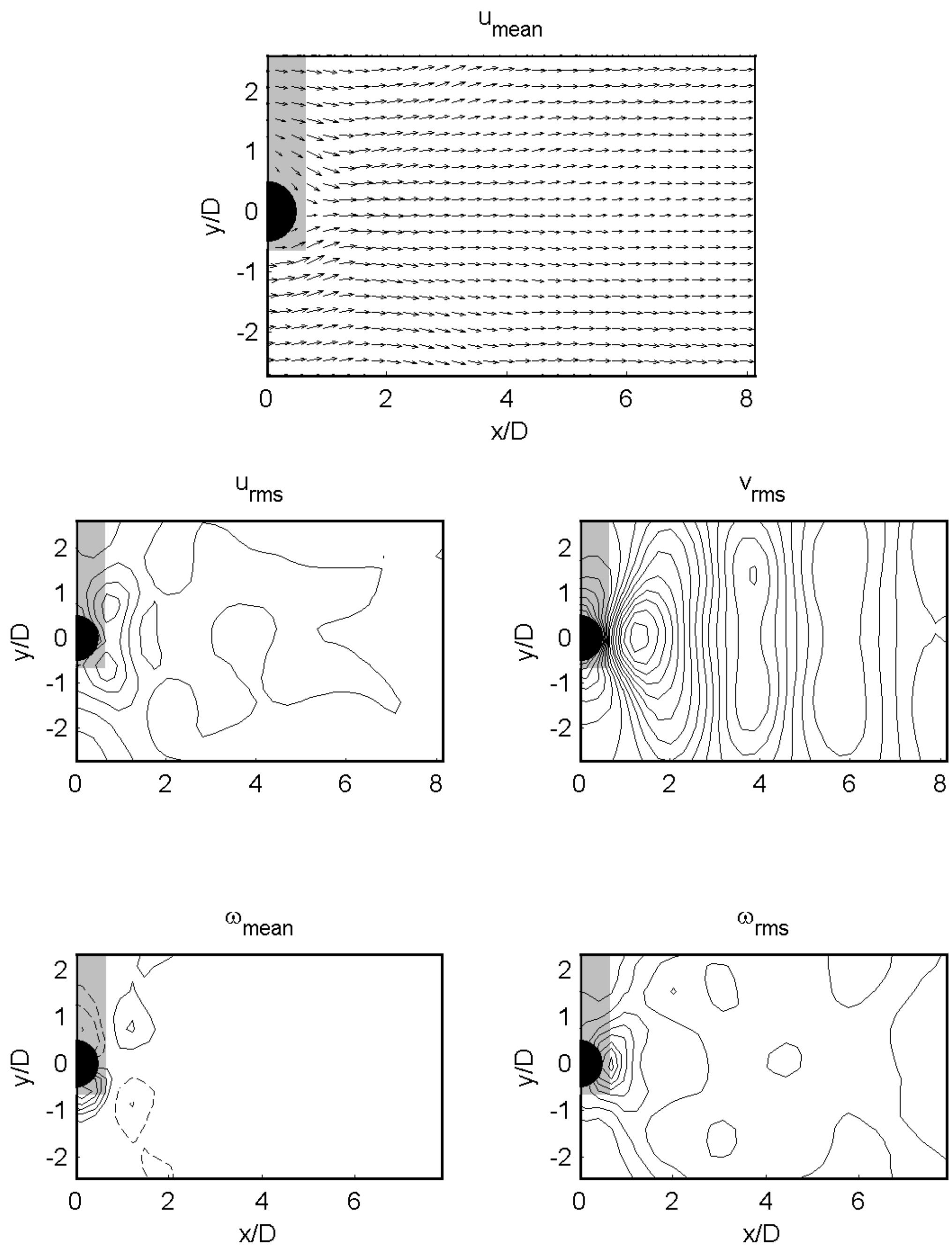

Figure 5.128: Mean and rms normalized velocity (u/U) and normalized vorticity (ωD/U) for case L7; rms velocity contours are at 0.1 intervals; vorticity contours are at 0.5 intervals, negative contours are dashed, positive contours are solid

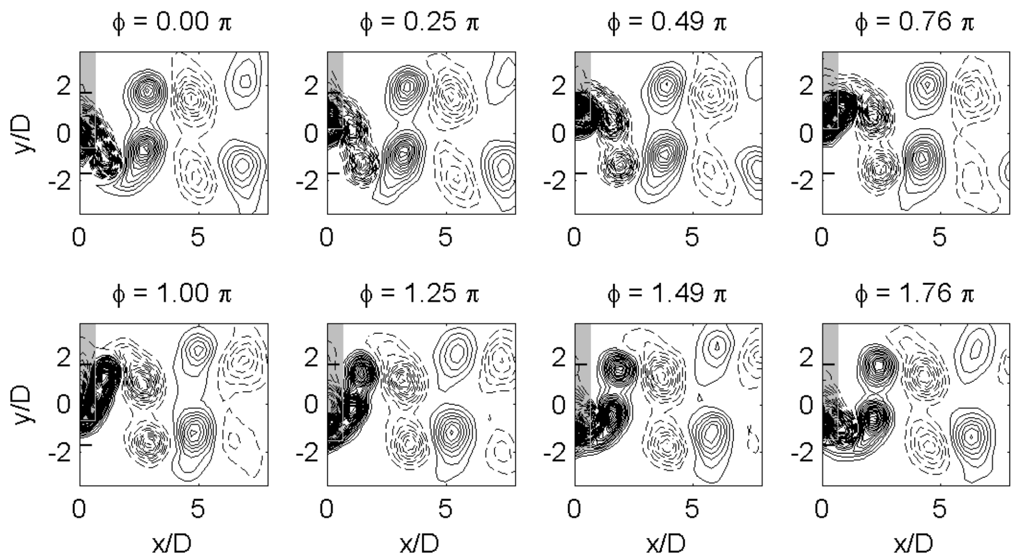

Figure 5.129: Phase-averaged normalized vorticity (ωD/U) for case L7; 1 cycle divided into 16 bins, every other bin shown; minimum contours ±0.2, contour spacing 0.2, positive contours solid, negative contours dashed

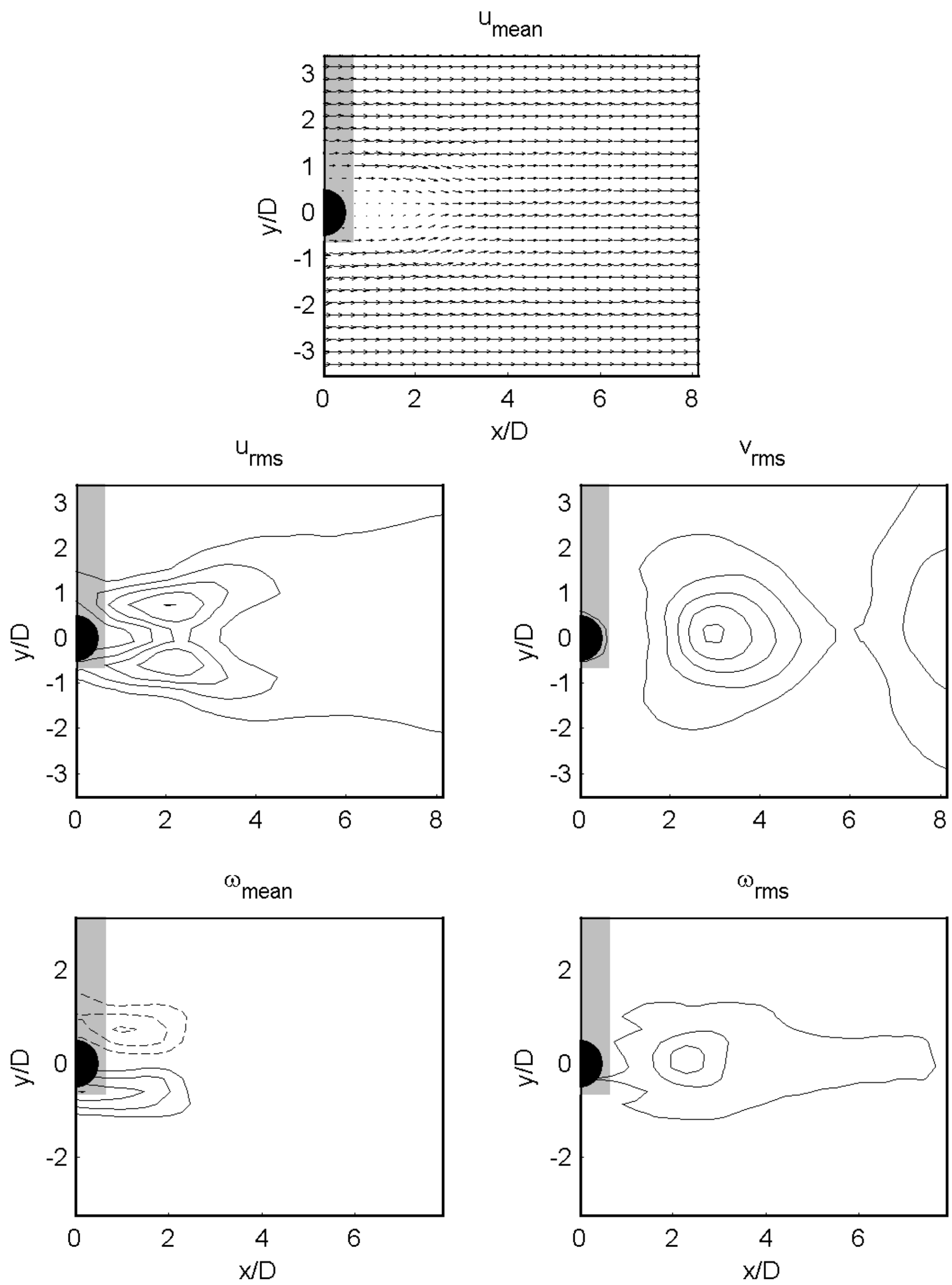

Figure 5.130: Mean and rms normalized velocity (u/U) and normalized vorticity (ωD/U) for case L8; rms velocity contours are at 0.1 intervals; vorticity contours are at 0.5 intervals, negative contours are dashed, positive contours are solid

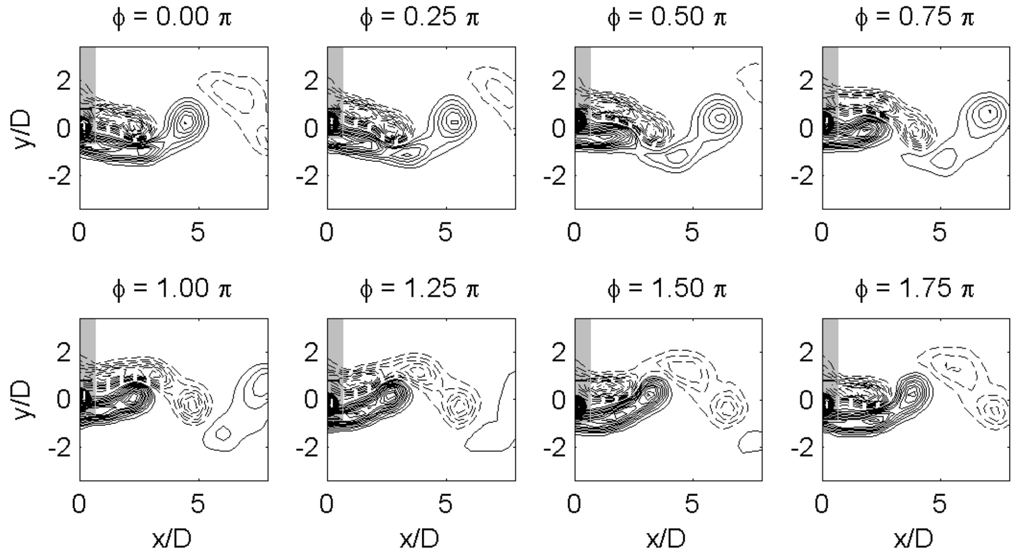

Figure 5.131: Phase-averaged normalized vorticity (ωD/U) for case L8; 1 cycle divided into 16 bins, every other bin shown; minimum contours ±0.2, contour spacing 0.2, positive contours solid, negative contours dashed

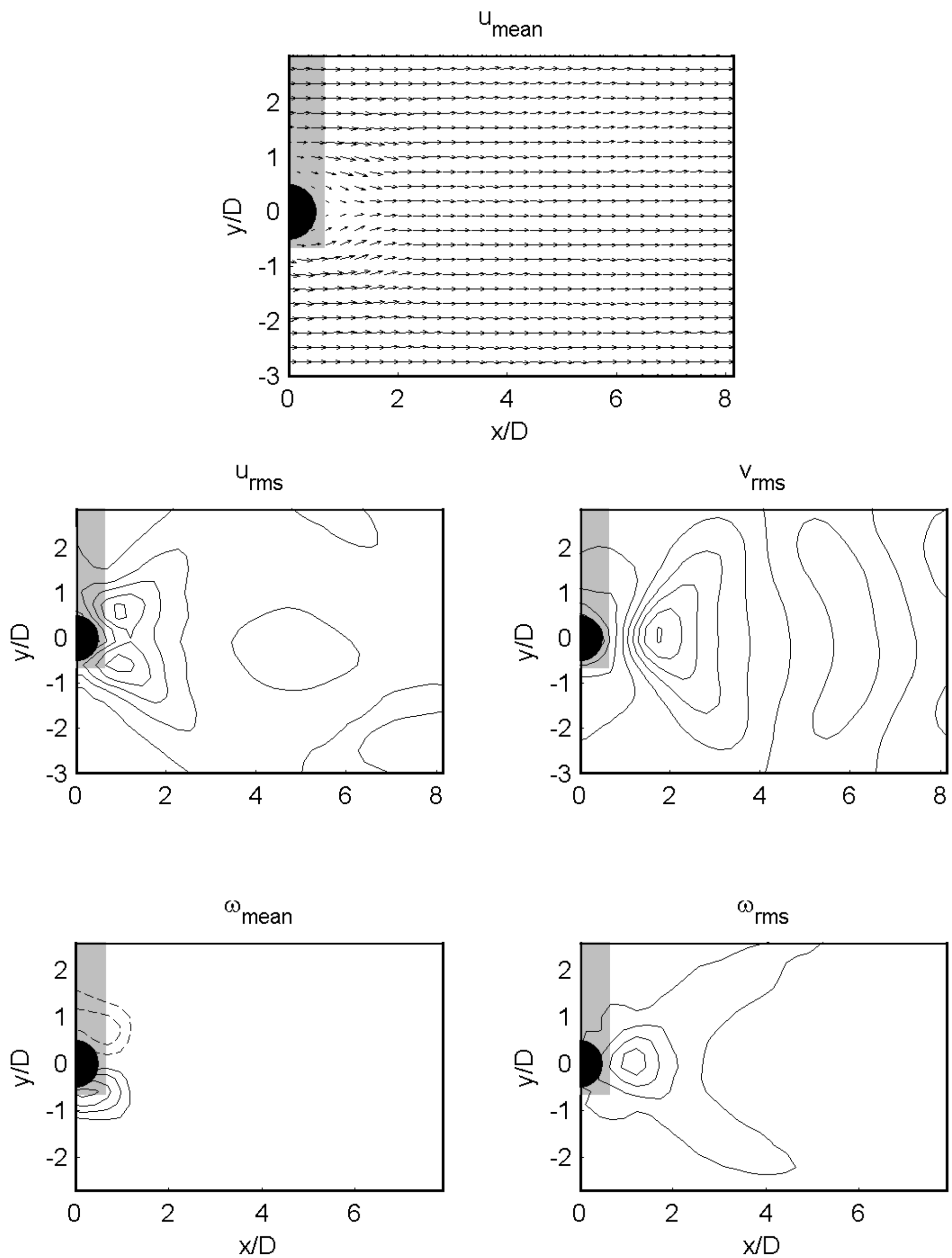

Figure 5.132: Mean and rms normalized velocity (u/U) and normalized vorticity (ωD/U) for case L9; rms velocity contours are at 0.1 intervals; vorticity contours are at 0.5 intervals, negative contours are dashed, positive contours are solid

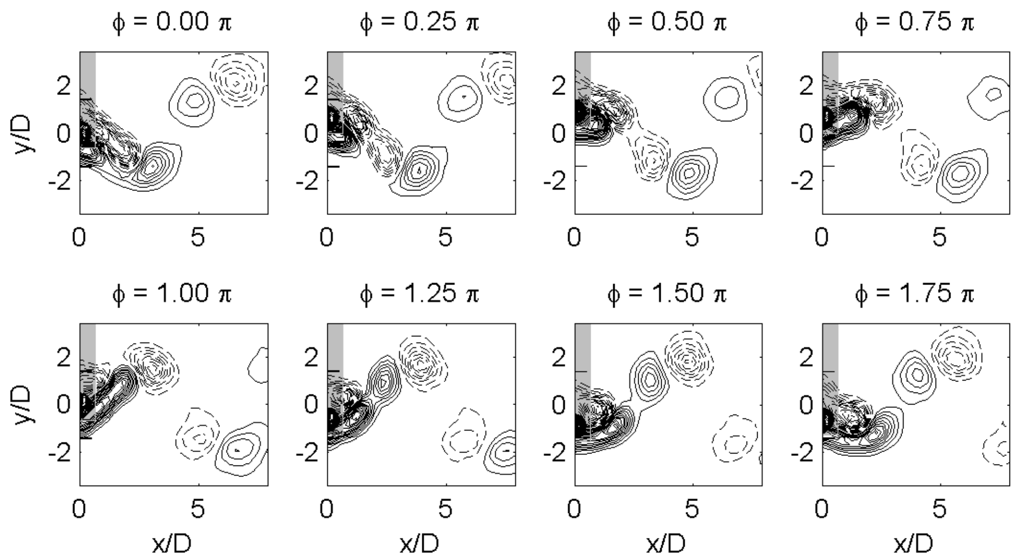

Figure 5.133: Phase-averaged normalized vorticity (ωD/U) for case L9; 1 cycle divided into 16 bins, every other bin shown; minimum contours ±0.2, contour spacing 0.2, positive contours solid, negative contours dashed

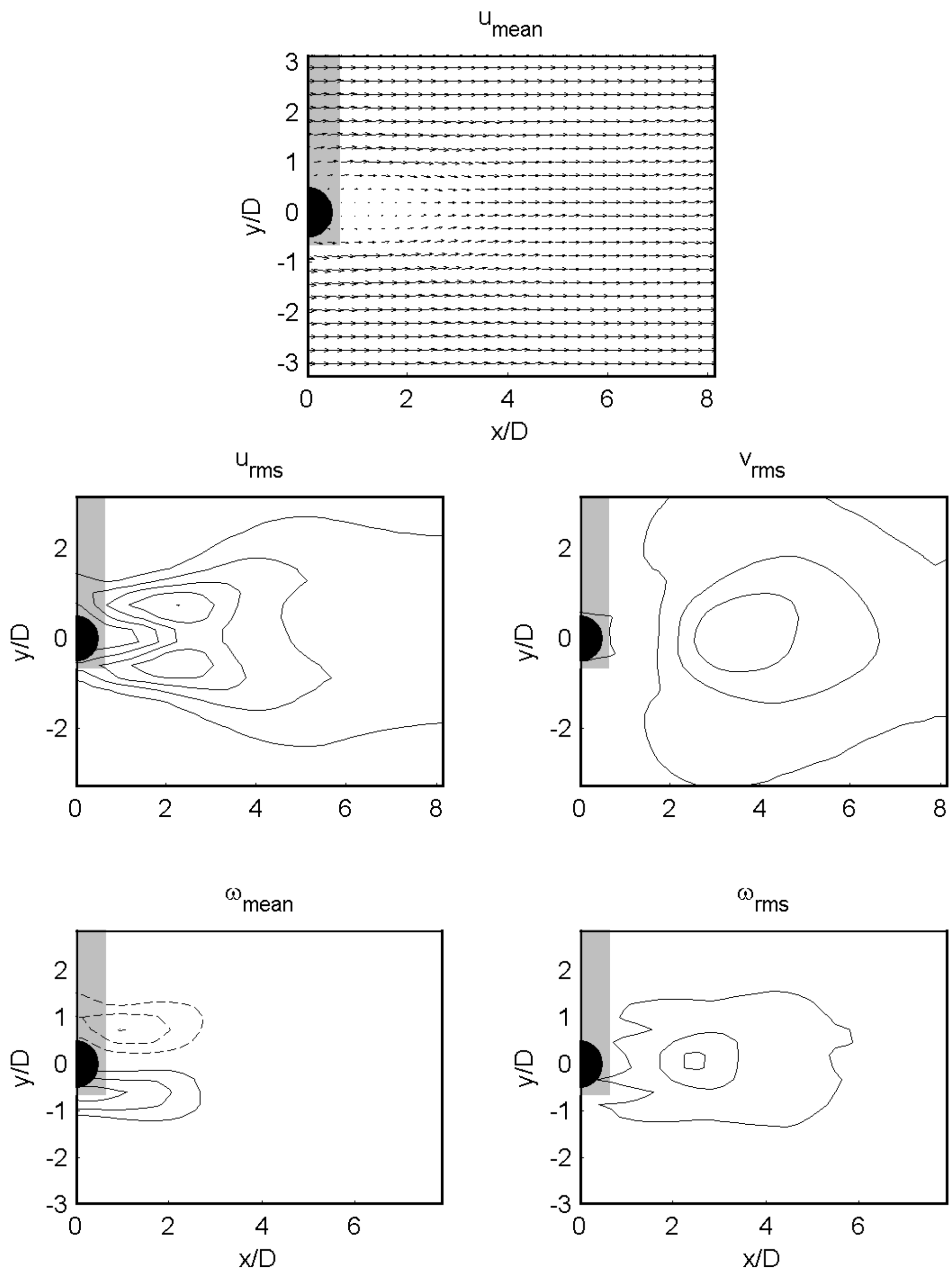

Figure 5.134: Mean and rms normalized velocity (u/U) and normalized vorticity (ωD/U) for case L10; rms velocity contours are at 0.1 intervals; vorticity contours are at 0.5 intervals, negative contours are dashed, positive contours are solid

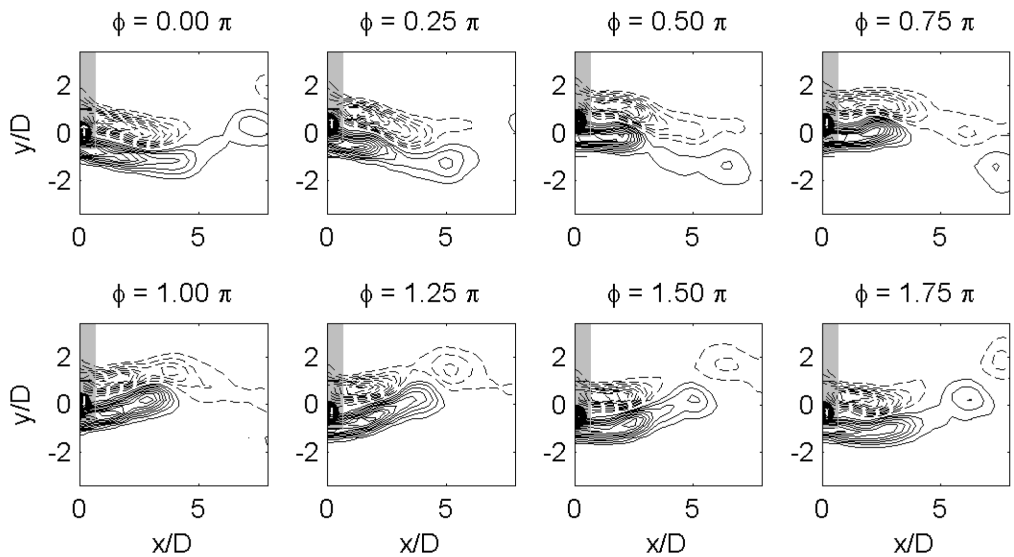

Figure 5.135: Phase-averaged normalized vorticity (ωD/U) for case L10; 1 cycle divided into 16 bins, every other bin shown; minimum contours ±0.2, contour spacing 0.2, positive contours solid, negative contours dashed

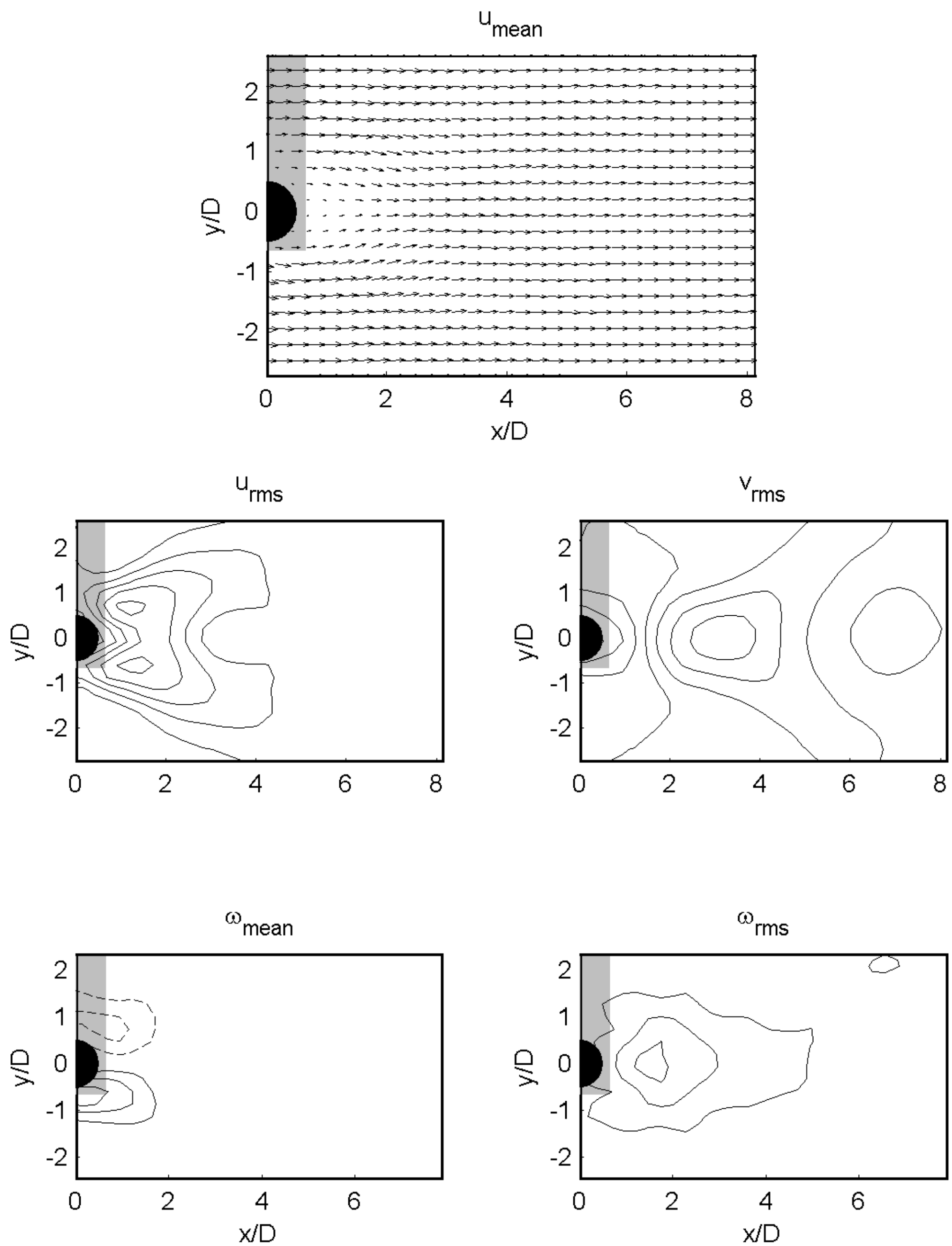

Figure 5.136: Mean and rms normalized velocity (u/U) and normalized vorticity (ωD/U) for case L11; rms velocity contours are at 0.1 intervals; vorticity contours are at 0.5 intervals, negative contours are dashed, positive contours are solid

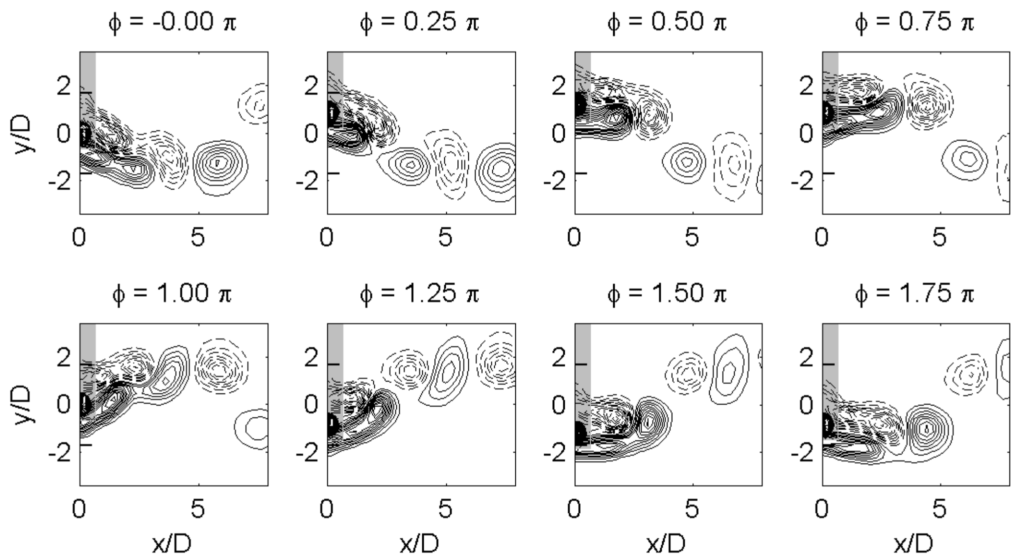

Figure 5.137: Phase-averaged normalized vorticity (ωD/U) for case L11; 1 cycle divided into 16 bins, every other bin shown; minimum contours ±0.2, contour spacing 0.2, positive contours solid, negative contours dashed

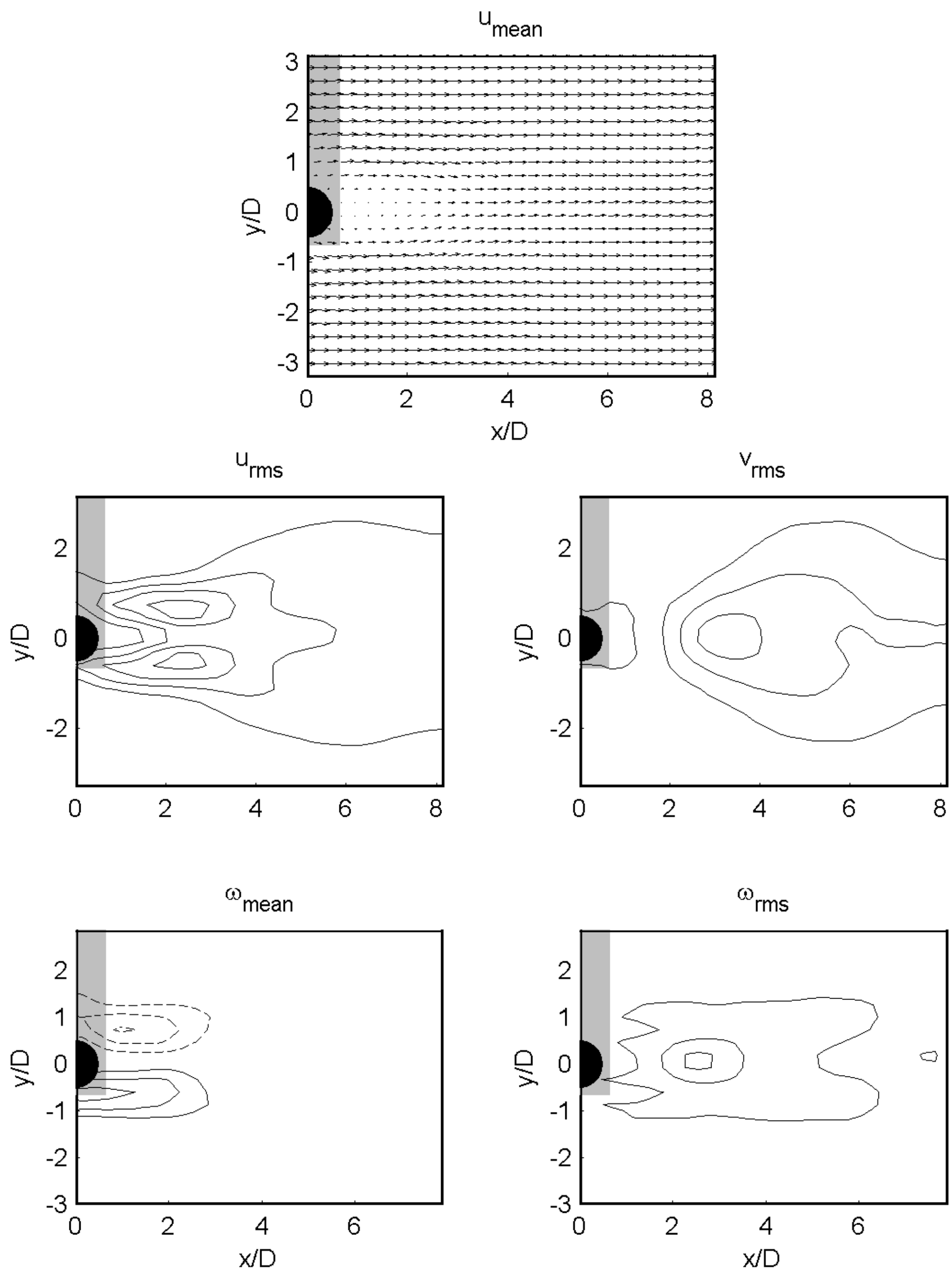

Figure 5.138: Mean and rms normalized velocity (u/U) and normalized vorticity (ωD/U) for case L12; rms velocity contours are at 0.1 intervals; vorticity contours are at 0.5 intervals, negative contours are dashed, positive contours are solid

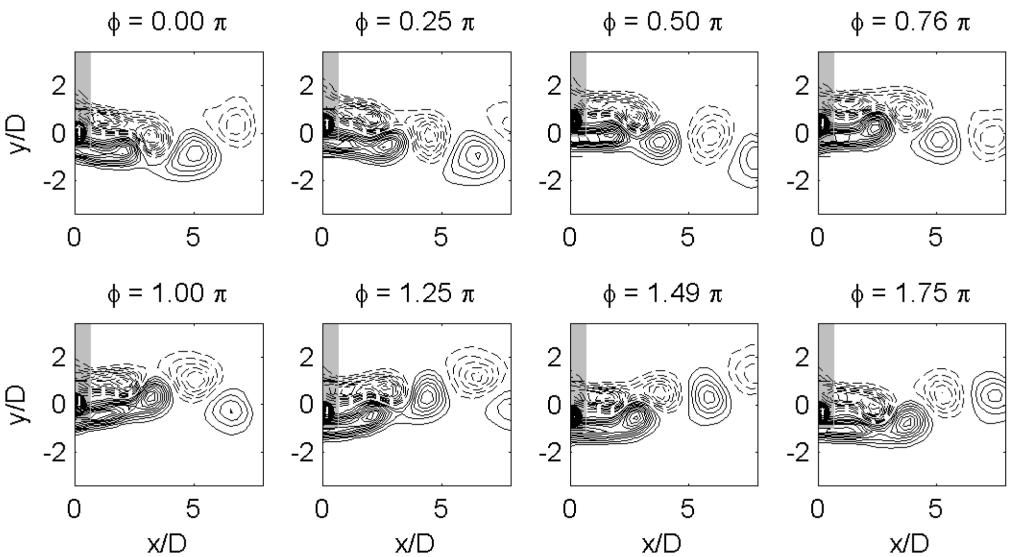

Figure 5.139: Phase-averaged normalized vorticity (ωD/U) for case L12; 1 cycle divided into 16 bins, every other bin shown; minimum contours ±0.2, contour spacing 0.2, positive contours solid, negative contours dashed

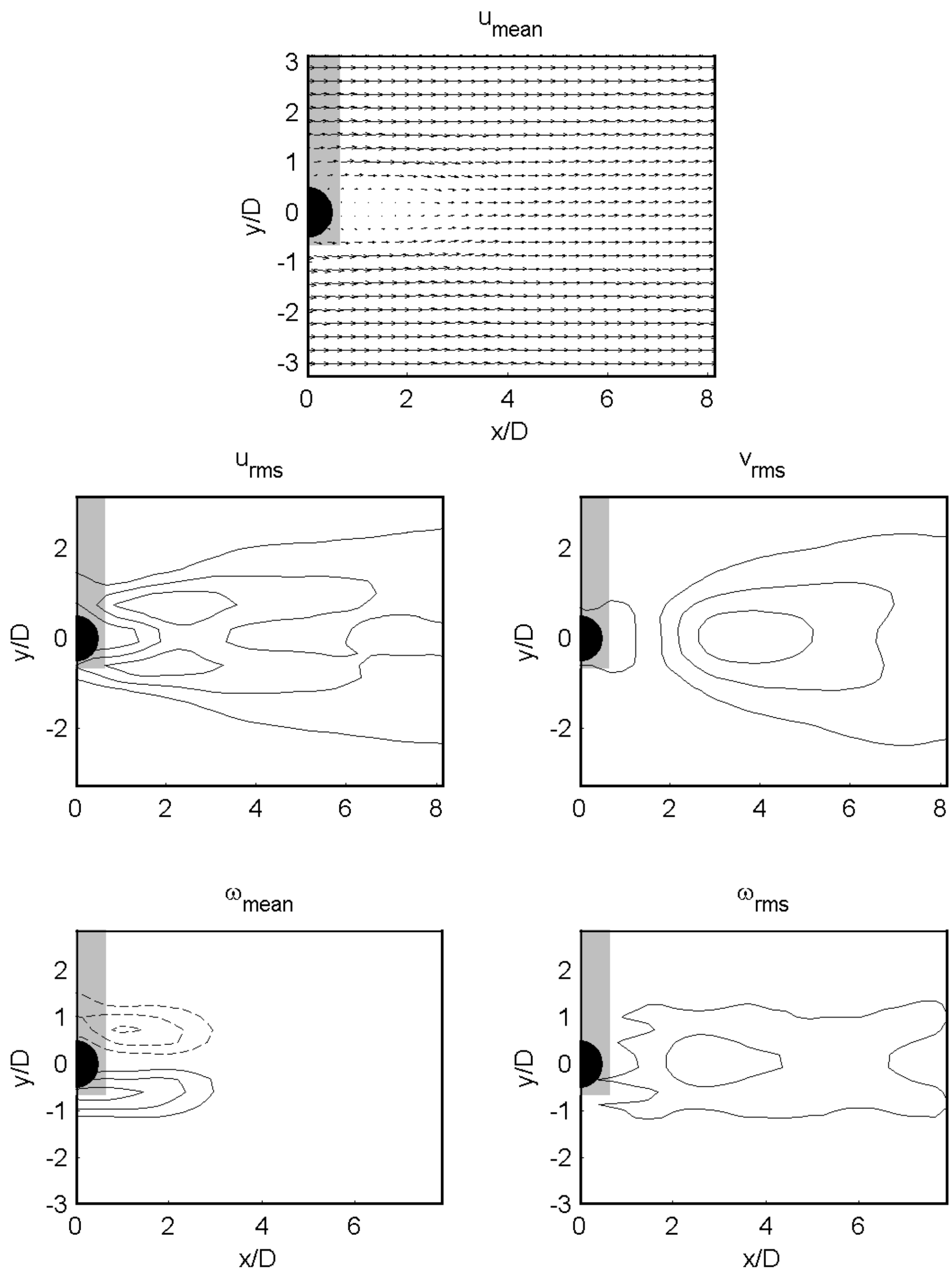

Figure 5.140: Mean and rms normalized velocity (u/U) and normalized vorticity (ωD/U) for case L13; rms velocity contours are at 0.1 intervals; vorticity contours are at 0.5 intervals, negative contours are dashed, positive contours are solid

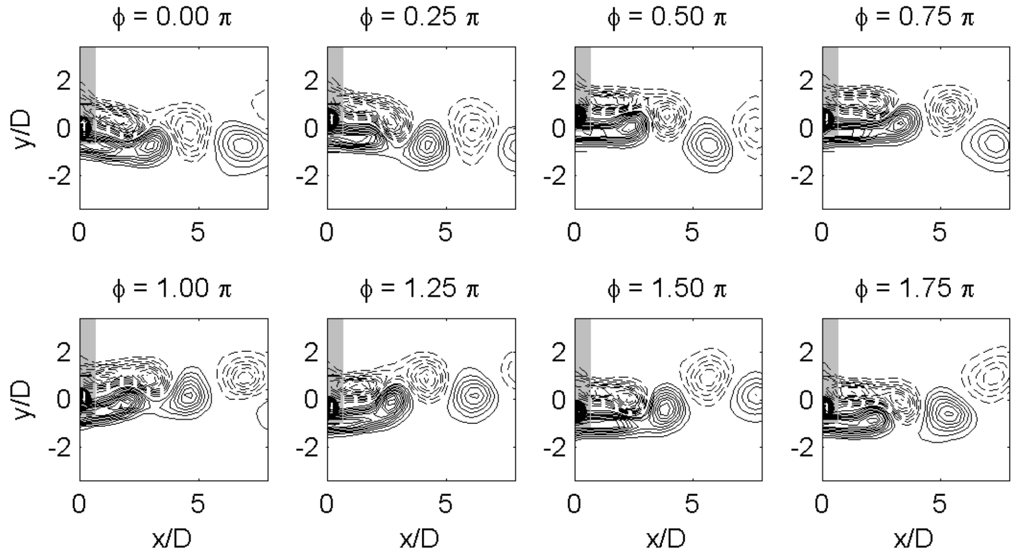

Figure 5.141: Phase-averaged normalized vorticity (ωD/U) for case L13; 1 cycle divided into 16 bins, every other bin shown; minimum contours ±0.2, contour spacing 0.2, positive contours solid, negative contours dashed

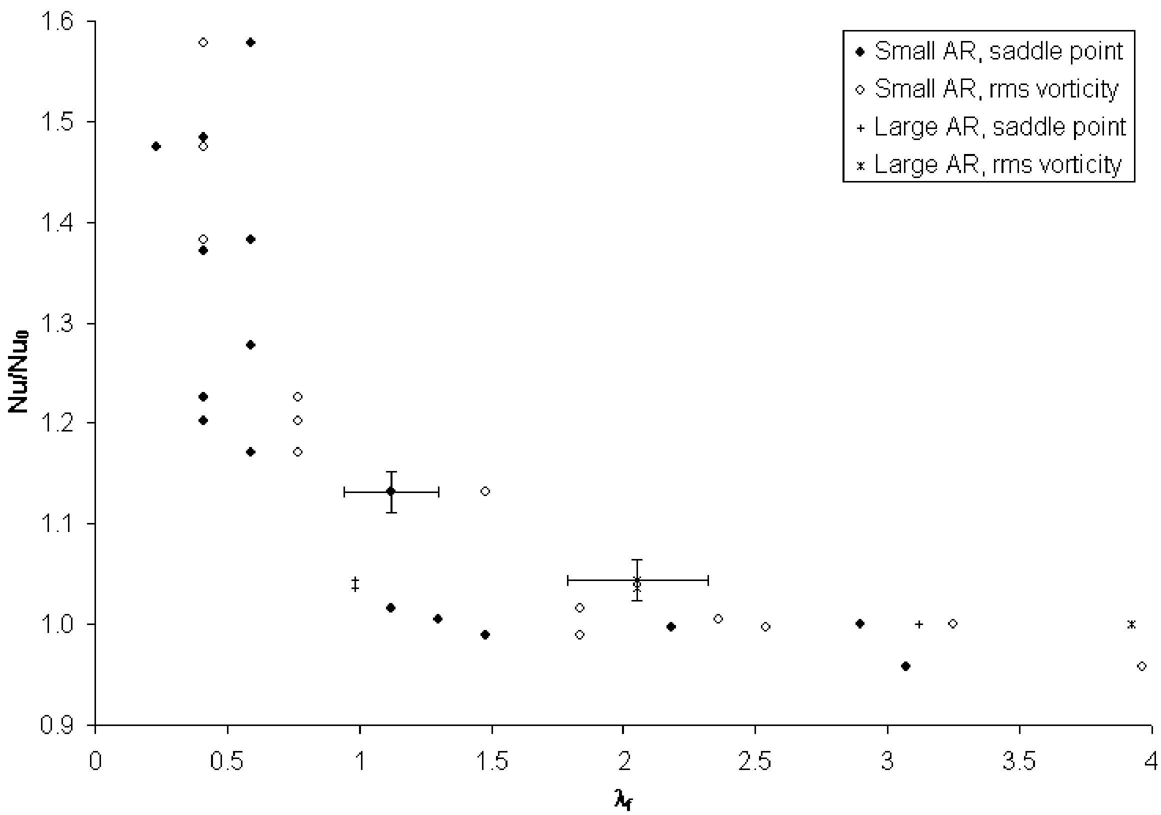

Figure 5.142: Normalized heat transfer coefficient (Nu/Nu_0) vs. formation length (λ_f) for all cases consisting of only single vortices (no pairs)

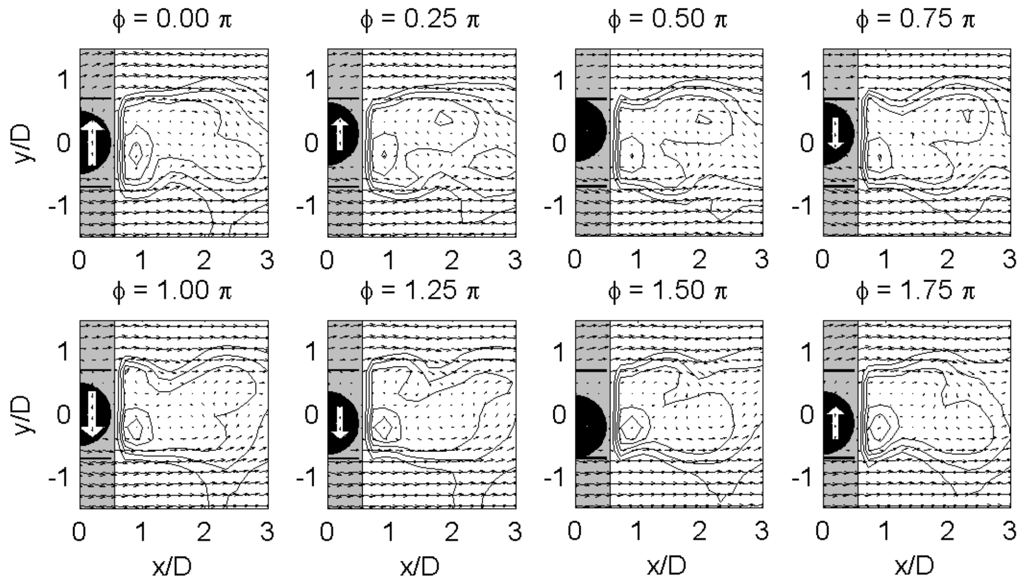

Figure 5.143: Phase-averaged velocity and normalized temperature ((T-T_∞)/(T_{surf}- T_∞)) for case S14; 1 cycle divided into 16 bins, every other bin shown; minimum contour 0.015, contour spacing 0.01

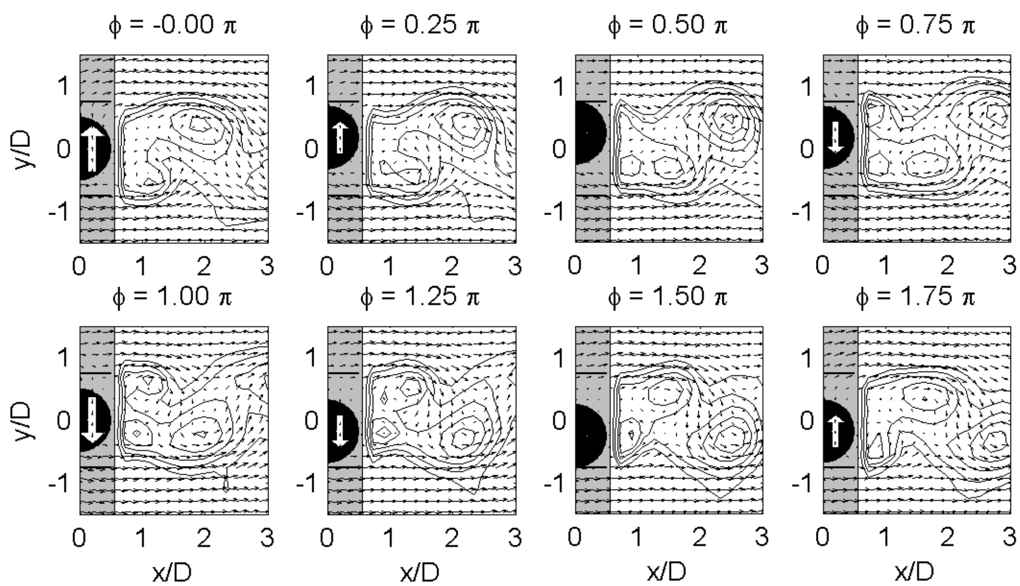

Figure 5.144: Phase-averaged velocity and normalized temperature ((T-T_∞)/(T_{surf}- T_∞)) for case S17; 1 cycle divided into 16 bins, every other bin shown; minimum contour 0.015, contour spacing 0.01

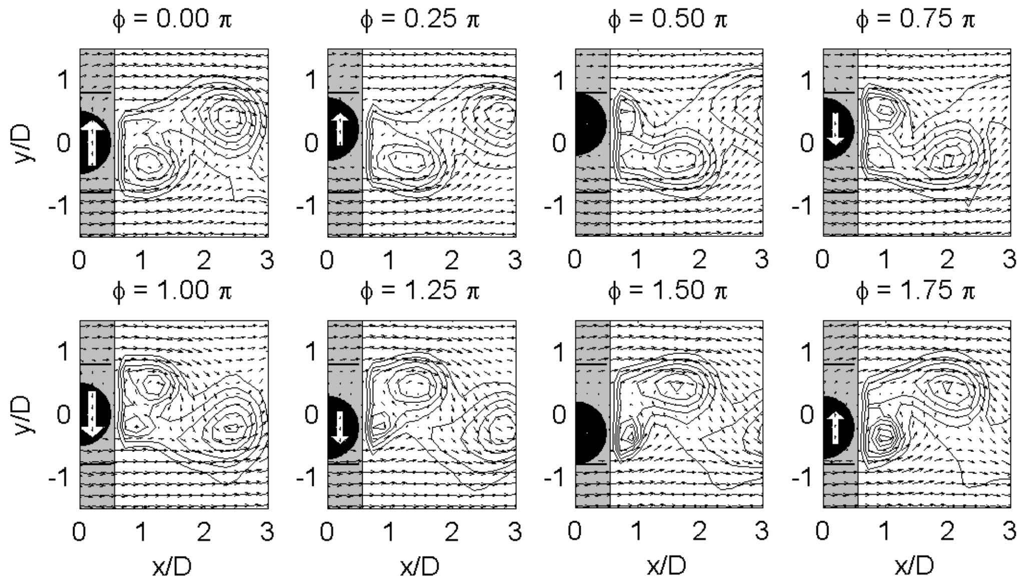

Figure 5.145: Phase-averaged velocity and normalized temperature (($T-T_\infty$)/($T_{surf}-T_\infty$)) for case S20; 1 cycle divided into 16 bins, every other bin shown; minimum contour 0.015, contour spacing 0.01

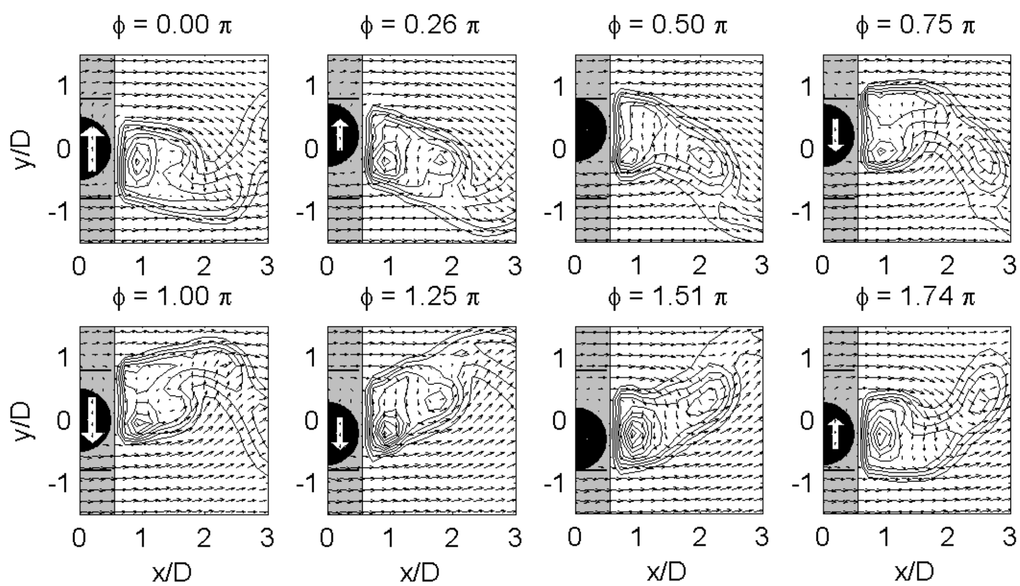

Figure 5.146: Phase-averaged velocity and normalized temperature (($T-T_\infty$)/($T_{surf}-T_\infty$)) for case S23; 1 cycle divided into 16 bins, every other bin shown; minimum contour 0.015, contour spacing 0.01

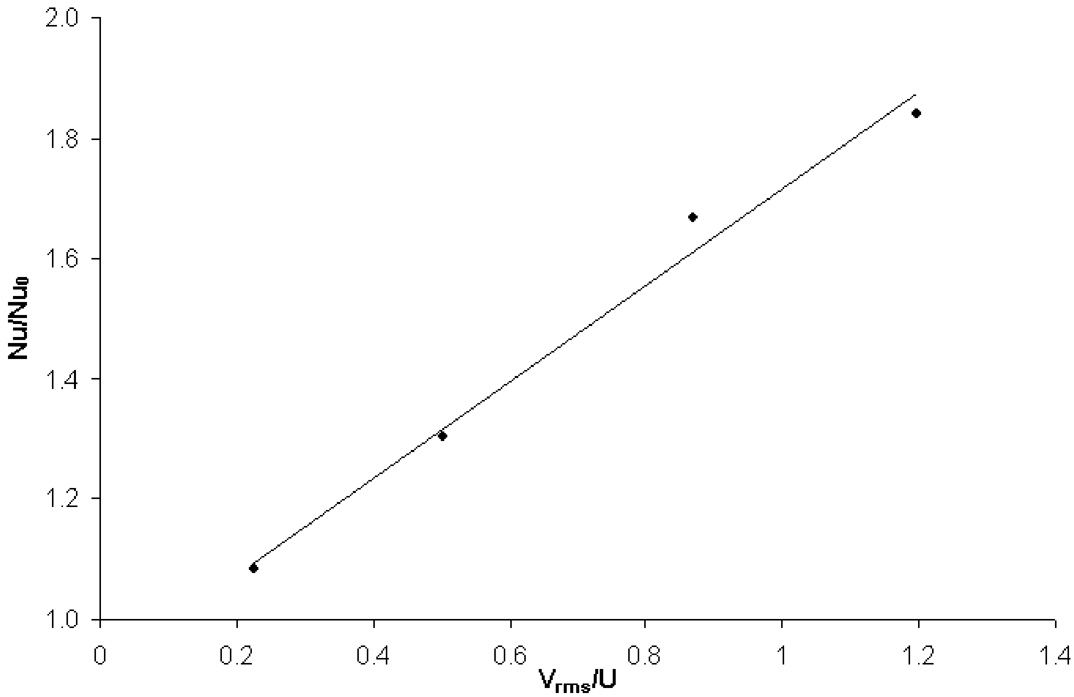

Figure 5.147: Normalized heat transfer coefficient (Nu/Nu_0) vs. normalized rms transverse velocity (V_{rms}/U) for cases S13, S18, S22 and S23

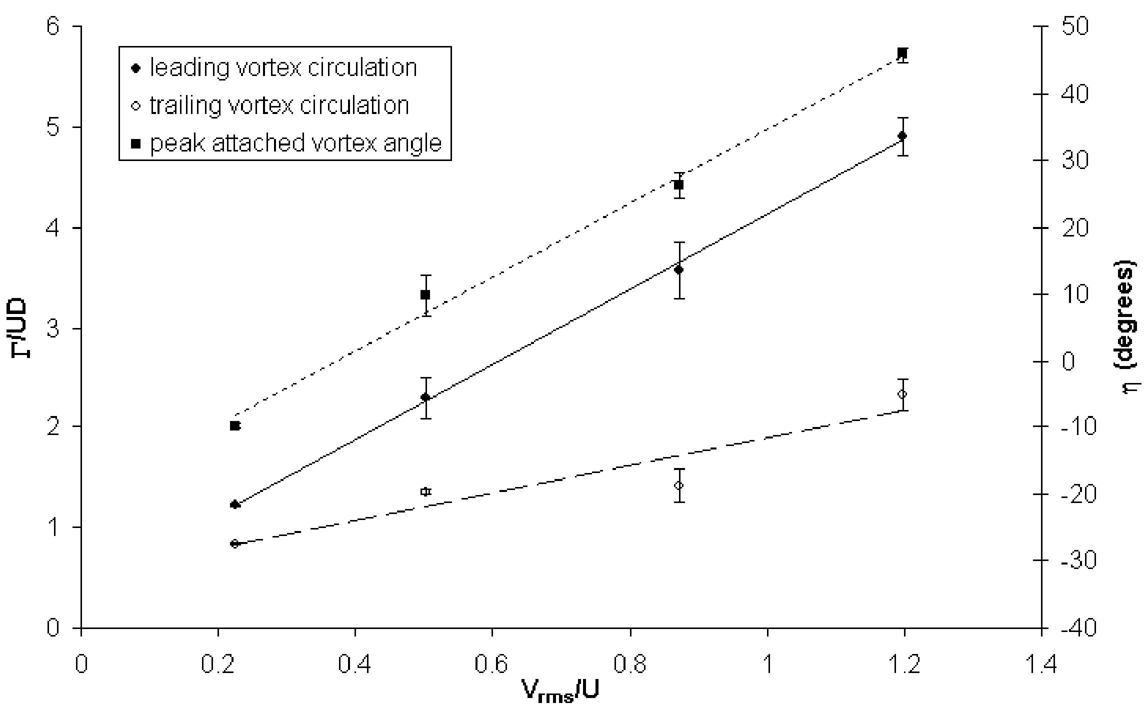

Figure 5.148: Normalized circulation and vortex shedding angle vs. normalized rms transverse velocity (V_{rms}/U) for cases S13, S18, S22 and S23

6 Conclusion

There were two main goals of this study: to understand the mechanism by which transverse cylinder oscillations modify the heat transfer from a heated circular cylinder in cross-flow and to explore the dynamics of the vortex formation process in the wake.

Two sets of experiments were carried out to accomplish these goals. In the first set, the cylinder's heat transfer coefficient was determined over a wide range of oscillation conditions, and the results were compared to established relationships between oscillation conditions and wake structure. The second set of experiments used DPIT/V to measure the temperature and velocity fields in the near-wake for a reduced set of cases. This allowed the vortex formation process and the effects of wake structure on heat transfer to be examined directly. The particular cases observed were chosen to be representative of the variety of wake structures that exist for this type of flow. Based upon the results of this investigation, a number of conclusions can be drawn.

First, heat transfer enhancement associated with oscillations at frequencies near the Strouhal frequency and its harmonics is limited to amplitude ratios less than about 0.5. For larger amplitude ratios, the cylinder heat transfer coefficient is primarily determined by the wake mode and the transverse velocity. The role of wake mode in determining the heat transfer coefficient was observed for the first time. While previous authors have been unsuccessful at correlating the transverse velocity with the heat transfer coefficient, it was shown in this investigation that within a particular wake mode and away from effects associated with the Strouhal frequency, the transverse cylinder velocity is the primary factor responsible for variations in heat transfer coefficient.

Two new mechanisms by which the wake structure affects the heat transfer were identified. The dynamics of the vortex formation process, including the movement of the vortices during roll-up, were found to affect the cylinder heat transfer coefficient significantly. The dependence of heat transfer coefficient on wake mode is explained by this mechanism. In addition, the spacing between shed vortices in the streamwise direction was correlated with heat transfer coefficient for the 2S mode. The streamwise spacing is believed to affect the heat transfer coefficient by influencing the entrainment of freestream temperature fluid by vortices as they are forming. In addition to these new mechanisms, the effect of roll-up distance discovered by Park (1998) was observed.

The transverse cylinder velocity was found to have two effects on heat transfer coefficient. For a fixed wake structure, the effectiveness of the wake vortices at enhancing heat transfer depends on their circulation. Additional vorticity produced by the cylinder's transverse oscillation rolls up in the wake and is therefore a factor in determining the circulation of the wake vortices. Transverse velocity also turns the wake with respect to the freestream flow, thereby spreading the heat transfer enhancement over a larger portion of the cylinder.

Aspect ratio appears to play a role in determining the heat transfer coefficient mainly for non-oscillating cylinders and cases with weak synchronization of the wake with the cylinder oscillations. Examinations of the wake structure at the mid-span for equivalent non-dimensional oscillation conditions revealed no significant differences for the two aspect ratios used in this study. This suggests that the different levels of heat transfer enhancement observed are due to end effects. An implication of this observation is that the benefits of a high aspect ratio heat exchanger element may be achievable using low aspect ratio oscillating elements. However, this idea requires further testing over a wider range of aspect ratios.

A new phenomenon was discovered in which the wake structure switches back and forth between distinct wake modes and between variations of the same wake mode. Temperature induced variations in the fluid viscosity are believed to be the cause of this mode-switching. It is hypothesized that this results in changes to the vorticity flux and kinetic energy flux into the wake, thereby changing the wake mode and the heat transfer coefficient. This discovery points to the role of viscosity and of the shear layer fluxes in determining wake mode, and this may lead to improved understanding of the vortex formation and pinch-off processes in wakes in general. This has broad relevance to bluff-body flows and unsteady separated flows, not just to heat transfer applications.

Additional research into mode-switching needs to be performed. Identifying the criteria for the occurrence of mode-switching would reveal a great deal about wake formation processes. The proposed model of the mode-switching mechanism needs to be quantified and tested. Further experiments in fluids with different viscosity-temperature relationships are needed. Also, numerical simulations in which the temperature dependence of viscosity can be prescribed or eliminated would be useful.

Appendix A
Digital particle image thermometry/velocimetry

Digital particle image thermometry/velocimetry (DPIT/V) is a combination of two techniques that allows the temperature field and the velocity field to be measured simultaneously in a thin cross section of a flow. Digital particle image velocimetry (DPIV) is a technique for determining the velocity field from consecutive images of particles suspended in a flow using cross-correlations. For DPIV, the color of the particles is not relevant, and experiments can be carried out using monochromatic light and reflective or fluorescent particles. Digital particle image thermometry (DPIT) refers to the extraction of temperature field information from the color of thermochromic liquid crystal (TLC) particles, which change their reflected wavelength with temperature, suspended in the flow. DPIT/V combines these two techniques by using the TLC particles as both temperature indicators and flow tracers.

DPIT/V is carried out by seeding the flow with TLC particles, illuminating a cross section with a sheet of white light and digitally recording color images of the illuminated particles. The images are then analyzed to determine the velocity and temperature fields in the flow. The intensity field of the images, i.e., the black and white image left when color information is removed, is used to determine the velocity field through standard DPIV. The color information in the images is used to determine the temperature field.

DPIV is the digital version of the particle image velocimetry technique and was first used by Willert and Gharib (1991). They captured images of particle-seeded flows illuminated with a sheet of laser light using a video camera and digitizer. Cross-correlations of small windows in consecutive images produced displacement estimates, which were converted to velocities using the known time separation between images. DPIV processing techniques have progress since this initial implementation. A comparison of widely used DPIV processing techniques can be found in McKenna and McGillis (2002).

DPIT depends upon the property of TLC that they selectively reflect light of a particular wavelength. The TLC acts as a Bragg scattering volume grating with a pitch determined by the arrangement of molecules. Individual molecules of TLC, also called chiral nematic liquid crystals because of their structure, become arranged in planes with the long axis of each molecule aligned in the same direction. The alignment directions of adjacent planes of molecules are slightly rotated with respect to one another. The distance normal to the planes required for a set of planes to undergo 360° of rotation defines the grating pitch. This pitch depends on the inter-plane separation distance and rotation angle, which both depend on temperature. Bragg scattering results in incident light being scattered at angles that depend on the wavelength of the light and the pitch of the grating. The apparent color of the TLC therefore depends on the temperature and on the angle between the incident light and the observer. Because the relationship between color and temperature is sensitive to chemical composition and to the optical arrangement, it is necessary to calibrate TLC for use in experiments. A complete discussion of TLC can be found in Parsley (1991).

TLC has been used extensively for measuring temperature on surfaces, and in recent years has been dispersed within fluids as well. Perhaps the most familiar examples of TLC on surfaces are “Mood Rings” and strip thermometers. The first reported use of TLC applied to a surface for fluid mechanics research was in a qualitative study by Klein (1968). More recently, TLC has been used to seed fluid flows in order the measure the temperature field within the flow. Rhee et al. (1984) pioneered this use, though their results were only qualitative. The DPIT technique in its present form was introduced by Dabiri and Gharib (1991) and was used to investigate the wakes of heated cylinders by Park et al. (2001).

The quantitative measurement of temperature fields using TLC has advanced considerably in recent years. A review of various color decomposition schemes used for TLC calibration is presented by Park (1998, §2.3). Sabatino et al. (2000) introduced a calibration technique that accounts for variation in viewing and illumination angles across the field of view for TLC applied to a surface. They essentially calibrated each pixel of their video camera independently. Günther and von Rohr (2002) dealt with the same viewing and illumination angle issues for fluid-dispersed TLC particles using a telecentric imaging system. According to Park (1998), the uncertainty in temperature for individual TLC particles is 5% to 20% of the useful temperature range. A range of uncertainties is used because the calibration curve is non-linear, so the uncertainty varies over the useful temperature range. For 32 pixel by 32 pixel averaging windows, this uncertainty is reduced to 2% to 10%.

There are other techniques available that measure the velocity and temperature field in a flow simultaneously. One common technique is the use two-color planar laser induced fluorescence (PLIF) and DPIV simultaneously. In this technique, the ratio of the intensities of two fluorescing dyes is related to temperature. One example of the use of this technique is Seuntiens et al. (2001) who studied the wake of a non-oscillating cylinder in a tow tank. While this technique is effective, it is better suited to large temperature differences than to the small temperature differences used in this study.

Appendix B
Steady, one-dimensional model for estimating heat transfer coefficient using embedded thermocouple data

An expression for the heat transfer coefficient is derived based upon the one-dimensional physical model of the cylinder structure described in §2.6. The resulting expression and the internal temperature distribution are then evaluated to determine the impact of the one-dimensional assumption.

Heat transfer inside the cylinder is described by the conductive heat equation, which in cylindrical coordinates is written as

$$\rho C\frac{\partial T}{\partial t} = k\left[\frac{1}{r}\frac{\partial}{\partial r}\left(r\frac{\partial T}{\partial r}\right) + \frac{1}{r^2}\frac{\partial^2 T}{\partial \theta^2} + \frac{\partial^2 T}{\partial z^2}\right] + p_{in}\,, \tag{B.1}$$

where T is temperature, t is time, r is the radial distance from the cylinder axis, θ is the angle in the plane perpendicular to the cylinder axis, and z is the coordinate along the cylinder axis. The power input per unit volume, p_{in}, is related to the total power input, P_{in}, by

$$p_{in} = \frac{P_{in}}{\pi L\left(R_b^2 - R_a^2\right)}. \tag{B.2}$$

For the model, L is taken to be the heated length of the cylinder plus the 6.35 mm unheated length at the free end.

Assuming that the temperature depends only on the radial coordinate and is steady, this equation becomes

$$\frac{1}{r}\frac{\partial}{\partial r}\left(r\frac{\partial T}{\partial r}\right) + \frac{p_{in}}{k} = 0. \tag{B.3}$$

With the appropriate values of p_{in} and k, equation (A.1) applies to all four regions of the cylinder. From the steady-state assumption, it is apparent that the heat flux at the surface must balance the power input

$$-k_d \left.\frac{dT}{dr}\right|_{r=R_d} = h\left(T_{surf} - T_\infty\right) = \frac{P_{in}}{2\pi R_d L}, \tag{B.4}$$

where h is the convective heat transfer coefficient, T_{surf} is the surface temperature of the cylinder and T_∞ is the freestream temperature. The steady-state assumption also requires that the temperature is uniform in the region $0 \le r \le R_a$, regardless of the material properties in that region. Since the thermocouple is entirely contained in region a, it is evident that

$$T(r) = T_{tc} \text{ for } 0 \le r \le R_a. \tag{B.5}$$

The solutions for the separate regions must match at the region boundaries in order to produce a continuous temperature distribution with finite heat flux.

The general solution of equation (B.1) is

$$T(r) = -\tfrac{1}{4} r^2 \frac{p_{in}}{k} + A \ln(r) + B, \tag{B.6}$$

where A and B are constants. Applying the boundary and matching conditions yields the solution

$$T_a(r) = T_{tc}, \tag{B.7a}$$

$$T_b(r) = T_{tc} - \frac{P_{in}}{2\pi L}\left[\frac{1}{k_b}\left\{\frac{1}{2}\left(\frac{R_a^2 - r}{R_b^2 - R_a^2}\right) - \left(\frac{R_a^2}{R_b^2 - R_a^2}\right)\ln\left(\frac{r}{R_a}\right)\right\}\right], \tag{B.7b}$$

$$T_c(r) = T_{tc} - \frac{P_{in}}{2\pi L}\left[\frac{1}{k_c}\ln\left(\frac{r}{R_b}\right) + \frac{1}{k_b}\left\{\frac{1}{2} - \left(\frac{R_a^2}{R_b^2 - R_a^2}\right)\ln\left(\frac{R_b}{R_a}\right)\right\}\right], \text{ and} \tag{B.7c}$$

$$T_d(r) = T_{tc} - \frac{P_{in}}{2\pi L}\left[\frac{1}{k_d}\ln\left(\frac{r}{R_c}\right) + \frac{1}{k_c}\ln\left(\frac{R_c}{R_b}\right) + \frac{1}{k_b}\left\{\frac{1}{2} - \left(\frac{R_a^2}{R_b^2 - R_a^2}\right)\ln\left(\frac{R_b}{R_a}\right)\right\}\right], \tag{B.7d}$$

where the subscript on T indicates the region in which each equation applies. A plot of this temperature profile is shown in Figure B.1 using realistic values for the various parameters. Writing the surface temperature in terms of the thermocouple temperature gives the relationship

$$T_{surf} = T_{tc} - \frac{P_{in}}{2\pi L}\left[\frac{1}{k_d}\ln\left(\frac{R_d}{R_c}\right) + \frac{1}{k_c}\ln\left(\frac{R_c}{R_b}\right) + \frac{1}{k_b}\left\{\frac{1}{2} - \left(\frac{R_a^2}{R_b^2 - R_a^2}\right)\ln\left(\frac{R_b}{R_a}\right)\right\}\right]. \quad \text{(B.8)}$$

Equation (B.8) expresses that the cylinder surface temperature differs from the thermocouple temperature by an amount that depends linearly on the power input, P_{in}. The constant multiplying P_{in} is only a function of the cylinder's material properties and dimensions.

Combining equation (B.4) with equation (B.8) yields the heat transfer coefficient

$$h = \frac{P_{in}/2\pi R_d L}{T_{tc} - \frac{P_{in}}{2\pi L}\left[\frac{1}{k_d}\ln\left(\frac{R_d}{R_c}\right) + \frac{1}{k_c}\ln\left(\frac{R_c}{R_b}\right) + \frac{1}{k_b}\left\{\frac{1}{2} - \left(\frac{R_a^2}{R_b^2 - R_a^2}\right)\ln\left(\frac{R_b}{R_a}\right)\right\}\right] - T_\infty}. \quad \text{(B.9)}$$

This can be rewritten in the form

$$h = \left(\frac{2\pi R_d L}{P_{in}}\left(T_{tc} - T_\infty\right) + C_{\Delta T}\right)^{-1}, \quad \text{(B.10)}$$

where $C_{\Delta T}$ is a constant given by

$$C_{\Delta T} = -R_d\left[\frac{1}{k_d}\ln\left(\frac{R_d}{R_c}\right) + \frac{1}{k_c}\ln\left(\frac{R_c}{R_b}\right) + \frac{1}{k_b}\left\{\frac{1}{2} - \left(\frac{R_a^2}{R_b^2 - R_a^2}\right)\ln\left(\frac{R_b}{R_a}\right)\right\}\right]. \quad \text{(B.11)}$$

It is also possible to determine $C_{\Delta T}$ through a calibration rather than using the result of the one-dimensional model. Such a calibration may account for additional details of the setup that are not accounted for in the model. However, the principal result that $T_{tc} - T_{surf}$ is proportional to P_{in} will be retained.

Since the heat transfer coefficient is not being measured directly, it is necessary to determine the uncertainty associated with the value obtained as a function of the measured quantity uncertainties. Working with equation (B.10), the relevant partial derivatives are

$$\begin{aligned}
\frac{\partial h}{\partial T_{tc}} &= -\frac{2\pi R_d L}{P_{in}}\left(\frac{2\pi R_d L}{P_{in}}(T_{tc} - T_\infty) + C_{\Delta T}\right)^{-2} = -\frac{1 - hC_{\Delta T}}{T_{tc} - T\infty} h, \\
\frac{\partial h}{\partial T_\infty} &= \frac{2\pi R_d L}{P_{in}}\left(\frac{2\pi R_d L}{P_{in}}(T_{tc} - T_\infty) + C_{\Delta T}\right)^{-2} = \frac{1 - hC_{\Delta T}}{T_{tc} - T\infty} h, \\
\frac{\partial h}{\partial P_{in}} &= \frac{2\pi R_d L(T_{tc} - T_\infty)}{P_{in}^2}\left(\frac{2\pi R_d L}{P_{in}}(T_{tc} - T_\infty) + C_{\Delta T}\right)^{-2} = \frac{1 - hC_{\Delta T}}{P_{in}} h, \\
\frac{\partial h}{\partial R_d} &= -\frac{2\pi L(T_{tc} - T_\infty)}{P_{in}}\left(\frac{2\pi R_d L}{P_{in}}(T_{tc} - T_\infty) + C_{\Delta T}\right)^{-2} = -\frac{1 - hC_{\Delta T}}{R_d} h, \\
\frac{\partial h}{\partial L} &= -\frac{2\pi R_d(T_{tc} - T_\infty)}{P_{in}}\left(\frac{2\pi R_d L}{P_{in}}(T_{tc} - T_\infty) + C_{\Delta T}\right)^{-2} = -\frac{1 - hC_{\Delta T}}{L} h
\end{aligned} \tag{B.12}$$

and

$$\frac{\partial h}{\partial C_{\Delta T}} = -\left(\frac{2\pi R_d L}{P_{in}}(T_{tc} - T_\infty) + C_{\Delta T}\right)^{-2} = -h^2$$

The relative uncertainty in the heat transfer coefficient is then given by the expression

$$\left(\frac{\delta_h}{h}\right)^2 = (1 - hC_{\Delta T})^2\left[\frac{\delta_{T_{tc}}^2 + \delta_{T_\infty}^2}{(T_{tc} - T_\infty)^2} + \left(\frac{\delta_{P_{in}}}{P_{in}}\right)^2 + \left(\frac{\delta_{R_d}}{R_d}\right)^2 + \left(\frac{\delta_L}{L}\right)^2\right] + h^2\delta_{C_{\Delta T}}^2, \tag{B.13}$$

where δ represents the uncertainty in the quantity indicated by the subscript. Equation (B.13) represents measurement uncertainties only and does not account for any error produced by the assumptions used in developing the model.

In order to evaluate the impact of the one-dimensional assumption on the accuracy of the calculated heat transfer coefficient, the temperature profile produced by this model was compared to a two-dimensional calculation of the internal cylinder temperature using local heat transfer coefficient data from the literature.

Data from Gau et al. (1999) was used to estimate the local heat transfer coefficient as a function of angular position for a non-oscillating cylinder (Figure 1.8). The non-oscillating cylinder case was chosen because it had the largest difference between the minimum and maximum local Nusselt numbers and was therefore expected to depart the most from the one-dimensional assumption. This data was from experiments in air at a Reynolds number of 1600, so the local Nusselt numbers reported were scaled by $Re^{0.466}$ and $Pr^{1/3}$ following the correlation of Hilpert (1933) in equation (1.9). A 3rd order polynomial least-squares fit in θ^2 was used to represent the scaled data analytically.

The two-dimensional calculation was carried out using the MATLAB PDE Toolbox. A model was constructed having the same geometry, dimensions, and physical properties as the one-dimensional model for the AR = 14.2 cylinder. The boundary condition was specified using the previously mentioned polynomial fit to the scaled data as the local heat transfer coefficient. The steady heat equation in two dimensions was then solved, and the temperature at each grid point was determined. As expected, the temperature field was not axisymmetric, and the temperature was higher on the trailing half of the cylinder surface than on the leading half. The average heat transfer coefficient was then calculated by averaging the temperature at all grid points located on the cylinder surface and applying equation (1.7).

For comparison, equation (B.9) was solved to find the expected T_{tc} corresponding to the average heat transfer coefficient. This value was then used in equations (B.7a-d) to find the temperature profile for all radii inside the cylinder. Figure B.2 shows the difference between the temperature for every grid point in the two-dimensional calculation and the temperature at the corresponding radius from the one-dimensional model. The two-dimensional solution forms an asymmetric but organized scatter around the one-dimensional solution.

An upper bound was placed on the relative error of the one-dimensional model using this calculation. The temperature at the smallest radius in the two-dimensional solution was taken as T_{tc} and used to calculate the heat transfer coefficient using the one-dimensional model. The resulting value was 1.9% less than the heat transfer coefficient of the two-dimensional calculation. Assuming that the local heat transfer coefficient for the non-oscillating case is the furthest from axisymmetric of any case, this places an upper bound on the error associated with the one-dimensional assumption. This small relative error is on the same order as other sources of uncertainty in the experiment.

It is also possible to think of the resulting error as an offset in the measured thermocouple temperature. The temperature at the smallest radius in the two-dimensional calculation is 0.1°C above the thermocouple temperature that corresponds to the correct average heat transfer coefficient. Since the thermocouple itself has an uncertainty of ±0.1°C, it is unlikely that the one-dimensional assumption will affect the results in any significant way.

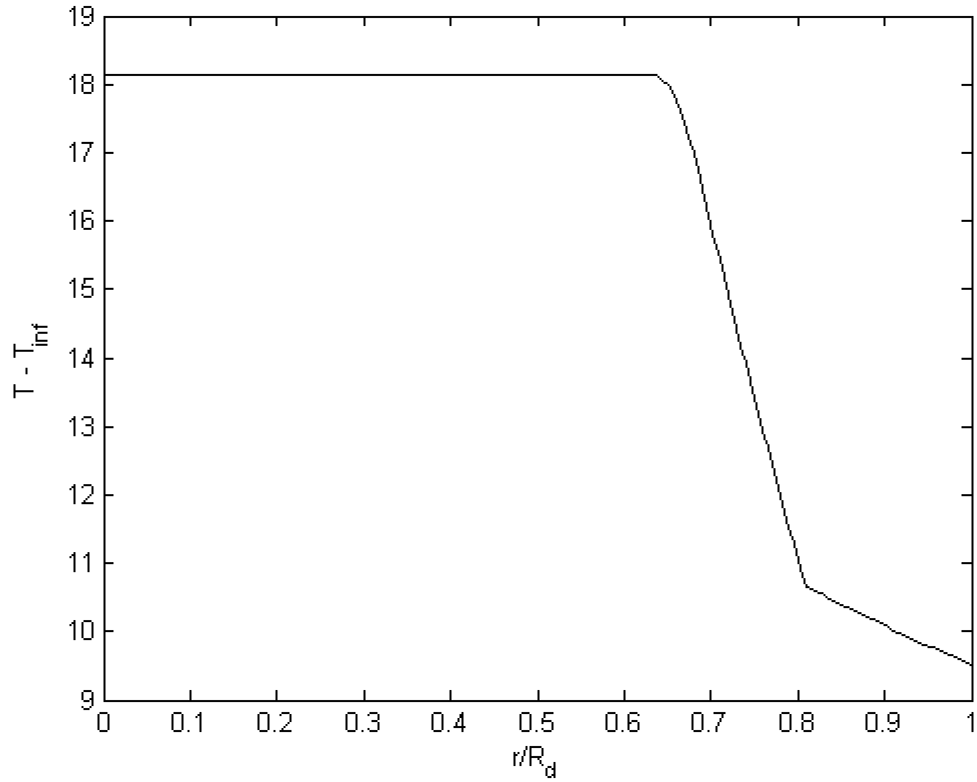

Figure B.1: Cylinder internal temperature profile using axisymmetric model with dimensions for large diameter cylinder and h = 1700 W/m^{2}K

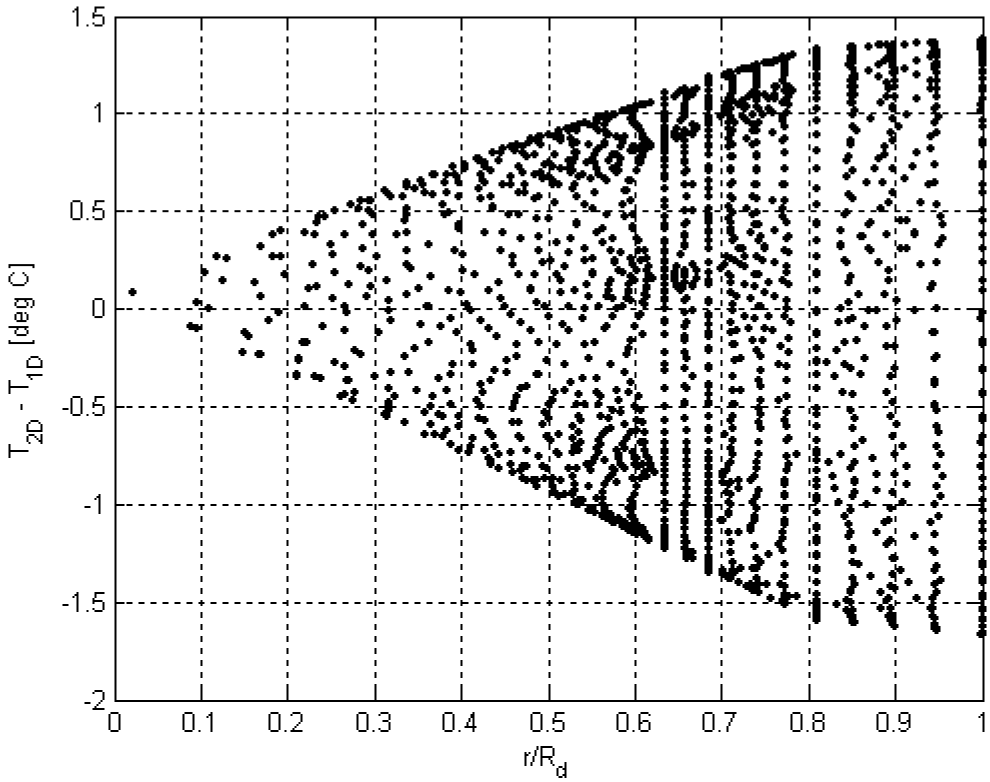

Figure B.2: Difference between cylinder temperatures calculated for one- and two-dimensional models for all angular coordinates

Appendix C
Unsteady, one-dimensional model of cylinder response to step change in heat transfer coefficient and determination of the cylinder thermal time constant

An unsteady, one-dimensional model of heat transfer inside the cylinder is developed in order to evaluate the time scale of temperature changes when the cylinder is subjected to a step change in heat transfer coefficient.

Starting from the same geometry as the steady model and equation (B.1), the temperature is again assumed to be independent of θ and z, but now the time dependence is retained. This yields the equation

$$\frac{\partial T}{\partial t} = \left(\frac{k}{\rho C}\right)\left(\frac{\partial^2 T}{\partial r^2} + \frac{1}{r}\frac{\partial T}{\partial r}\right) + \frac{p_{in}}{\rho C} = \alpha\left(\frac{\partial^2 T}{\partial r^2} + \frac{1}{r}\frac{\partial T}{\partial r}\right) + \frac{\alpha}{k}p_{in}, \tag{C.1}$$

where T = T(r,t) and α is the thermal diffusivity. The initial and boundary conditions are chosen to represent a situation where the heat transfer coefficient undergoes a step change, such that

$$h = \begin{cases} h_i, t < 0 \\ h_f, t \geq 0 \end{cases}, \tag{C.2}$$

where the subscripts i and f indicate the initial and final states. Combining equation (B.9) with equations (B.7a-d) and setting $h = h_i$ gives the initial condition T(r,0) = $T_i(r)$. The boundary conditions are given by

$$\begin{aligned} -k_d \left.\frac{\partial T}{\partial r}\right|_{r=R_d} &= h_f\left[T(R_d,t) - T_\infty\right] \\ \left.\frac{\partial T}{\partial r}\right|_{r=0} &= 0 \end{aligned} . \tag{C.3}$$

Equation (C.1) can be simplified by making the substitution

$$T(r,t) = \tilde{T}(r,t) + T_i(r), \tag{C.4}$$

where $\tilde{T}$ is the difference between the instantaneous temperature and the initial condition. The governing equation becomes

$$\frac{\partial \tilde{T}}{\partial t} = \alpha\left(\frac{\partial^2 \tilde{T}}{\partial r^2} + \frac{1}{r}\frac{\partial \tilde{T}}{\partial r}\right) \tag{C.5}$$

by using the fact that the power input and the initial condition form a solution to the steady equation (equation B.3). Using the steady solution boundary condition that

$$-k_d \left.\frac{dT_i}{dr}\right|_{r=R_d} = h_i\left[T_i(R_d) - T_\infty\right], \tag{C.6}$$

the boundary condition at the surface becomes

$$-k_d \left.\frac{\partial \tilde{T}}{\partial r}\right|_{r=R_d} = h_f \tilde{T}(R_d,t) + (h_f - h_i)\left[T_i(R_d) - T_\infty\right], \tag{C.7}$$

where the second term on the right hand side is a constant. At the center of the cylinder, the boundary condition remains

$$\left.\frac{\partial \tilde{T}}{\partial r}\right|_{r=0} = 0. \tag{C.8}$$

Though equation (C.5) is separable, the surface boundary condition (equation C.7) is not. Therefore, the unsteady model was solved numerically for a variety of heat transfer coefficients. It was found that the temperature at any particular radius exponentially approaches the longtime solution after a brief initial period of about 1 - 3 seconds for the AR = 14.2 cylinder, and about 1 - 2 sec for the AR = 21.3 cylinder.

Figure C.1 shows the temperature at the cylinder surface and on the cylinder axis for one particular case.

Since the initial time is short compared to the time scale of the exponential decay for both cylinders, it is disregarded in determining the thermal time constant for the cylinders. The thermal time constant, τ, is defined as the time required for the difference between the instantaneous temperature at a point to decay to 1/e times the initial difference at that point, such that

$$\frac{T(r,\tau)-T(r,t\to\infty)}{T_i(r)-T(r,t\to\infty)}=\frac{1}{e}. \qquad \text{(C.9)}$$

The longtime solution is taken to be the solution of the steady model for $h = h_f$.

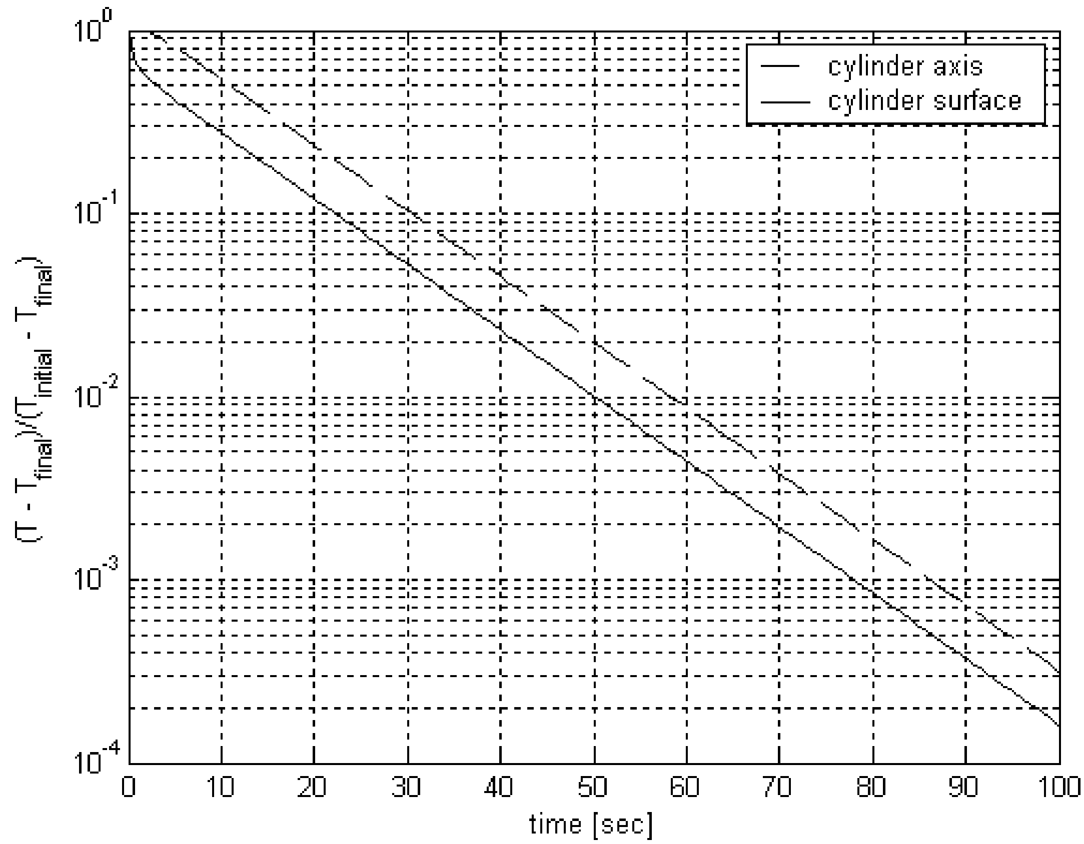

Figure C.1: Normalized surface and axial temperatures vs. time for model of cylinder subjected to step change in heat transfer coefficient using properties of the AR = 14.2 cylinder with Nu_f/Nu_0 = 2.38

References

Bishop, R. E. D. and Hassan, A. Y. 1964. The lift and drag forces on a circular cylinder oscillating in a flowing fluid. *Proceedings of the Royal Society (London) Series A* **277**:51-75.

Brika, D. and Laneville, A. 1993. Vortex-induced vibrations of a long flexible circular cylinder. *Journal of Fluid Mechanics* **250**:481-508.

Carberry, J., Sheridan, J. and Rockwell, D. 2001. Forces and wake modes of an oscillating cylinder. *Journal of Fluids and Structures* **15**:523-532.

Cheng, C.-H., Chen, H.-N. and Aung, W. 1997. Experimental study of the effect of transverse oscillation on convection heat transfer from a circular cylinder. *Journal of Heat Transfer* **119**:474-482.

Cheng, C.-H. and Hong, J.-L. 1997. Numerical prediction of lock-on effect on convective heat transfer from a transversely oscillating circular cylinder. *International Journal of Heat and Mass Transfer* **40**(8):1825-1834.

Dabiri, D. and Gharib, M. 1991. Digital particle image thermometry: The method and implementation. *Experiments in Fluids* **11**:77-86.

Gau, C., Wu, J. M. and Liang, C. Y. 1999. Heat transfer enhancement and vortex flow structure over a heated cylinder oscillating in the crossflow direction. *Journal of Heat Transfer* **121**:789-795.

Gharib, M., Rambod, E. and Shariff, K. 1998. A universal time scale for vortex ring formation. *Journal of Fluid Mechanics* **360**:121-140.

Hilpert, R. 1933. *Forsch. Geb. Ingenieurwes.*, **4**, 215.

Incropera, F. P. and Dewitt, D. P. 1996. *Fundamentals of Heat and Mass Transfer*, 4th ed., John Wiley and Sons, New York.

Jeon, D. and Gharib, M. 2003. (pre-print) On the relationship between the vortex formation process and cylinder wake vortex patterns. *Journal of Fluid Mechanics*.

Karanth, D., Rankin, G. W. and Sridhar, K. 1994. A finite difference calculation of forced convective heat transfer from an oscillating cylinder. *International Journal of Heat and Mass Transfer* **37**(11):1619-1630.

Kezios, S. P. and Prasanna, K. V. 1966. Effect of vibration on heat transfer from a cylinder in normal flow. ASME Paper No. 66-WA/HT-43.

Khalak, A and Williamson, C. H. K. 1999. Motions, forces and mode transitions in vortex-induced vibrations at low mass-damping. *Journal of Fluids and Structures* **13**:813-851.

Klein, E. J. 1968. Application of liquid crystal to boundary layer flow visualization. AIAA Paper No.68-376.

McKenna, S. P. and McGillis, W. R. 2002. Performance of digital image velocimetry processing techniques. *Experiments in Fluids* **32**(1):106-115.

Norberg, C. 1994. An experimental investigation of the flow around a circular cylinder: influence of aspect ratio. *Journal of Fluid Mechanics* **258**:287-316.

Norberg, C. 2003. Fluctuating lift on a circular cylinder: review and new measurements. *Journal of Fluids and Structures* **17**:57-96.

Park, H. G. 1998. *A Study of Heat Transfer Processes in the Wake of a Stationary and Oscillating Circular Cylinder Using Digital Particle Image Velocimetry / Thermometry*. Ph.D. Thesis, California Institute of Technology.

Park, H. G., Dabiri, D. and Gharib, M. 2001. Digital particle image velocimetry/thermometry and application to the wake of a heated circular cylinder. *Experiments in Fluids* **30**:327-338.

Parsley, M. 1991. *The Hallcrest Handbook of Thermochromic Liquid Crystal Technology*, Hallcrest, Glenview, IL.

Perry, A.E. and Fairlie, B.D. 1974. Critical points in flow patterns. *Advances in Geophysics*, **18B**:299-315.

Pottebaum, T. S. and Gharib, M. 2003. (submitted) The pinch-off process in a starting buoyant plume. *Experiments in Fluids*.

Rhee, H. S., Koseff, J. R. and Street, R. L. 1984. Flow visualization of a recirculating flow by rheoscopic liquid and liquid crystal techniques. *Experiments in Fluids* **2**:57-64.

Sabatino, D. R., Praisner, T. J. and Smith, C. R. 2000. A high-accuracy calibration technique for thermochromic liquid crystal temperature measurements. *Experiments in Fluids* **28**:497-505.

Saxena, U. C. and Laird, A. D. K. 1978. Heat transfer from a cylinder oscillating in a cross-flow. *Journal of Heat Transfer* **100**:684-689.

Seuntiens, H. J., Kieft, R. N., Rindt, C. C. M. and van Steenhoven, A. A. 2001. 2D temperature measurements in the wake of a heated cylinder using LIF. *Experiments in Fluids* **31**:588-595.

Sreenivasan, K. and Ramachandran, A. 1961. Effect of vibration on heat transfer from a horizontal cylinder to a normal air stream. *International Journal of Heat and Mass Transfer* **3**:60-67.

Taneda, S. 1956. Experimental investigation of the wakes behind cylinders and plates at low Reynolds numbers, *Journal of Physical Society of Japan*, **11**, p. 302.

Willert, C. E. and Gharib, M. 1991. Digital particle image velocimetry. *Experiments in Fluids* **10**:181-193.

Williamson, C. H. K. and Roshko, A. 1988. Vortex formation in the wake of an oscillating cylinder. *Journal of Fluids and Structures* **2**:355-381.

Zhukauskas, A. 1972. “Heat transfer from tubes in cross flow,” in Hartnett, J.P. and Irvine, T.F. Jr., Eds., *Advances in Heat Transfer*, Vol. 8, Academic Press, New York.